

AD-A052 674

AUBURN UNIV ALA

COMPUTER AIDED OPTICAL NONDESTRUCTIVE FLAW DETECTION SYSTEM FOR--ETC(U)

SEP 77 J A SCHAEFFEL, B R MULLINIX

DAAK40-77-C-0028

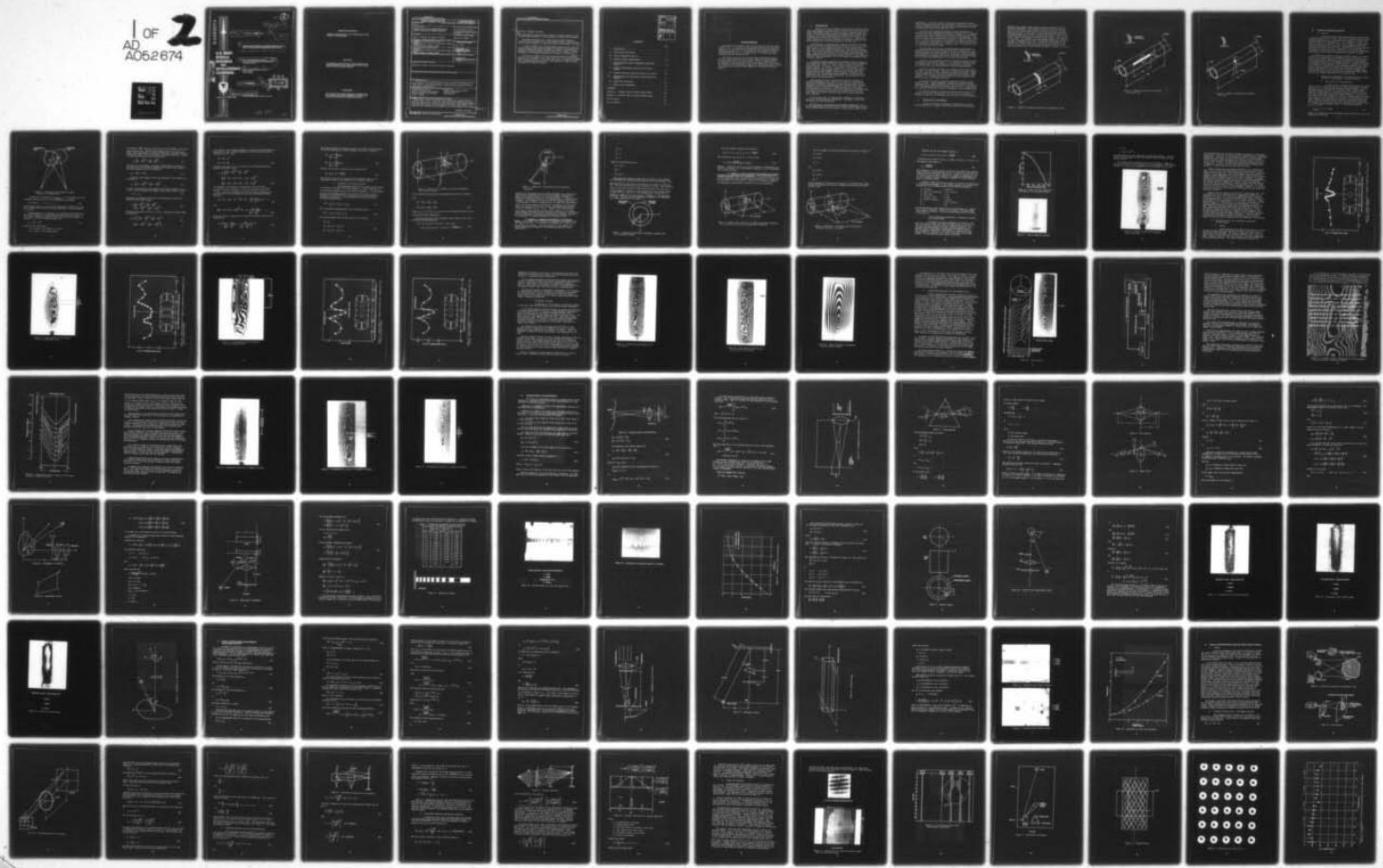
DRDMI-T-78-5

NL

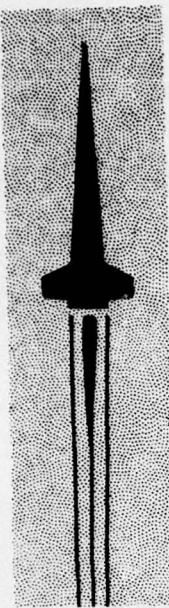
UNCLASSIFIED

F/6 11/5

1 OF 2
AD-A052674



ADA052674



2

18 DRDMI-T

9 Final TECHNICAL REPORT T-78-5

19 78-5

6 COMPUTER AIDED OPTICAL NONDESTRUCTIVE FLAW
DETECTION SYSTEM FOR COMPOSITE MATERIALS

JDC FILE COPY

**U.S. ARMY
MISSILE
RESEARCH
AND
DEVELOPMENT
COMMAND**



Redstone Arsenal, Alabama 35809

10 John A. Schaeffel, Bobby R. Mullinix,
Ground Equipment and Missile Structures Directorate
Technology Laboratory

and
William F. Ranson, Weldon F. Swinson
Auburn University
Auburn, Alabama

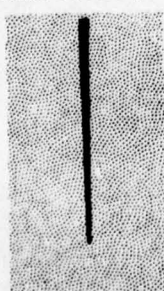
11 26 Sept 1977

12 182 p.

DDC
REF ID: B
APR 14 1978
B

15 DAAK40-77-C-0028

Approved for public release; distribution unlimited.



DMI FORM 1000, 1 APR 77

046 850

mt

DISPOSITION INSTRUCTIONS

**DESTROY THIS REPORT WHEN IT IS NO LONGER NEEDED. DO NOT
RETURN IT TO THE ORIGINATOR.**

DISCLAIMER

**THE FINDINGS IN THIS REPORT ARE NOT TO BE CONSTRUED AS AN
OFFICIAL DEPARTMENT OF THE ARMY POSITION UNLESS SO DESIG-
NATED BY OTHER AUTHORIZED DOCUMENTS.**

TRADE NAMES

**USE OF TRADE NAMES OR MANUFACTURERS IN THIS REPORT DOES
NOT CONSTITUTE AN OFFICIAL INDORSEMENT OR APPROVAL OF
THE USE OF SUCH COMMERCIAL HARDWARE OR SOFTWARE.**

UNCLASSIFIED

SECURITY CLASSIFICATION OF THIS PAGE (When Data Entered)

UNCLASSIFIED

SECURITY CLASSIFICATION OF THIS PAGE(When Data Entered)

Block 20. ABSTRACT (Continued)

The fringe density plots were made by manual and computer methods, and the flaw sizes were determined. The displacements and strains were computed.

The results show that flaws in their fiber reinforced composite structures can be detected and the size determined either by optical holographic, shearing speckle, or single beam speckle interferometric techniques.

A complete nondestructive testing system to detect, locate, size, and quantify flaws in fiber reinforced composite missile launch tubes and motor cases was designed including the hardware and software. The system was assembled, interfaced, checked, and the data from it validated. Complete documentation on the system components are presented or referenced.

The system as presented utilizes the shearing speckle techniques to determine if a flaw exists in the launch tube; if so, it indicates the region where the flaw is located. The point-by-point method of Young's Fringes is used to determine the surface strain in the region of the flaw and if the item should be accepted or rejected.

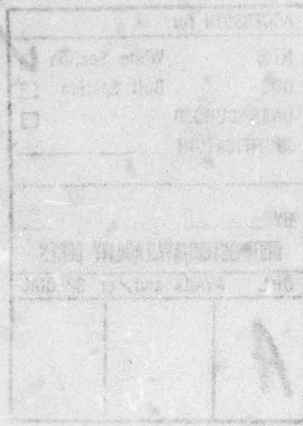
UNCLASSIFIED

SECURITY CLASSIFICATION OF THIS PAGE(When Data Entered)

ACCESSION for	
NTIS	White Section <input checked="" type="checkbox"/>
DDC	Buff Section <input type="checkbox"/>
UNANNOUNCED <input type="checkbox"/>	
JUSTIFICATION _____	
BY _____	
DISTRIBUTION/AVAILABILITY CODES	
Dist.	AVAIL and/or SPECIAL
A	

CONTENTS

	Page
I. INTRODUCTION	3
II. DEFINITION OF THE PROBLEM	4
III. OPTICAL HOLOGRAPHIC ANALYSIS	8
IV. SHEARING SPECKLE INTERFEROMETRY	42
V. DOUBLE EXPOSURE SPECKLE PHOTOGRAPHY SINGLE BEAM ANALYSIS	67
VI. SPECKLE INTERFEROMETRIC ANALYSIS USING YOUNG'S FRINGES	77
VII. COMPUTER AIDED DATA REDUCTION SYSTEMS AND SOFTWARE	109
VIII. COMPUTER AIDED DATA REDUCTION SYSTEMS HARDWARE AND OPERATION	140
IX. SUMMARY AND CONCLUSIONS	151
X. FUTURE SYSTEM IMPROVEMENTS	153
REFERENCES	154
Appendix A. COMPUTER CODE FOR VIDICON CAMERA SYSTEM	157
Appendix B. COMPUTER CODE FOR ROTATING MIRROR SYSTEM	166
LIST OF TABLES	176
LIST OF FIGURES	176



ACKNOWLEDGMENTS

The authors hereby express their sincere gratitude and deep appreciation to Mr. V. G. Irelan for his assistance with the electronics and lasers, Mr. O. C. Fruchtnicht for making the fiber reinforced composite cylindrical specimen, Dr. Y. Y. Hung for his consultation on speckle interferometry, and Mr. W. B. Matkin and Ms. D. K. Russell for their assistance with the laboratory work.

The contract support of the in-house effort from Sperry Support Services on the electronic and mechanical hardware design and fabrication was timely and of excellent quality. Credit is especially due Mr. Michael E. Casciola who served as project engineer, Mr. David Himes for electronics and documentation support, Mr. Phil Catlett and J. B. Cecil for design support, and Mr. Howard Shahan for mechanical fabrication support.

I. INTRODUCTION

Growth in the use of composite materials for structural applications has generated an urgent need for the detection and evaluation of flaws inadvertently induced in such structures by manufacturing procedures. Such detection and evaluation procedures can be grouped, quite naturally, with other nondestructive test (NDT) methods used in the inspection and evaluation of homogeneous structures. It appears that recent advances in the fields of optical and acoustical holography may permit applications of these technologies to the NDT field.

In recent years, filament-wrapped composite structures have been utilized in small solid-propellant rocket motors and launch tubes with great success. Use of composite materials in this application has merit due to the high strength-to-weight ratio, the low cost of manufacture, and the ease of assembly of the rocket motor case and grain components. Due to the size and nature of such rocket motors and launch tubes, production would occur in an automated fashion at very high rates. Obviously, such high production rates will require an automated system of quality control.

It has been found by experience that flaws are likely to occur in the manufacture of small rocket motor cases in the form of unbonded surfaces where bonds should be. These unbonded regions can occur for several reasons. For example, if the region is contaminated with a foreign substance such as water, grease, etc., the bond will not form. Also, failure to apply adhesive properly to the entire region will prevent the bond from forming. Such conditions are bound to occur occasionally in a mass-production-type operation. The problem is to detect such flaws, assess their significance, and discard the faulty motor case if conditions warrant.

Electro-optical devices associated with optical holography or speckle interferometry can be used for the detection of such flaws. The optical holographic technique is based upon the premise that the character of the surface displacements of a structure with a flaw are different when the structure is loaded than when it is not loaded. Such differences in character can be vividly detected interferometrically by comparing holograms of the loaded and unloaded flawed structure. These comparisons produce fringe patterns with distinct aberrations near a flaw [1].

At the present time, the experimental techniques for detecting flaws have been demonstrated qualitatively. Assessment of flaw sizes and shapes have been demonstrated.

The objective of this work was to determine the magnitude of the surface displacement and surface strains of three hollow composite cylindrical pressure vessels in the vicinity of three typical flaws (or flaw

simulations). Structural analysis to model such structures is evaluated and suggestions are made for improvement. Section II of this report defines the fiber reinforced composite specimens containing known flaws including dimensional details and flaw sizes.

The theory and experimental analysis of optical holography as applied to the three specimens are included in Section III. A technique for real-time optical holography can be used to observe how the fringe pattern behaves under loading conditions which are time dependent. This provides a rapid way to optimize the loading for a specific type of specimen. A method to determine the size and shape of flaws from the optical holographic fringe patterns is presented. The computer software for this technique was developed and a computer plot of "U" curves was used to locate and quantify the flaws.

The equations needed to apply shearing speckle interferometry to thin-walled cylindrical launch tubes are derived in Section IV. This method is proven to be valid through the use of a cantilever beam where the displacements are easily measured or calculated. Shearing speckle interferograms are presented for each of three different types of flaws. This is a good whole-field method to detect and locate flaws.

The theory for a single beam analysis using double-exposure speckle photography is presented in Section V. Its validity is verified using a cantilever beam. It can be shown that this theory is equivalent to the point-by-point data interpretation of Young's Fringe Analysis.

Section VI presents the theory for the point-by point data interpretation of Young's Fringes. Equations to compute the surface strains from the fringe data for the cylindrical specimen are included. Sample fringe patterns and data plotted in graphic forms show results of this technique. It is perhaps the simplest method to use to determine the surface strains in the region of a flaw.

In Section VII, the data reduction systems and software are discussed in detail. System components included are the vidicon camera, rotating mirror, computer interfaces, and the main computer code description. The computer codes for the vidicon camera and the rotating mirror data reduction systems are included in Appendices A and B, respectively.

The system's hardware and operation including the electronic subsystems are covered in Section VIII. Sections IX and X contain the summary, conclusions, and recommendations for future system improvements.

II. DEFINITION OF THE PROBLEM

To aid in the task of developing an experimental technique for flaw detection in composite structures, three test structures were

designed with simulated flaws placed in specific locations and with specific orientations. The simulated flaws were created by placing thin strips of Teflon plastic between the two helical wraps of filaments at the center of the walls of the hollow cylindrical structures. The Teflon strips were intended to inhibit bonding of the resin in the composite between layers at the location of the strips. Thus, the two center layers of the composite structure would be free to move relative to each other. The purpose of the three models designed for study was to permit a comparison to be made of experimental and analytical predictions of the displacements on the surface of the cylinders in the vicinity of the flaws. All models were manufactured with 60° helix wraps and details of each type specimen are shown in Figures 1, 2, and 3.

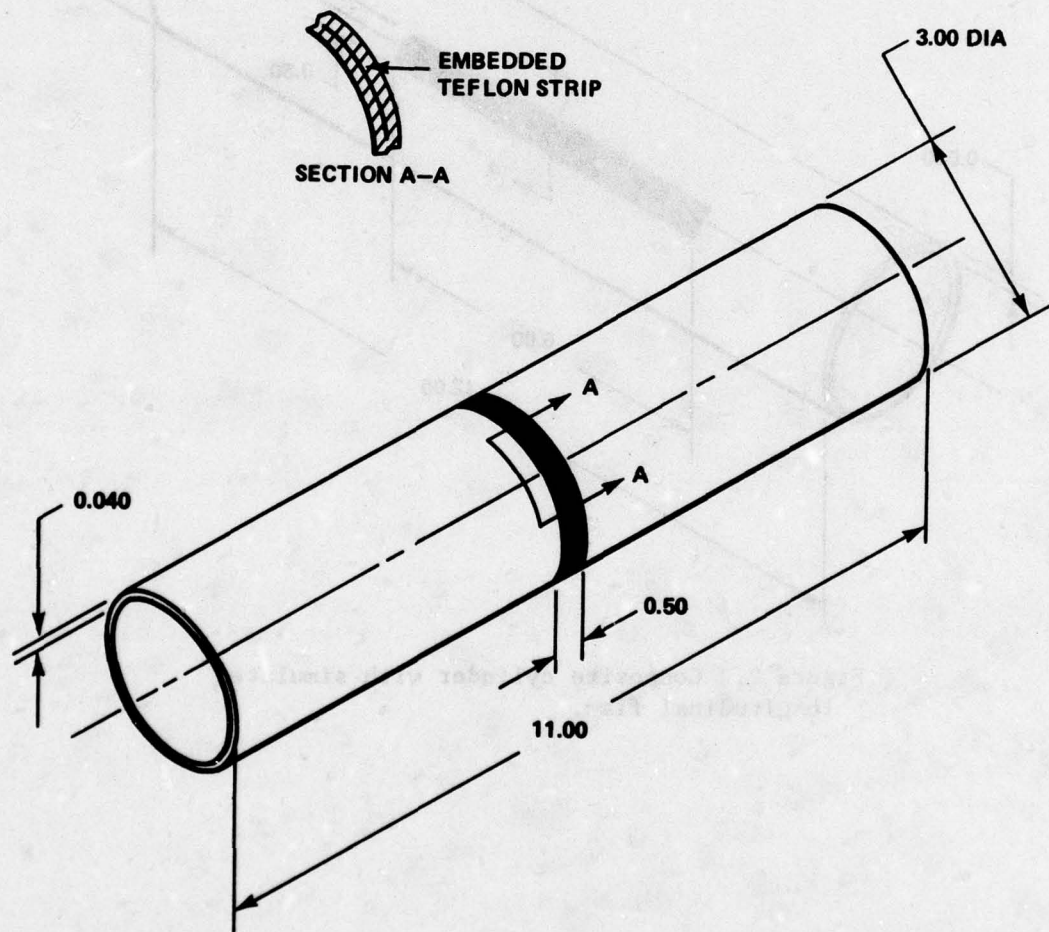


Figure 1. Composite cylinder with simulated circumferential flaw.

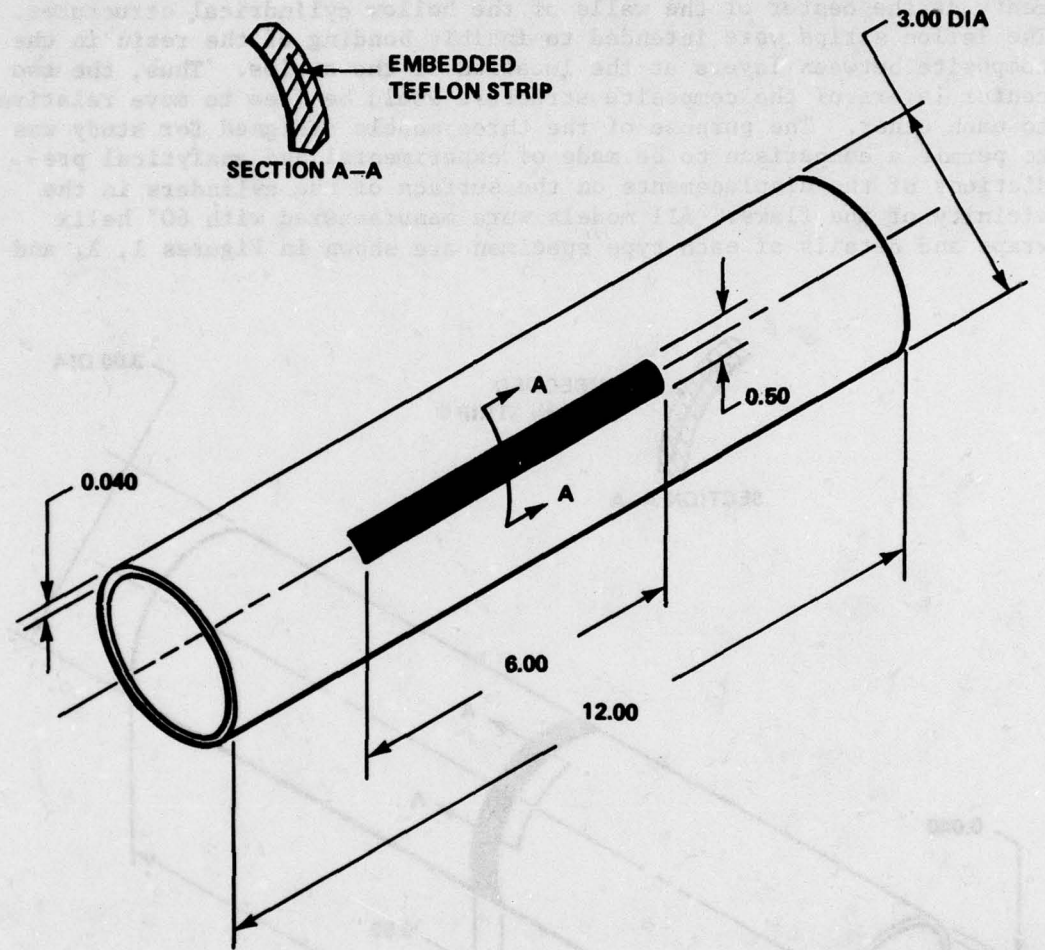


Figure 2. Composite cylinder with simulated longitudinal flaw.

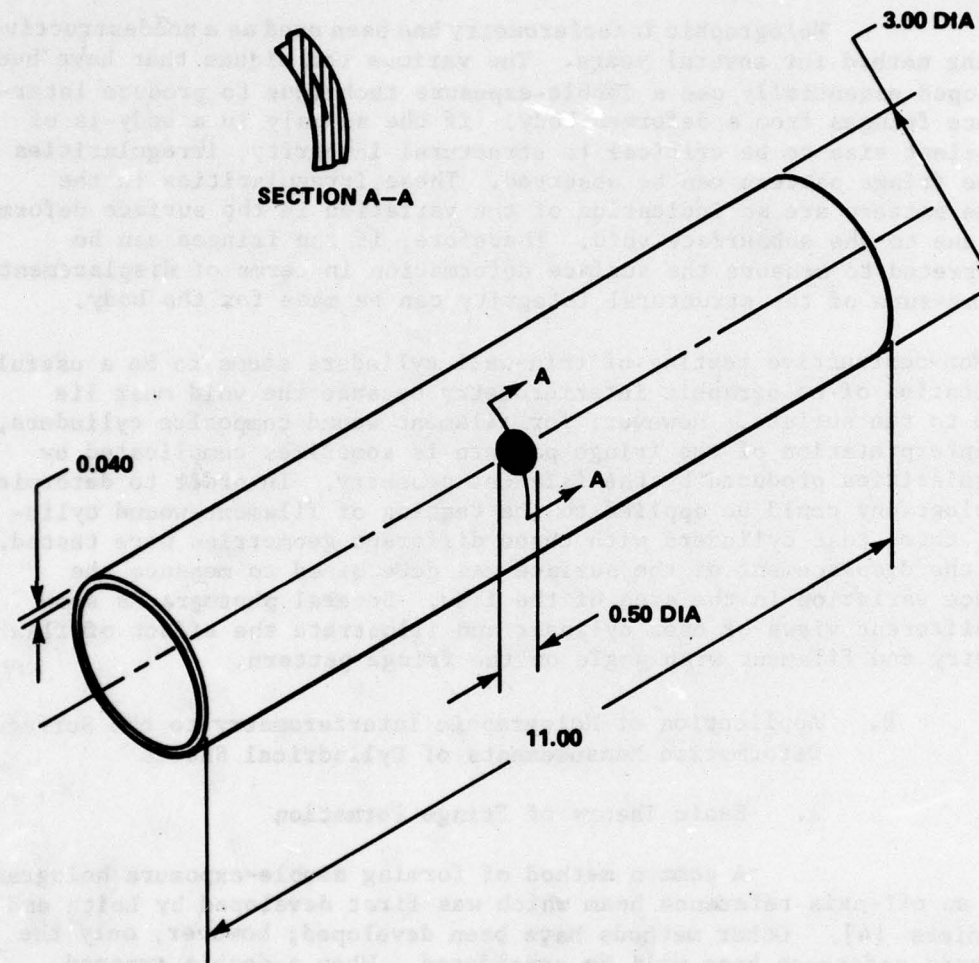


Figure 3. Composite cylinder with simulated spot flaw.

III. OPTICAL HOLOGRAPHIC ANALYSIS

A. General

Holographic interferometry has been used as a nondestructive testing method for several years. The various techniques that have been developed essentially use a double-exposure technique to produce interference fringes from a deformed body. If the anomaly in a body is of sufficient size to be critical to structural integrity, irregularities in the fringe pattern can be observed. These irregularities in the fringe pattern are an indication of the variation in the surface deformation due to the subsurface void. Therefore, if the fringes can be interpreted to measure the surface deformation in terms of displacements, some measure of the structural integrity can be made for the body.

Non-destructive testing of thin-wall cylinders seems to be a useful application of holographic interferometry because the void must lie close to the surface. However, for filament wound composite cylinders, the interpretation of the fringe pattern is sometimes complicated by irregularities produced by the filament geometry. In order to determine if holography could be applied to the testing of filament-wound cylinders, three test cylinders with three different geometries were tested. Also, the displacement of the surface was determined to measure the surface variation in the area of the flaw. Several photographs show the different views of each cylinder and illustrate the effect of flaw geometry and filament wrap angle on the fringe pattern.

B. Application of Holographic Interferometry to the Surface Deformation Measurements of Cylindrical Shells

1. Basic Theory of Fringe Formation

A common method of forming double-exposure holograms uses an off-axis reference beam which was first developed by Leith and Upatnieks [4]. Other methods have been developed; however, only the off-axis reference beam will be considered. When a double exposed hologram is reconstructed, interference fringes are formed on the body due to any displacement of the body between exposures. If the displacement results from deformation as shown in Figure 4 then the fringes are a measure of this deformation. This result is obtained due to the phase change of the light due to deformation of the body between exposures. The basic equation which predicts the interference fringes is the intensity of the virtual image. The intensity of the virtual image in a doubly exposed hologram is given in the following equation [3, 4, 5, 6, 7]:

$$I_{VIRUAL} = C [1 + \cos \Delta \theta] \quad (1)$$

where C is a constant and $\Delta \theta$ is the phase change of the light due to the deformation of the body.

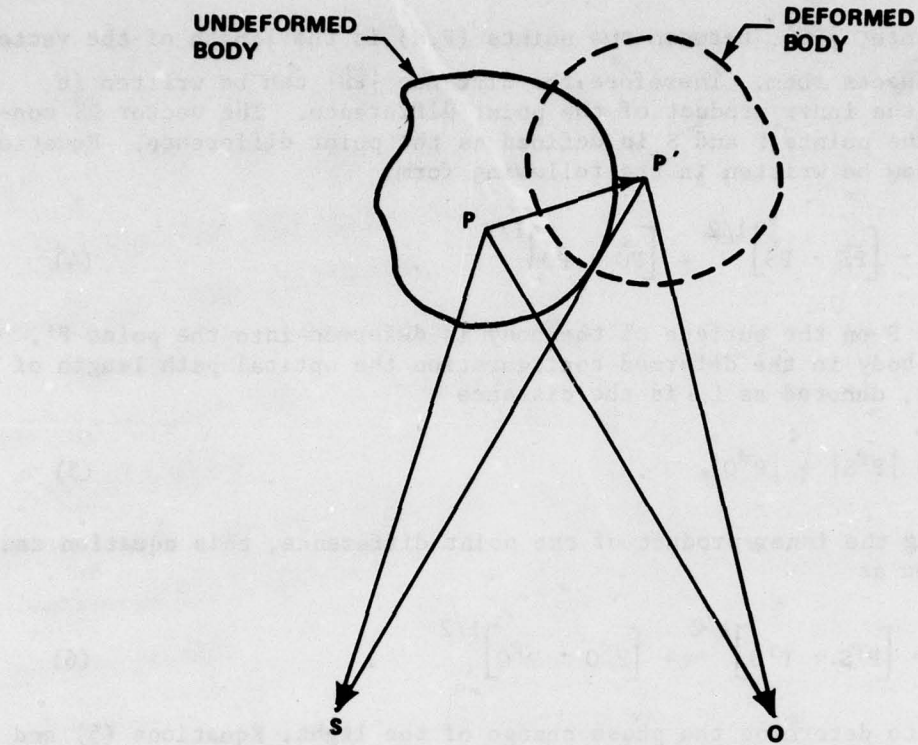


Figure 4. Geometrical relationships for phase change for a deformed body.

A fringe will be defined with $I_{VIRUAL} = 0$. From Equation (1) the following condition results from the definition of a fringe

$$\Delta\theta = (2n-1)\pi \quad n = 1, 2, 3, \dots \quad . \quad (2)$$

The counting number, n , is called the fringe order. Equation (2) is the basic equation which relates the fringe information to the deformation of the body.

The phase change $\Delta\theta$ in Equation (2) is determined from the optical path length change of the light between exposures of the hologram. In the reference condition (undeformed state) the optical path length is denoted by L_1 and is the distance (Figure 4).

$$L_1 = \overrightarrow{|PS|} + \overrightarrow{|PO|} \quad (3)$$

where S is the light source

P is a point on the surface of the body

O is a point in the hologram plane.

The distance, $|\vec{PS}|$, between two points (P, S) is the length of the vector which connects them. Therefore, the distance $|\vec{PS}|$ can be written in terms of the inner product of the point difference. The vector \vec{PS} connecting the points P and S is defined as the point difference. Equation (3) can now be written in the following form:

$$L_1 = \left[\vec{PS} \cdot \vec{PS} \right]^{1/2} + \left[\vec{PO} \cdot \vec{PO} \right]^{1/2} . \quad (4)$$

The point P on the surface of the body is deformed into the point P' . With the body in the deformed configuration the optical path length of the light, denoted as L_2 , is the distance

$$L_2 = |\vec{P'S}| + |\vec{P'O}| . \quad (5)$$

Using the inner product of the point difference, this equation can be written as

$$L_2 = \left[\vec{P'S} \cdot \vec{P'S} \right]^{1/2} + \left[\vec{P'O} \cdot \vec{P'O} \right]^{1/2} . \quad (6)$$

In order to determine the phase change of the light, Equations (5) and (6) are used to determine the change in optical path length Δ , where

$$\Delta = L_1 - L_2 . \quad (7)$$

Substitution of Equations (5) and (6) into Equation (7) yields for the optical path length change

$$\Delta = \left[\vec{PS} \cdot \vec{PS} \right]^{1/2} + \left[\vec{PO} \cdot \vec{PO} \right]^{1/2} - \left[\vec{P'S} \cdot \vec{P'S} \right]^{1/2} - \left[\vec{P'O} \cdot \vec{P'O} \right]^{1/2} . \quad (8)$$

The phase change $\Delta\theta$ is related to Δ by $2\pi/\lambda$, therefore the phase change is written as

$$\Delta\theta = \frac{2\pi}{\lambda} \left\{ \left[\vec{PS} \cdot \vec{PS} \right]^{1/2} + \left[\vec{PO} \cdot \vec{PO} \right]^{1/2} - \left[\vec{P'S} \cdot \vec{P'S} \right]^{1/2} - \left[\vec{P'O} \cdot \vec{P'O} \right]^{1/2} \right\} . \quad (9)$$

This equation, while completely general, is not in a form convenient for numerical use. Let the point difference of the body before and after deformation be $\vec{P}\vec{P}'$, then

$$\vec{P}\vec{S} = \vec{P}'\vec{S} + \vec{P}\vec{P}'$$

$$\vec{P}\vec{O} = \vec{P}'\vec{O} + \vec{P}\vec{P}'$$

(10)

Therefore, Equation (9) can be written in the following form using equation (16), which yields

$$\begin{aligned} \Delta\theta = \frac{2\pi}{\lambda} & \left\{ \left[\vec{P}\vec{S} + \vec{P}\vec{S} \right]^{1/2} + \left[\vec{P}\vec{O} \cdot \vec{P}\vec{O} \right]^{1/2} \right. \\ & - \left. \left[(\vec{P}\vec{S} \cdot \vec{P}\vec{S}) - 2(\vec{P}\vec{S} \cdot \vec{P}\vec{P}') + (\vec{P}\vec{P}' \cdot \vec{P}\vec{P}') \right]^{1/2} \right. \\ & - \left. \left[(\vec{P}\vec{O} \cdot \vec{P}\vec{O}) - 2(\vec{P}\vec{O} \cdot \vec{P}\vec{P}') + (\vec{P}\vec{P}' \cdot \vec{P}\vec{P}') \right]^{1/2} \right. . \end{aligned} \quad (11)$$

In holographic interferometry, displacements of points between exposures are small; therefore, it will be assumed here that $|\vec{P}\vec{P}'|^2 \ll |\vec{P}\vec{P}'|$. Using this information the last two terms in Equation (11) can be written in the following form for small deformations between exposures:

$$(\vec{P}\vec{S} \cdot \vec{P}\vec{S}) - 2(\vec{P}\vec{S} \cdot \vec{P}\vec{P}') \stackrel{1/2}{\simeq} \vec{P}\vec{S} \cdot \vec{P}\vec{S} - \frac{\vec{P}\vec{S} \cdot \vec{P}\vec{P}'}{\vec{P}\vec{O} \cdot \vec{P}\vec{O}^{1/2}} + \dots \quad (12)$$

and

$$\left[(\vec{P}\vec{O} \cdot \vec{P}\vec{O}) - 2(\vec{P}\vec{O} \cdot \vec{P}\vec{P}') \right]^{1/2} \simeq \vec{P}\vec{O} \cdot \vec{P}\vec{O} - \frac{\vec{P}\vec{O} \cdot \vec{P}\vec{P}'}{\left[\vec{P}\vec{O} \cdot \vec{P}\vec{O} \right]^{1/2}} + \dots \quad (13)$$

Using the results in Equations (12) and (13), the phase change can now be written as

$$\Delta\theta = \frac{2\pi}{\lambda} \left[\frac{\vec{P}\vec{S}}{\left[\vec{P}\vec{S} \cdot \vec{P}\vec{S} \right]^{1/2}} + \frac{\vec{P}\vec{O}}{\left[\vec{P}\vec{O} \cdot \vec{P}\vec{O} \right]^{1/2}} \right] \cdot \vec{P}\vec{P}' . \quad (14)$$

The terms in brackets in Equation (14) are unit vectors in the direction \vec{PS} and \vec{PO} ; therefore, the following change in notation is employed:

$$\vec{ps} = \frac{\vec{PS}}{\left[\vec{PS} \cdot \vec{PS} \right]^{1/2}}$$

$$\vec{po} = \frac{\vec{PO}}{\left[\vec{PO} \cdot \vec{PO} \right]^{1/2}} . \quad (15)$$

Equation (2) can now be written in the following form:

$$[\vec{ps} + \vec{po}] \cdot \vec{PP'} = \frac{(2n-1)\lambda}{2} . \quad (16)$$

These results are still in a general form and special cases will be considered in regard to the deformation of cylindrical shells.

2. Deformation of Cylindrical Shells

The displacement vector $\vec{PP'}$ of a point on the surface of the shell is resolved into three components, a radial component U_r , a circumferential component U_ϕ , and longitudinal component U_z . The experimental geometry and coordinate system of the cylinder are shown in Figure 5. The point P on the surface can be represented in either cartesian or cylindrical coordinates. In the cartesian system let $\vec{PP'}$ have the following representation:

$$\vec{PP'} = U_{X_1} \vec{e}_1 + U_{X_2} \vec{e}_2 + U_{X_3} \vec{e}_3 , \quad (17)$$

and the following representation in the cylindrical system

$$\vec{PP'} = U_r \vec{e}_r + U_\phi \vec{e}_\phi + U_z \vec{e}_z . \quad (18)$$

The relation between the unit base vectors are as follows:

$$\vec{e}_z = \vec{e}_2$$

$$\vec{e}_r = \vec{e}_1 \sin \phi + \vec{e}_3 \cos \phi$$

$$\vec{e}_\phi = \vec{e}_1 \cos \phi - \vec{e}_3 \sin \phi . \quad (19)$$

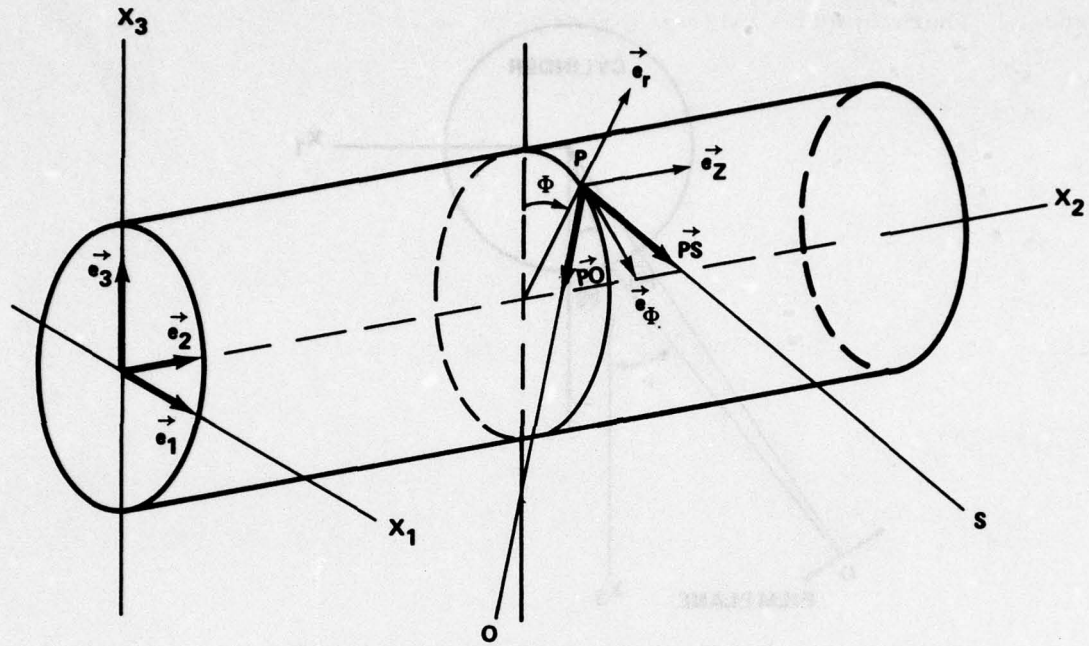


Figure 5. Geometry used to measure the surface deformation of cylindrical shells.

Let the vectors \vec{ps} and \vec{po} have the representations shown in Figure 6.

Then,

$$\begin{aligned}\vec{ps} &= \ell_1 \vec{e}_1 + \ell_2 \vec{e}_2 + \ell_3 \vec{e}_3 \\ \vec{po} &= m_1 \vec{e}_1 + m_2 \vec{e}_2 + m_3 \vec{e}_3\end{aligned}\quad (20)$$

where ℓ_1, ℓ_2, ℓ_3 and m_1, m_2, m_3 are the set of direction cosines of the vectors \vec{ps} and \vec{po} , respectively.

Using the notation for the cylindrical shell, Equation (16) can be written in the following form:

$$\begin{aligned}(\ell_1 + m_1) (U_r \sin \Phi + U_\Phi \cos \Phi) + (\ell_2 + m_2) U_z \\ + (\ell_3 + m_3) (U_r \cos \Phi - U_\Phi \sin \Phi) = \frac{(2n-1)\lambda}{2}\end{aligned}\quad (21)$$

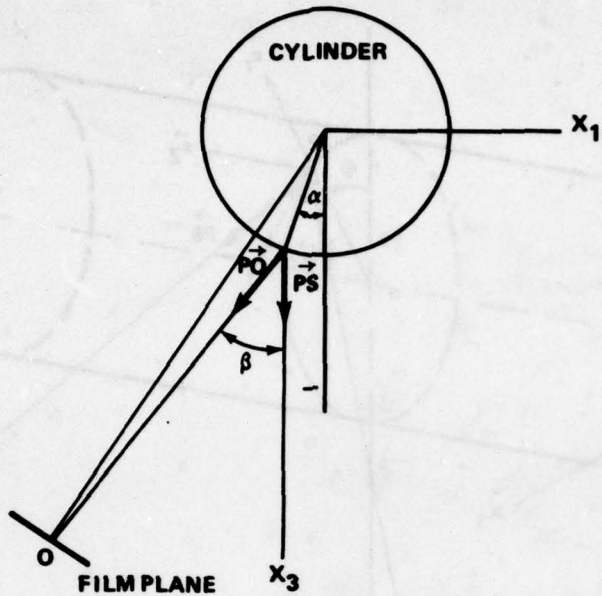


Figure 6. Geometrical relationships for the directions \vec{PS} and \vec{PO} .

Equation (21) illustrates that the fringe information in a single hologram contains information for all three displacement components that cannot be determined uniquely from a single hologram. In order to determine the components uniquely three holograms must be recorded simultaneously. Each hologram will have an equation relating fringe order to displacements as given in Equation (21). In each case, the direction cosines to the unit vectors \vec{ps} and \vec{po} will be different for each hologram. This general procedure will require considerable data reduction in order to determine U_r , U_ϕ , and U_z . However, some simplifications can be made in many problems; and with careful selection of the experimental geometry the amount of data reduction can be reduced. Two examples will be considered to illustrate the application of Equation (21) to the measurement of surface deformation of cylindrical shells.

(a) Example 1: Symmetrical Deformation of Cylindrical Shells. The cylinder will be assumed to be deformed symmetrically about the longitudinal axis. For this case, the component $U_\phi = 0$ and U_r , U_z are assumed to be nonzero. Direction cosines for this geometry are shown schematically in Figure 6. The direction cosines for the PS direction are

$$\ell_1 = 0$$

$$\ell_2 = 0$$

$$\ell_3 = 1$$

Values for the \vec{PO} direction are

$$m_1 = -\sin \beta$$

$$m_2 = 0$$

$$m_3 = \cos \beta$$

This particular geometry assumes that the surface of the cylinder is illuminated with collimated light parallel to the X_3 direction. The direction of \vec{ps} is the same at every point on the surface of the cylinder. Also, the direction cosine m_2 is assumed to be zero. This direction cosine is the angle between the observation direction and the X_2 axis. If the hologram is located at a long distance from the cylinder and the cylinder axis X_2 is parallel to the hologram plate, then m_2 will be negligible compared to the other values. Therefore, it can be assumed to be zero. The only non-zero displacement component to be measured is U_r as shown schematically in Figure 7.

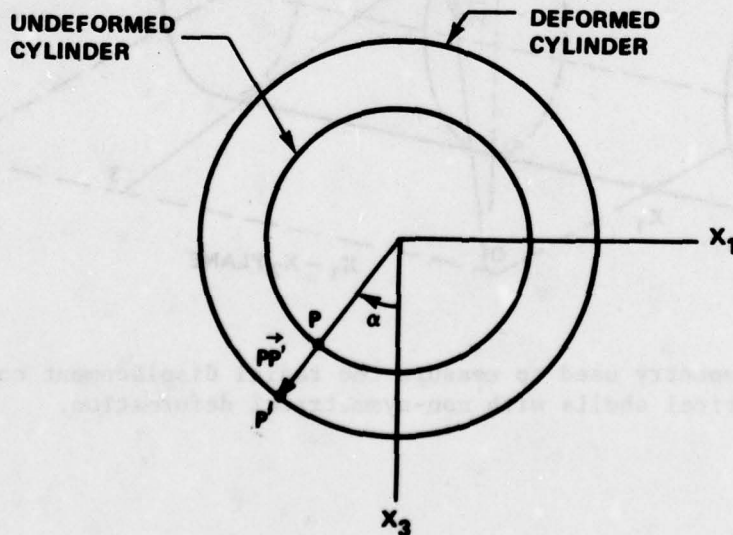


Figure 7. Symmetrical deformation displacement component $\vec{PP'}$ for a circular cylinder.

For this example, Equation (21) reduces to

$$-\sin \beta U_r + (1 + \cos \beta) U_r \cos \phi = \frac{(2n-1)\lambda}{2} \quad . \quad (22)$$

This equation can be solved for U_r , which yields

$$U_r = \frac{(2n-1)\lambda}{2[(1 + \cos \beta) \cos \phi - \sin \beta]} \quad . \quad (23)$$

Example 1 illustrates that for the case of symmetrical deformation, and with proper selection of the experimental geometry, U_r can be determined from a single hologram.

(b) Example 2: Radial Deformation Measurements of Cylindrical Shells with Non-Symmetrical Deformation. The second example will consider the general case of the deformation of cylindrical shells. Only in this example the radial deformation of cylindrical is to be measured with non-zero values of U_θ and U_z . Figure 8 is a schematic diagram of the experimental configuration to measure the radial deformation.

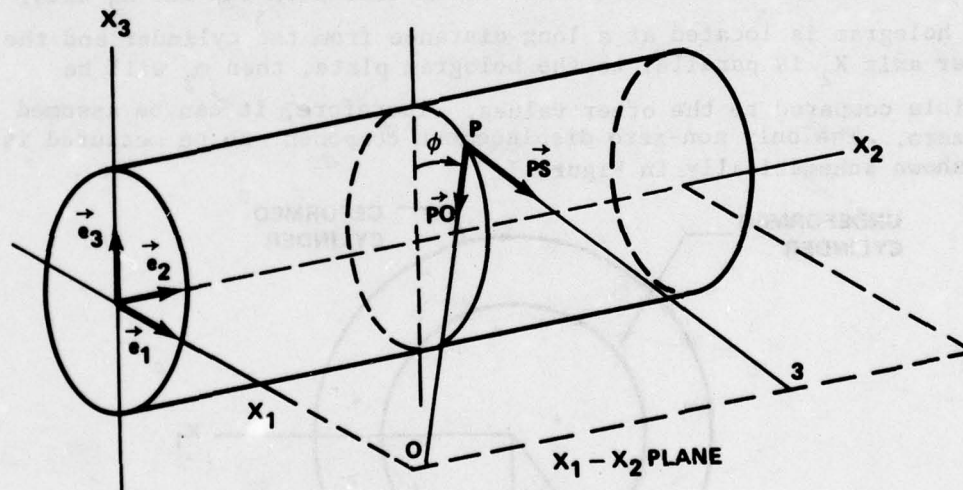


Figure 8. Geometry used to measure the radial displacement component for cylindrical shells with non-symmetrical deformation.

For this example the direction cosines are chosen to be (Figure 9)

$$l_1 = \cos \theta$$

$$l_2 = \sin \theta$$

$$l_3 = 0$$

and

$$m_1 = \cos \theta$$

$$m_2 = \sin \theta$$

$$m_3 = 0$$

In this example all light rays are assumed to be collimated with illuminating and observation directions in symmetric directions with respect to the X_1 axis.

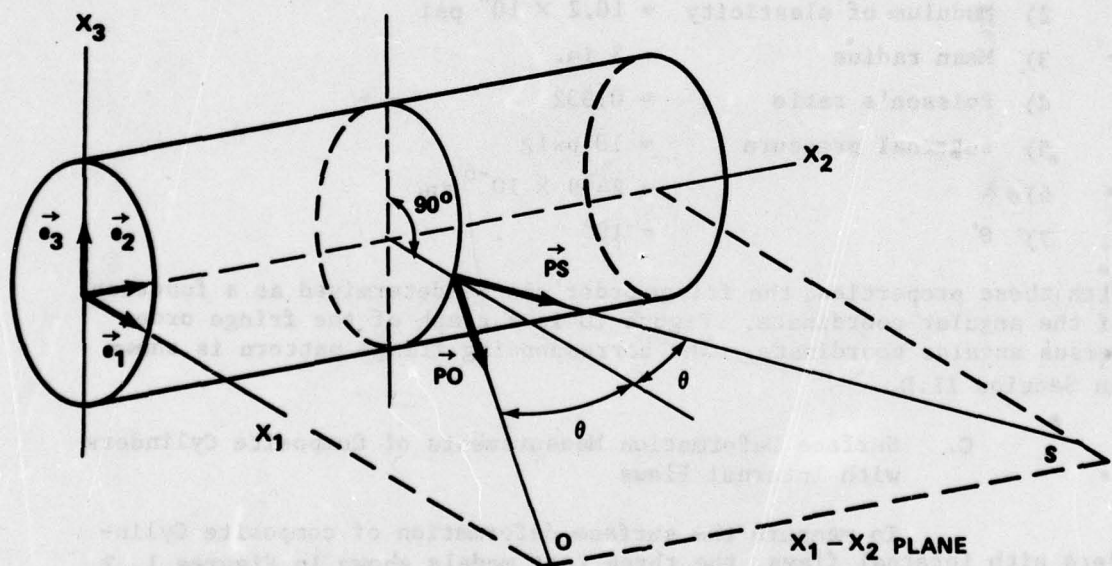


Figure 9. Geometrical relationships for the \vec{PS} and \vec{PO} directions in the $X_1 - X_2$ plane.

Equation (21) for this example reduces to

$$2 \cos \theta (U_r \sin \Phi + U_\Phi \cos \Phi) = \frac{(2n-1)\lambda}{2} \quad . \quad (24)$$

If observations are made in the $X_1 X_2$ plane, then $\sin \Phi = 1$, $\cos \Phi = 0$, and Equation (24) reduces to

$$U_r = \frac{(2n-1)\lambda}{4 \cos \theta} \quad . \quad (25)$$

As in Example 1, if proper choice is made with the experimental geometry then the general form of Equation (21) can be reduced to a form that is amenable to use in numerical computations. These two examples are used to illustrate how the basic equation in holographic interferometry can be used to measure uniquely the radial component of surface displacement of cylindrical shells.

A numerical example was chosen in order to illustrate the application of the equations in Example 2. This example assumes the cylinder to be aluminum with the following geometrical and material properties:

- 1) Thickness = 0.020 in.
- 2) Modulus of elasticity = 10.2×10^6 psi
- 3) Mean radius = 3 in.
- 4) Poisson's ratio = 0.332
- 5) Internal pressure = 10 psig
- 6) λ = 24.9×10^{-6} in.
- 7) θ = 10° .

With these properties, the fringe order can be determined as a function of the angular coordinate. Figure 10 is a graph of the fringe order versus angular coordinate. The corresponding fringe pattern is shown in Section II.D.

C. Surface Deformation Measurements of Composite Cylinders with Internal Flaws

To measure the surface deformation of composite Cylinders with internal flaws, the three test models shown in Figures 1, 2, and 3 were made with simulated flaws in specified locations. Each cylinder was pressurized and the radial surface deformation was measured using an experimental configuration as shown in Figure 11. This holographic configuration will produce an interference fringe pattern which is a measure of the radial displacement of the outer surface. The following data were used for each test:

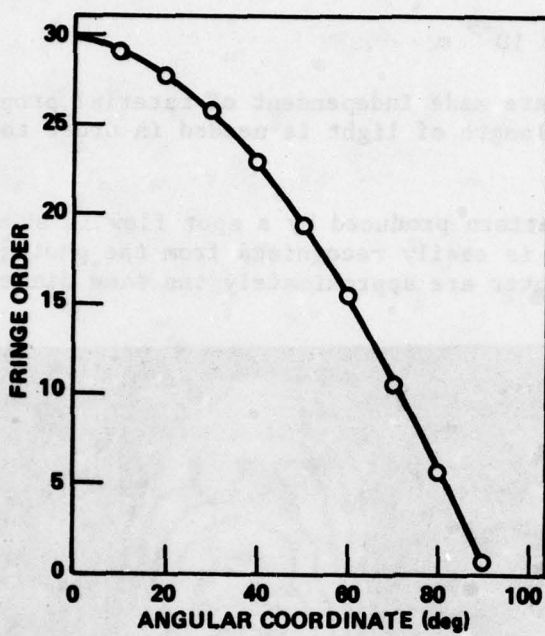


Figure 10. Fringe order for symmetrical deformation of an aluminum cylinder.

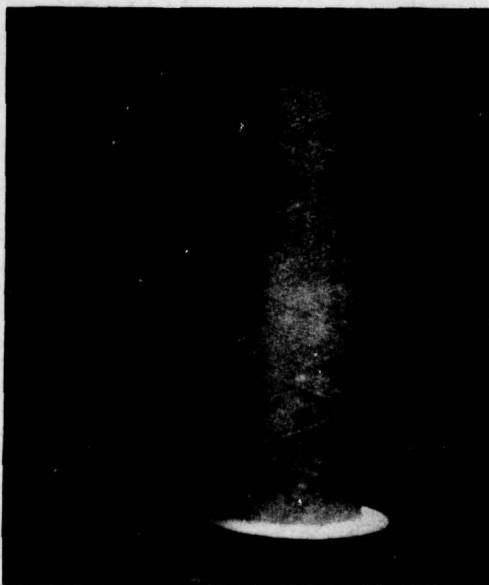


Figure 11. Typical composite cylinder.

$$\theta = 8.5^\circ$$

$$\lambda = 632.8 \times 10^{-9} \text{ m}$$

The measurements are made independent of material properties. Only the geometry and wavelength of light is needed in order to measure the surface deformation.

The fringe pattern produced by a spot flaw is shown in Figure 12. This type of flaw is easily recognized from the photograph. The circular fringes in the center are approximately the same diameter as the flaw.

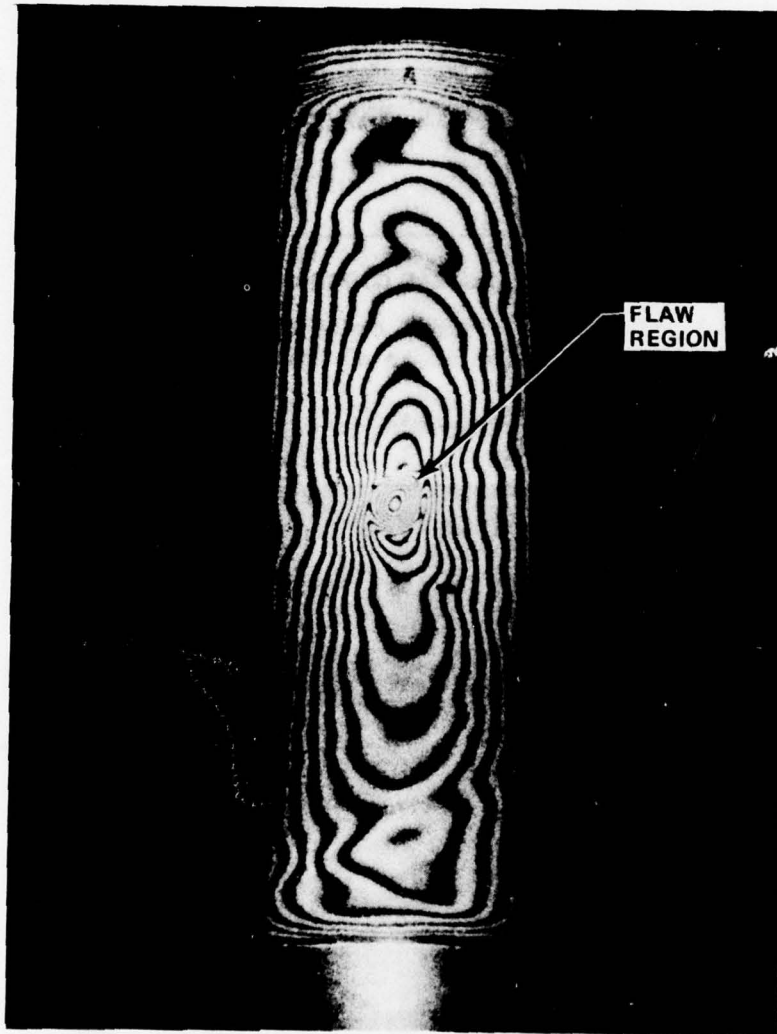


Figure 12. Fringe pattern for the cylinder with a spot flaw.

In the regions away from the flaw the fringes are parallel to the longitudinal axis. This type of fringe pattern is characteristic of symmetrical deformation. Therefore, if the cylinder were free of internal voids, the fringes would be a series of parallel lines away from any end effects. For this case the radial deformation was calculated along a line in the center of the cylinder. The displacements are shown in graphical form in Figure 13. As can be seen from this figure the radial displacement changes by a large amount in the region near the flaw.

Figure 14 shows the fringe pattern produced by the circumferential flaw. As can be seen from the photograph this fringe pattern is more complex than the spot flaw. The internal pressure for this cylinder was 20 psig. At the higher pressures the deformation from the wrap angle geometry becomes significant. The areas of the cylinder where the layers overlap act as a stiffener effect to the shell. Therefore, the fringe pattern is not one that is characteristic of a symmetrical deformation of an isotropic cylinder. However, the presence of the circumferential flaw can be seen in the photograph. Figure 15 shows the radial deformation of the cylinder with an internal circumferential flaw. This type of flaw is not as easily seen in the photograph. However, it is believed that the spot flaw is a more realistic type of flaw that will occur in a production situation.

Figure 16 shows a composite cylinder with a longitudinal flaw. The fringe pattern for this flaw geometry is significantly changed by the presence of the flaw. This type of flaw geometry produces a complex fringe pattern similar to the circumferential flaw. However, this flaw is not expected to be representative of a production-type flaw. Radial deformation for this flaw geometry is not as easy to determine as in the previous examples. As can be seen from the photograph, the radial deformation is essentially constant along the longitudinal axis of the flaw. Therefore, the radial deformation was plotted as a function of the angular coordinate relative to the cylinder centerline. Figure 17 shows the fringe order data as it appears on the photograph. The distance measured on the photograph relative to the cylinder centerline is then used to determine the angular coordinate. After the angular coordinate is known then the radial deformation can be calculated. Figure 18 shows the radial deformation for the longitudinal flaw geometry.

D. Flaw Detection in Fiber Glass Epoxy Thin-Walled Pressure Vessels

1. General

Weapon sophistication points out the need for a higher strength-to-weight ratio and especially for small structures that are used once and then discarded. This higher strength-to-weight ratio has necessitated structures made from composite materials such as glass and epoxy. However, along with these more efficient structures, undetermined stress distributions exist. The stress distribution solutions for

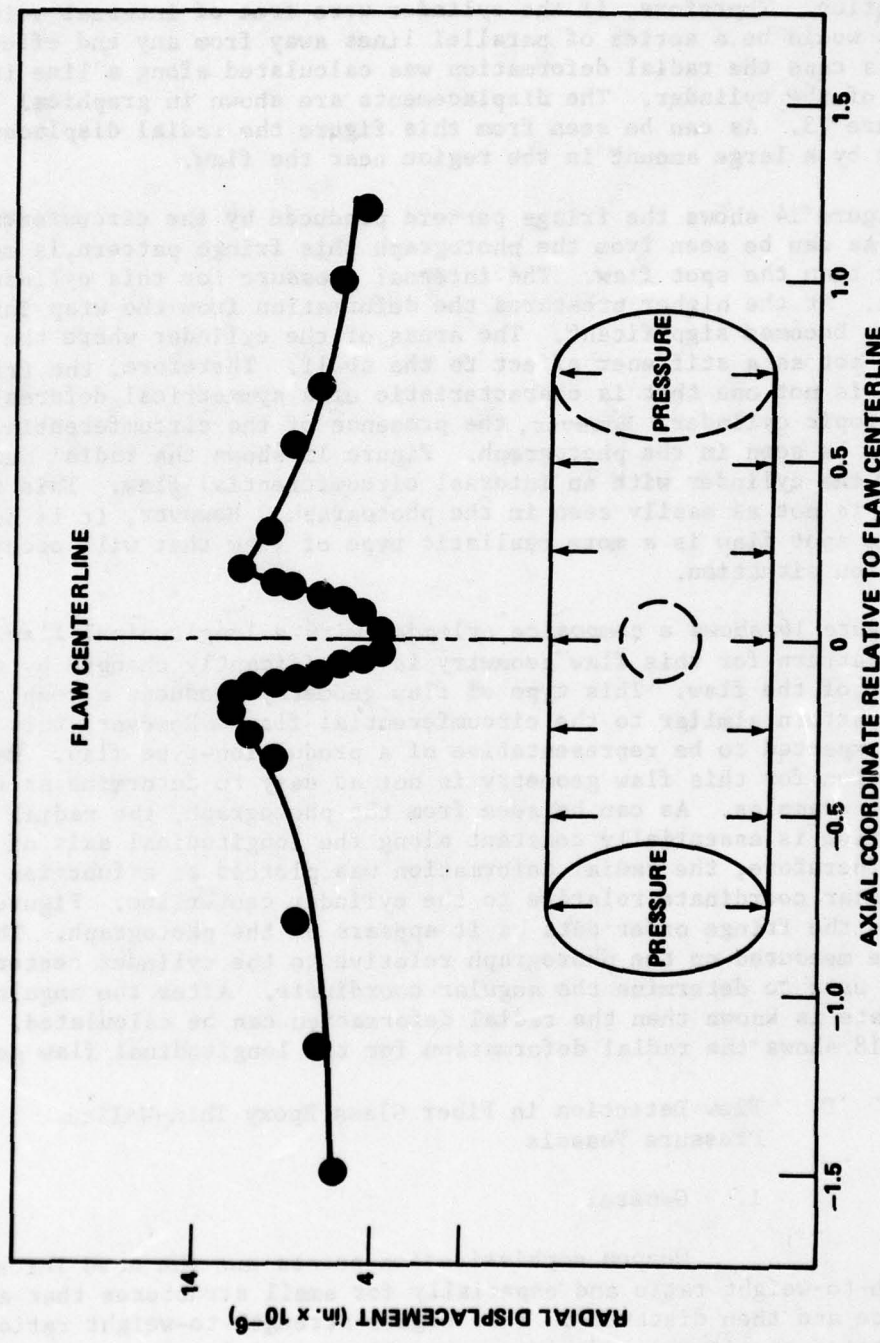


Figure 13. Surface deformation of composite cylinder with a spot flaw, internal pressure 10 psig.

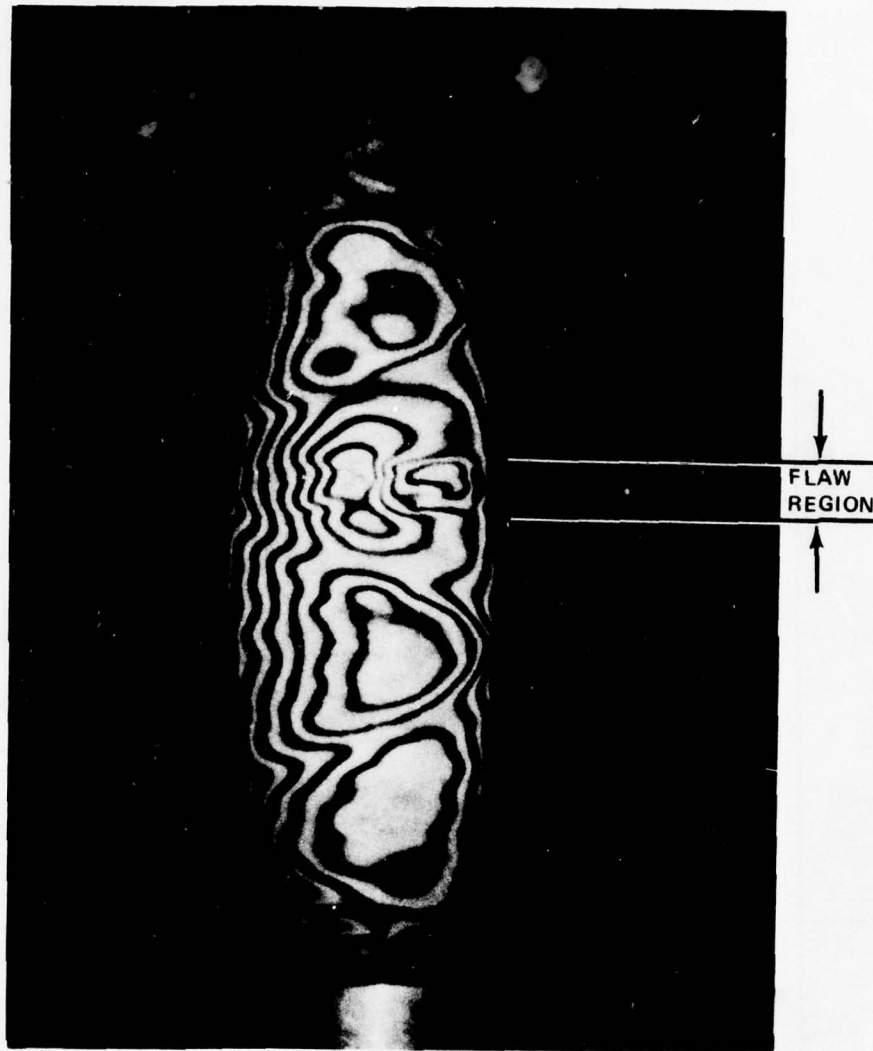


Figure 14. Fringe pattern for the cylinder
with a circumferential flaw.

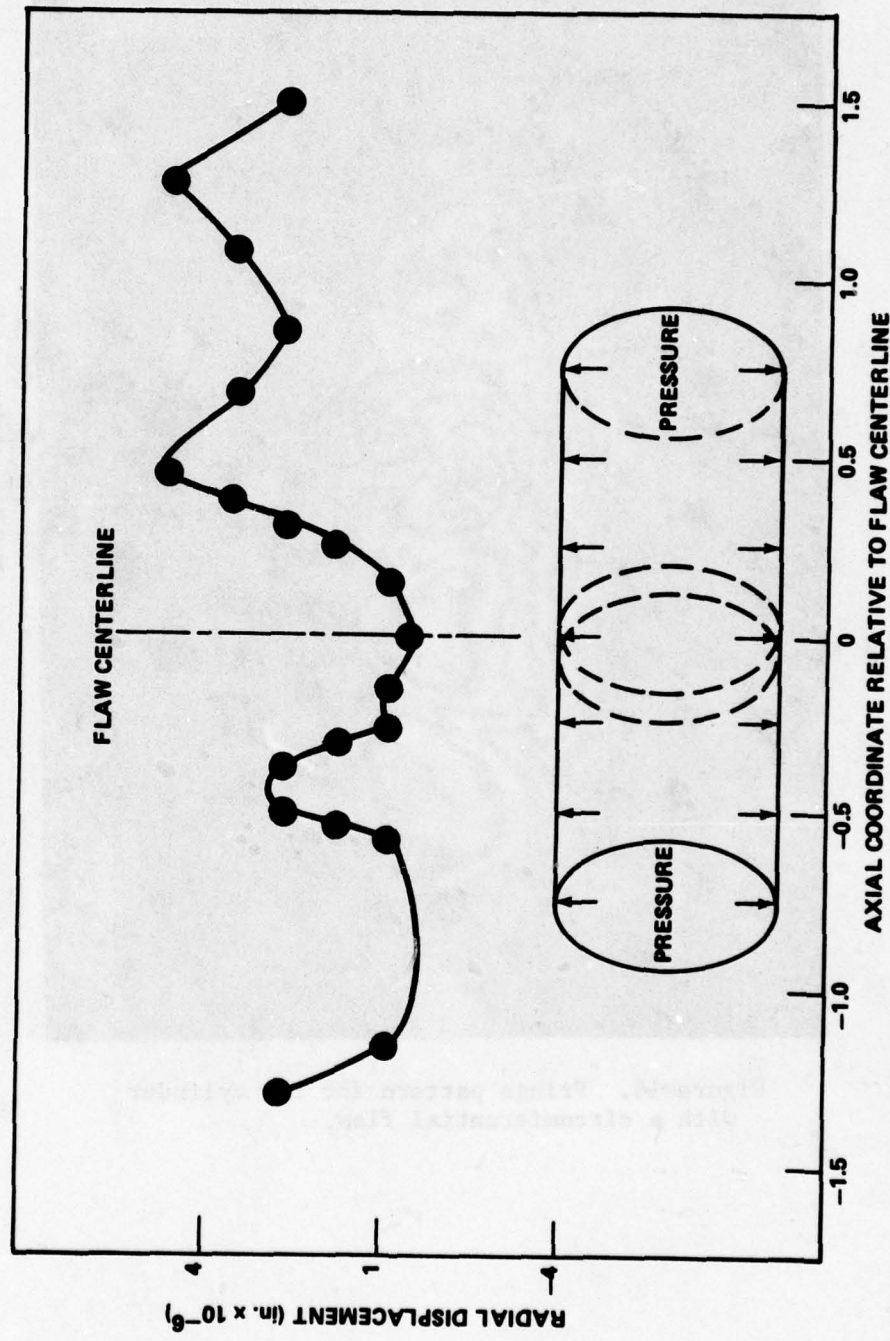


Figure 15. Surface deformation of composite cylinder with a circumferential flaw, internal pressure 20 psig.

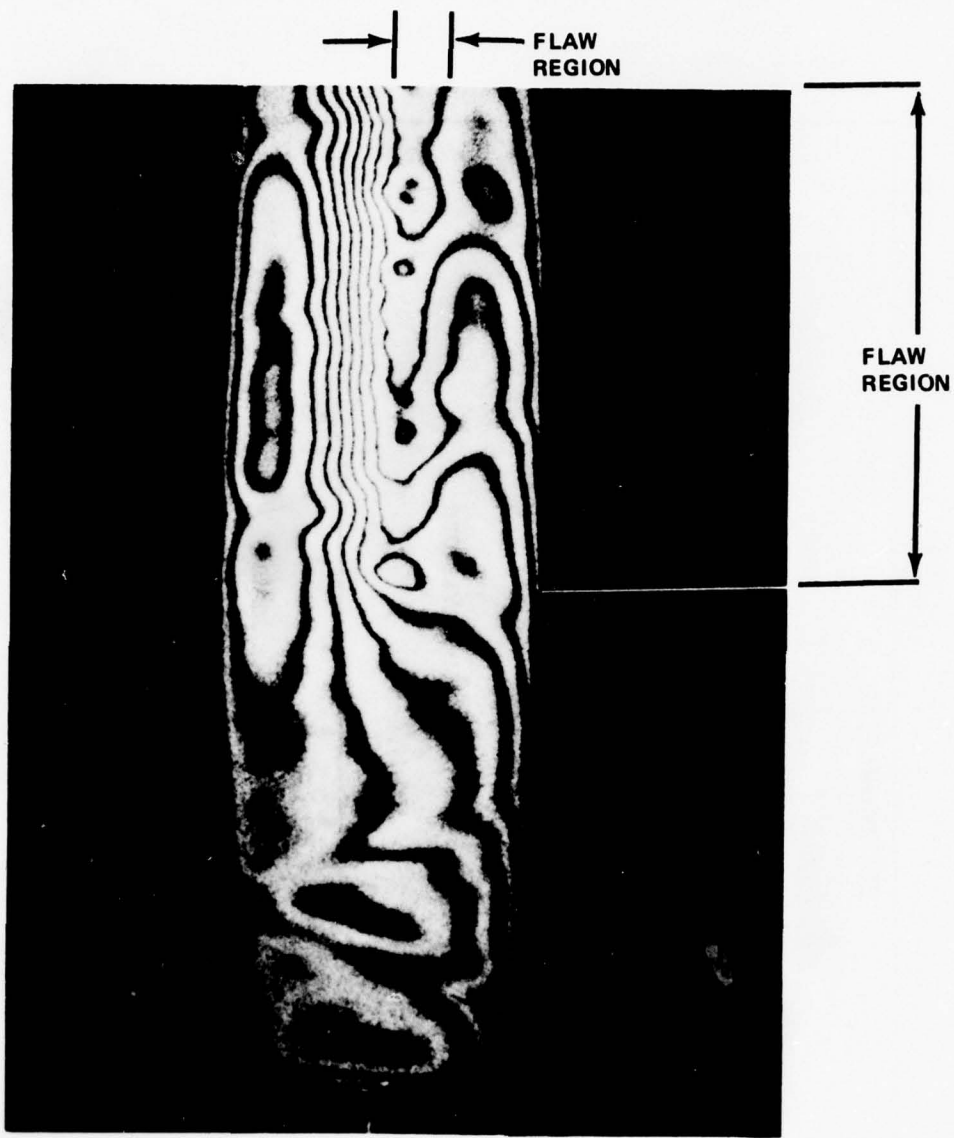


Figure 16. Fringe pattern for the cylinder with a longitudinal flaw.

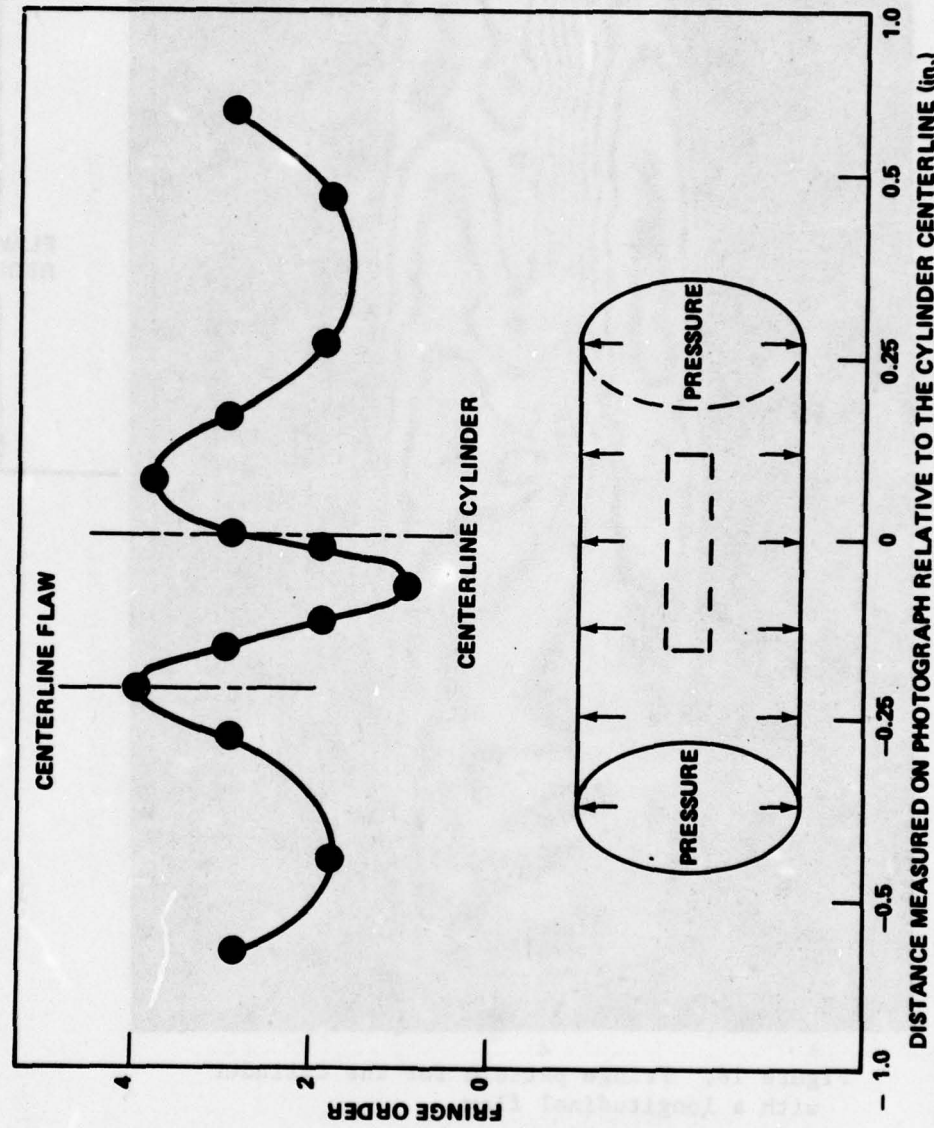


Figure 17. Fringe orders of a composite cylinder with a longitudinal flaw, internal pressure 10 psig.

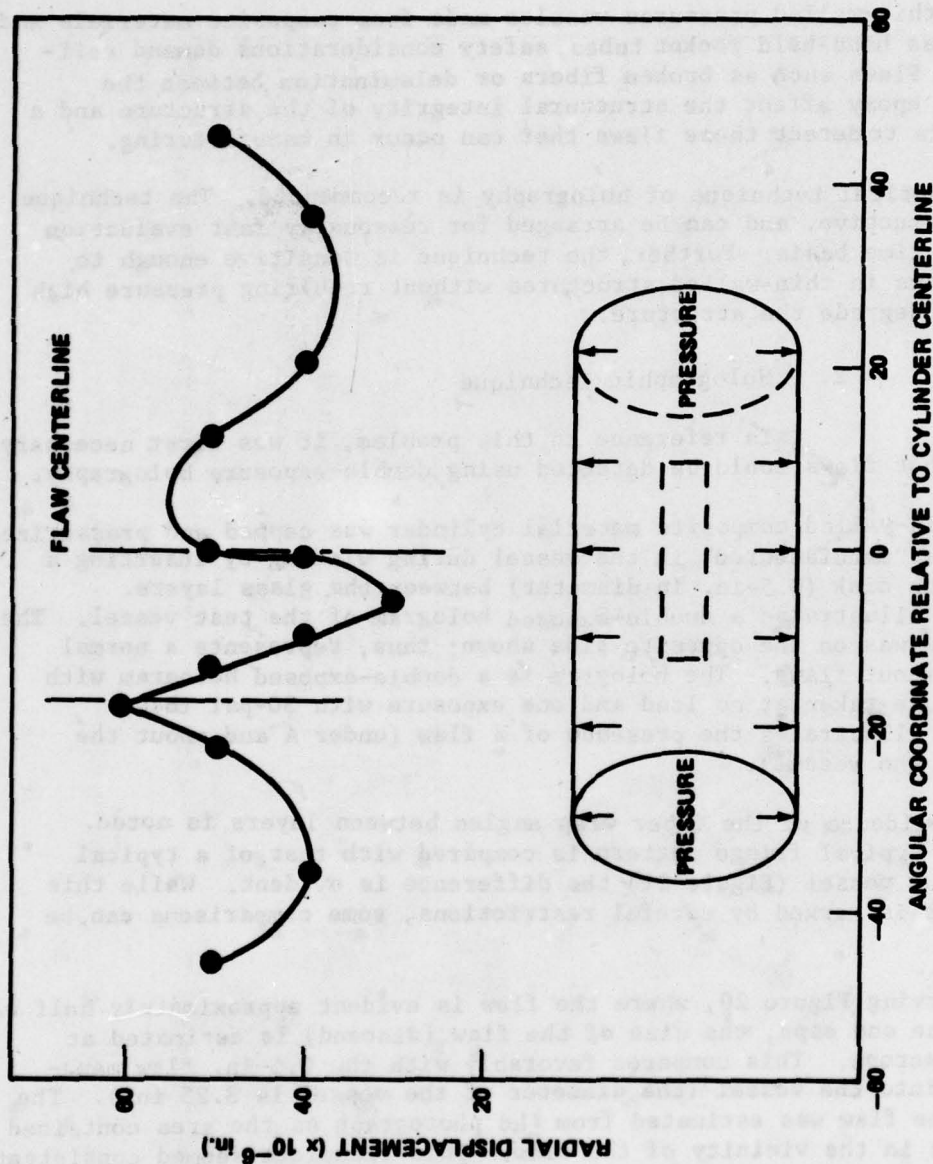


Figure 18. Surface deformation of composite cylinder with a longitudinal flaw,
internal pressure 10 psig.

homogeneous structures are not valid. Until adequate analytical techniques can be developed, more testing is needed to evaluate structural integrity of composite-material structures.

For thin-walled pressure vessels made from composite materials and utilized as hand-held rocket tubes, safety considerations demand reliability. Flaws such as broken fibers or delamination between the glass and epoxy affect the structural integrity of the structure and a need exists to detect these flaws that can occur in manufacturing.

The optical technique of holography is recommended. The technique is nondestructive, and can be arranged for reasonably fast evaluation on a real-time basis. Further, the technique is sensitive enough to detect flaws in thin-walled structures without requiring pressure high enough to degrade the structure.

2. Holographic Technique

In reference to this problem, it was first necessary to show that flaws could be detected using double-exposure holography.

A thin-walled composite material cylinder was capped and pressurized. A flaw was "manufactured" in the vessel during winding by inserting a thin teflon disk (0.5-in. in diameter) between the glass layers. Figure 19 illustrates a double-exposed hologram of the test vessel. The known flaw was on the opposite side shown; thus, represents a normal vessel without flaws. The hologram is a double-exposed hologram with one exposure taken at no load and one exposure with 30-psi load. Figure 20 illustrates the presence of a flaw (under A and about the center of the vessel).

The evidence of the fiber wrap angles between layers is noted. When this typical fringe pattern is compared with that of a typical homogeneous vessel (Figure 21) the difference is evident. While this difference is marked by careful restrictions, some comparisons can be made.

Observing Figure 20, where the flaw is evident approximately half way between the end caps, the size of the flaw (disbond) is estimated at 0.45-in. across. This compares favorably with the 0.5-in. flaw manufactured into the vessel (the diameter of the vessel is 3.25 in.). The size of the flaw was estimated from the photograph as the area contained by fringes in the vicinity of the flaw. This technique seemed consistent on other photographs of similar flaws and seems sufficient to estimate the size of flaw.

While the technique of double-exposure holography can be used to detect flaws, complicating factors exist and must be resolved.

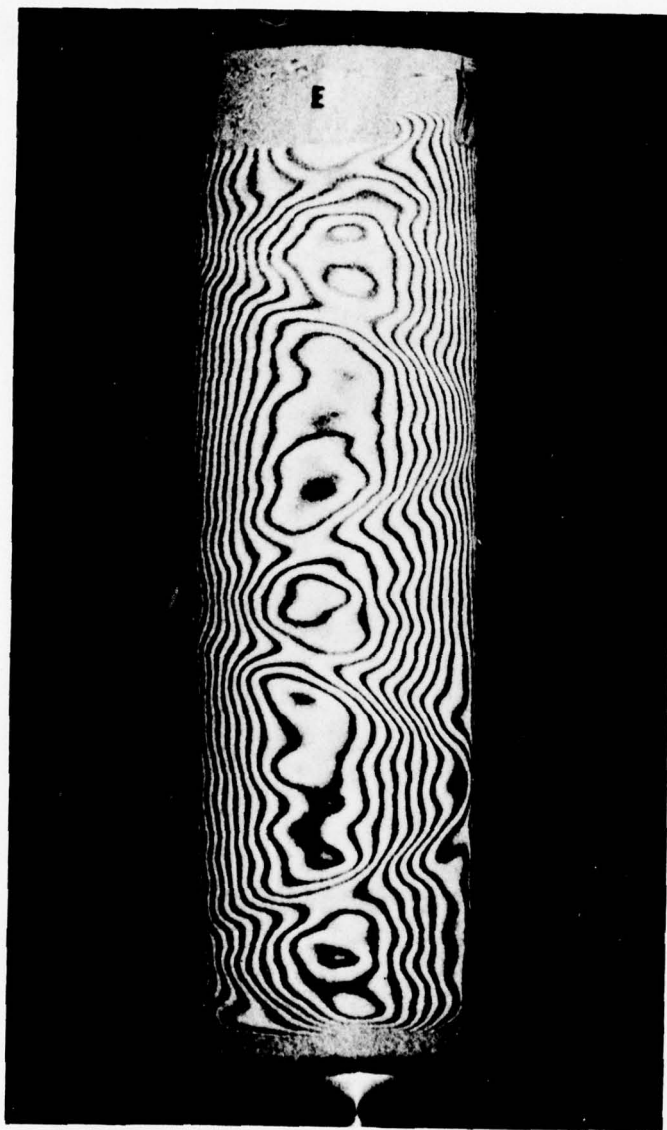


Figure 19. Double-exposed hologram of the test vessel.

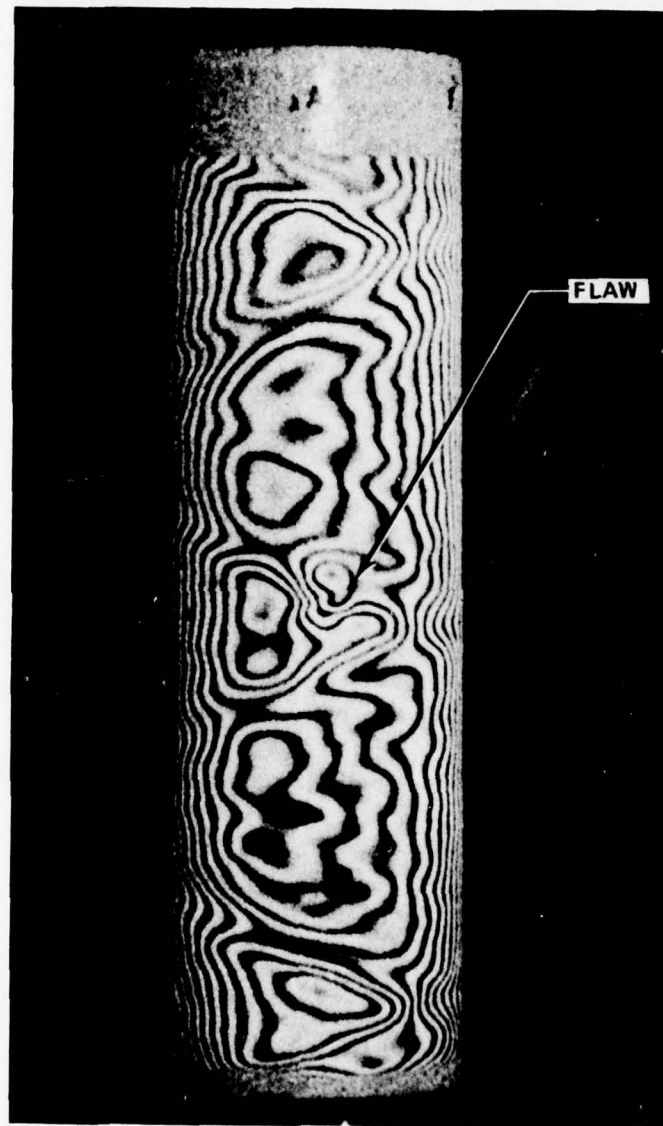


Figure 20. Flaw location under Section A at the center of the vessel.

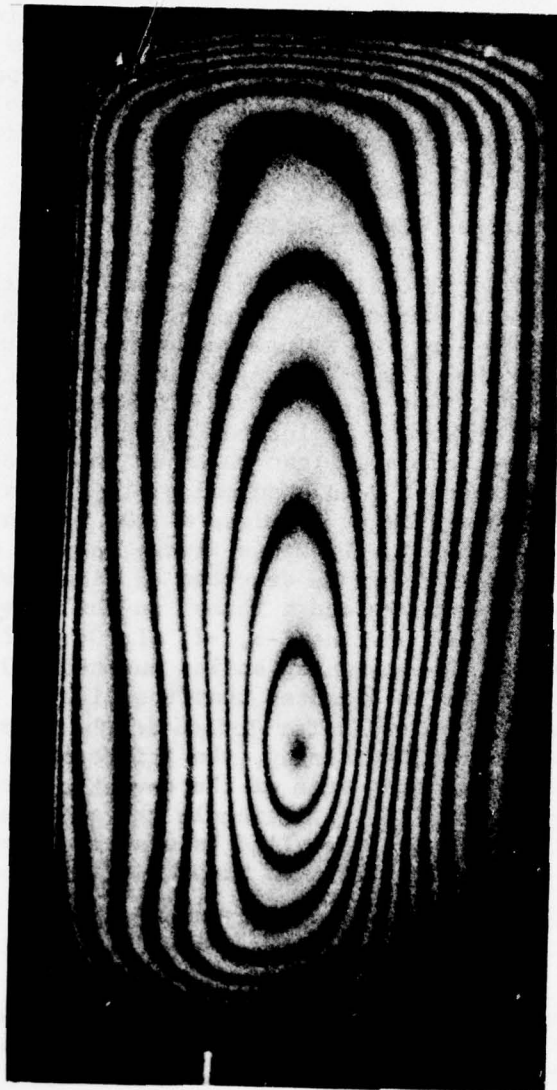


Figure 21. Typical hologram of homogeneous aluminum pressure vessel.

One complication is the need to develop the holographic film, which requires time and thus is not ideal as an inspection technique for mass production of these pressure vessels. This complication can be eased by using a photopolymer instead of film which allows an investigator to observe the fringe pattern as it occurs (real time). One video tape was made of the event to demonstrate capability and the possibility of later evaluation. The preparation and use of the photopolymer material is described later in Section V of this chapter with photographs of the resulting fringe patterns.

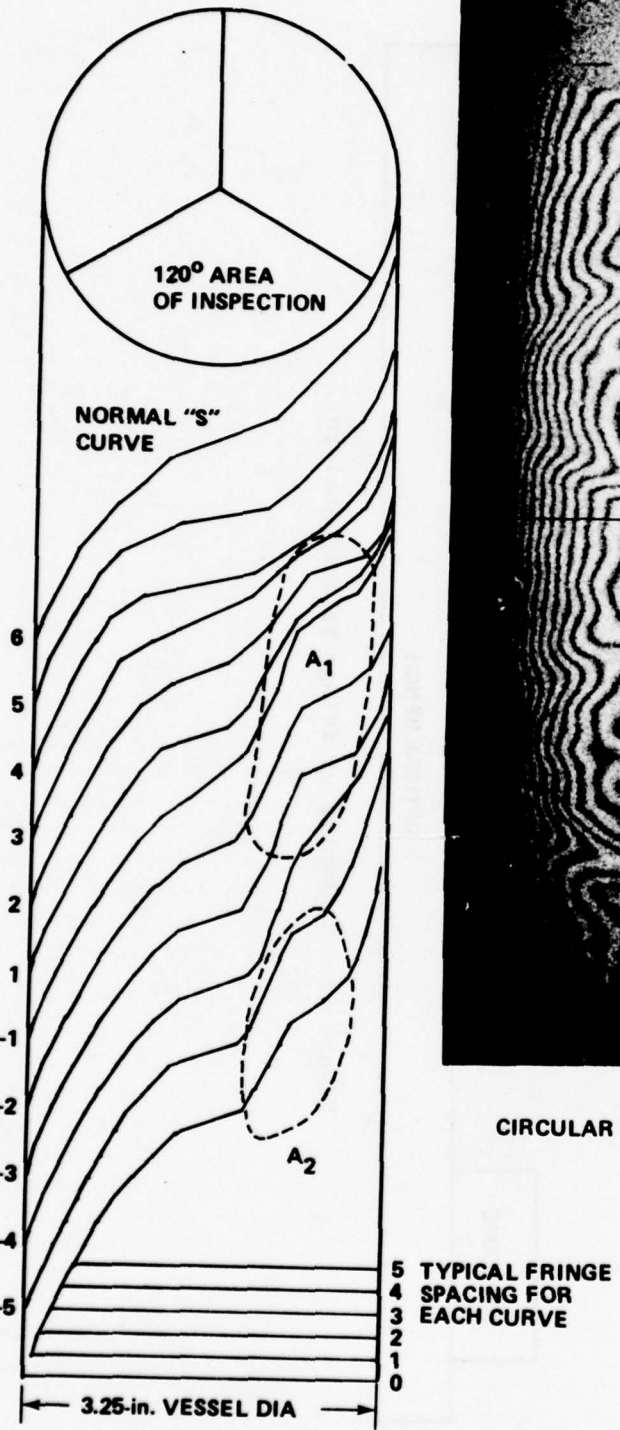
E. Computerized Digitization of the Fringe Patterns

Another complication is the need to read the fringe patterns and detect flaws automatically. After considering several approaches, one reasonable way is to scan the fringe pattern with a photometer at small increments along the axis of the cylinder and note shifts from a normal "s" curve. Such a plot is presented in Figure 22. Line zero goes through the center of a flaw and is located under "A" of the figure. The fringe number is plotted as a light meter would detect a fringe scanning across the photograph. In a normal plot (with a flaw) such as along line 6 the fringe spacing is close at the beginning, followed by large fringe spacing and finally close fringe spacing as noted on the plot. Evidence of a flaw can be detected on line 3 where the fringe plot deviates from the "s" curve and a "hump" on the curve is noted. This type of effect is noted on lines -3, -2, -1, 0, 1, 2, 3, 4 and established the size of the flaw which scales out to be 0.59 in. which compares favorably since it is expected that the disbond is slightly larger than the known 0.5-in.-diameter Teflon in the vessel. Thus, by taking a photometer scan and digitizing, the fringe spacings (curve tangents) can be stored and note made of the deviation from the normal "s" curve indicating a flaw. In this example the area enclosed by A_1 represents the flaw. Attention is called to a second trouble spot which is just below A_1 and labeled A_2 . This appears to be caused by layers of glass interacting at a bias angle and suggests a possible "flaw" that can be in vessels due to the lay of the windings.

To enhance the flaw detection and reduce the time required to test each cylinder, computer software was developed to scan, digitize, and analyze the holographic fringe patterns in regions where flaws were located using a Fringe Pattern Analyzer. The approximate size of the flaws was determined. "U" curves were utilized in the computer plots in an effort to capitalize on the symmetric properties of the fringe patterns and make flaws more easily detected.

The Fringe Pattern Analyzer is a computerized system for scanning, digitalizing, processing, and displaying line information recorded on film ranging in size from 16mm movie film to 4×5-in. cut film (Figure 23). The scanning unit is a stepping spot scanner in which a spot is stepped

FRINGE PLOT CORRESPONDING TO NUMBERED LINES ON PHOTOGRAPH



CIRCULAR FLAW - 30 psig

Figure 22. Flaw detection.

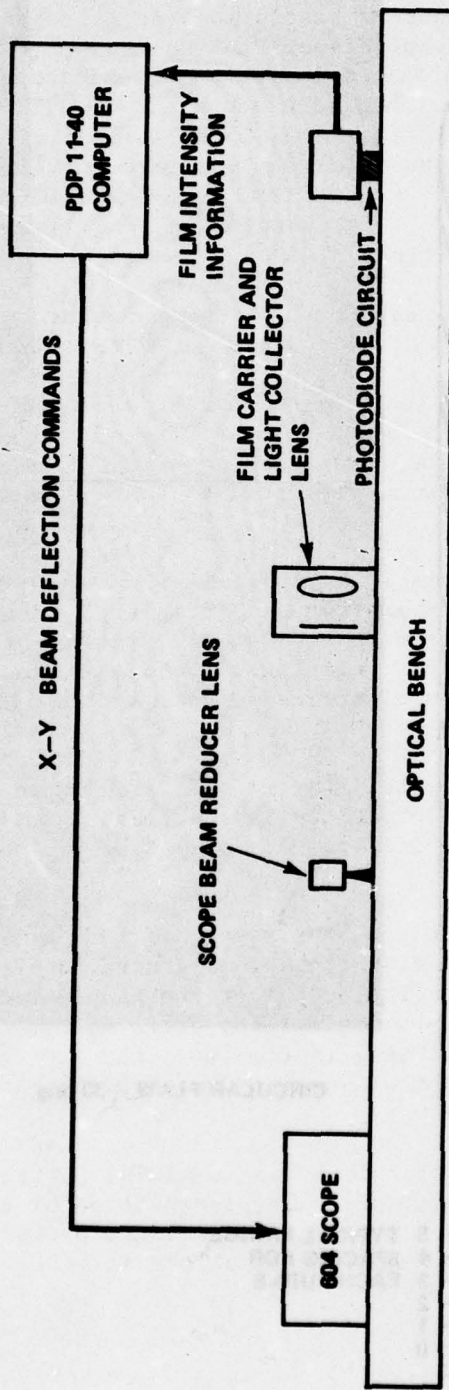


Figure 23. Schematic of fringe pattern analyzer.

over the screen of a Tektronix 604 display scope by means of a digital-to-analog converter under computer program control. The digital-to-analog converters have 10 bits of resolution and drive the X and Y axis of the display scope. The spot diameter of the scope is approximately 0.015 in. which permits approximately 300 resolvable spots to be laid down across the 5-in. dimension of the scope screen. The image of the screen is then focused on the film area to be scanned and, consequently, the scanning resolution on the film is approximately 1/300 of the long dimension of the scope image on the film. The light which is transmitted by the film is collected by a large condensing lens system and brought to focus on a 2-in. photomultiplier.

The components of the scanning unit are mounted on a heavy 2-m optical bench so that they may be accurately and reproducibly positioned on the optical bench with sufficient accuracy so that no additional focusing is necessary. The 4 x 5-in. film carrier attachment is loaded by placing the film to be scanned between two glass plates. Accurate vertical and rotational positioning of the film may be maintained if the lower edge of the film is permitted to contact both of the positioning pins.

The data-collection cycle is controlled by the system software. The data cycle commences upon issuing an "intensify" command. This command causes the scope interface to issue an "intensify" pulse about 25 μ sec in duration. The light reaching the photocathode of the photomultiplier is converted to an electrical signal and amplified internally within the tube.

The output of the photomultiplier is amplified in an amplifier mounted in the base of the photomultiplier carriage. This signal is then sent to the computer cabinet in a coaxial cable for an additional stage of amplification.

After the last amplification, the signal is fed to a sample-and-hold circuit which is actuated by a "hold" signal generated about 20 μ sec after the "intensify" pulse. The output of the sample and hold is digitized by an 8-bit analog-to-digital converter (ADC). The conversion takes 4 μ sec. When the digitizing is complete, the ADC sends a "done" signal to the computer and the data are transferred to the computer under program control.

The Fringe Pattern Analyzer is equipped with a Tektronix 4601 hard-copy unit which prints out a graphical representation of the digitized fringe pattern. Comparison of the digitized fringe pattern with the original assures that the correct fringe pattern is being analyzed by the computer.

A film transparency of the fringe pattern in Figure 23 was digitized using the Fringe Pattern Analyzer. A computer graphical representation of the fringe pattern in the region of the flaws is shown in Figure 24. The scanning interval was 0.2 in. around the circumference of the cylinder. The fringe-density plots of the "U" curves corresponding to the "s" curves plotted by hand are shown in Figure 25. The flaws are both

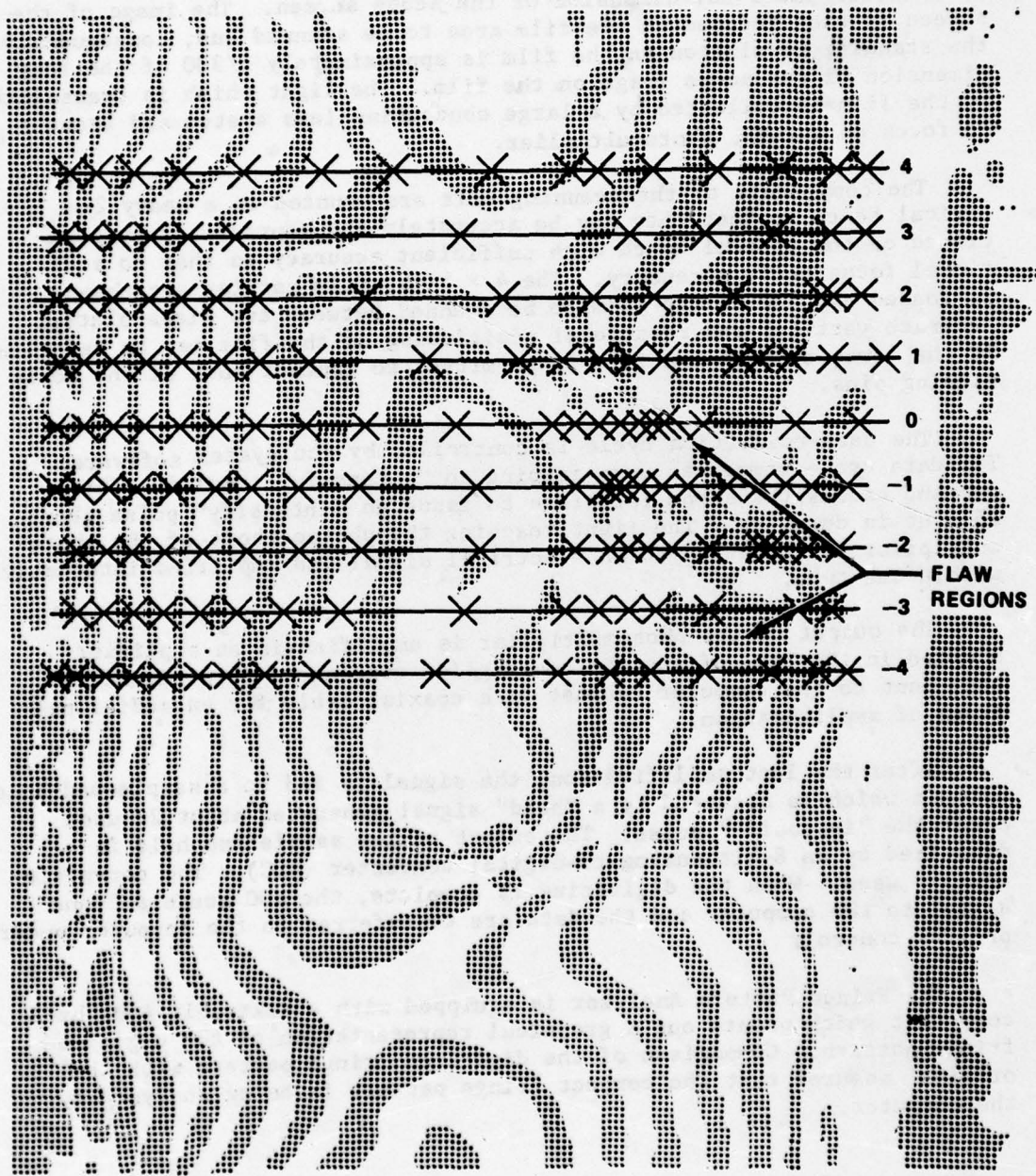


Figure 24. A computer graphics representation of the holographic fringe pattern from a composite cylinder.

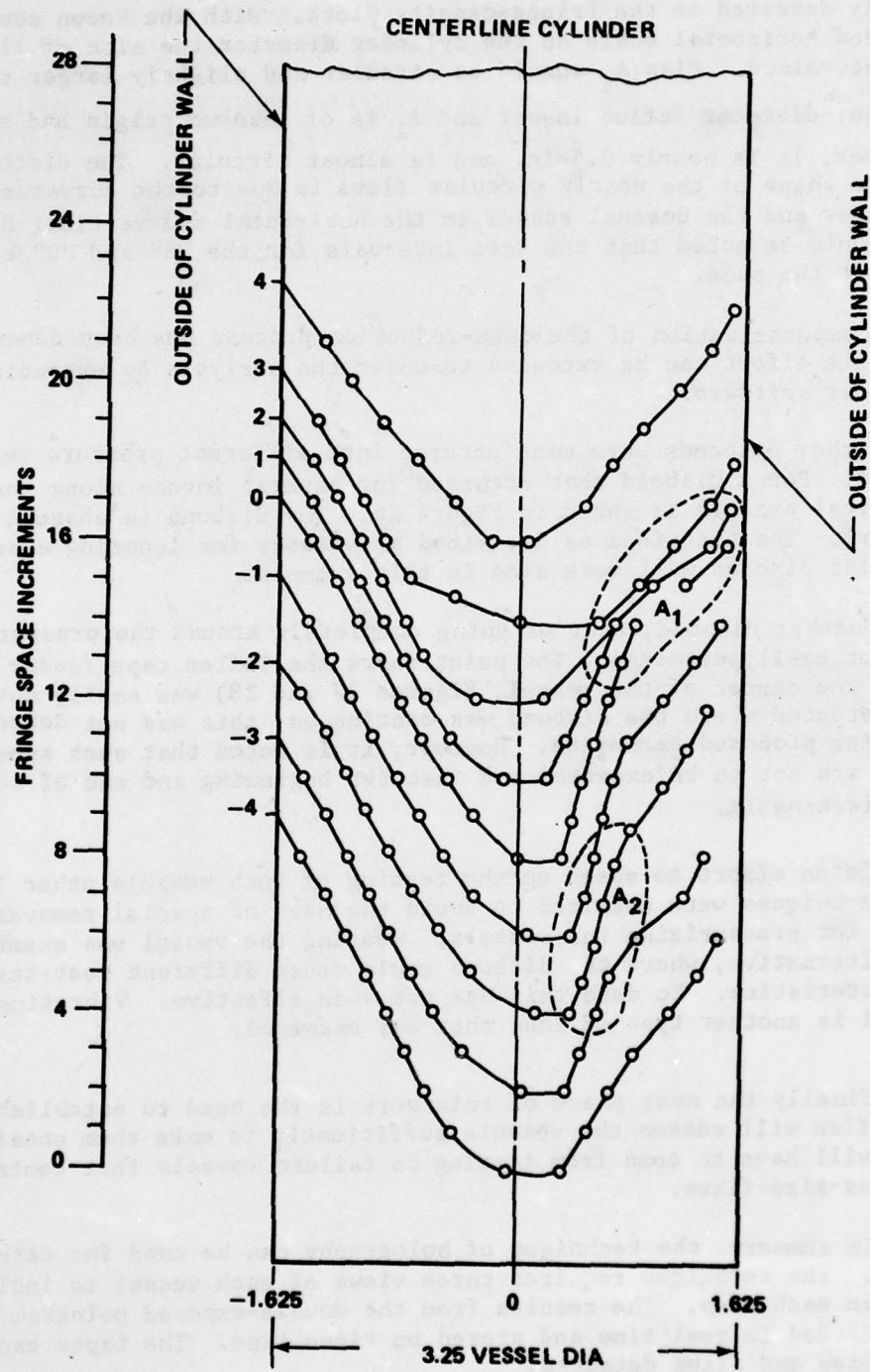


Figure 25. Fringe density plots by computer of the fringe patterns in Figures 23 and 24.

easily detected on the fringe-density plots. With the known scan interval and horizontal scale on the cylinder diameter the size of flaw can be determined. Flaw A_1 should be circular and slightly larger than the 0.5-in.-diameter Teflon insert and A_2 is of unknown origin and size.

However, it is nearly 0.5-in. and is almost circular. The distortion in the shape of the nearly circular flaws is due to the curvature of the cylinder and the unequal scales in the horizontal and vertical directions. It should be noted that the scan intervals for the "S" and "U" curves are not the same.

Computerization of the data-reduction process has been demonstrated and this effort can be extended to cover the analysis by extending the computer software.

Other disbonds were manufactured into different pressure vessels and tested. For a disbond that occurred for several inches along the length, a typical example is shown in Figure 26. The disbond is above A in the picture. The technique as described previously for locating a small circular disbond will work also in this example.

Another disbond, that of going completely around the pressure vessel was not easily detected. The point where the Teflon tape (under A and about the center of the vessel, Figures 27 and 28) was easily noted and detected where the disbond was continuous; this was not detectable with the proposed technique. However, it is noted that such symmetrical flaws are not to be expected and that the beginning and end of such flaws are discernable.

In an effort to speed up the testing of such vessels other loading techniques were examined to avoid the need of special removable plugs for pressurizing the vessels. Heating the vessel was examined as one alternative, where the disbond would cause different heat-transfer characteristics. To date this has not been effective. Vibrating the vessel is another type of load that was examined.

Finally the next phase of this work is the need to establish what size flaw will weaken the vessels sufficiently to make them unsafe. This will have to come from testing to failure vessels that contain various-size flaws.

In summary, the technique of holography can be used for detecting flaws. The technique requires three views of each vessel to include 120° in each view. The results from the double-exposed hologram can be recorded in real time and stored on video tape. The tapes can be digitized and flaws detected.

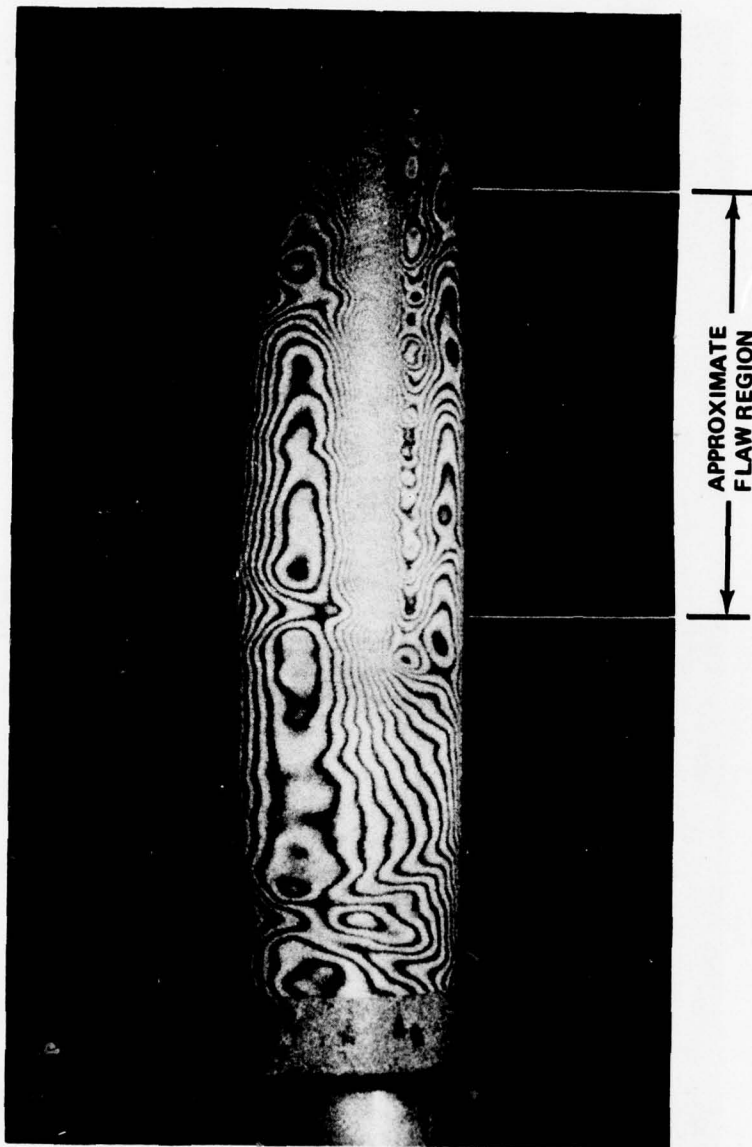


Figure 26. Longitudinal disbond in a composite cylinder.



Figure 27. Circumferential disbond in a composite cylinder.

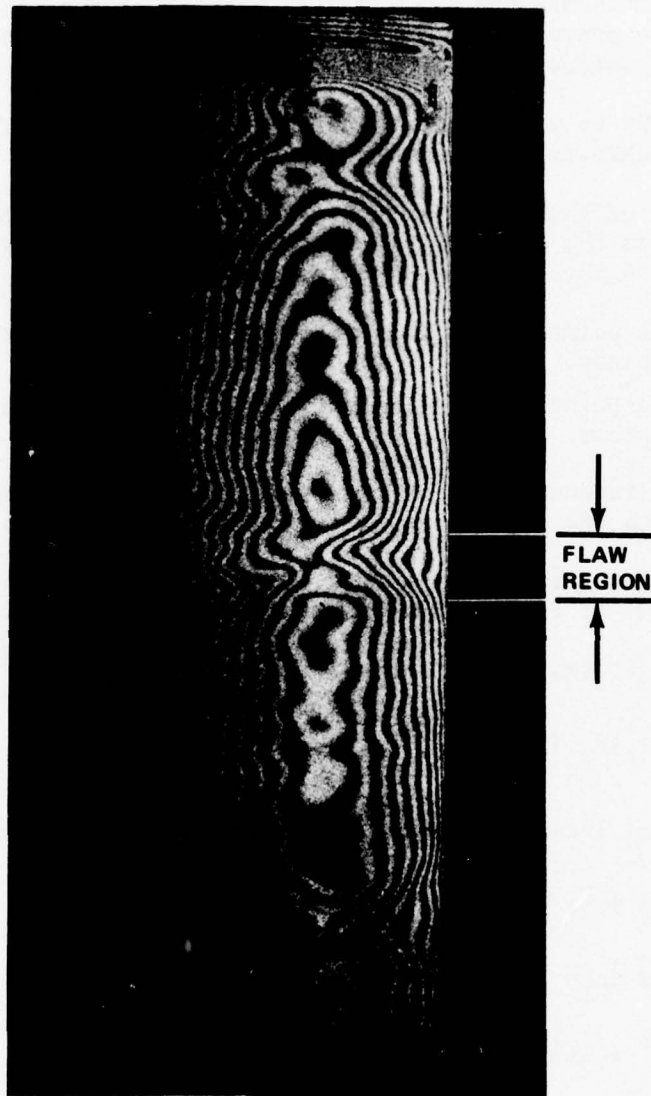


Figure 28. Circumferential disbond in a composite cylinder.

IV. SHEARING SPECKLE INTERFEROMETRY

The theory and experimental results of shearing speckle interferometry are presented in this section with their potential for flaw detection in composite cylinders.

Figure 29 is a schematic diagram of the experimental apparatus for shearing speckle interferometry.

Because of the wedge in the system, the following conditions will be formed when the lens plus the wedge images the points P and P_1 on the film plane. A shear in the $+x$ direction is assumed:

- a) The point P will image at a point (x, y) and a point $(x + \Delta_1, y)$ in the film plane.
- b) The point P_1 will image due to the shear, at a point (x, y) in the film plane.

Now the intensity of the two images due to double exposure of the plate in which the object was deformed between exposures is considered.

At a point (x, y) in the film plane, the image point of P and the sheared image of P_1 will have the following light amplitudes:

$$\begin{aligned}\bar{E}_P &= \bar{A} e^{i\theta_p(x, y)} \\ \bar{E}_{P_1} &= \bar{A} e^{i\theta_{P_1}(x, y)}\end{aligned}\tag{26}$$

The total intensity of the first exposure can be written as

$$I_1 = (\bar{E}_P + \bar{E}_{P_1}) \cdot (\bar{E}_P^* + \bar{E}_{P_1}^*)\tag{27}$$

where \bar{E}_P^* and $\bar{E}_{P_1}^*$ denote complex conjugates, or

$$I_1 = 2A^2 + 2A^2 \cos \theta\tag{28}$$

where $\theta = \theta_p(x, y) - \theta_{P_1}(x, y)$

where I_1 now is the intensity at the film plane due to the first exposure.

Now the intensity for the second exposure is considered. The light amplitudes for the second exposure can be written in the following form:

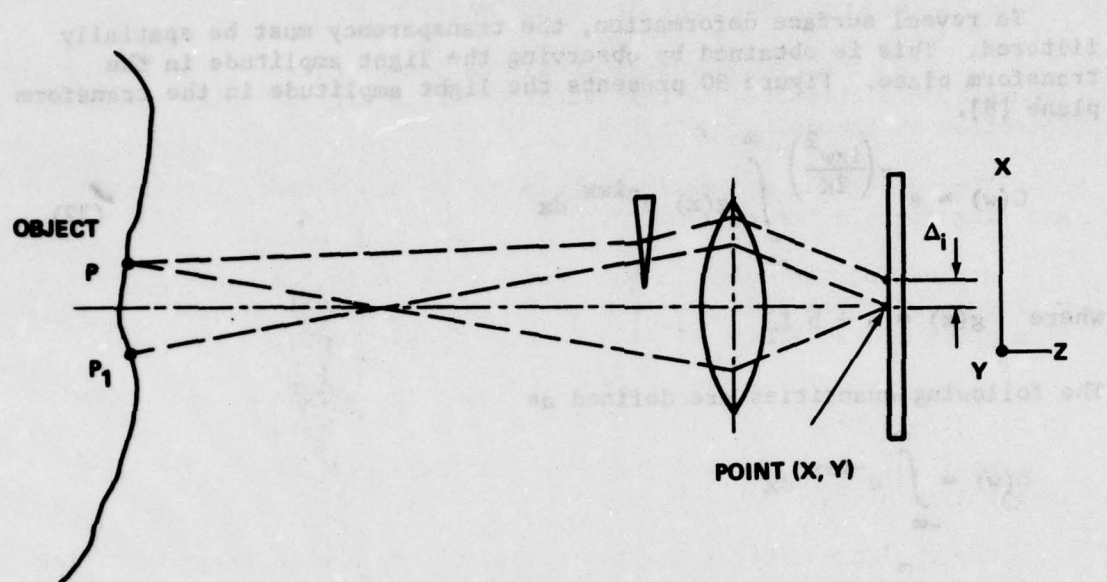


Figure 29. Shearing speckle interferometry.

$$\begin{aligned}\bar{E}_{p'} &= \bar{A} e^{i(\theta_p + \Delta\theta_p)} \\ \bar{E}_{p_1'} &= \bar{A} e^{i(\theta_{p_1} + \Delta\theta_{p_1})}\end{aligned}\quad . \quad (29)$$

The intensity of the second exposure is

$$I_2 = (\bar{E}_{p'} + \bar{E}_{p_1'}) \cdot (\bar{E}_{p'}^* + \bar{E}_{p_1'}^*) \quad . \quad (30)$$

or

$$I_2 = 2A^2 + 2A^2 \cos(\theta + \Delta\theta)$$

where $\Delta\theta = \Delta\theta_p - \Delta\theta_{p_1}$.

The total intensity for the two exposures is given by

$$I_{\text{TOTAL}} = I_1 + I_2$$

or

$$I_{\text{TOTAL}} = 4A^2 + 2A^2 \cos \theta + 2A^2 \cos(\theta + \Delta\theta) \quad . \quad (31)$$

To reveal surface deformation, the transparency must be spatially filtered. This is obtained by observing the light amplitude in the transform plane. Figure 30 presents the light amplitude in the transform plane [8].

$$G(w) = e^{-\left(\frac{izw^2}{2K}\right)} \int_{-\infty}^{\infty} g(x) e^{-iwx} dx \quad (32)$$

where $g(x) = a + b I_T$

The following quantities are defined as

$$\delta(w) = \int_{-\infty}^{\infty} e^{-iwx} dx$$

$$C(w) = \int_{-\infty}^{\infty} \cos \theta e^{-iwx} dx$$

$$S(w) = \int_{-\infty}^{\infty} \sin \theta e^{-iwx} dx$$

The light amplitude in the transform plane can be put in the following form

$$G(w) = e^{-\left(\frac{izw^2}{2K}\right)} [(a + 4bA^2) \delta(w) + 2A^2 b C(w) (1 + \cos \Delta\theta) + 2A^2 b S(w) \sin \Delta\theta] \quad (33)$$

Displacement information is related to the minimum of the light intensity in the transform plane which will be minimum when $(1 + \cos \Delta\theta)$ and $\sin \Delta\theta$ are both zero. Therefore, when $\cos \Delta\theta = (2n - 1)\pi$, it will define a fringe. To interpret the physical meaning of the fringes, first the shear or deviation of the light passing through a wedge is considered.

Figure 31 presents the following:

$$\delta = (\theta_{i1} - \theta_{t1}) + (\theta_{t2} - \theta_{i2})$$

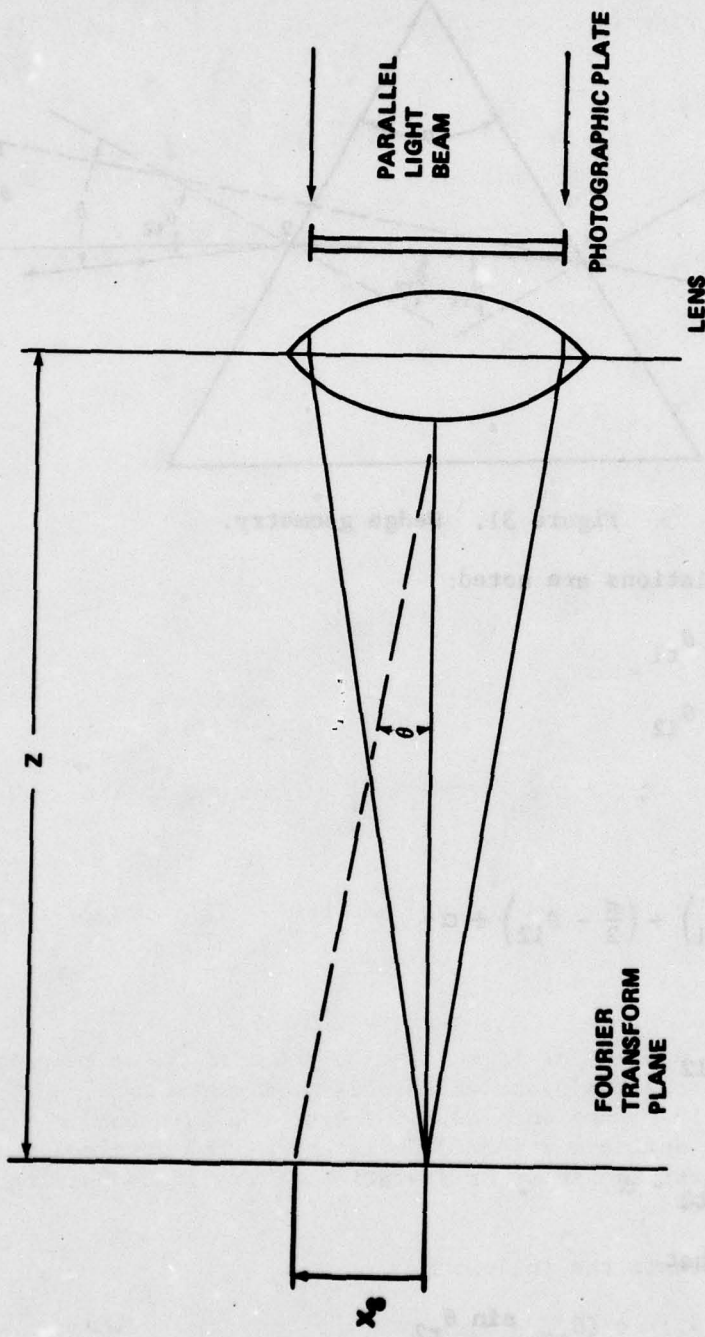


Figure 30. Arrangement for transform analysis.

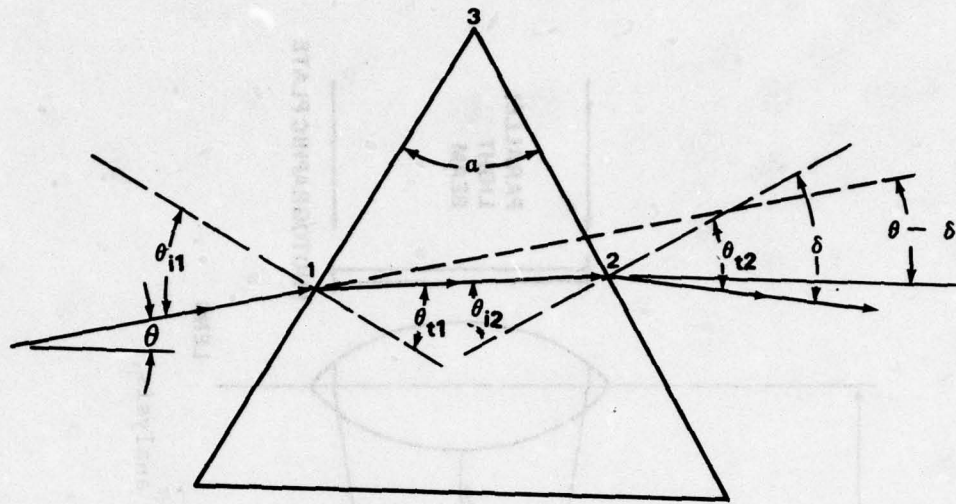


Figure 31. Wedge geometry.

The following relations are noted:

$$\alpha_{312} = \frac{\pi}{2} - \theta_{t1}$$

$$\alpha_{321} = \frac{\pi}{2} - \theta_{i2}$$

$$\alpha_{132} = \alpha ;$$

thus,

$$\pi = \left(\frac{\pi}{2} - \theta_{t1} \right) + \left(\frac{\pi}{2} - \theta_{i2} \right) + \alpha$$

or

$$\alpha = \theta_{t1} + \theta_{i2}$$

and

$$\delta = \theta_{i1} + \theta_{t2} - \alpha .$$

It is recalled that

$$n = \frac{\sin \theta_{i1}}{\sin \theta_{t1}} , \quad n = \frac{\sin \theta_{t2}}{\sin \theta_{i2}}$$

where n is the index of refraction of the wedge.

For small angles

$$n = \frac{\theta_{i1}}{\theta_{t1}}, \quad n = \frac{\theta_{t2}}{\theta_{i2}};$$

substituting,

$$\delta = n(\theta_{t1} + \theta_{i2}) - \alpha$$

or

$$\delta = (n - 1) \alpha$$

where

δ = the deviation angle

α = the wedge angle

To note the effect of the wedge on the optical arrangement, a source (s) on the lens axis that has an image at s' (Thin Lens Theory) is considered (Figure 32). This location was derived from

$$\frac{1}{s} + \frac{n}{s''} = \frac{n-1}{R_1} \quad (34)$$

where s'' is the image location for the light source intersecting the first lens surface and assuming air as the first medium and from

$$-\frac{n}{s''} + \frac{1}{s'} = \frac{1-n}{R_2} \quad (35)$$

for the new wave surface leaving the second lens surface. Combining Equations (34) and (35)

$$\frac{1}{s} + \frac{1}{s'} = (n - 1) \left(\frac{1}{R_1} - \frac{1}{R_2} \right) = \frac{1}{f} \quad (36)$$

where f is the lens focal length. If a wedge is positioned as illustrated in Figure 33 the source "appears" to the lens to be located at s_A instead of s due to the angle change ($\theta - \delta$) in Figure 31. It is also noted that

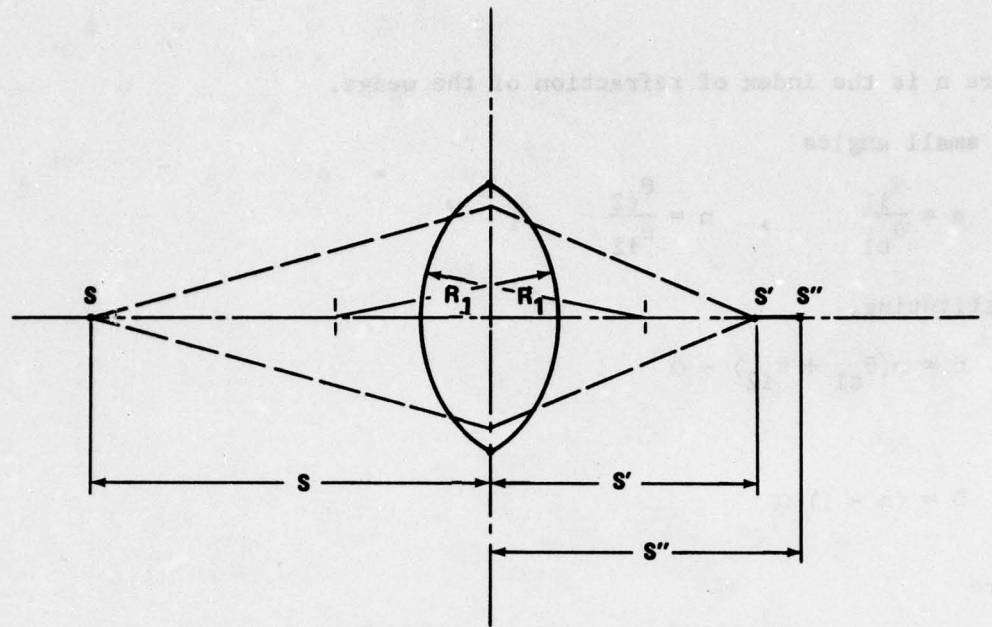


Figure 32. Lens geometry.

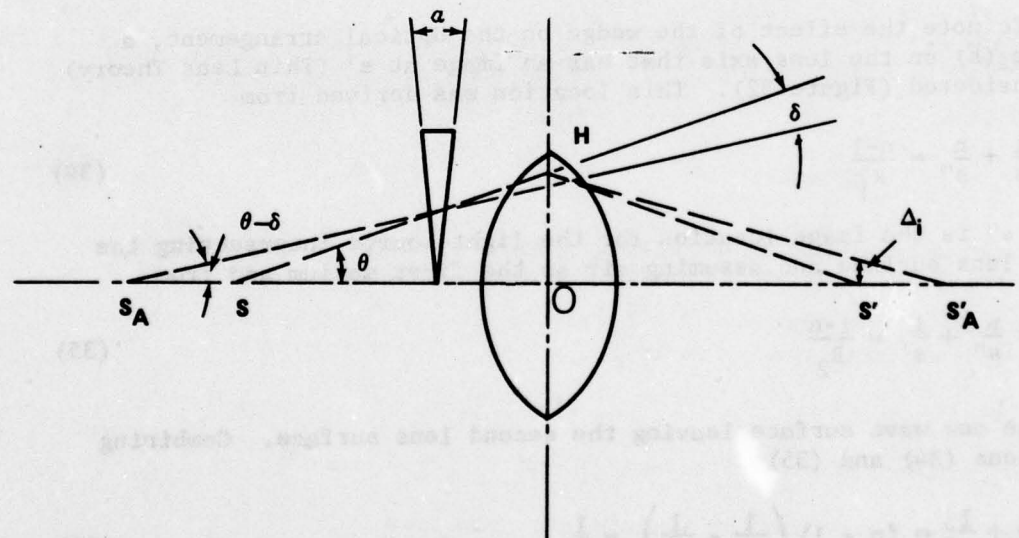


Figure 33. Wedge effect.

$$s_A (\theta - \delta) = s(\theta) \text{ for small angles}$$

and

$$\frac{1}{s} + \frac{1}{s'} = \frac{1}{s_A} + \frac{1}{s'_A}$$

or

$$\frac{1}{s'} = -\frac{\delta}{\theta s} + \frac{1}{s'_A}$$

Let Δ_1 = amount of shift, then as can be reasoned from Figure 33,

$$\Delta_1 = (s'_A - s') \frac{OH}{s'_A} = (s'_A - s') \frac{s\theta}{s'_A} = \left(1 - \frac{s'}{s'_A}\right) s\theta$$

or

$$\Delta_1 = \left[1 - \left(\frac{1}{s'} + \frac{\delta}{\theta s}\right) s'\right] s\theta$$

Finally,

$$\Delta_1 = \delta s' \quad (37)$$

or

$$\Delta_1 = (n - 1) \alpha s' \quad (38)$$

Next when an object is illuminated by a single beam as shown schematically in Figure 34 due to the wedge, the two points P and P_1 are imaged at the same point on the film plane. The spatial separation on the film plane is denoted by Δ_1 .

Also let

$$D_o = s = \text{distance of object (point } P \text{) from lens}$$

$$D_i = D_w = \text{distance of image plate from lens.}$$

If the image is not full scale the magnification,

$$m = D_i/D_o$$

can be accounted for in the shift as

$$\Delta_o = \frac{\Delta_i}{m} = \frac{\Delta_i D_o}{D_i} = (n - 1) \alpha D_o \quad (39)$$

Now the phase variation of the two points P and P_1 is considered. The displacement vectors of the points P and P_1 are

$$\begin{aligned} \overrightarrow{PP'} &= U_1 \overrightarrow{e_1} \\ \overrightarrow{P_1P'_1} &= U'_1 \overrightarrow{e_1} \end{aligned} \quad (40)$$

with

$$\overrightarrow{P_1P'_1} = U_1 (x_1 + \Delta x_1) \overrightarrow{e_1} \quad (41)$$

when P_1 is in the close neighborhood of P . Phase change of the two points can now be written as

$$\begin{aligned} \Delta\theta_2 &= \frac{2\pi}{\lambda} [\overrightarrow{p_1s} + \overrightarrow{p_1o}] \cdot \overrightarrow{P_1P'_1} \\ \Delta\theta_1 &= \frac{2\pi}{\lambda} [\overrightarrow{ps} + \overrightarrow{po}] \cdot \overrightarrow{PP'} \end{aligned} \quad (42)$$

It is assumed that the units vectors are parallel; this allows the phase difference to be written as (Figure 35)

$$\begin{aligned} \Delta\theta &= \frac{2\pi}{\lambda} [\overrightarrow{ps} + \overrightarrow{po}] \cdot (\overrightarrow{P_1P'_1} - \overrightarrow{PP'}) \\ &= \frac{2\pi}{\lambda} \left[(l_s + l_o) \left(\frac{\partial u}{\partial x} \Delta x + \frac{\partial u}{\partial y} \Delta y + \frac{\partial u}{\partial z} \Delta z \right) \right. \\ &\quad + (m_s + m_o) \left(\frac{\partial v}{\partial x} \Delta x + \frac{\partial v}{\partial y} \Delta y + \frac{\partial v}{\partial z} \Delta z \right) \\ &\quad \left. + (n_s + n_o) \left(\frac{\partial w}{\partial x} \Delta x + \frac{\partial w}{\partial y} \Delta y + \frac{\partial w}{\partial z} \Delta z \right) \right] \end{aligned} \quad (43)$$

Fringes will occur when

$$\Delta\theta = \pi, 3\pi, 5\pi, \dots (2n - 1)\pi \quad \text{for } n = 1, 2, \dots \quad (44)$$

thus

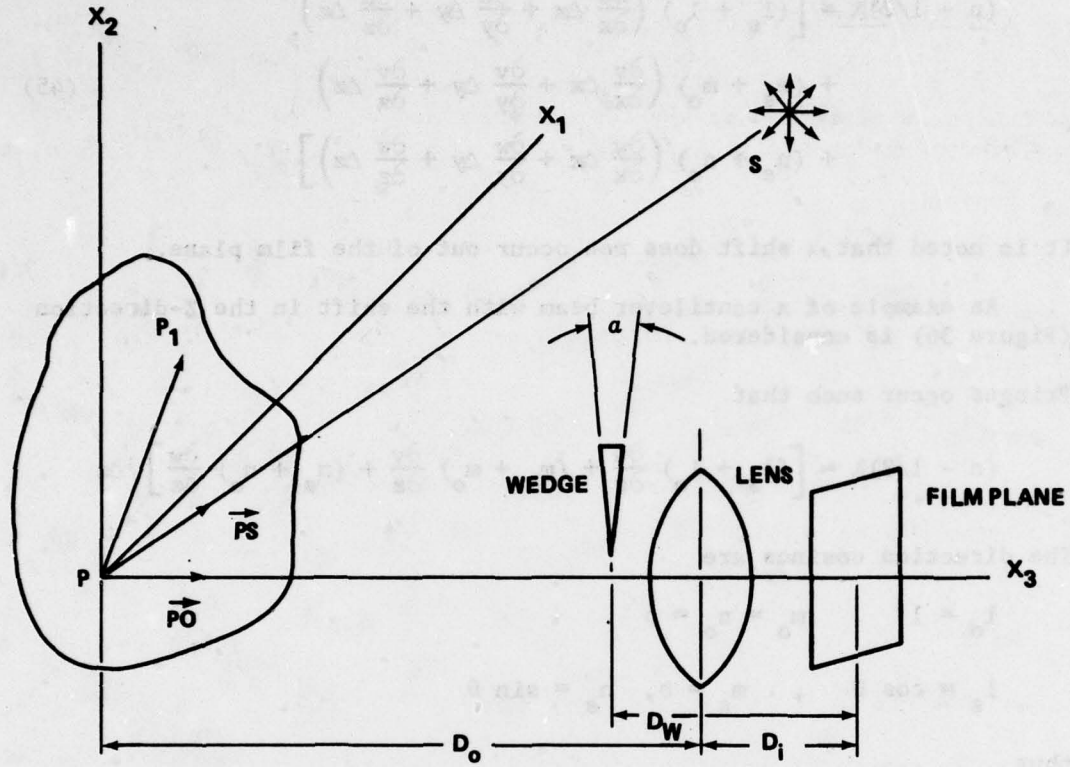


Figure 34. Arrangement for analysis.

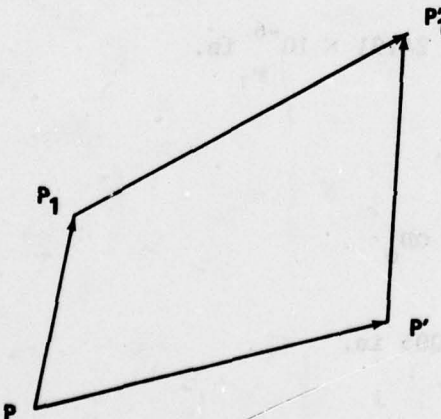


Figure 35. Displacement vectors.

$$\begin{aligned}
 (n - 1/2)\lambda = & \left[(l_s + l_o) \left(\frac{\partial u}{\partial x} \Delta x + \frac{\partial u}{\partial y} \Delta y + \frac{\partial u}{\partial z} \Delta z \right) \right. \\
 & + (m_s + m_o) \left(\frac{\partial v}{\partial x} \Delta x + \frac{\partial v}{\partial y} \Delta y + \frac{\partial v}{\partial z} \Delta z \right) \\
 & \left. + (n_s + n_o) \left(\frac{\partial w}{\partial x} \Delta x + \frac{\partial w}{\partial y} \Delta y + \frac{\partial w}{\partial z} \Delta z \right) \right] . \quad (45)
 \end{aligned}$$

It is noted that a shift does not occur out of the film plane.

An example of a cantilever beam with the shift in the Z-direction (Figure 36) is considered.

Fringes occur such that

$$(n - 1/2)\lambda = \left[(l_s + l_o) \frac{\partial u}{\partial z} + (m_s + m_o) \frac{\partial v}{\partial z} + (n_s + n_o) \frac{\partial w}{\partial z} \right] \Delta z .$$

The direction cosines are

$$l_o = 1, \quad m_o = n_o = 0$$

$$l_s = \cos \theta, \quad m_s = 0, \quad n_s = \sin \theta$$

thus

$$(n - 1/2)\lambda = \left[(1 + \cos \theta) \frac{\partial u}{\partial z} + \sin \theta \frac{\partial w}{\partial z} \right] \Delta z .$$

Other data include

$$\lambda = \frac{6328 (10^{-8})}{2.54} = 24.91 \times 10^{-6} \text{ in.}$$

$$\cos \theta = 0.9421$$

$$\sin \theta = 0.3353$$

$$\Delta z = \Delta_o = (n - 1) \Delta D_o$$

$$\Delta z = 0.0899 \text{ in.}$$

$$u|_{x=1} = \delta_1 = 0.005 \text{ in.}$$

$$l = 6 \text{ in.}$$

$$v = 0.37$$

$$b = 0.25 \text{ in.}$$

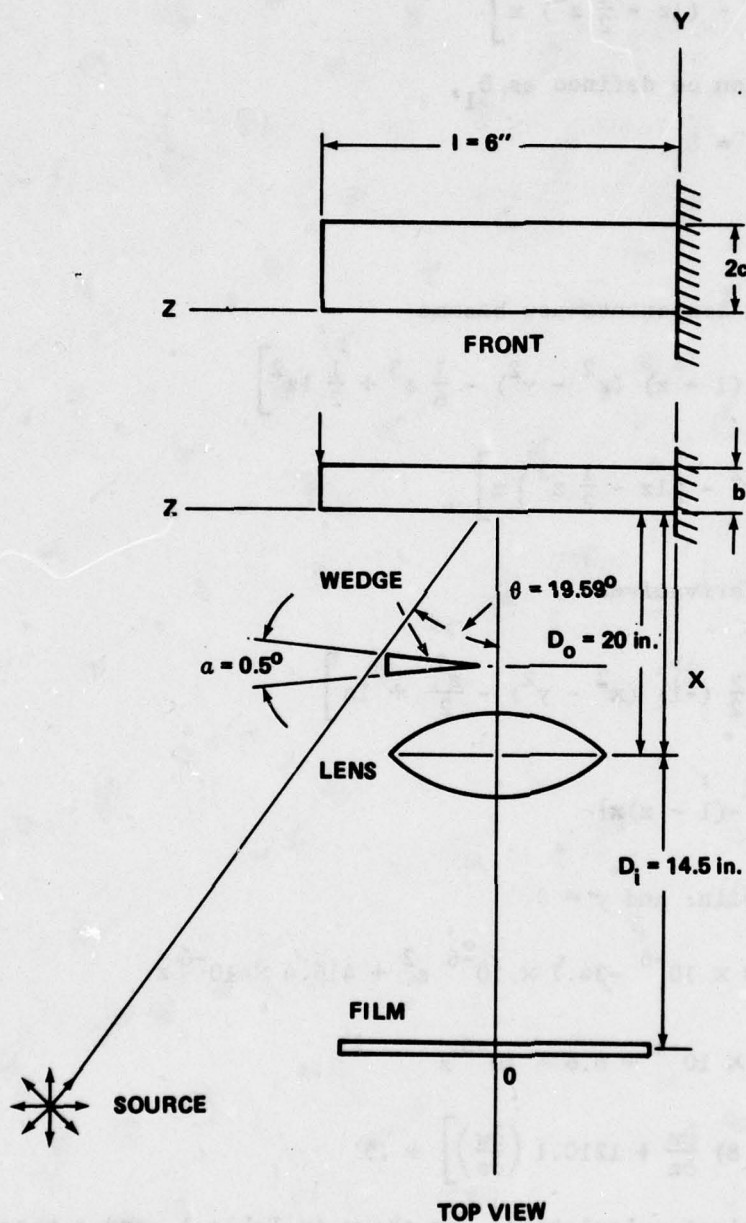


Figure 36. Experimental arrangement.

The displacement components are

$$u = \frac{W_x}{EI} \left[\frac{\nu}{2} (1 - z)(x^2 - y^2) - \frac{1}{6} z^3 + \frac{1}{2} lz^2 \right]$$

$$w = \frac{W_x}{EI} \left[xy^2 - (lz - \frac{1}{2} z^2) x \right] \quad (46)$$

Let the deflection be defined as δ_1 ,

$$u(0, 0, 1) = \delta_1$$

$$W_x = \frac{3EI\delta_1}{l^3}$$

The displacement components now become

$$u = \frac{3\delta_1}{l^3} \left[\frac{\nu}{2} (1 - z)(x^2 - y^2) - \frac{1}{6} z^3 + \frac{1}{2} lz^2 \right] \quad (47)$$

$$w = \frac{3\delta_1}{l^3} \left[xy^2 - \left(lz - \frac{1}{2} z^2 \right) x \right]$$

Taking partial derivatives

$$\frac{\partial u}{\partial z} = \frac{3\delta_1}{l^3} \left[\frac{\nu}{2} (-1)(x^2 - y^2) - \frac{z^2}{2} + lz \right] \quad (48)$$

$$\frac{\partial w}{\partial z} = \frac{3\delta_1}{l^3} [-(1 - z)x]$$

Taking $x = 0.125$ in. and $y = 0$

$$\frac{\partial u}{\partial z} = -0.200 \times 10^{-6} - 34.7 \times 10^{-6} z^2 + 416.4 \times 10^{-6} z$$

$$\frac{\partial w}{\partial z} = -51.6 \times 10^{-6} + 8.6 \times 10^{-6} z$$

$$n = \left[(7008.8) \frac{\partial u}{\partial z} + 1210.1 \left(\frac{\partial w}{\partial z} \right) \right] + .5$$

The theoretical calculations are shown in Table 1, and a theoretical fringe plot is shown in Figure 37. The experimental photograph is illustrated in Figure 38. The results were also imaged using a TV system with

a vidicon tube; the results are shown in Figure 39. A comparison between experiment and theory is illustrated in Figure 40; the agreement is obvious.

TABLE 1. THEORETICAL CALCULATION FOR CANTILEVER BEAM

z	$\frac{\partial u}{\partial z} (10^4)$	$\frac{\partial w}{\partial z} (10^4)$	n
0	-0.002	-0.516	0.436
0.5	1.993	-0.473	1.840
1.0	3.815	-0.430	3.122
1.5	5.463	-0.387	4.282
2.0	6.938	-0.344	5.321
2.5	8.239	-0.301	6.238
3.0	9.367	-0.258	7.034
3.5	10.321	-0.215	7.708
4.0	11.102	-0.172	8.260
4.5	11.709	-0.129	8.691
5.0	12.143	-0.086	9.000
5.5	12.403	-0.043	9.189
6.0	12.490	0	9.254

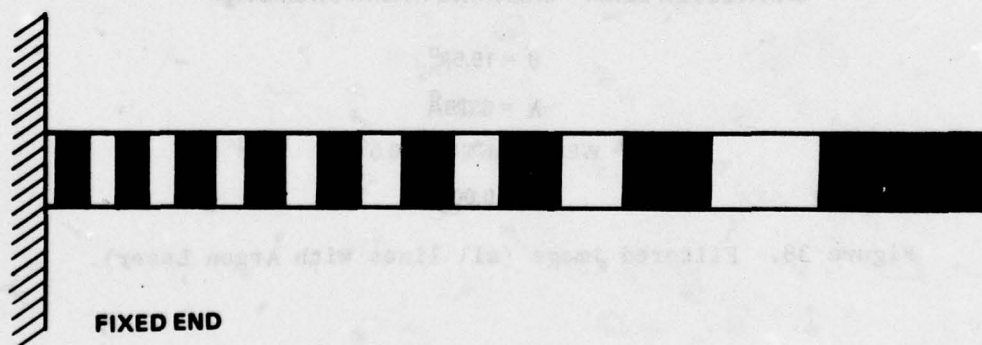
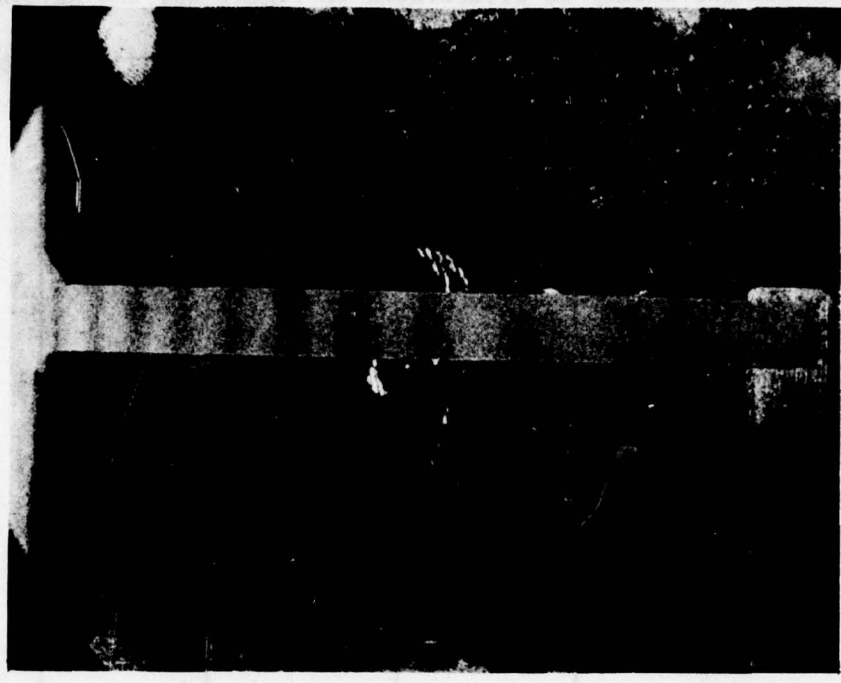


Figure 37. Theoretical fringes.



CANTILEVER BEAM - SHEARING INTERFEROMETRY

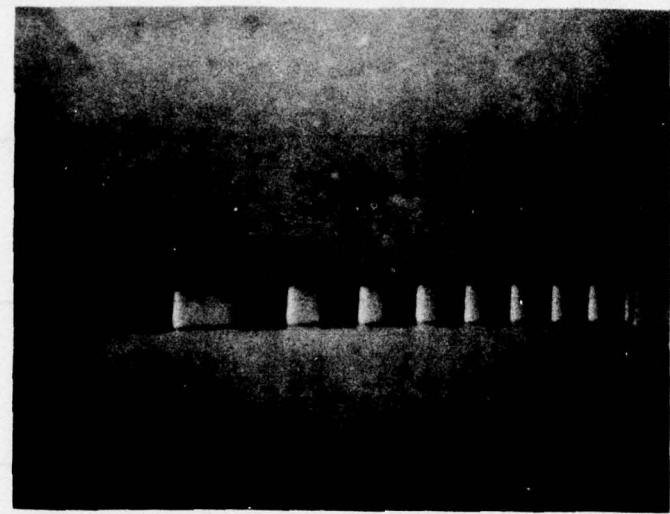
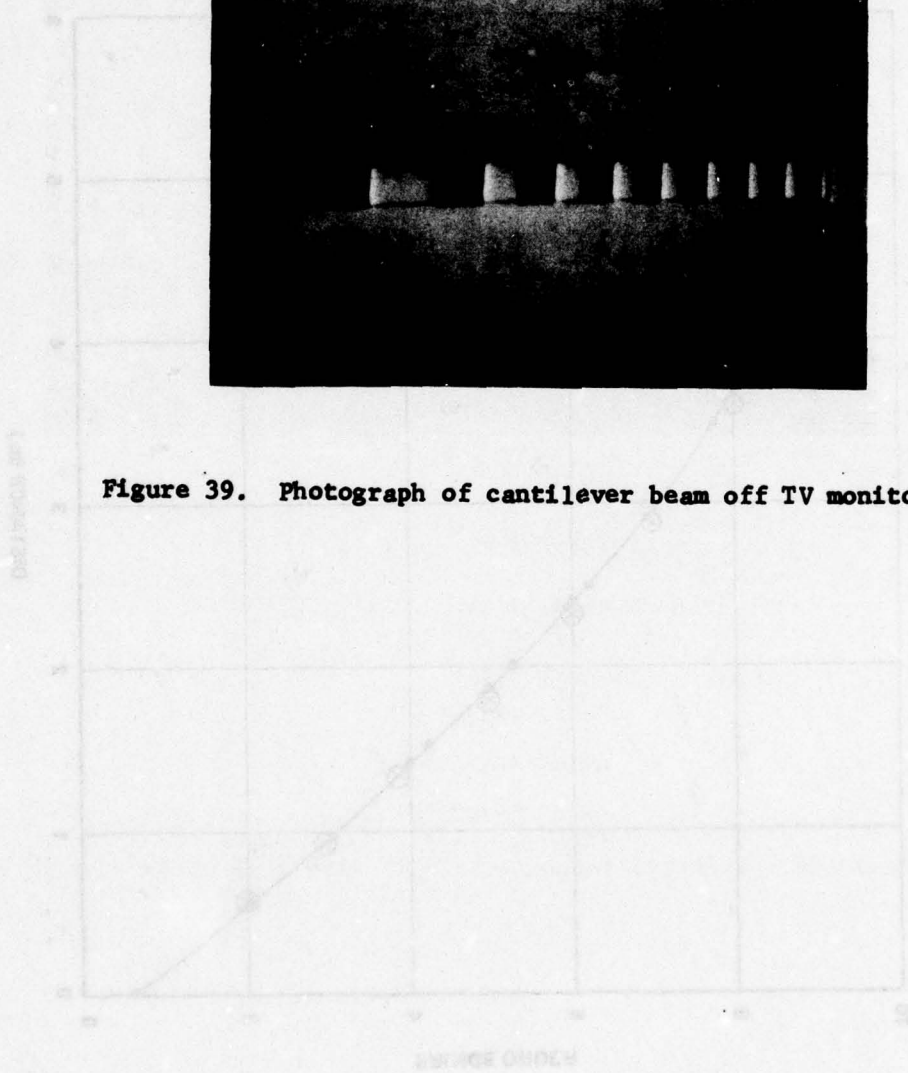
$\theta = 19.59^\circ$

$\lambda = 6328\text{\AA}$

WEDGE ANGLE - 0.5°

$\delta = 0.005 \text{ in.}$

Figure 38. Filtered image (all lines with Argon Laser).



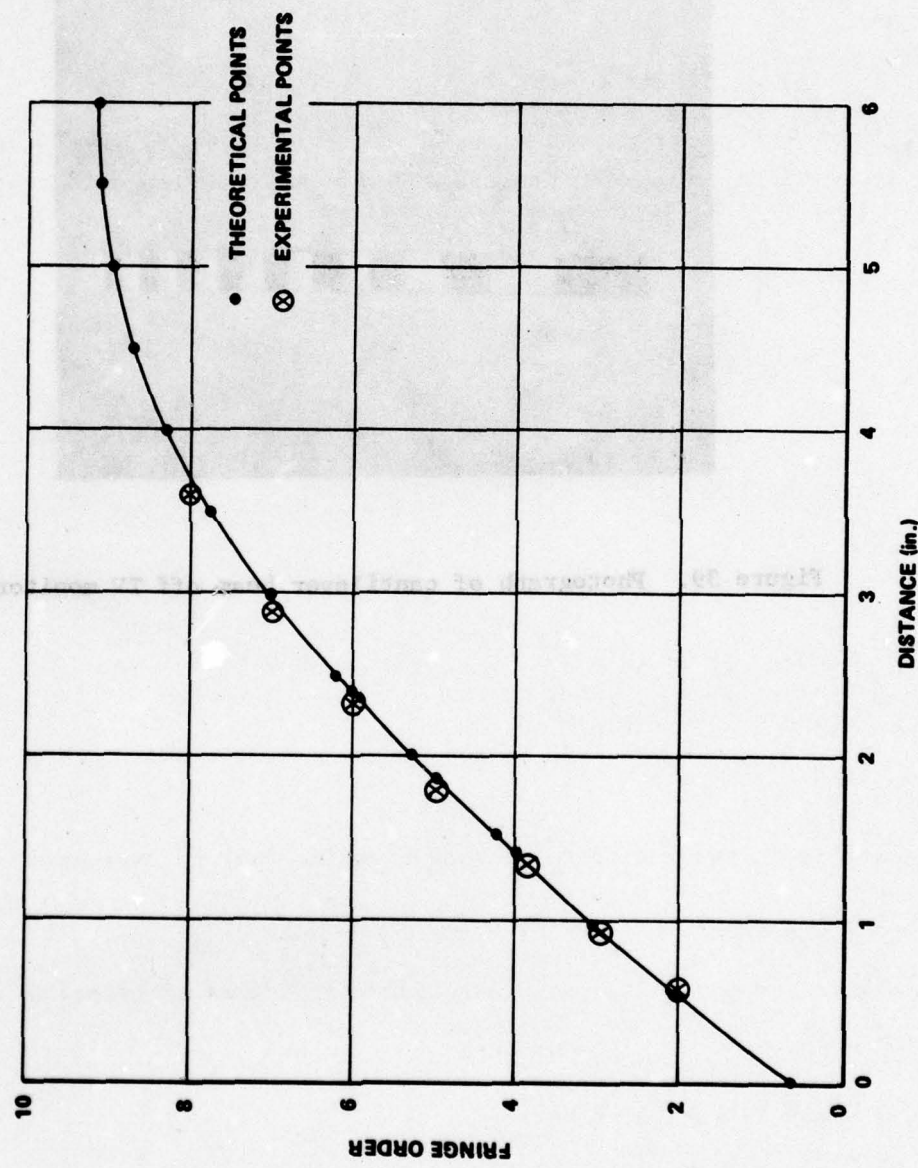


Figure 40. Comparison of theory and experiment.

This technique was next examined using a cylinder (Figure 41). The rectangular components of the radial deformation are

$$\begin{aligned}\delta_x &= \delta_r \cos \theta \\ \delta_y &= \delta_r \sin \theta\end{aligned}\quad (49)$$

where

$$\delta_r = \frac{pr^2}{Et} \left(1 - \frac{\nu}{2}\right) \quad (50)$$

when the cylindrical vessel is assumed to be thin-walled with capped ends. In terms of displacement components,

$$\begin{aligned}u &= \frac{pr^2}{Et} \left(1 - \frac{\nu}{2}\right) \cos \theta \\ v &= \frac{pr^2}{Et} \left(1 - \frac{\nu}{2}\right) \sin \theta\end{aligned}\quad (51)$$

The experiment is set up as illustrated in Figure 42. Unit vectors are

$$\begin{aligned}\vec{ps} &= \sin \beta \vec{i} + \cos \beta \vec{j} \\ \vec{po} &= \vec{j}\end{aligned}$$

or

$$\begin{aligned}l_o &= 0 & l_s &= \sin \beta \\ m_o &= 1 & m_s &= \cos \beta \\ n_o &= 0 & n_s &= 0\end{aligned}$$

The shift is in the x direction; thus Equation (45) is expressed as

$$\left(n - \frac{1}{2}\right)\lambda = \left[\sin \beta \frac{\partial u}{\partial x} + (1 + \cos \beta) \frac{\partial v}{\partial x}\right] \Delta x \quad . \quad (52)$$

The relation between polar and cartesian coordinates is recalled:

$$r^2 = x^2 + y^2 \quad \theta = \arctan \frac{y}{x} \quad (53)$$

and the chain rule derivatives

$$\frac{\partial u}{\partial x} = \frac{\partial u}{\partial r} \frac{\partial r}{\partial x} + \frac{\partial u}{\partial \theta} \frac{\partial \theta}{\partial x}$$

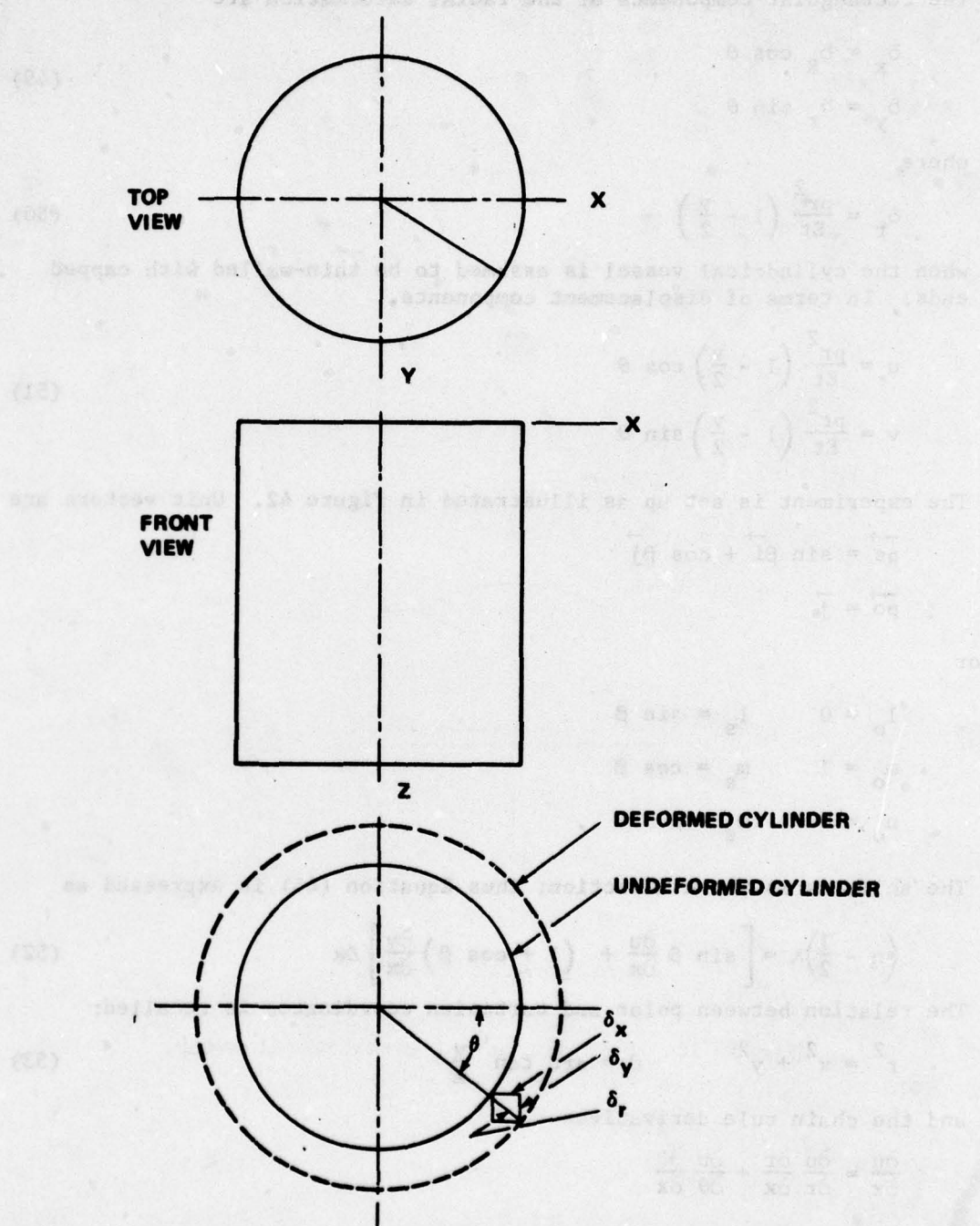


Figure 41. Pressure vessel.

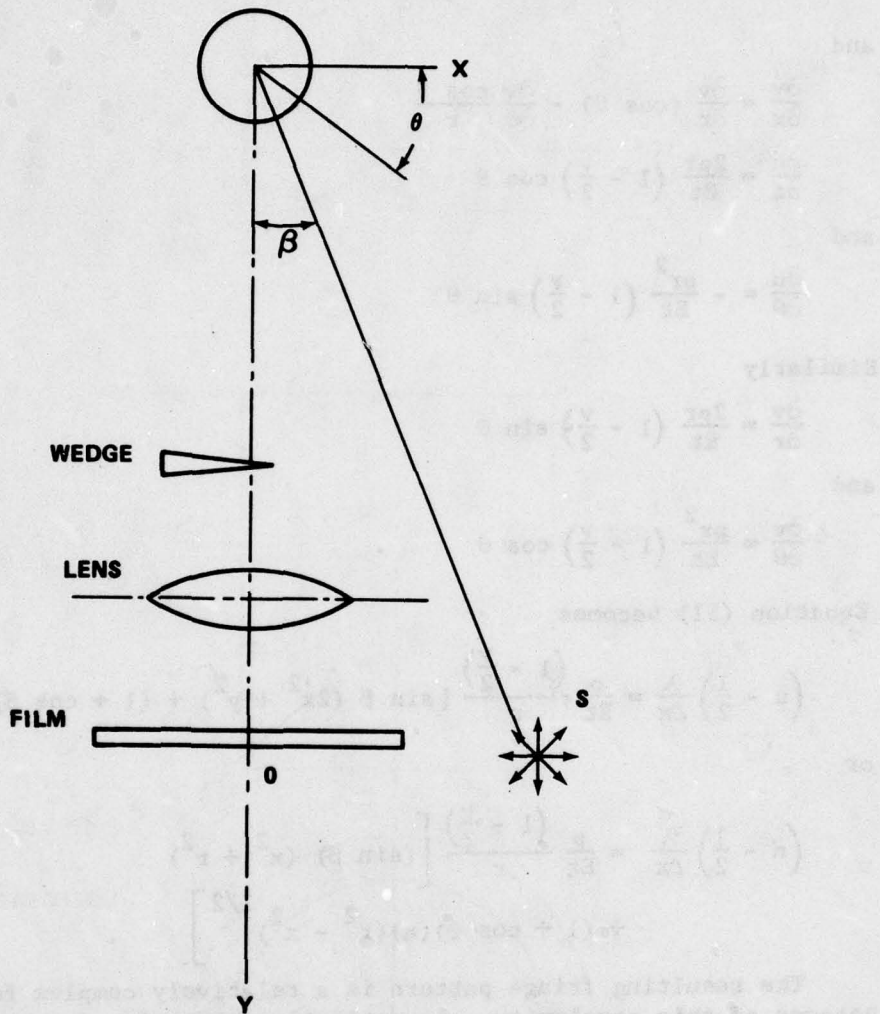


Figure 42. Pressure vessel experimental setup.

or

$$\frac{\partial u}{\partial x} = \frac{\partial u}{\partial r} (\cos \theta) - \frac{\partial u}{\partial \theta} \frac{\sin \theta}{r} \quad (54)$$

and

$$\frac{\partial v}{\partial x} = \frac{\partial v}{\partial r} (\cos \theta) - \frac{\partial v}{\partial \theta} \frac{\cos \theta}{r} \quad (55)$$

$$\frac{\partial u}{\partial r} = \frac{2pr}{Et} \left(1 - \frac{\nu}{2}\right) \cos \theta \quad (56)$$

and

$$\frac{\partial u}{\partial \theta} = - \frac{pr^2}{Et} \left(1 - \frac{\nu}{2}\right) \sin \theta$$

Similarly

$$\frac{\partial v}{\partial r} = \frac{2pr}{Et} \left(1 - \frac{\nu}{2}\right) \sin \theta \quad (57)$$

and

$$\frac{\partial v}{\partial \theta} = \frac{pr^2}{Et} \left(1 - \frac{\nu}{2}\right) \cos \theta$$

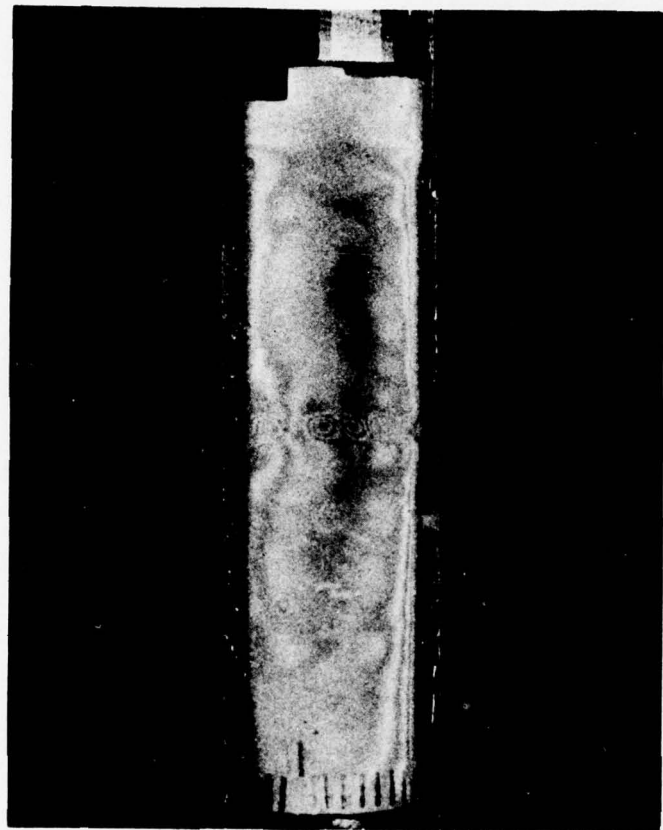
Equation (51) becomes

$$\left(n - \frac{1}{2}\right) \frac{\lambda}{\Delta x} = \frac{p}{Et} \frac{\left(1 - \frac{\nu}{2}\right)}{r} [\sin \beta (2x^2 + y^2) + (1 + \cos \beta) (xy)] \quad (58)$$

or

$$\left(n - \frac{1}{2}\right) \frac{\lambda}{\Delta x} = \frac{p}{Et} \frac{\left(1 - \frac{\nu}{2}\right)}{r} \left[(\sin \beta) (x^2 + r^2) + (1 + \cos \beta) (x)(r^2 - x^2)^{1/2} \right] \quad (59)$$

The resulting fringe pattern is a relatively complex function of x . Because of this complexity, a quantitative analysis of a homogeneous cylinder is not straightforward. In application to a composite cylinder, quantitative analysis would be even less feasible. A qualitative fringe pattern for composites is possible as noted in Figures 43 through 45, but the complexity of assigning a quantity to a given flaw makes this technique less desirable than some of the other techniques.



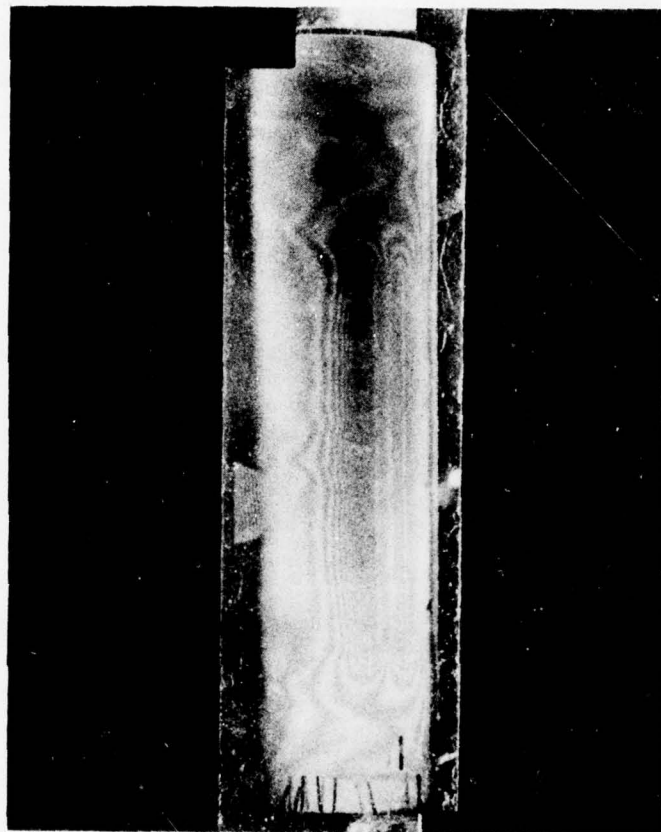
HORIZONTAL SHEAR - WEDGE ANGLE 0.25°

$\theta = 29.67^\circ$

$\lambda = 6328 \text{ \AA}$

$\Delta p = 20 \text{ psi}$

Figure 43. Circumferential flaw, filtered image.



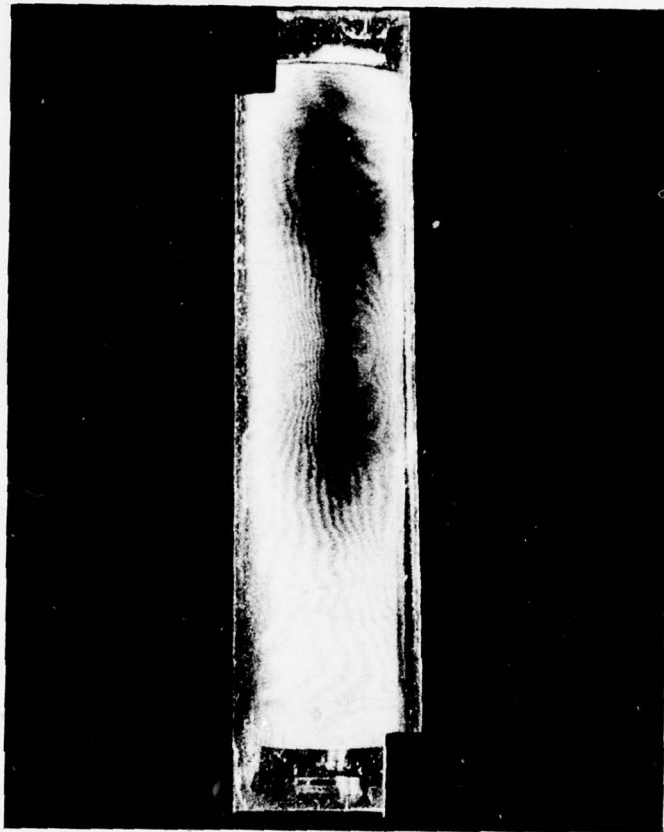
HORIZONTAL SHEAR – WEDGE ANGLE 0.25°

$\theta = 29.67^\circ$

$\lambda = 6328 \text{ \AA}$

$\Delta p = 20 \text{ psi}$

Figure 44. Longitudinal flaw, filtered image.



HORIZONTAL SHEAR – WEDGE ANGLE 0.25°

$\theta = 29.67^\circ$

$\lambda = 6328 \text{ \AA}$

$\Delta p = 20 \text{ psi}$

Figure 45. Spot flaw, filtered image.

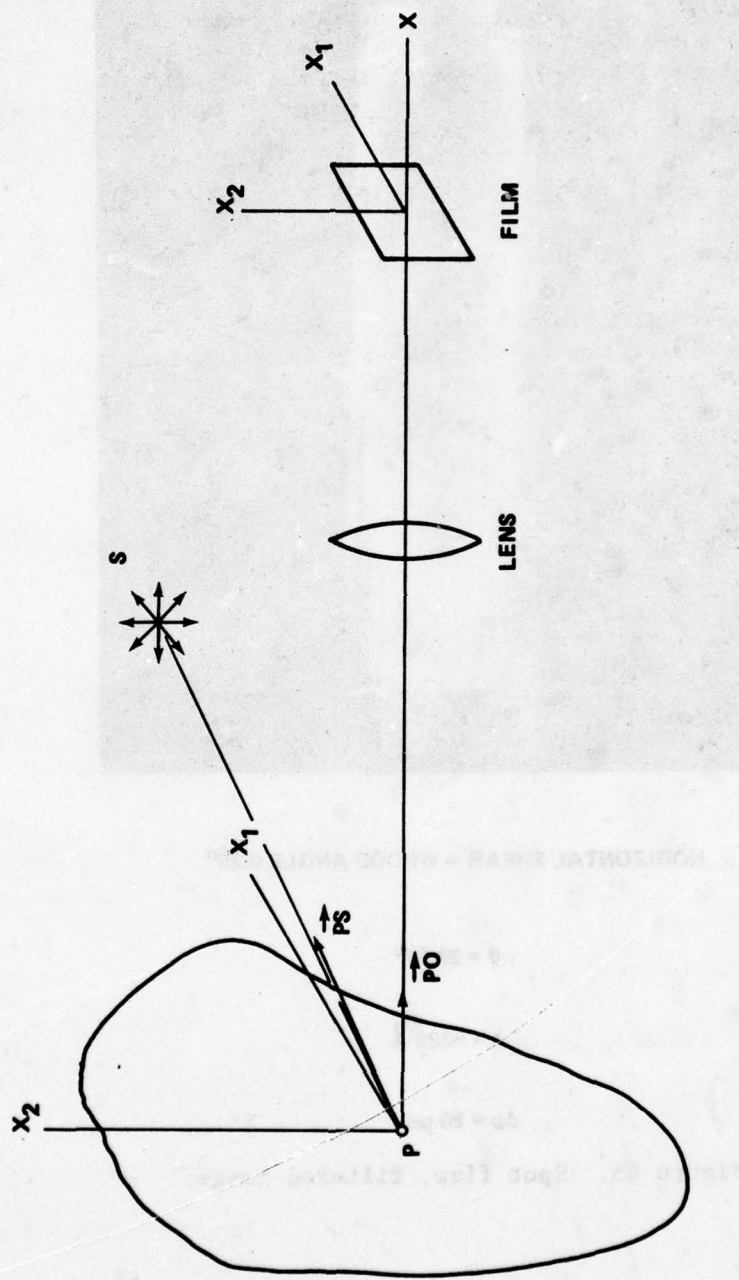


Figure 46. Arrangement for single beam analysis.

V. DOUBLE EXPOSURE SPECKLE PHOTOGRAPHY SINGLE BEAM ANALYSIS

An object is illuminated by a single beam as shown in Figure 46. The location of the light source is shown schematically as S where P is a point on the surface of the object. A double-exposure technique is considered where the body is imaged two times on the same film before and after deformation. For the first exposure, the complex light amplitude can be expressed in the following form:

$$\bar{E}(x_1, x_2) = \bar{A}(x_1, x_2) e^{i\theta(x_1, x_2)} \quad (60)$$

where x_1 and x_2 are the film plane coordinates.

If the object is deformed and the point P is displaced to a point P' , then the image on the film plane will be shifted to new coordinates x'_1 and x'_2 . The complex light amplitude is

$$\bar{E}'(x'_1, x'_2) = \bar{A}(x'_1, x'_2) e^{i[\theta(x'_1, x'_2) + \Delta\theta]} \quad (61)$$

The intensity of the first exposure is

$$I_1 = \bar{E}_1 \bar{E}_1^*$$

or

$$I_1 = A^2(x_1, x_2) \quad (62)$$

The intensity of the second exposure is

$$I_2 = \bar{E}'(\bar{E}')^*$$

or

$$I_2 = A^2(x'_1, x'_2) \quad (63)$$

The total intensity is I_T where

$$I_T = I_1 + I_2 \quad (64)$$

Physically what has been done is to image the point P at the location x_1, x_2 at the film plane coordinates. After the body has been deformed, the point P now at P' is imaged at the film plane coordinates x'_1, x'_2 .

If the displacement vector $\overrightarrow{PP'}$ is written in the following manner

$$\overrightarrow{PP'} = u_i \overrightarrow{e_i} \quad , \quad (65)$$

then the displacement vector in the film plane can be written as

$$\vec{[PP' (x_1 x_2)]} = M \vec{PP' (x_1 x_2)} \quad (66)$$

FILM

where M = magnification of camera, typically $M < 1$ and

$$u_{1f} = M u_1$$

$$u_{2f} = M u_2$$

The coordinates at the film plane for the second exposure are

$$x'_1 = x_1 + u_{1f}$$

$$x'_2 = x_2 + u_{2f}$$

and

$$\vec{(PP')_f} = u_{1f} \vec{e_1} + u_{2f} \vec{e_2} \quad (67)$$

The total intensity after the second exposure can be written in terms of coordinates in the form

$$I_T = A^2(x_1, x_2) + A^2(x_1 + u_{1f}, x_2 + u_{2f}) \quad (68)$$

The amplitude transmission of the photographic plate is $g(x, y)$. Let the amplitude of transmission be linear with exposure (reasonable assumption for most films that are used), then

$$g(x_1, x_2) = a + b I_T \quad (69)$$

where a, b are constants.

For convenience the x_2 coordinate is suppressed in the following discussion, thus

$$g(x) = a + b \left[A^2(x) + A^2(x + u_{1f}) \right] \quad (70)$$

Burch and Tokarski [8] have derived the following expression:

$$G(w) = e^{\left[\frac{izw^2}{2k} \right]} \int a + b \left[A^2(x) + A^2(x + u_{1f}) \right] e^{(-iwx)} dx \quad (71)$$

This expression is the Fourier Transform of the amplitude transmission function of the photographic plate where w is given by (Figure 30):

$$w = \frac{2\pi}{\lambda} \tan \theta = \frac{2\pi x_s}{z\lambda} \quad (72)$$

where x_s is the coordinate on the screen or Fourier Transform plane and the limits of integration are from $-\infty$ to $+\infty$. The equation for $G(w)$ is derived from the Kirchoff diffraction formula and with Equation (70)

$$G(w) = e^{\left[\frac{izw^2}{2k}\right]} \int_a^b A^2(x) + A^2(x + u_{1f}) e^{(-iwx)} dx \quad (73)$$

let

$$\delta(w) = \int e^{(-iwx)} dx \quad (74)$$

where $\delta(w)$ is called the delta function;

then,

$$G(w) = a e^{\left[\frac{izw^2}{2k}\right]} \delta(w) + b e^{\left[\frac{izw^2}{2k}\right]} \int A^2(x) + A^2(x + u_{1f}) e^{(-iwx)} dx \quad (75)$$

Use the shift theorem on the second term

$$\int \left[A^2(x + u_{1f}) \right] e^{(-iwx)} dx = \int A^2(x) e^{(-iwx)} e^{(iu_{1f}w)} dx \quad (76)$$

$$\text{Define } F[A] = \int A^2(x) e^{(-iwx)} dx \quad (77)$$

Thus,

$$G(w) = a e^{\left[\frac{izw^2}{2k}\right]} \delta(w) + b e^{\left[\frac{izw^2}{2k}\right]} F[A] [1 + e^{(iu_{1f}w)}] \quad (78)$$

The intensity at the transform plane is

$$I_F = G(w) G(w^*) \quad (79)$$

or

$$I_F = b^2 F[A]^2 [1 + e^{(-iwu_{1f})} + e^{(iwu_{1f})}]$$

or

$$I_F = 2b^2 F[A]^2 [1 + \cos(wu_{1f})] \quad . \quad (80)$$

A fringe will be defined when $I_F = 0$; therefore,

$$[1 + \cos(wu_{1f})] = 0$$

when

$$\cos(wu_{1f}) = -1$$

or

$$wu_{1f} = (2n - 1)\pi$$

It is recalled that

$$w = \frac{2\pi}{\lambda} \left(\frac{x_s}{z} \right)$$

and

$$n = \left(\frac{x_s}{z\lambda} \right) u_{1f} + \frac{1}{2} \quad (81)$$

Figure 47 is referenced to interpret Equation (81). The information at location x_s is selected by placing an aperture to pass only the light in the immediate neighbor of x_s . This light is then imaged on the film. Thus x_s being fixed the imaged fringe information is proportional to u_{1f} or

$$u_{1f} = \left(n - \frac{1}{2} \right) \frac{\lambda z}{x_s} m_1 \quad (82)$$

where m_1 is the magnification of the new image relative to the original object. An experiment was set up to note the results of the theory reflected in Equation (82). The experimental arrangement is shown in Figure 48. The coordinates relative to the cantilever beam are shown in Figure 49.

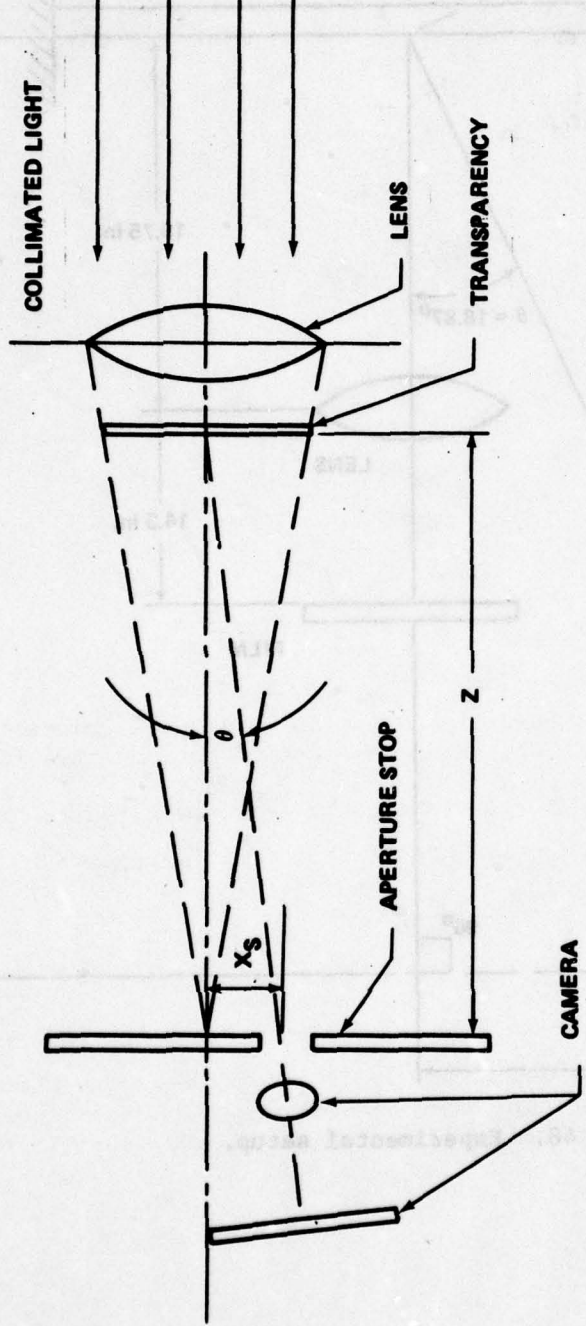


Figure 47. Arrangement for data collection.

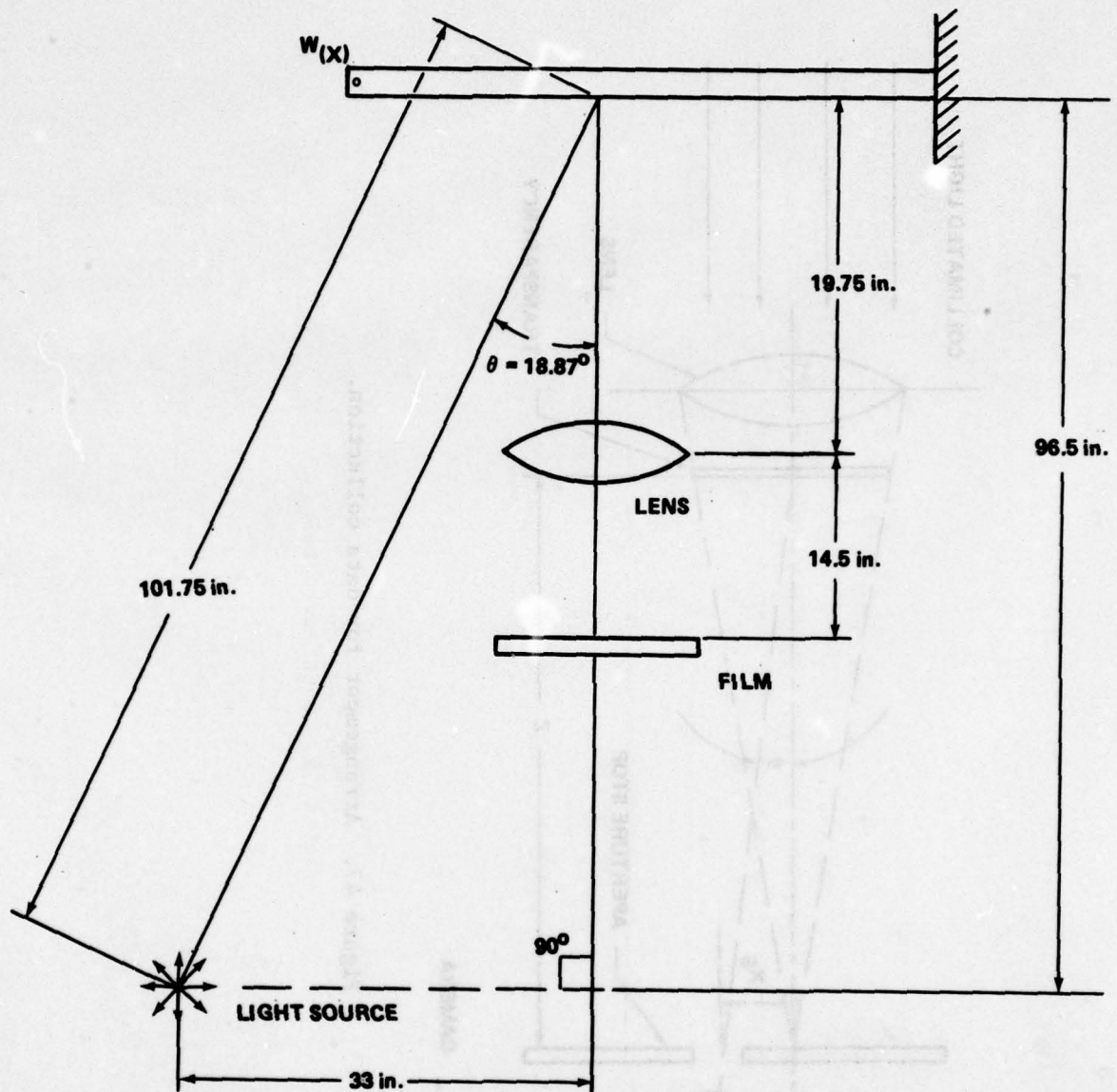


Figure 48. Experimental setup.

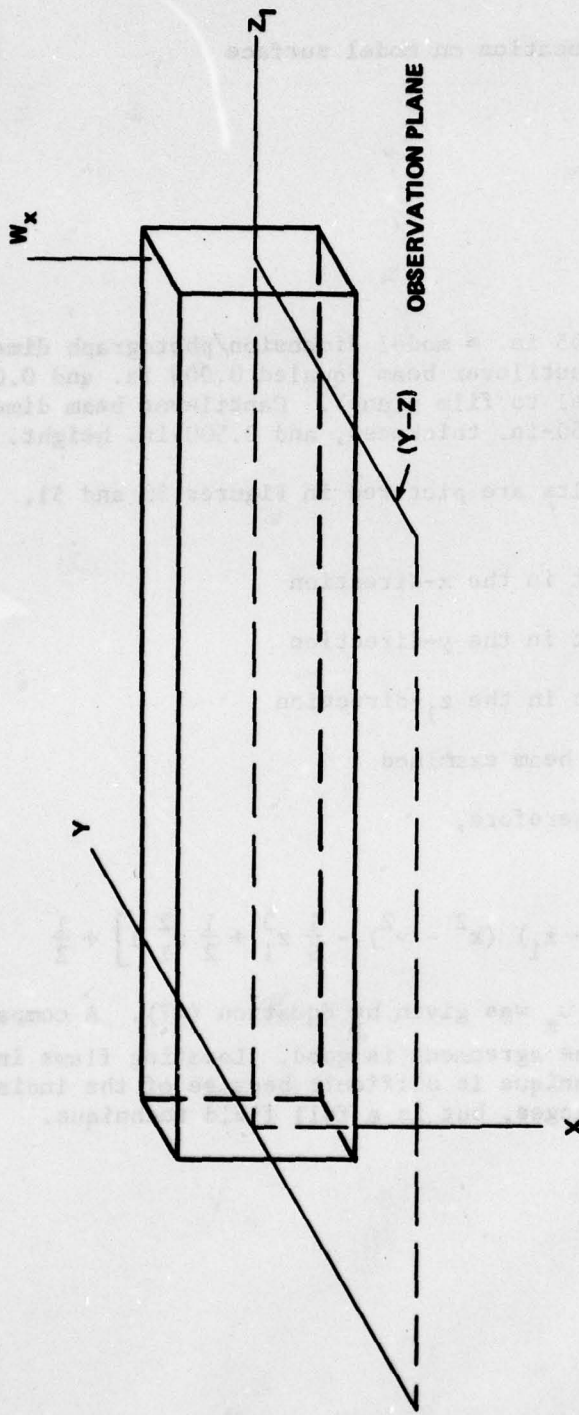


Figure 49. Cantilever beam.

Other data include:

z_1 = coordinate location on model surface

z = 33 in.

x_s = 0.98 in.

λ = 20.26 μ in.

ν = 0.37

Scale factor = 4.55 in. = model dimension/photograph dimension. Deflection on end of cantilever beam equaled 0.003 in. and 0.006 in. (in a direction parallel to film plane). Cantilever beam dimensions were 6-in. length, 0.250-in. thickness, and 0.500-in. height.

Experimental results are pictured in Figures 50 and 51. For comparison with theory let

u_x = displacement in the x -direction

u_y = displacement in the y -direction

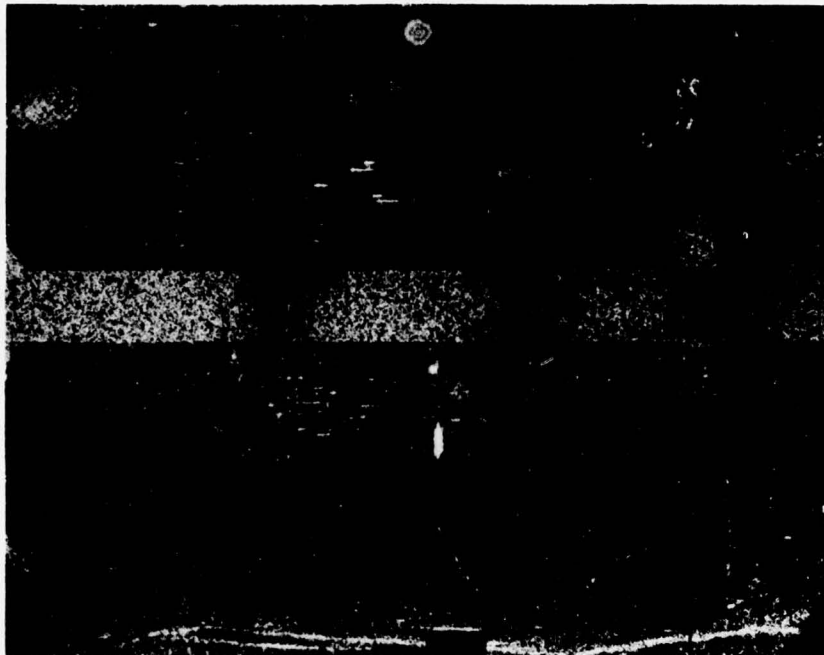
u_{z1} = displacement in the z_1 -direction

and for the cantilever beam examined

$u_{z1} \gg u_x$; therefore,

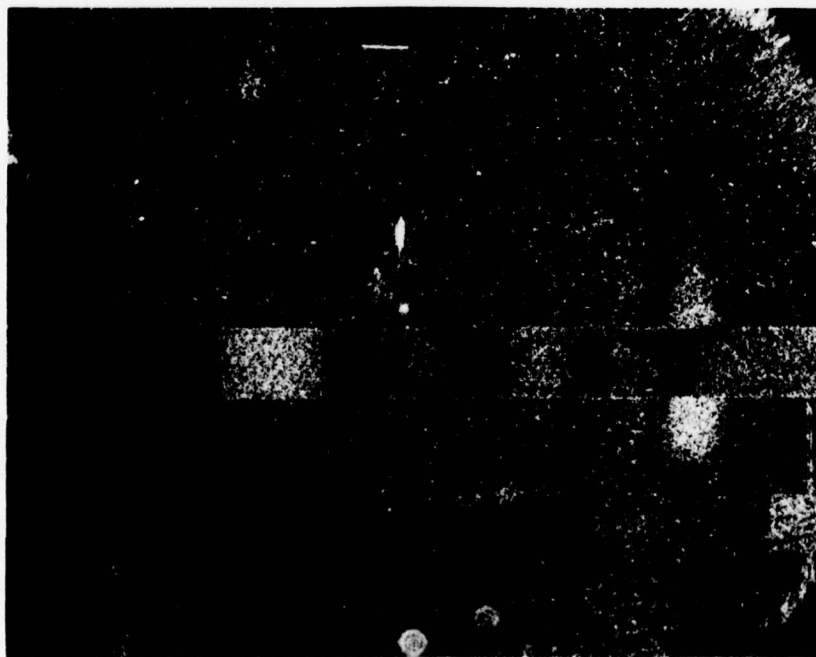
$$n = \frac{x_s}{\lambda z} \frac{3m\delta}{l^3} \left[\frac{\nu}{2} (1 - z_1) (x^2 - y^2) - \frac{1}{6} z_1^3 + \frac{1}{2} z_1^2 l \right] + \frac{1}{2} \quad (83)$$

where the displacement u_z was given by Equation (47). A comparison is shown in Figure 52. The agreement is good. Locating flaws in composite structures by this technique is difficult because of the indistinct (relative to holography) fringes, but is a full field technique.



$\theta = 18.87^\circ$
 $\lambda = 5145\text{\AA}$
 $\delta = 0.003 \text{ in.}$

Figure 50. Cantilever beam, Young's fringes.



$\theta = 18.87^\circ$
 $\lambda = 5145\text{\AA}$
 $\delta = 0.006 \text{ in.}$

Figure 51. Cantilever beam, Young's fringes.

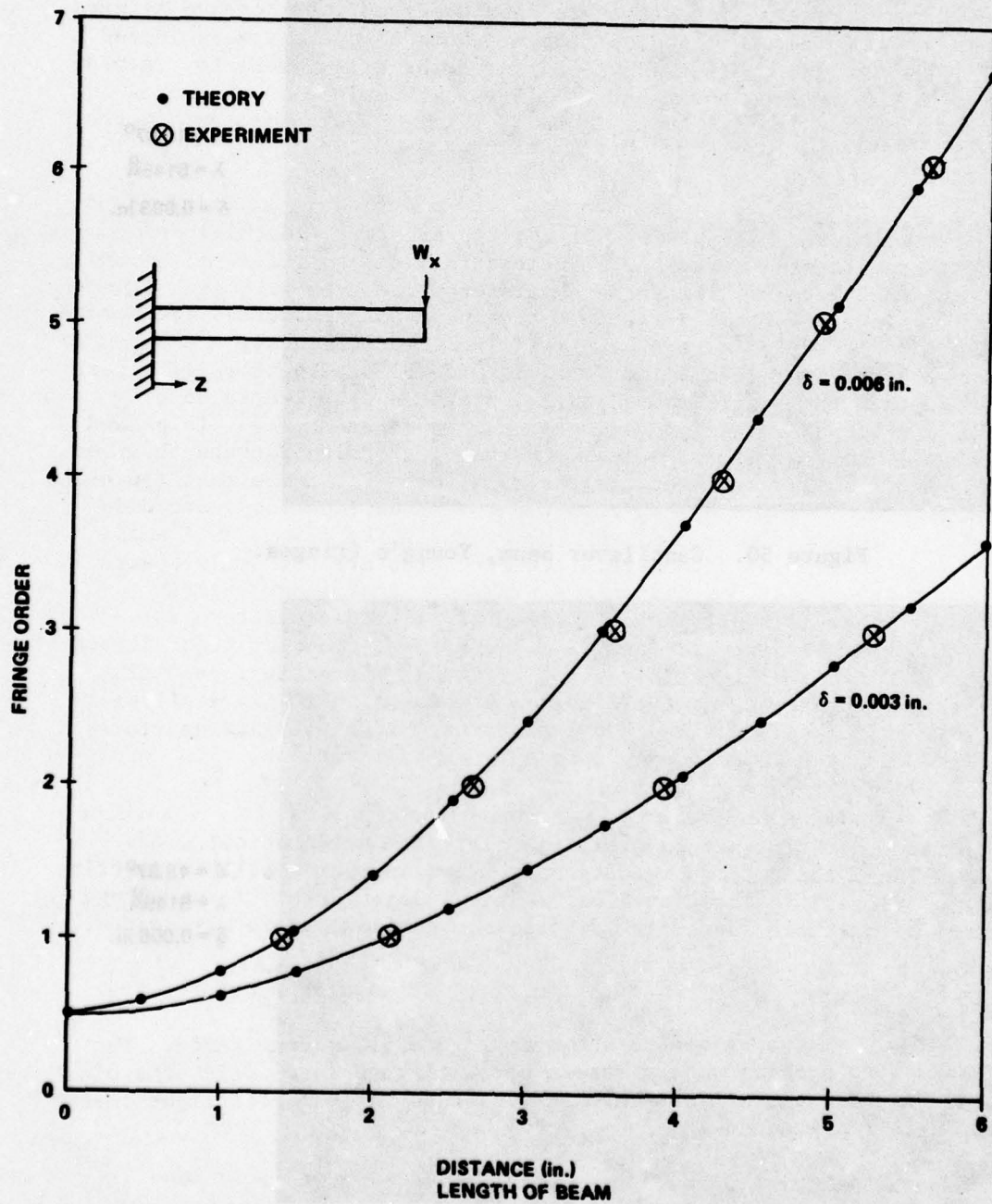


Figure 52. Comparison of theory and experiment.

VI. SPECKLE INTERFEROMETRIC ANALYSIS USING YOUNG'S FRINGES

A. General

Several investigators have observed interference fringes from laser produced speckle displacements when a test piece is loaded [9, 10, 11, 12, 13]. Figure 53 illustrates the arrangement for recording the necessary double-exposed film: one exposure with the model unloaded and one with the model loaded. Figure 54 illustrates how the model can be observed.

If each speckle point is thought of as an aperture emitting light, then several things take place. First, the aperture (speckle) produces interference patterns (Fraunhofer diffraction) due to its size; secondly, any nearby aperture will produce interference patterns with each other (Young's fringes). Finally, because the speckles (apertures) are numerous and randomly oriented the patterns mentioned previously are obscured by each other. Now, if a film record is made of the speckles of a test model and then the model loaded and the previous film record double exposed (Figure 53), fringes can be seen when coherent light is passed through a small region of the film and the diffraction pattern observed (Figure 54). This occurs because the film records the aperture (speckle) in the undeformed model state, then the apertures (speckles) are displaced in the loaded model and again recorded on the film. In a small region of the film the second recorded apertures are uniformly spaced relative to the first set and when a small coherent light beam is passed through this small region of film a diffraction pattern is observed identical to those observed when a small coherent light illuminates a small region in a diffraction grating. The pattern resulting comes from interference of the light as it passes through a small aperture (Fraunhofer diffraction) and interference from multiple apertures (diffraction grating) uniformly spaced in a small region.

The fringes, caused when light passes through a small rectangular slit (Fraunhofer diffraction), will initially be mathematically described. Then, the pattern resulting from two apertures will be described (Young's fringes) followed by a mathematical description of the fringe patterns of multiple apertures (diffraction grating) uniformly spaced.

B. Fraunhofer Diffraction by a Rectangular Aperture

The arrangement shown in Figure 55 is considered. The lens serves to project onto a screen parallel rays that would otherwise diverge from the centerline. A unit vector to the parallel light rays along OH is represented as

$$\vec{a}_1 = \vec{\ell i} + \vec{mj} + \vec{nk} \quad . \quad (84)$$

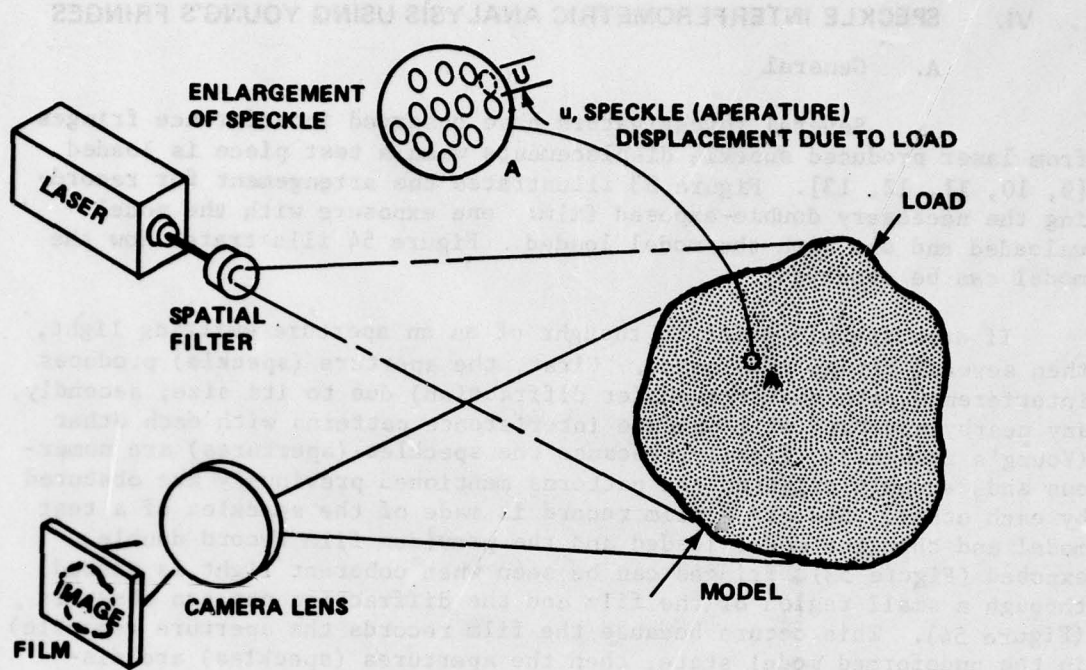


Figure 53. Collection of speckle interferometric data.

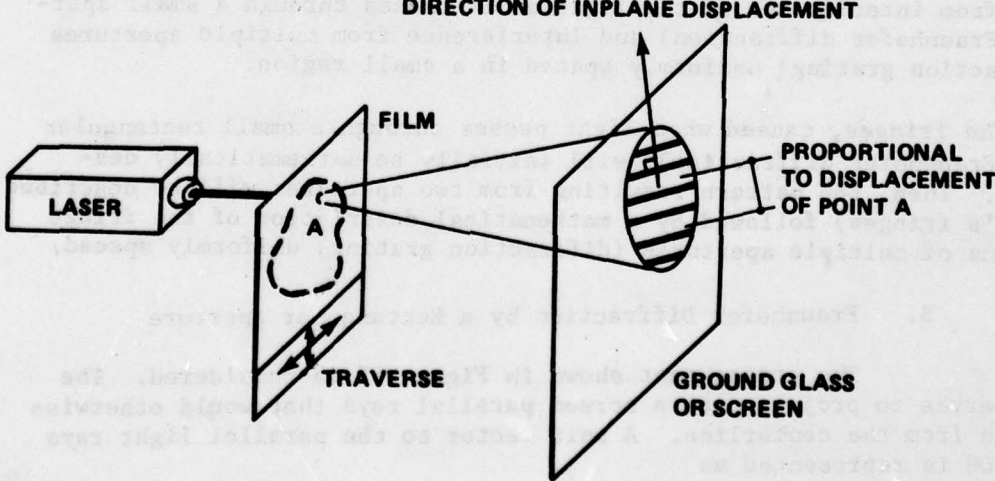


Figure 54. Data analysis.

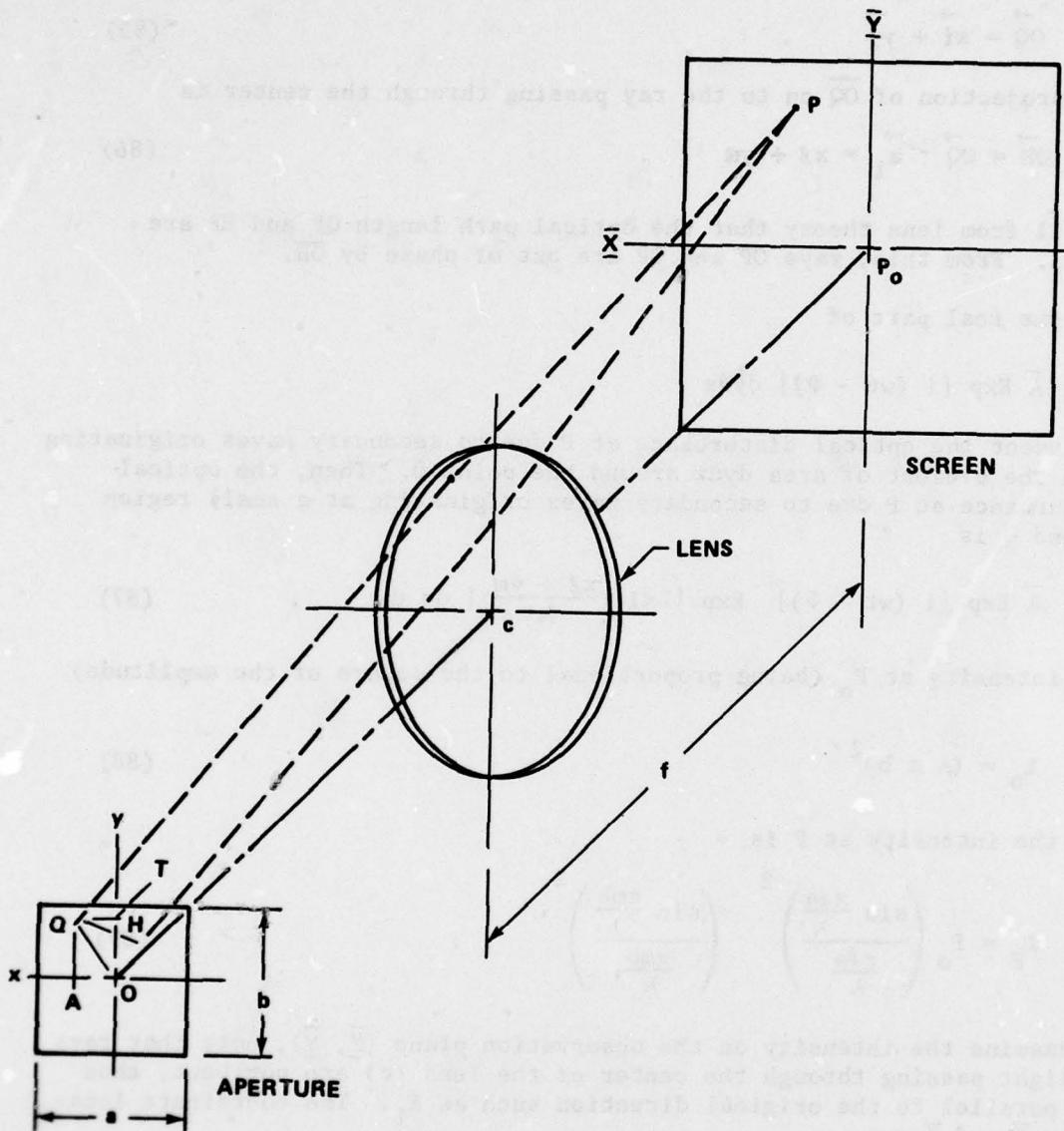


Figure 55. Rectangular aperture arrangement.

Note that \overline{OH} is on a ray passing through the center of the aperture. Point Q is a representative point in the plane of the aperture and located as

$$\overrightarrow{OQ} = \overrightarrow{x}i + \overrightarrow{y}j \quad . \quad (85)$$

The projection of \overrightarrow{OQ} on to the ray passing through the center is

$$\overrightarrow{OH} = \overrightarrow{OQ} \cdot \overrightarrow{a_1} = x\ell + ym \quad . \quad (86)$$

Recall from lens theory that the optical path length QP and HP are equal. From this, rays OP and QP are out of phase by \overline{OH} .

Let the real part of

$$\bar{A} \exp [i(wt - \Phi)] dy dx$$

represent the optical disturbance at P due to secondary waves originating from the element of area $dy dx$ around the point O. Then, the optical disturbance at P due to secondary waves originating at a small region around Q is

$$\bar{A} \exp [i(wt - \Phi)] \exp [2\pi i \frac{x\ell + ym}{\lambda}] dy dx \quad . \quad (87)$$

The intensity at P_o (being proportional to the square of the amplitude) is

$$I_o = (A a b)^2 \quad (88)$$

and the intensity at P is

$$I_p = I_o \left(\frac{\sin \frac{\pi \ell a}{\lambda}}{\frac{\pi \ell a}{\lambda}} \right)^2 \left(\frac{\sin \frac{\pi m b}{\lambda}}{\frac{\pi m b}{\lambda}} \right)^2 \quad . \quad (89)$$

To examine the intensity on the observation plane (\bar{x} , \bar{y}), note that rays of light passing through the center of the lens (c) are not bent, thus are parallel to the original direction such as \bar{a}_1 . The coordinate locations \bar{x} and \bar{y} are

$$\bar{x} = |\overline{CP}| \quad \ell \approx f\ell \quad (90)$$

$$\bar{y} = |\overline{CP}| \quad m \approx fm$$

for small angles relative to the center line and where f is the lens focal length. Equation (89) now can be expressed as

$$I_P = I_o \left(\frac{\sin \frac{\pi \bar{X}a}{\lambda f}}{\frac{\pi \bar{X}a}{\lambda f}} \right)^2 \left(\frac{\sin \frac{\pi \bar{Y}b}{\lambda f}}{\frac{\pi \bar{Y}b}{\lambda f}} \right)^2 \quad (91)$$

Since the variables \bar{X} and \bar{Y} are separable in Equation (91), only

$$\frac{dI_P}{d\bar{X}} = 0$$

and

$$\frac{dI_P}{d\bar{Y}} = 0$$

need be examined for maxima and minima on the \bar{XY} plane. Thus, maxima and minima occur when

$$\sin \frac{\pi \bar{X}a}{\lambda f} = 0 \text{ yielding } \frac{\pi \bar{X}a}{\lambda f} = 0, \pi, 2\pi, \dots n_1 \pi \quad (92)$$

and

$$\tan \frac{\pi \bar{X}a}{\lambda f} = \frac{\pi \bar{X}a}{\lambda f} \quad (93)$$

From Equation (92) the initial value of zero will produce a maximum in Equation (91). The other values from Equation (92), $\pi, 2\pi, \dots, n_1 \pi$, give minima values of zero in Equation (91). The approximate values for the solution of Equation (93) are 0 (exact), $3\pi/2, 5\pi/2, \dots$. All values correspond to maxima.

C. Fraunhofer Diffraction by Two Nearby Apertures

The interference pattern produced on a screen by two equal sized apertures is considered. As illustrated in Figure 56, consider two apertures located along the X axis and projected on the screen. Let $l = \sin \theta$, $m = 0$, and $n = \cos \theta$; thus, the optical disturbances at P from A_1 and A_2 are

$$\bar{E}_1 = \bar{A} a b \frac{\sin \frac{\pi l a}{\lambda}}{\frac{\pi l a}{\lambda}} \text{ Exp} [i (wt - \Phi_1)] \quad (94)$$

and

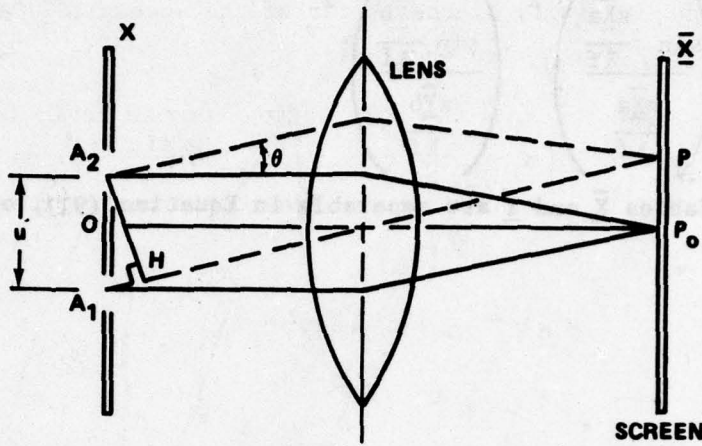


Figure 56. Fraunhofer diffraction by two apertures.

$$\bar{E}_2 = \bar{A} a b \frac{\sin \frac{\pi la}{\lambda}}{\frac{\pi la}{\lambda}} \exp [i (wt - \phi_2)]$$

The phase difference at P due to the different path lengths $A_1 P$ and $A_2 P$ is

$$\frac{2\pi |A_1 H|}{\lambda} = \frac{2\pi u \sin \theta}{\lambda} \quad . \quad (95)$$

Then

$$I_P = I_o \left(\frac{\sin \frac{\pi la}{\lambda}}{\frac{\pi la}{\lambda}} \right)^2 \cos^2 \left(\frac{\pi u \sin \theta}{\lambda} \right)$$

$$= I_o \left(\frac{\sin \frac{\pi a \bar{x}}{\lambda}}{\frac{\pi a \bar{x}}{\lambda}} \right)^2 \cos^2 \left(\frac{\pi u \sin \theta}{\lambda} \right) \quad (96)$$

where I_0 is the intensity at the center of the screen (P_0) and ℓ is approximated as \bar{X}/f and also equals $\sin \theta$.

Equation (96) contains the diffraction term as noted for a single aperture and now an interference term, $\cos^2 \left(\frac{\pi u \sin \theta}{\lambda} \right)$, due to two apertures close together. Emphasis is called to the cosine function where zero intensity occurs if

$$u = \pm \frac{\lambda}{2 \sin \theta} \cong \pm \frac{\lambda f}{2 \bar{X}}$$

$$u = \left(\frac{3}{2} \right) \frac{\lambda}{\sin \theta} \cong \pm \frac{3}{2} \frac{\lambda f}{\bar{X}} \quad (97)$$

$$u \cong \pm \left(\frac{2m_1 - 1}{2} \right) \frac{\lambda f}{\bar{X}} \text{ for } m_1 = 1, 2, 3, \dots$$

Also, if u becomes less than $a/2$, then the dominating function is the sine function. The distance between apertures is the information that will give the displacement; therefore, if the total displacement at a point is less than one-half the aperture (speckle) size then this technique has limitations. A representative speckle size is 300 μin . and 150 μin . should be thought of as a minimum limitation on total displacement at a point.

D. Interference Patterns from Multiple Apertures

Consider the final case of multiple apertures, the same size and equally spaced about the X -axis as illustrated in Figure 57. The optical disturbance at P due to the first aperture is given by Equation (94) and for the N^{th} aperture as

$$\bar{E}_N = \bar{E}_{n+1} = \bar{A}_{ab} \frac{\sin \frac{\pi \ell a}{\lambda}}{\frac{\pi \ell a}{\lambda}} \text{ Exp} \left[i \left(wt - \Phi_1 + \frac{2\pi n u \sin \theta}{\lambda} \right) \right] \quad (98)$$

The total optical disturbance from N diffracted beams is

$$\bar{E}_P = \bar{E}_1 + \bar{E}_2 + \bar{E}_3 + \dots + \bar{E}_N \quad (99)$$

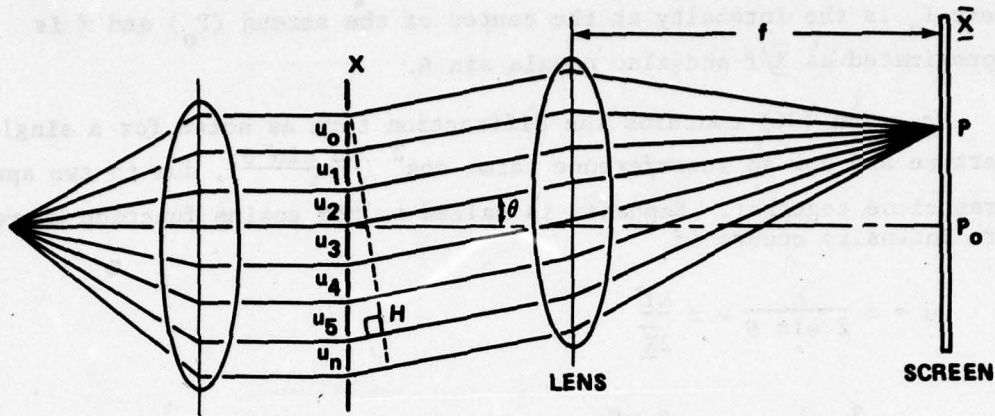


Figure 57. Multiple apertures.

and the intensity at any point is

$$I_p = (Aab)^2 \left[\frac{\sin \frac{\pi a \sin \theta}{\lambda}}{\frac{\pi a \sin \theta}{\lambda}} \right]^2 \left[\frac{\sin \left(\frac{N\pi u \sin \theta}{\lambda} \right)}{\sin \left(\frac{\pi u \sin \theta}{\lambda} \right)} \right]^2 \quad (100)$$

For the case of $U = 2a$ and $N = 10$, an illustration of Equation (100) is shown in Figure 58. It should be noted that if $u = a$, no fringes will occur; and represents the minimum limiting case for engineering applications. If $u > a$ two or more fringes will be evident on the screen. Now consider the application, if an image is recorded of the speckle pattern on a model made by illumination with a coherent light source, these many speckles are recorded as apertures on the film. When the model is loaded, the speckles (apertures) shift. By double exposing the first film record, a second set of apertures is recorded.

In a small region of the film, the second set of apertures is equally spaced relative to the first. The spacing equals the in-plane displacement vector. The out-of-plane displacement effects only the focus of the image and has almost no effect on the aperture spacing. When a coherent light is used to illuminate, the film record in a small region where the in-plane displacements are essentially equal to the projected diffraction pattern intensity is described by Equation (100) or as

$$I_p = C \left[\frac{\sin \frac{\pi a \bar{X}}{\lambda f}}{\frac{\pi a \bar{X}}{\lambda f}} \right]^2 \left[\frac{\sin \frac{N\pi \bar{X}}{\lambda f} u}{\sin \frac{\pi \bar{X} u}{\lambda f}} \right]^2 \quad (101)$$

$$I_p = (Aab)^2 \left[\frac{\sin \left(\frac{\pi a \sin \theta}{\lambda} \right)}{\left(\frac{\pi a \sin \theta}{\lambda} \right)} \right]^2 \left[\frac{\sin \left(\frac{N\pi u \sin \theta}{\lambda} \right)}{\sin \left(\frac{\pi u \sin \theta}{\lambda} \right)} \right]^2$$

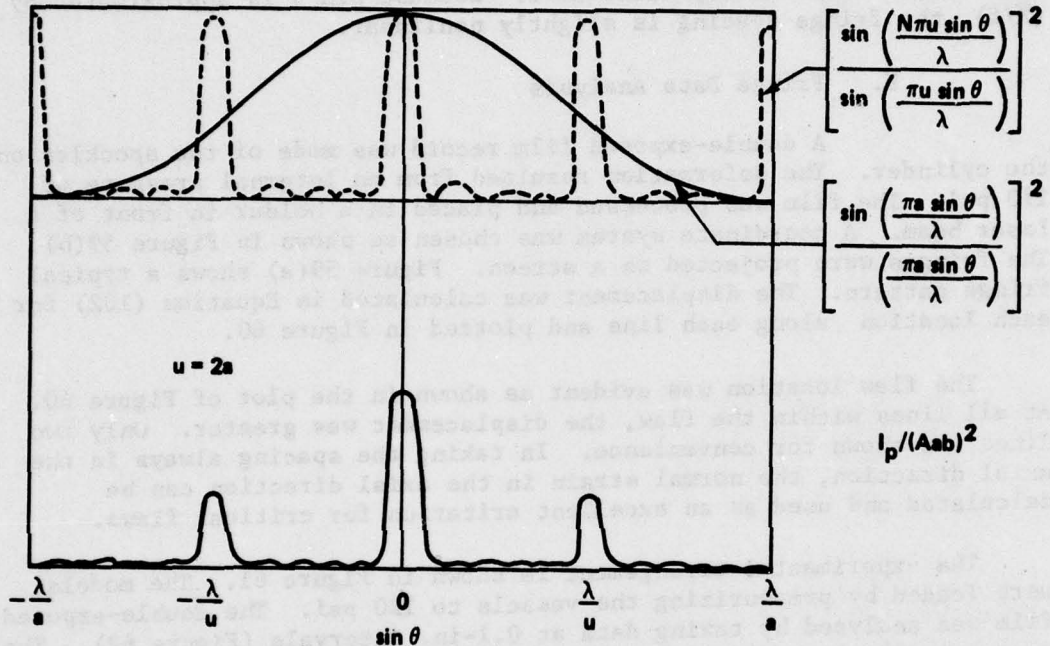


Figure 58. Intensity distribution of multiple apertures.

where

C = a proportionality constant

a = average speckle size

f = lens focal length or distance to the screen

λ = wave length of the light source

\underline{x} = coordinate distance on the screen

u = in-plane displacement

Maxima occur where

$$u = m_1 \frac{\lambda f}{\underline{x}} \text{ for } m_1 = 0, 1, 2, \dots \quad (102)$$

where m_1 is the fringe order.

Instead of using the lens focal length to evaluate the displacement, the technique works without a lens and the distance f is the distance from the film to the screen. This speckle technique was applied to flaw detection in composite cylinders. These data are included in Figures 59 and 60. The minimum spacing representing total displacement is 100 μ in. The maximum displacements depend on resolution of the fringes where 20,000 μ in. is representative. Because $\sin \theta$ is approximated by (X/f) , the fringe spacing is slightly nonlinear.

E. Fringe Data Analysis

A double-exposed film record was made of the speckles on the cylinder. The deformation resulted from an internal pressure of 110 psi. The film was processed and placed in a holder in front of a laser beam. A coordinate system was chosen as shown in Figure 59(b). The fringes were projected on a screen. Figure 59(a) shows a typical fringe pattern. The displacement was calculated in Equation (102) for each location along each line and plotted in Figure 60.

The flaw location was evident as shown in the plot of Figure 60. At all lines within the flaw, the displacement was greater. Only two lines are shown for convenience. In taking the spacing always in the axial direction, the normal strain in the axial direction can be calculated and used as an excellent criterion for critical flaws.

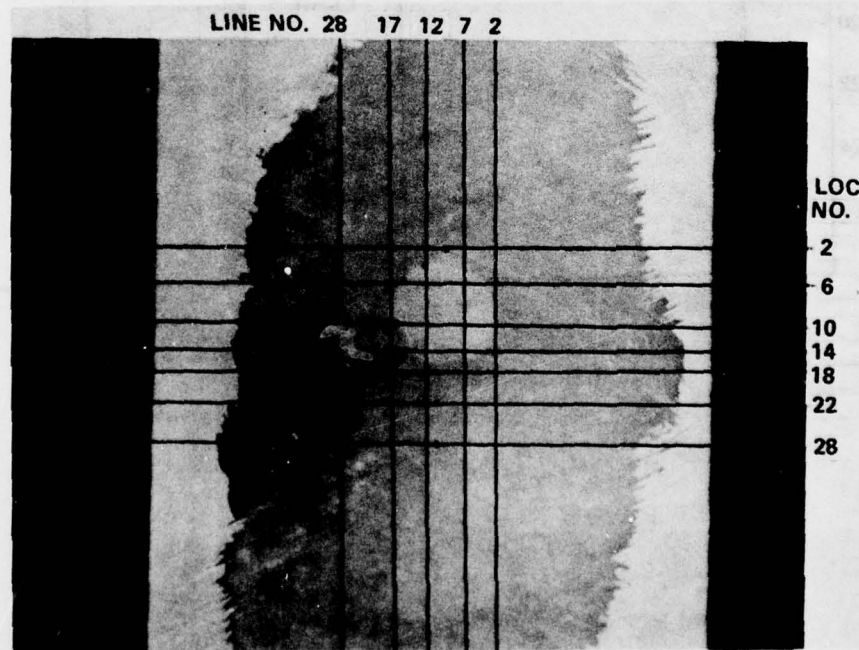
The experimental arrangement is shown in Figure 61. The models were loaded by pressurizing the vessels to 120 psi. The double-exposed film was analyzed by taking data at 0.1-in. intervals (Figure 62). The x , y axis was located arbitrarily. Figure 63 shows the effect on the fringes in the vicinity of a flaw. At each location (x, y) , the fringe spacing was measured in the y direction (axis of the cylinder) and displacement in the y direction calculated using Equation (102). The results of the spot flaw illustrated in Figure 3 are shown in Figures 64 through 69. The results of the longitudinal flaw illustrated in Figure 2 are shown in Figures 70 through 75. The results of the circumferential flaw illustrated in Figure 1 are shown in Figures 76 through 80.

The results of the spot flaw displacements note 0 to 400 μ in. in unflawed regions. In the vicinity of the flaw (graphs in the neighborhood of $x = 0.8$ through 1.1 in. and $y = 1.1$ through 1.6 in.), the displacements change abruptly indicating high strain. Figure 63 illustrated how the fringes change. Figure 69 shows strain values in the direction of the cylinder axis (normal strain on an area perpendicular to the y axis) that are larger than $2000 (10^{-6})$ in./in. The flaw size and location are evident. Similar results are shown in Figures 76 and 80 for the longitudinal and circumferential flaws. Because of the minimum stability (in comparison with holography and correlation fringe techniques) and because of the ease of quantizing the results in comparison with holography,

correlation fringe, shearing speckle interferometry, and single beam speckle techniques, this technique of Young's fringes is a most promising method of flaw quantification.



(a) TYPICAL YOUNG'S FRINGE PROJECTION



(b) GRID SYSTEM

Figure 59. Cylinder with spot flaw and Young's fringes shown with the grid system.

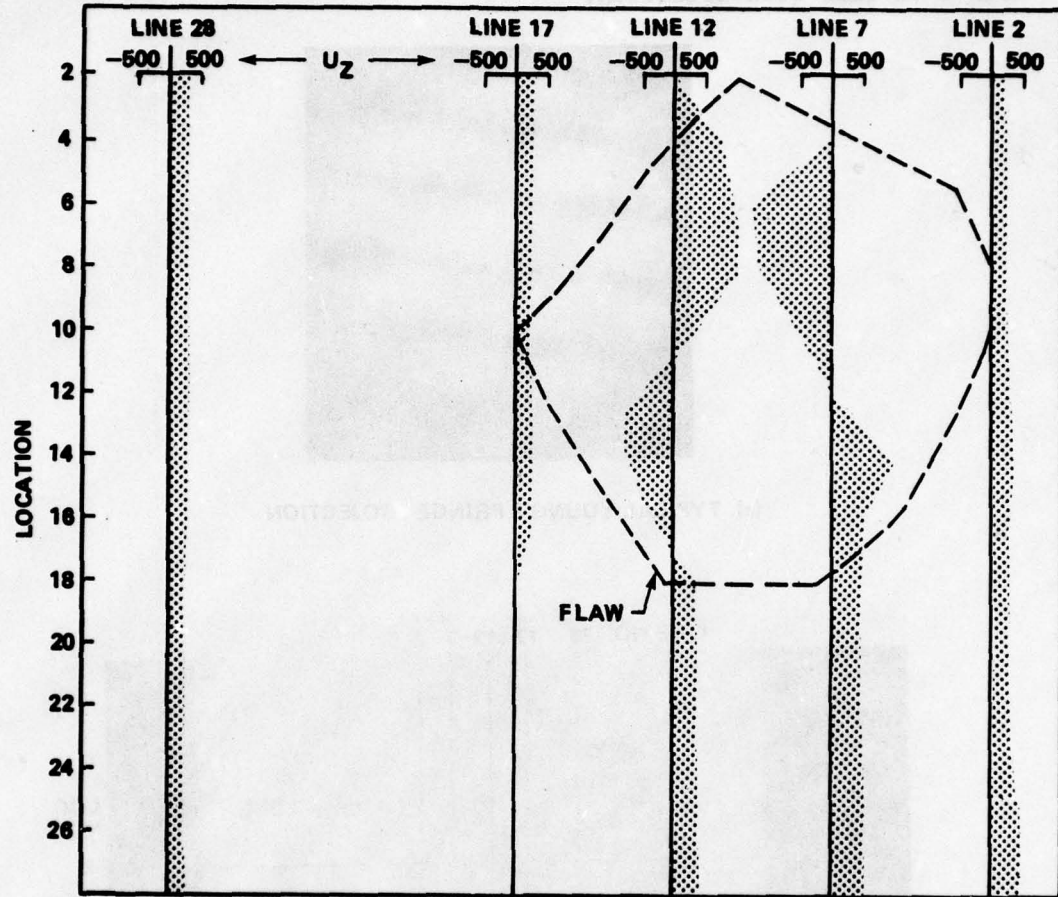
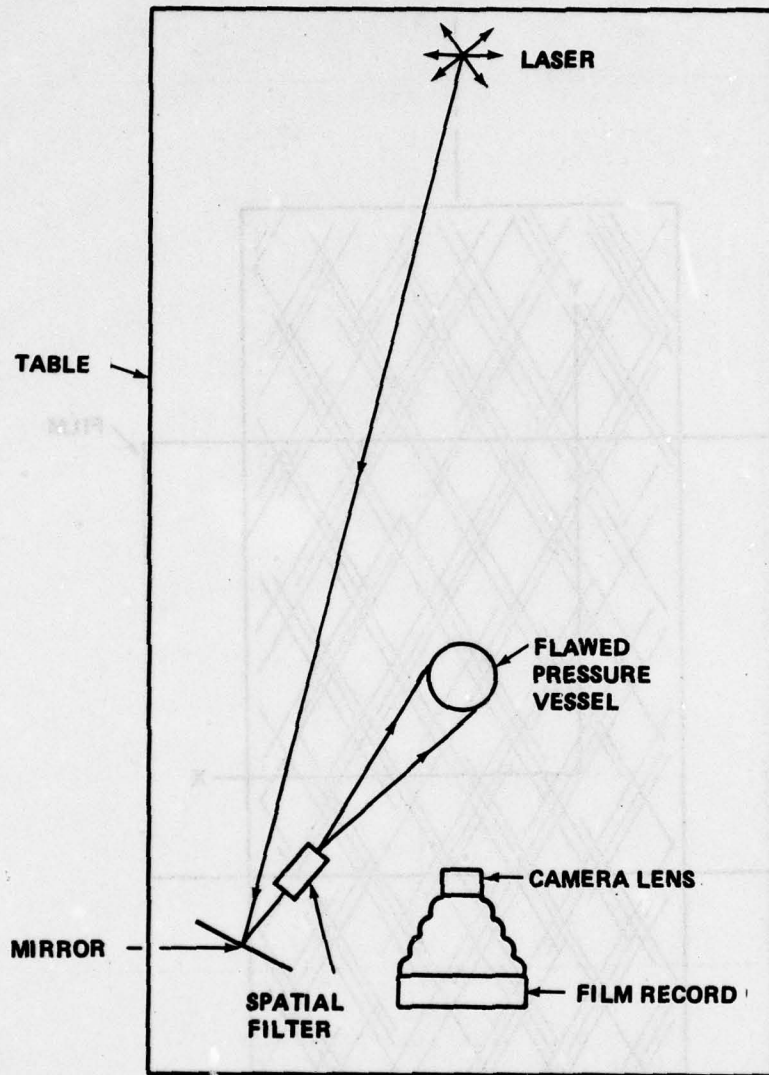


Figure 60. Grid locations versus axial displacements (microinches).



TOP VIEW

Figure 61. Experimental arrangement.

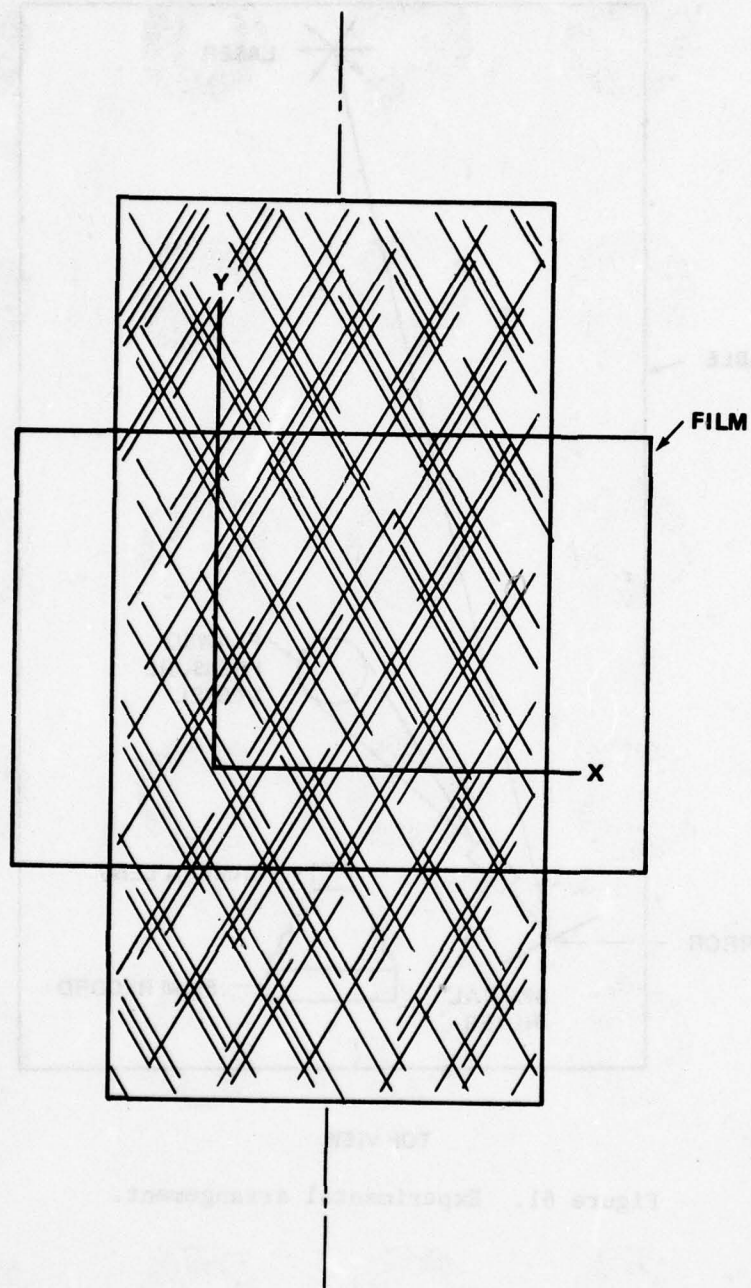


Figure 62. Coordinate axis.

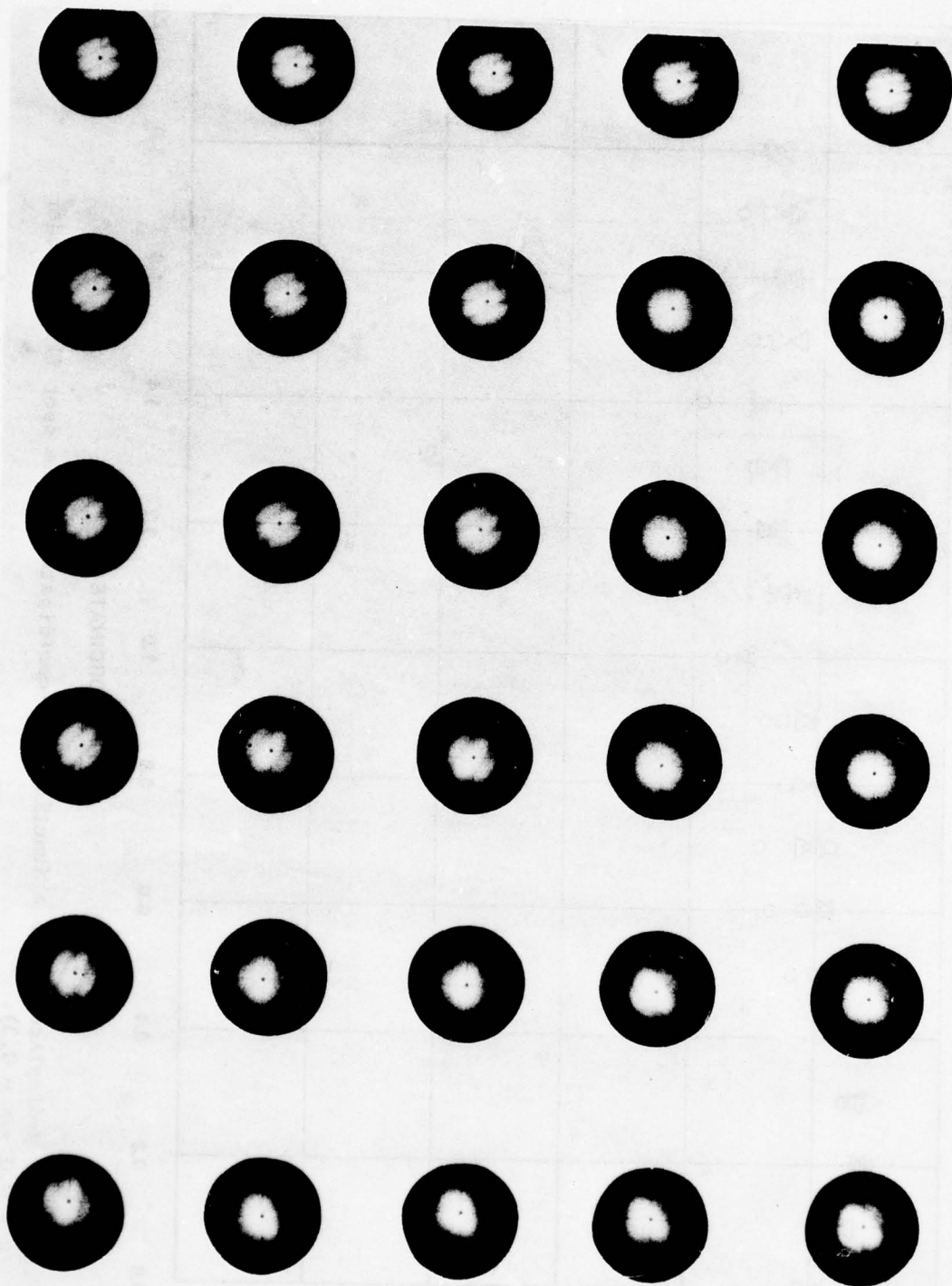


Figure 63. Fringe pictures (every 0.2 in.).

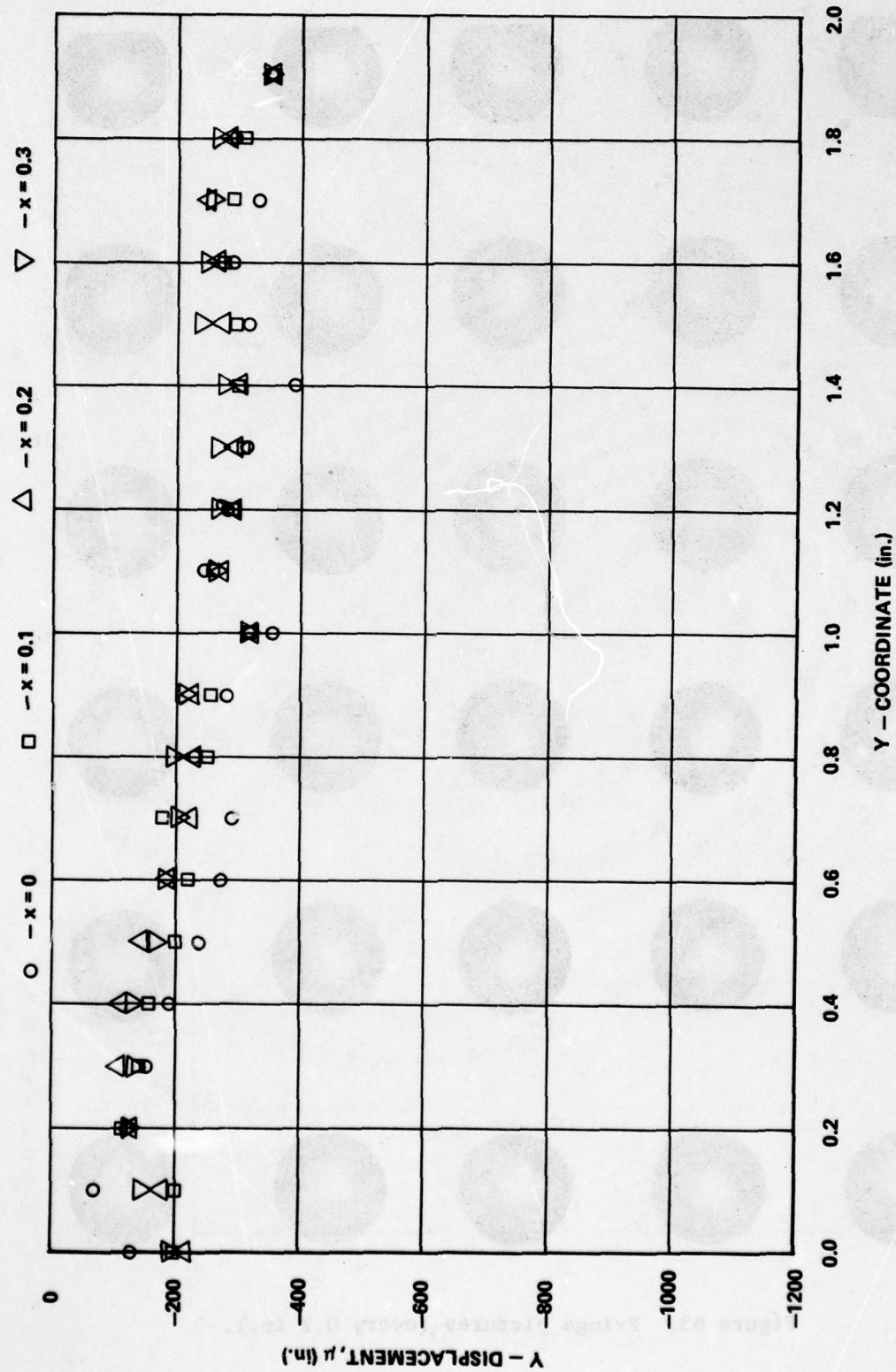


Figure 64. y-displacement as a function of y-coordinate for the spot flaw cylinder
 $(x = 0.0 - x = 0.3)$.

AD-A052 674

AUBURN UNIV ALA
COMPUTER AIDED OPTICAL NONDESTRUCTIVE FLAW DETECTION SYSTEM FOR--ETC(U)
SEP 77 J A SCHAEFFEL, B R MULLINIX

DAAK40-77-C-0028

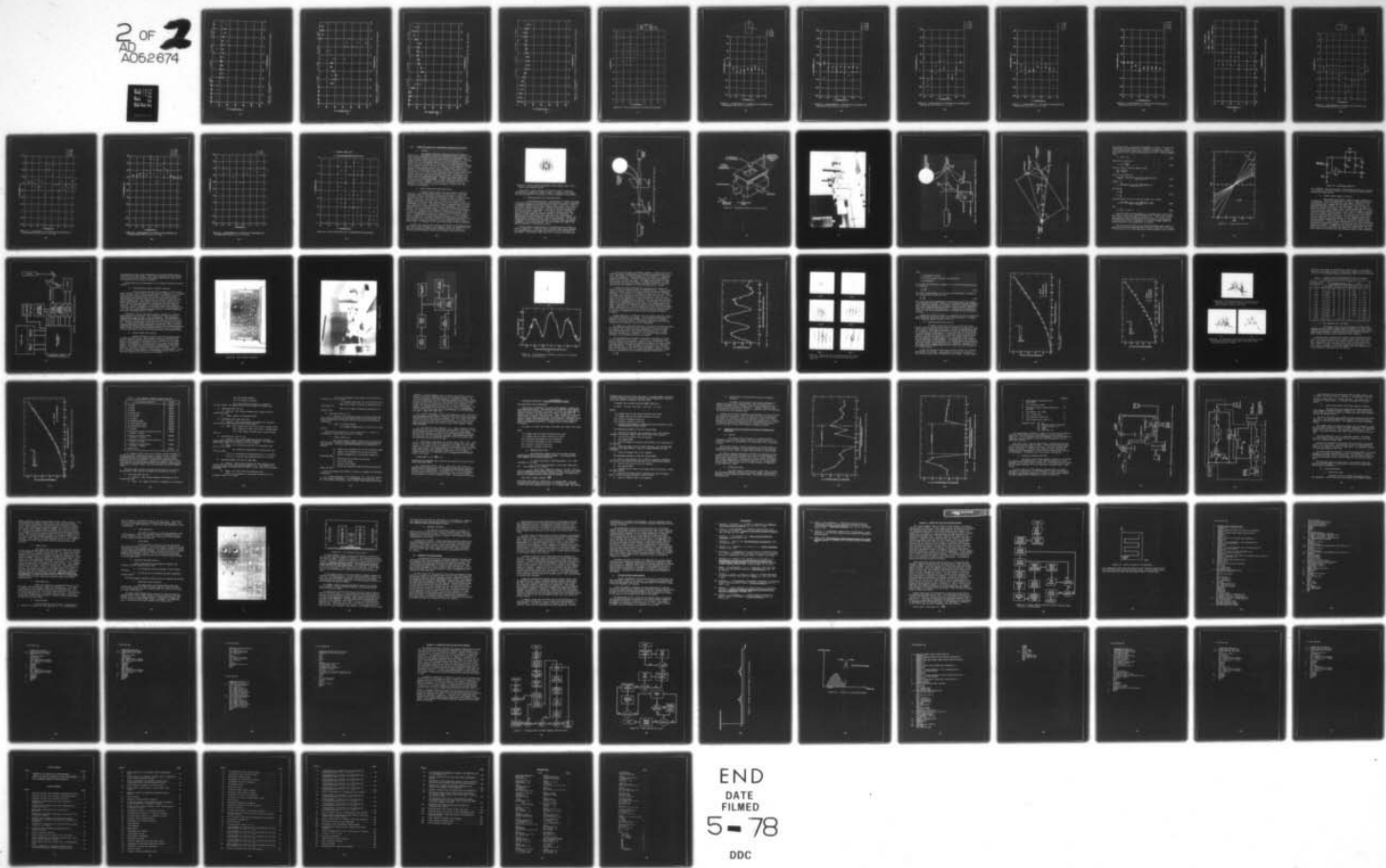
NL

UNCLASSIFIED

DRDMI-T-78-5

F/G 11/5

2 OF 2
AD-A052 674



END
DATE
FILED
5-78
DDC

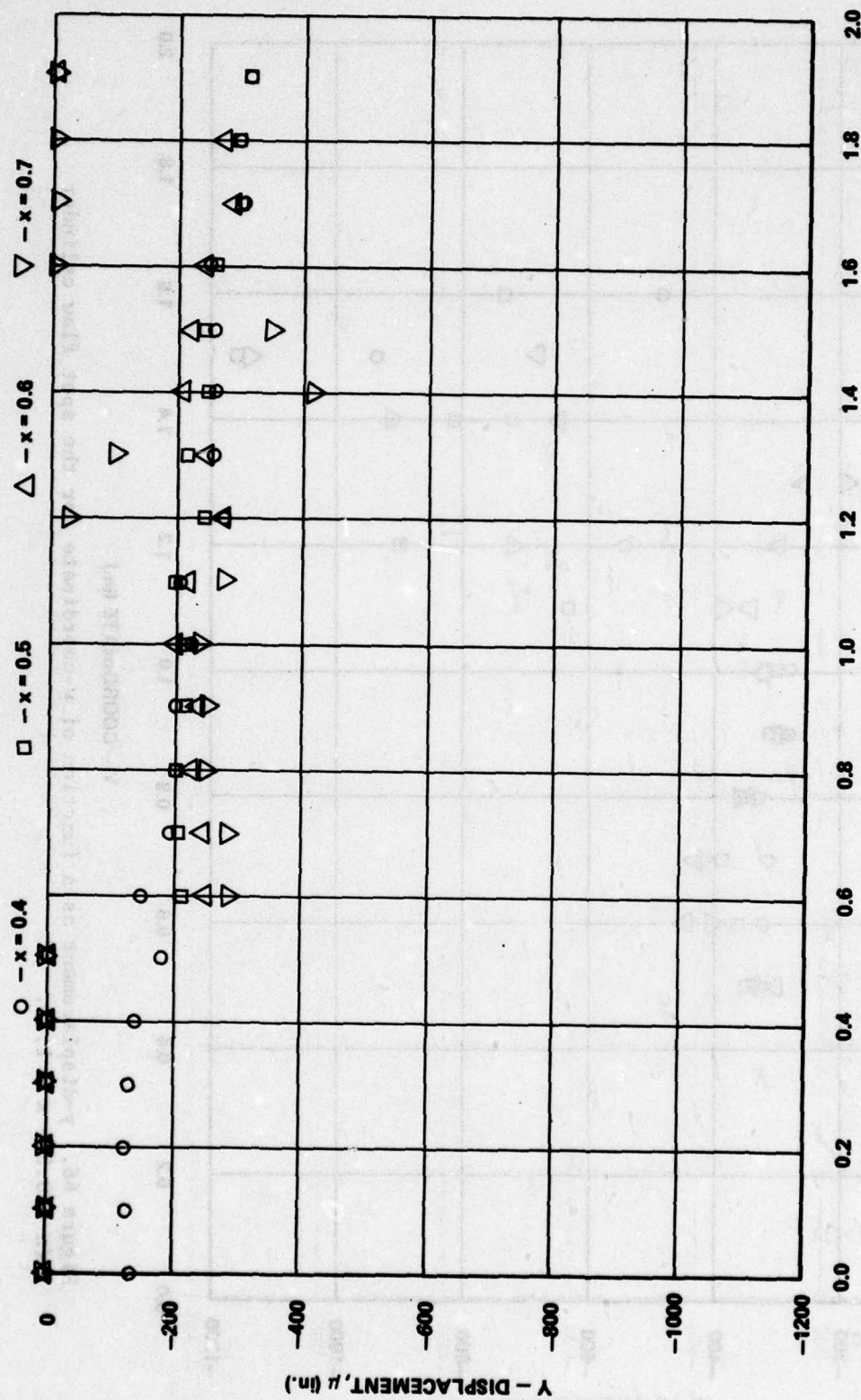


Figure 65. y-displacement as a function of y-coordinate for the spot flaw cylinder
($x = 0.4 - x = 0.7$).

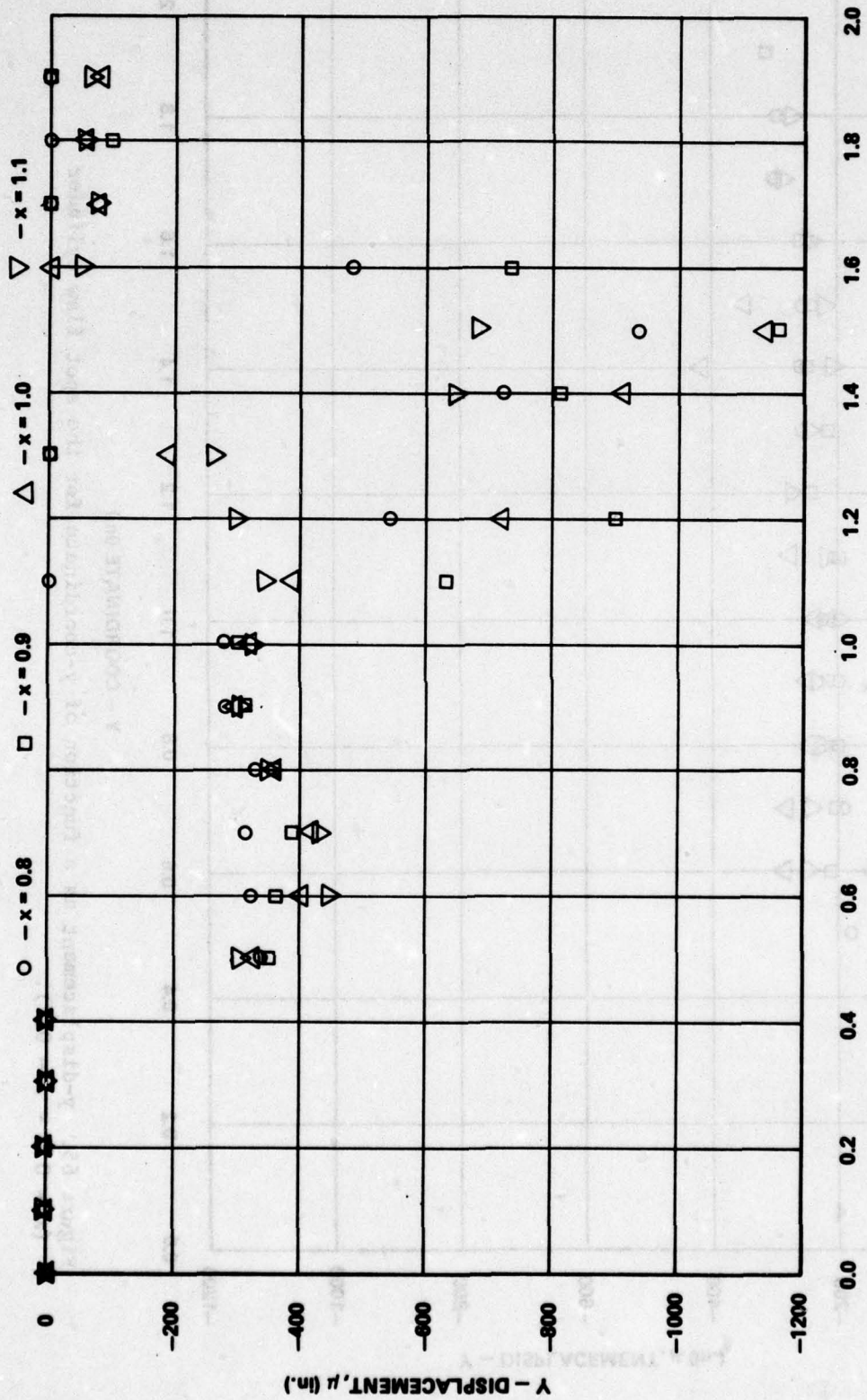


Figure 66. y-displacement as a function of y-coordinate for the spot flaw cylinder
($x = 0.8 - y = 1.1$).

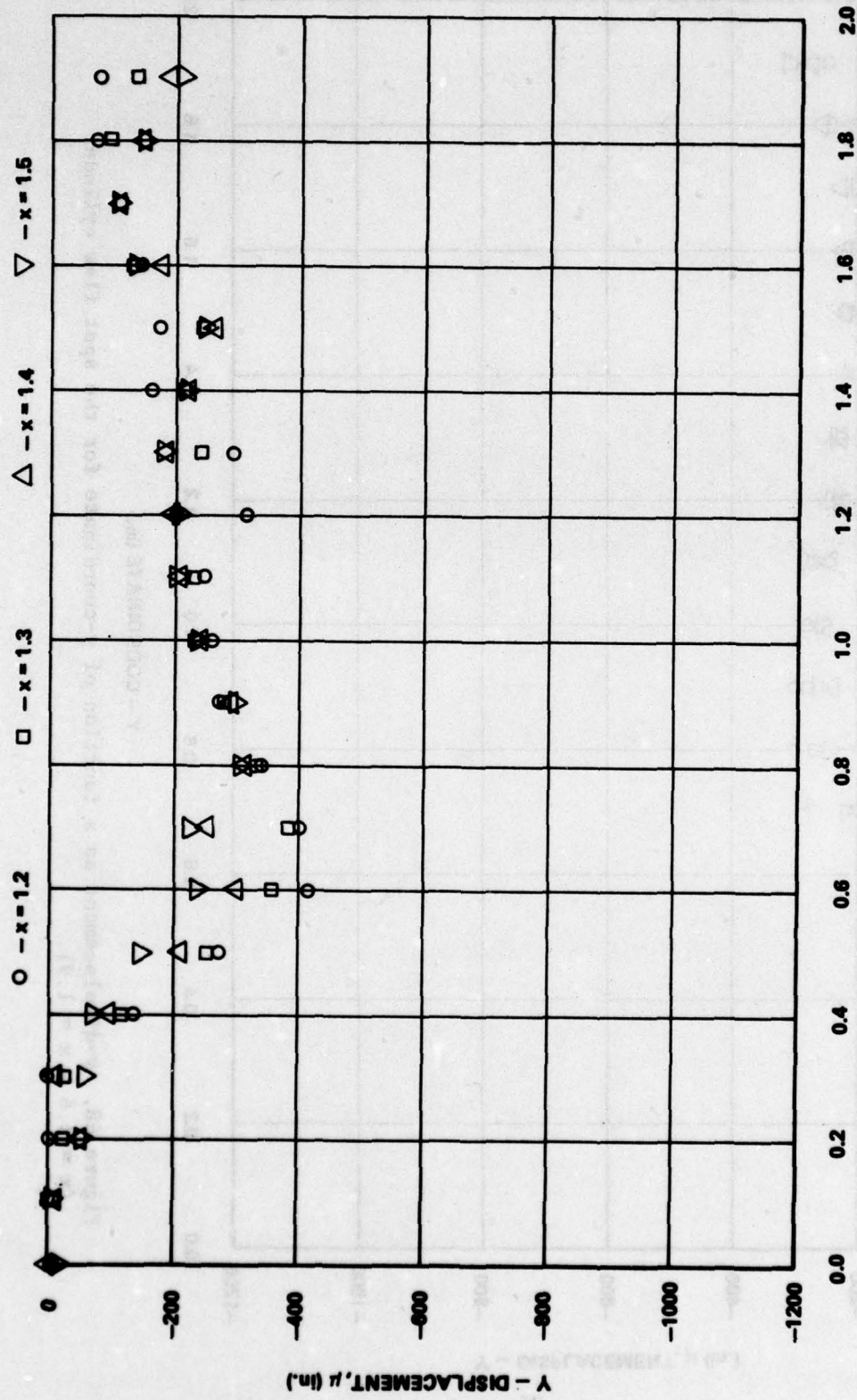


Figure 67: y-displacement as a function of y-coordinate for the spot flaw cylinder
($x = 1.2 - x = 1.5$).

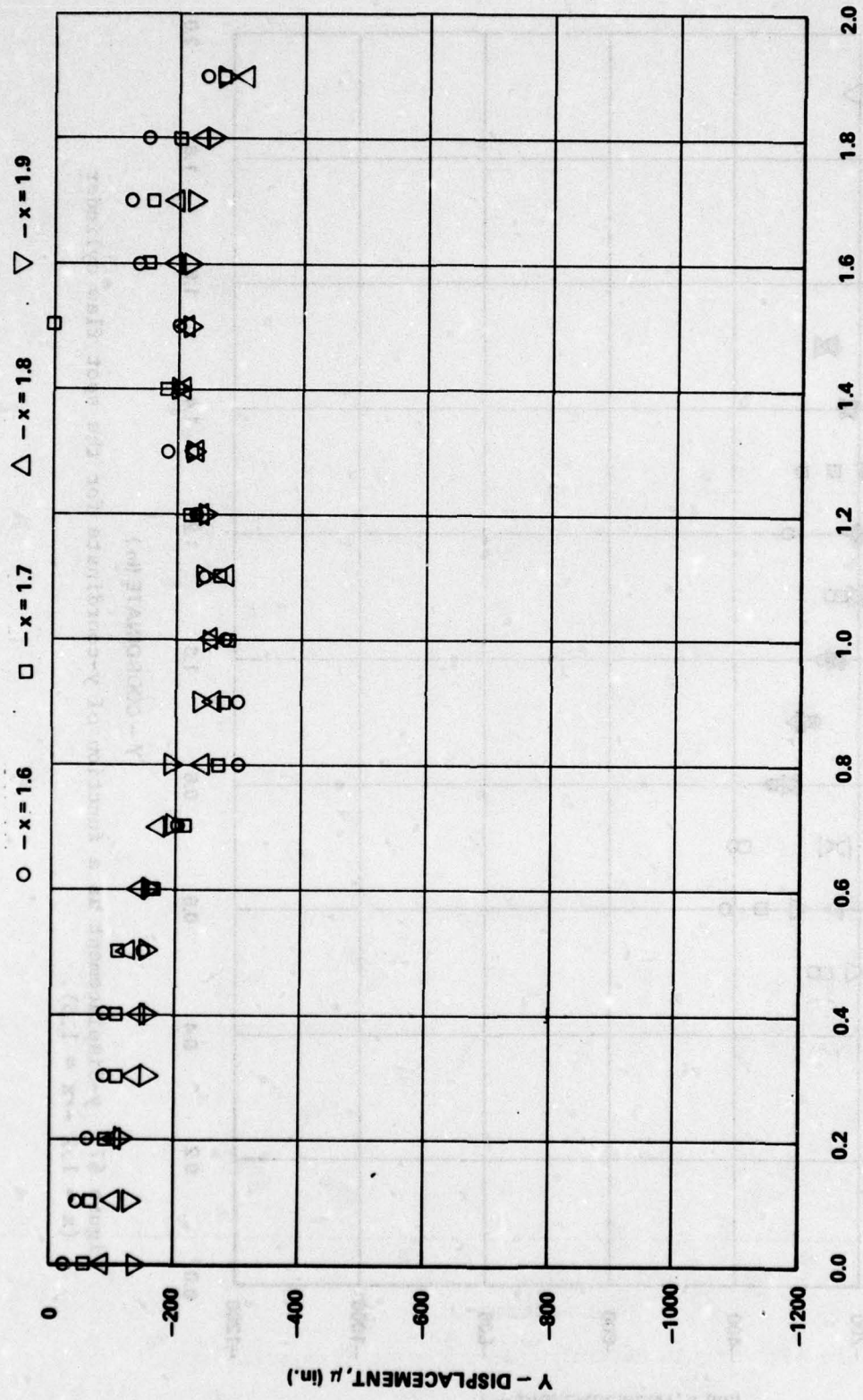


Figure 68. y-displacement as a function of y-coordinate for the spot flaw cylinder ($x = 1.6 - x = 1.9$).

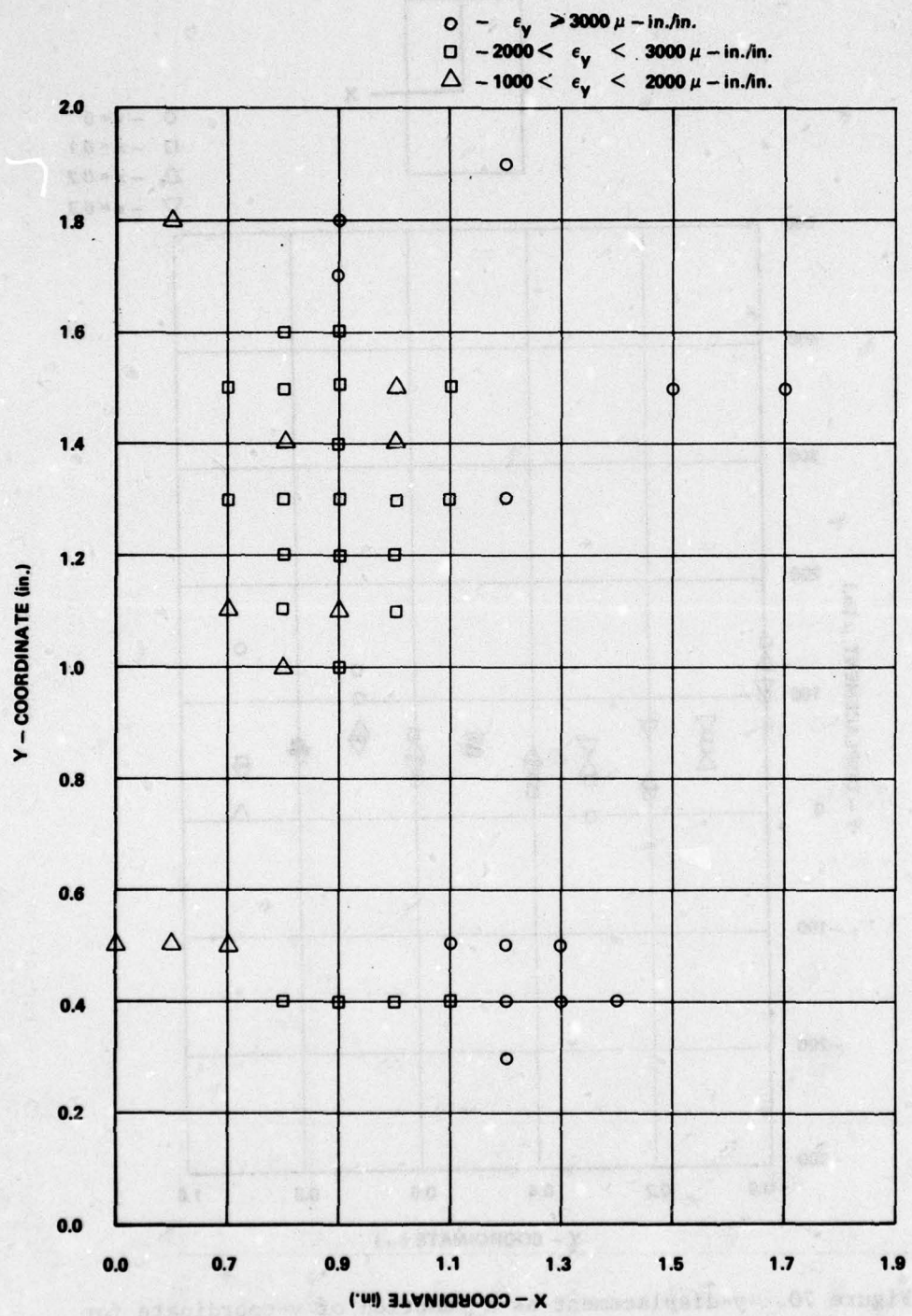


Figure 69. Strain distribution for spot flaw cylinder.

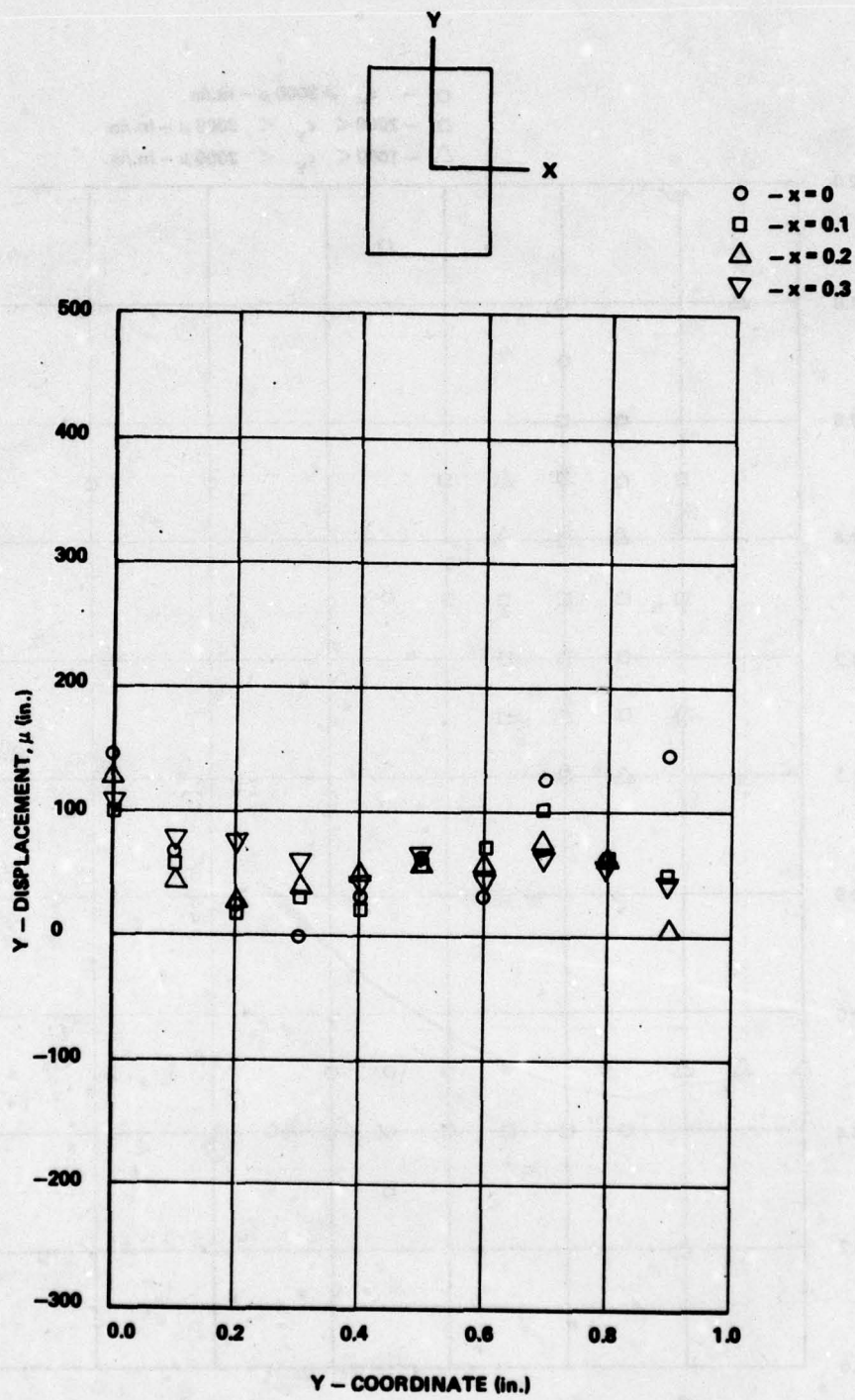


Figure 70. y-displacement as a function of y-coordinate for longitudinal flaw ($x = 0$ - $x = 0.3$).

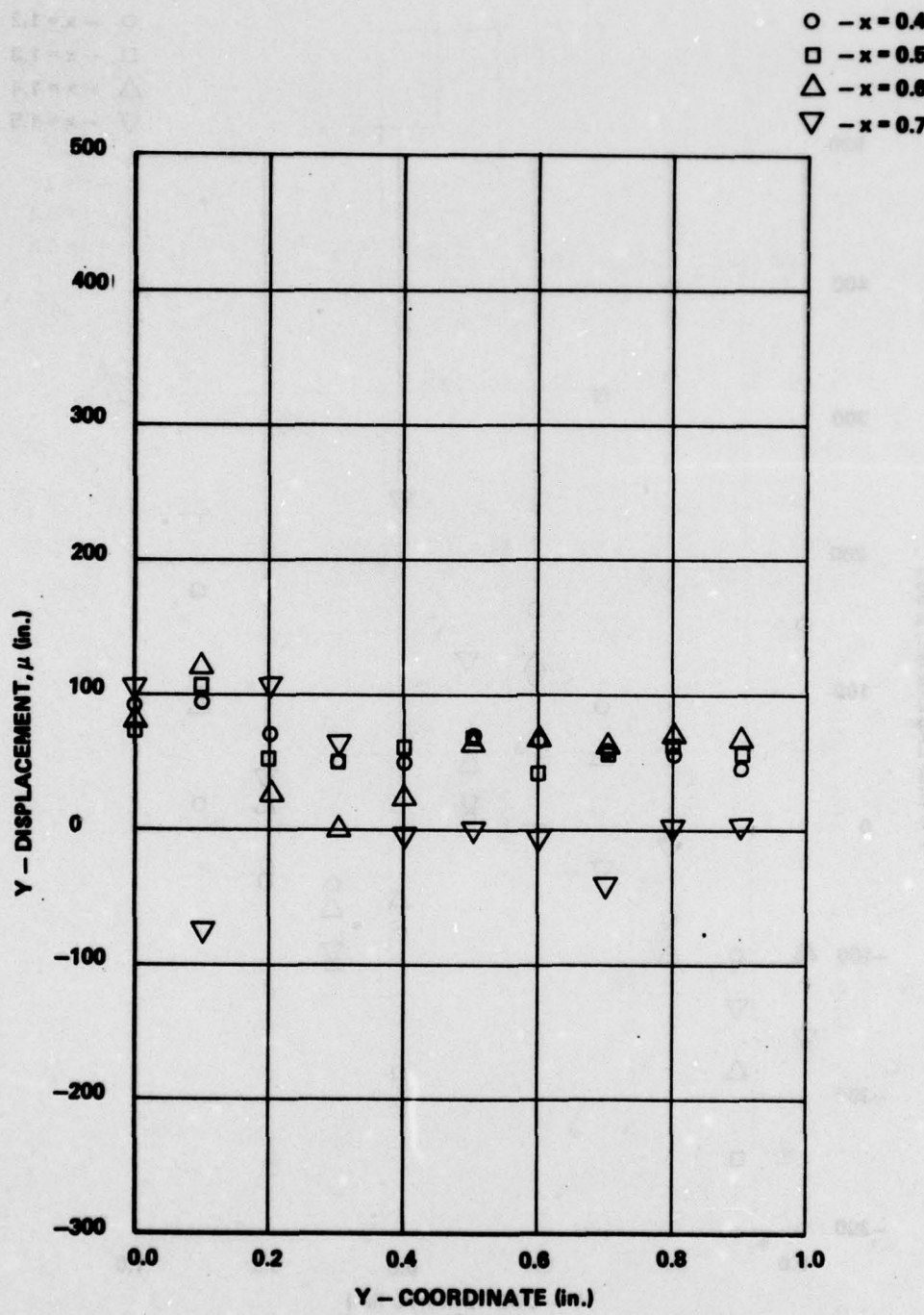


Figure 71. y-displacement as a function of y-coordinate for longitudinal flaw ($x = 0.4$ - $x = 0.7$).

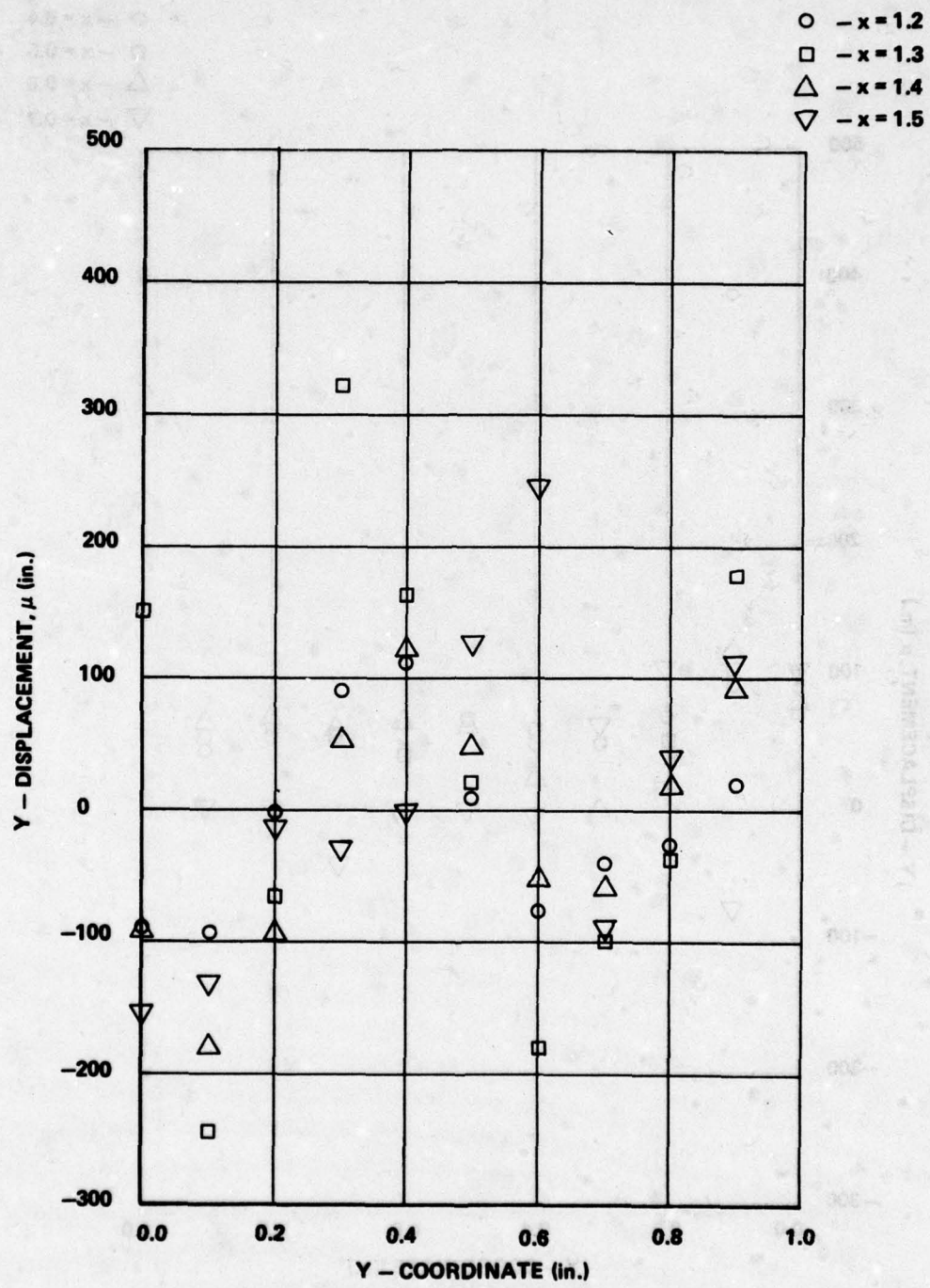


Figure 72. y -displacement as a function of y -coordinate for longitudinal flaw ($x = 0.8 - x = 1.1$).

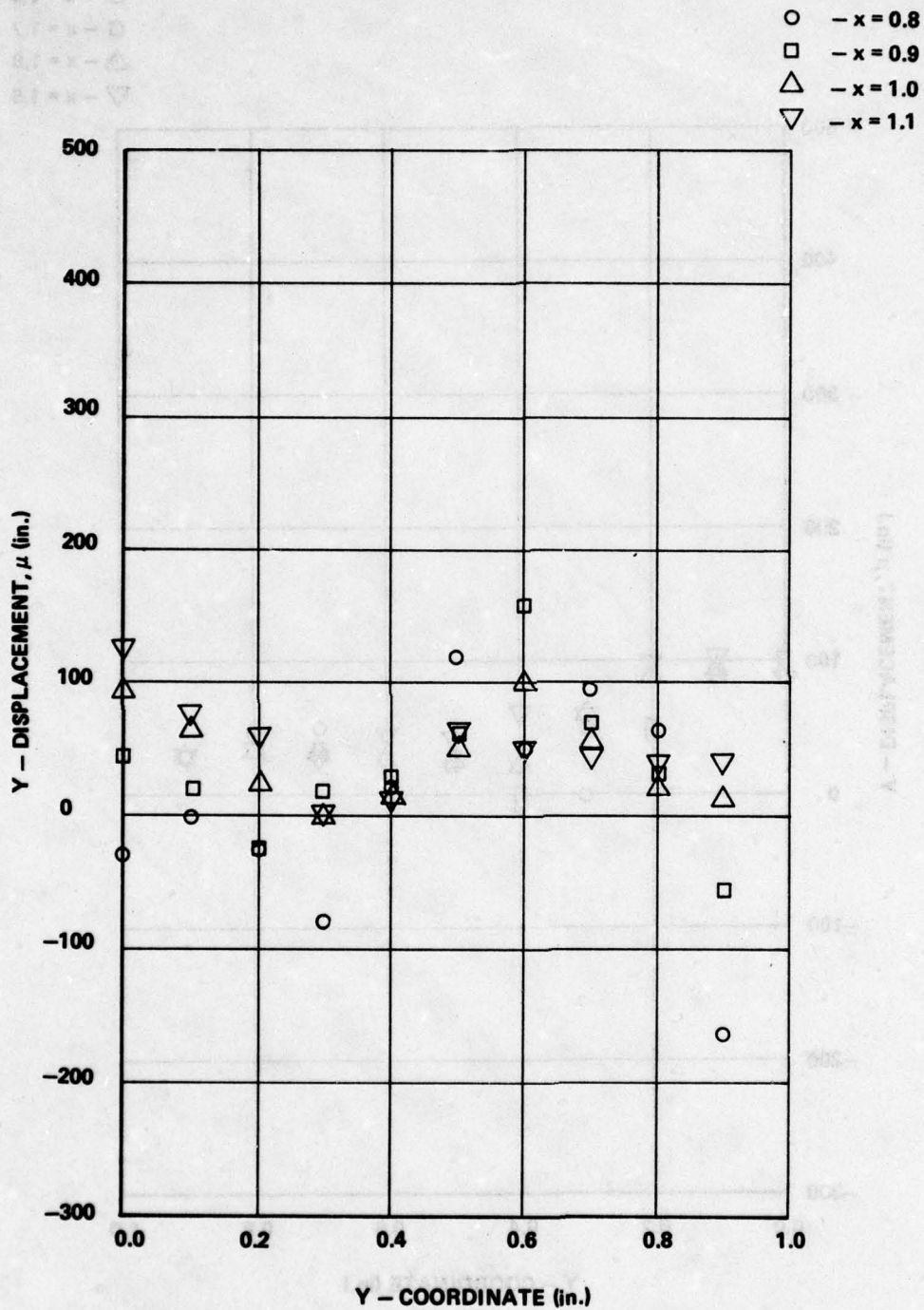


Figure 73. y-displacement as a function of y-coordinate for longitudinal flaw ($x = 1.2 - x = 1.5$).

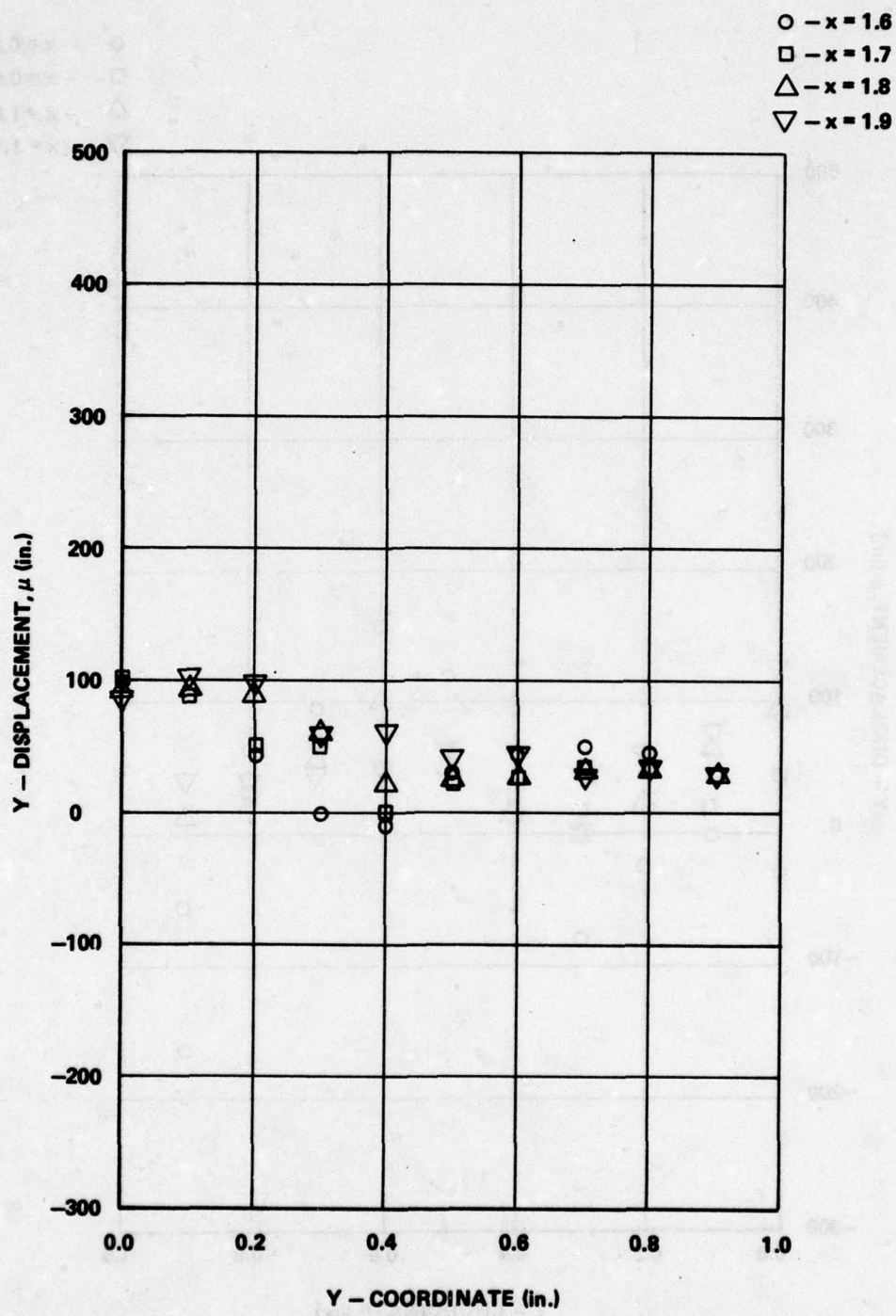


Figure 74. y-displacement as a function of y-coordinate for longitudinal flaw ($x = 1.6$ - $x = 1.9$).

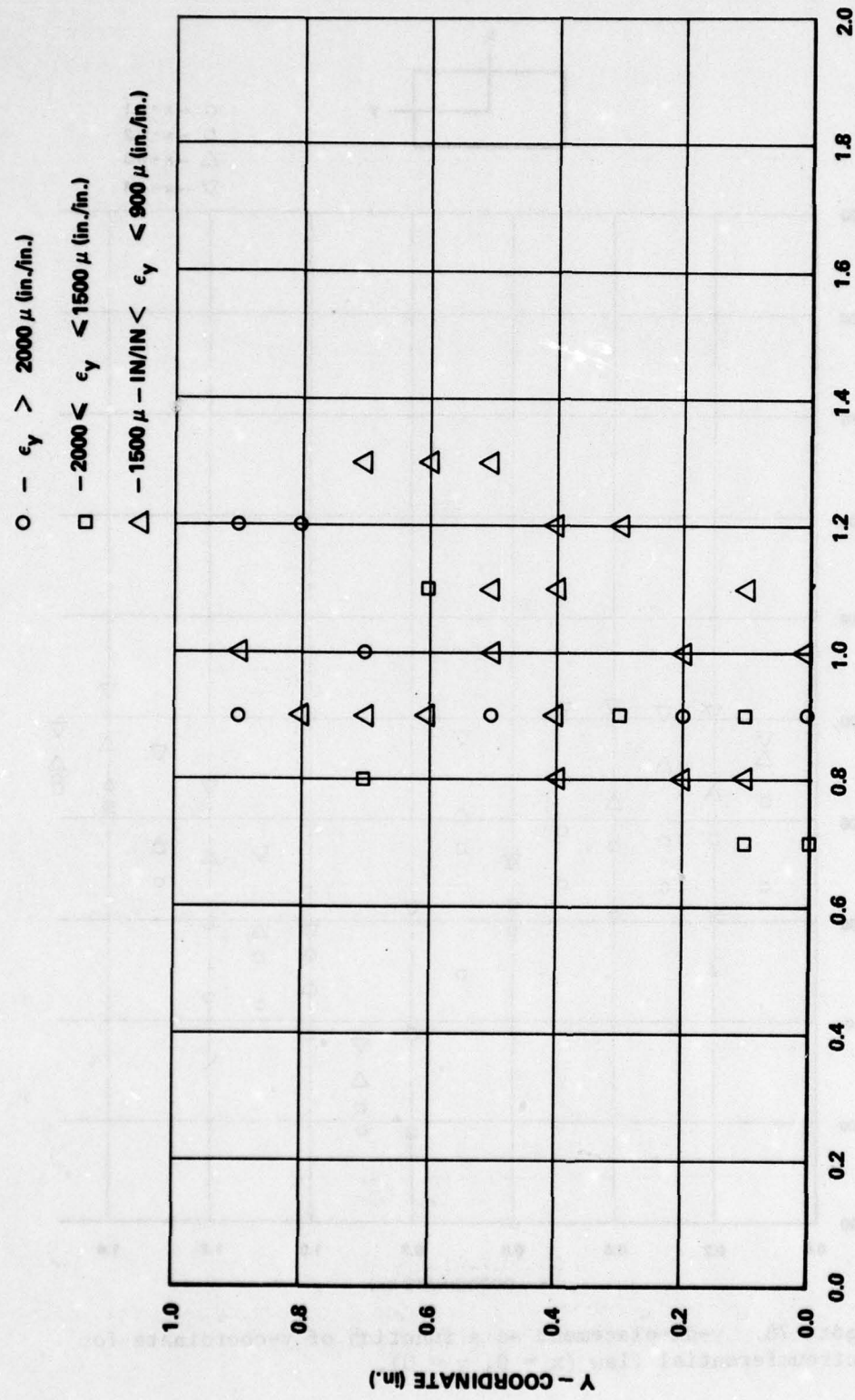


Figure 75. Strain distribution for longitudinal flaw cylinder.

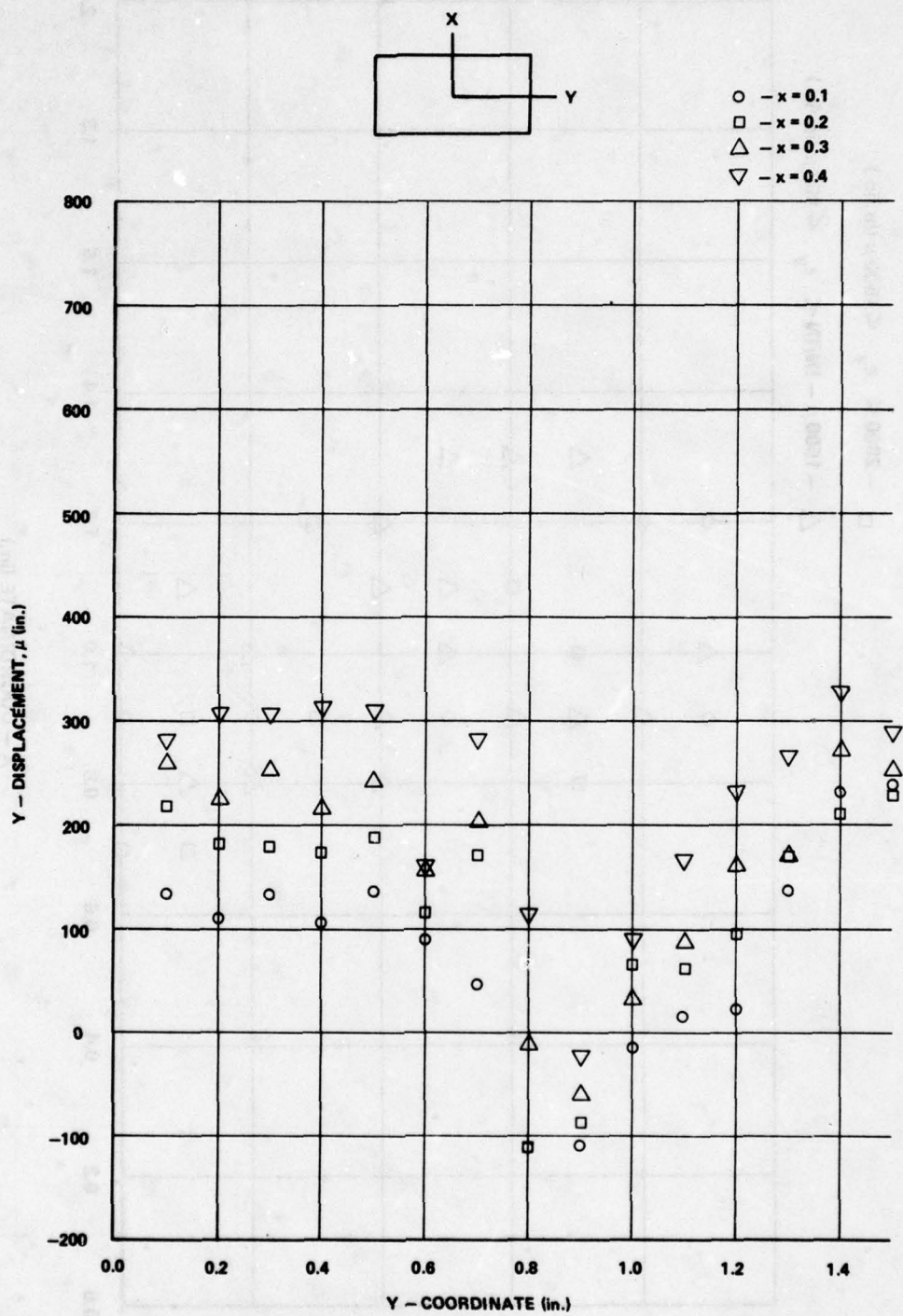


Figure 76. y -displacement as a function of y -coordinate for circumferential flaw ($x = 0$, $y = 0$).

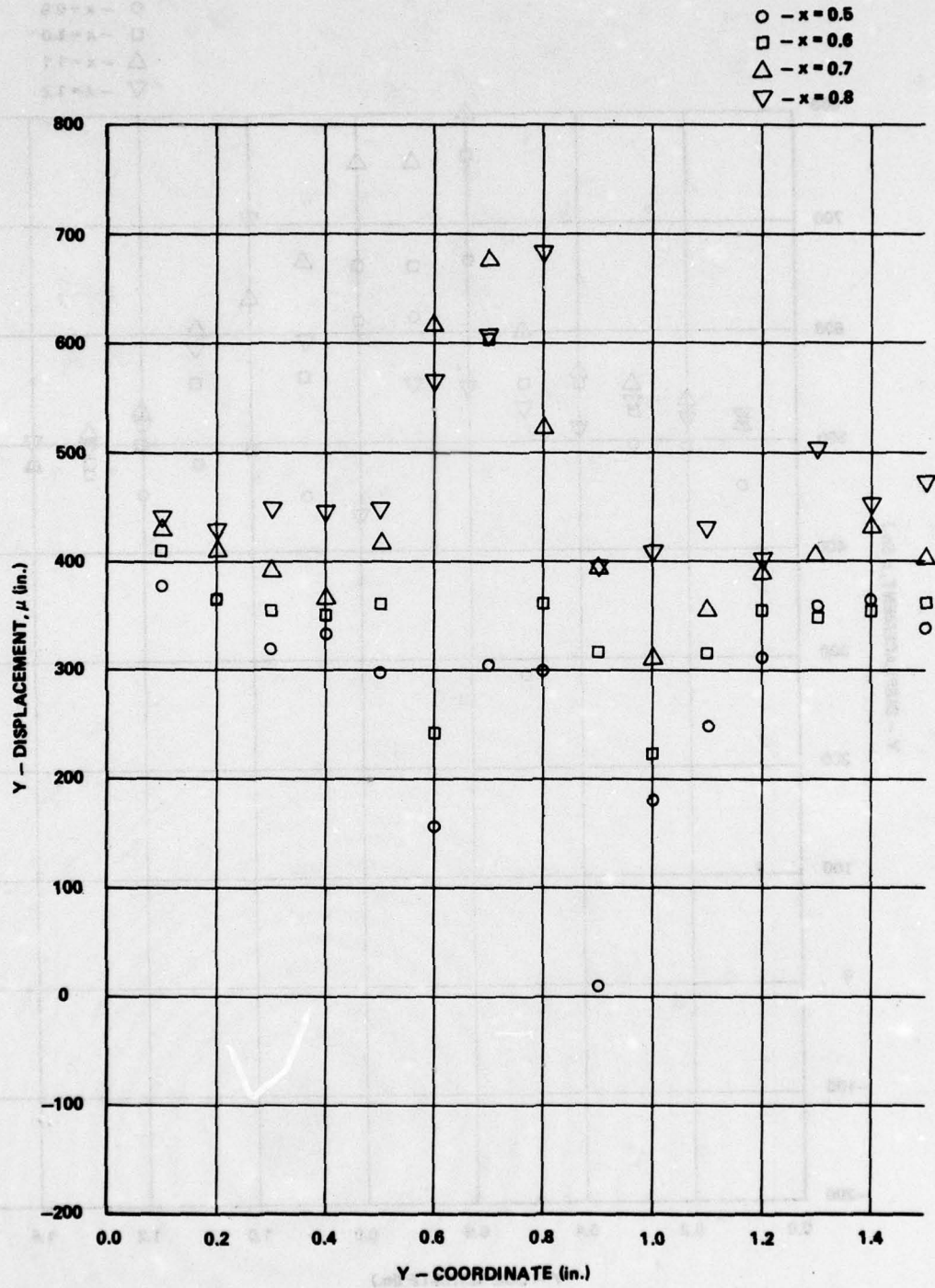


Figure 77. y-displacement as a function of y-coordinate for circumferential flaw ($x = 0.5 - x = 0.8$).

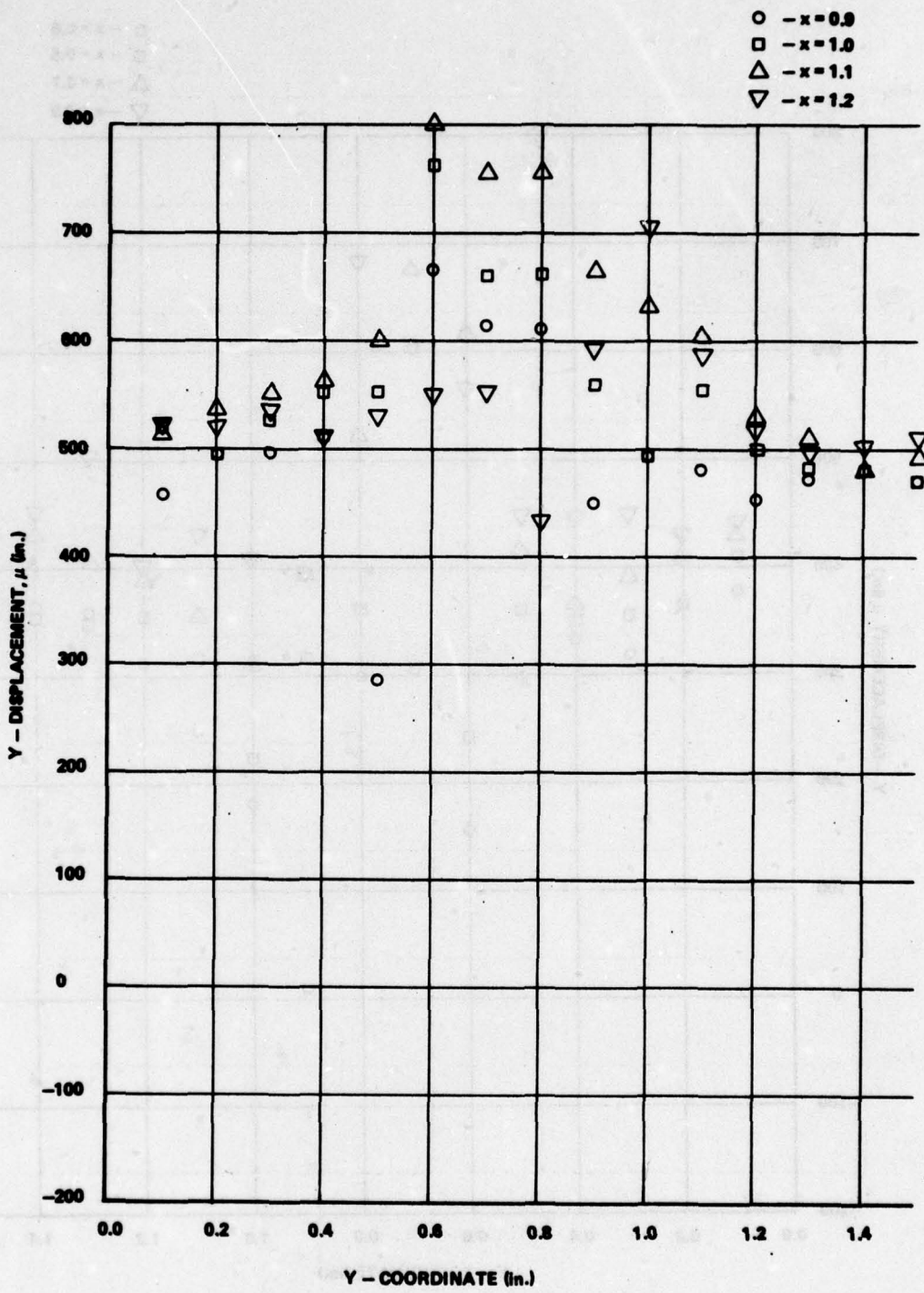


Figure 78. y-displacement as a function of y-coordinate for circumferential flaw ($x = 0.9$ - $x = 1.2$).

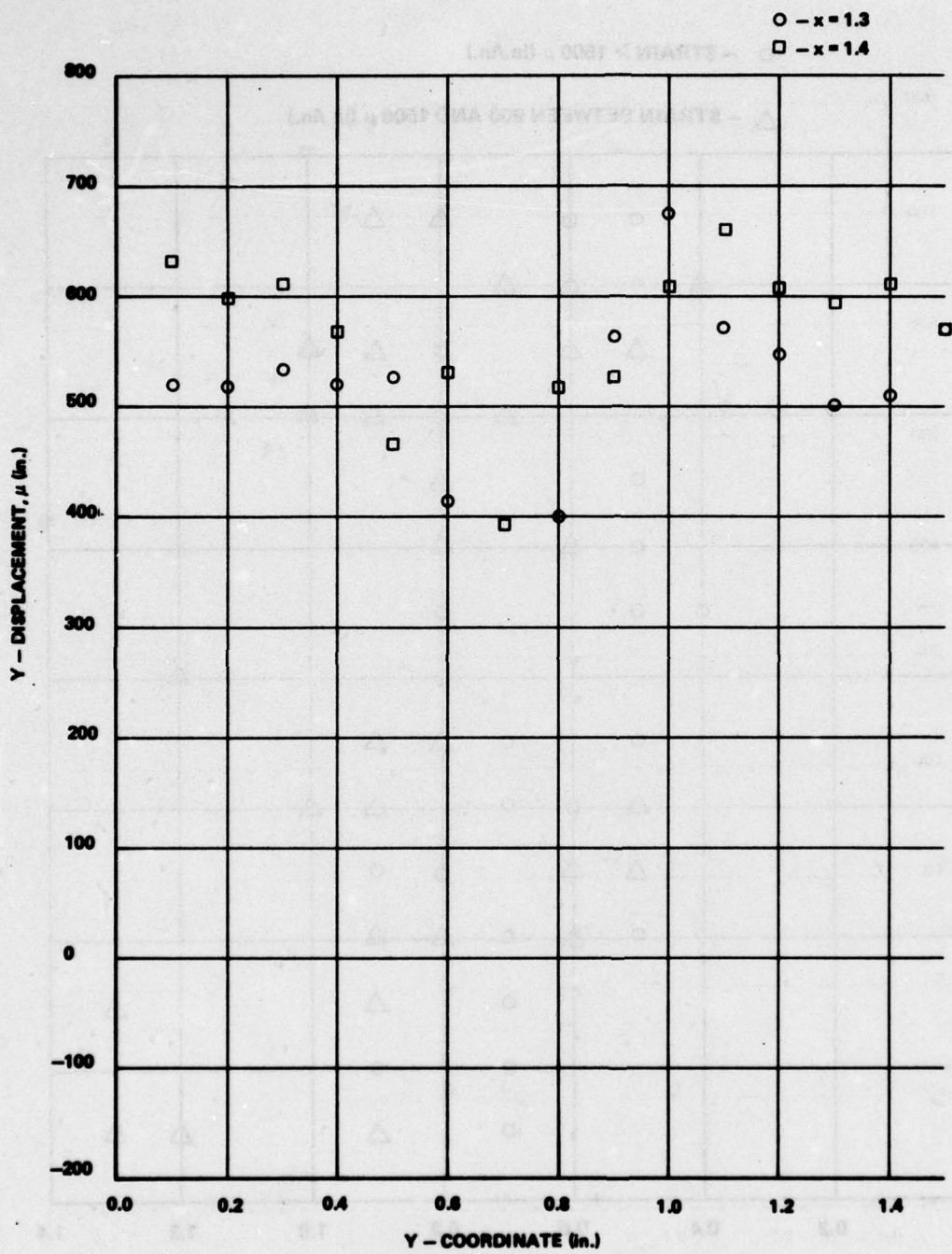


Figure 79. y-displacement as a function of y-coordinate for circumferential flaw ($x = 1.3$ - $x = 1.4$).

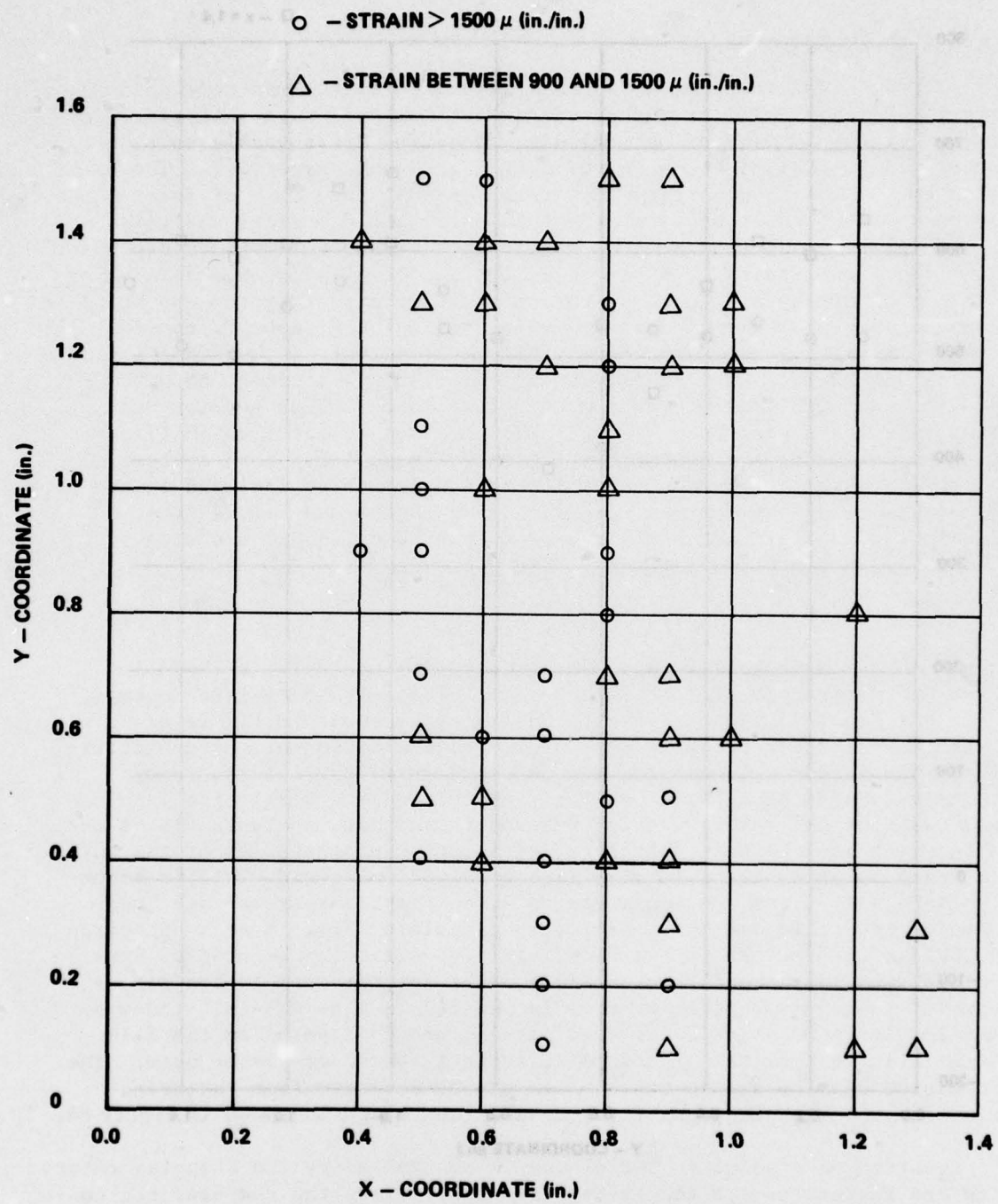


Figure 80. Strain distribution for circumferential flaw cylinder.

VII. COMPUTER AIDED DATA REDUCTION SYSTEMS AND SOFTWARE

A. General

The computer aided data reduction system was developed primarily for applications in speckle interferometric data analysis. However, other applications of optical data reduction are amenable to this type of fringe analysis such as reflecting grid and Moire'[14]. The basic system consists of two parts which are an optical recording of interference data and the computer hardware used in the numerical analysis. Optical recording of the data can be obtained by several methods depending on the required results. If only one-dimensional displacement data using speckle photography are desired, then a rotating mirror system can be employed. Two-dimensional data analysis utilizes a vidicon TV camera system which is also used in whole field data analysis such as the reflecting grid and Moire'. An x-y film translation stage is common to both systems along with some of the computer interfaces. This section will discuss each data recording system. Examples are selected which illustrate the data analysis procedures. A user's manual for both systems is also discussed. Computer codes for both systems are included in the appendices for easy reference. Applications of computer aided data reduction to nondestructive testing of composite cylinders are also included in this section.

B. Vidicon Camera Data Recording System

A typical fringe pattern used for analysis is shown in Figure 81. This type of fringe pattern is produced when a laser beam is passed through a photographic transparency as shown in Figure 82. Interference fringes are a measure of the object motion or surface deformation of the body. Theory for the description of the interference effects is presented in Section VIII. Because only a small area is illuminated by the laser, the information in the data analysis yields the displacement at a point. Therefore, to obtain a complete map of the surface, each point on the film will have to be illuminated. This is accomplished by an x-y translation stage in which the transparency has been mounted. The stage has the capacity to translate 6 in. in each direction in 0.001-in. increments with a 0.0001-in. repositioning accuracy. Synchronous stepping motors provide the control for the translation directions. A photographic transparency is mounted in a 4- × 5-in. window as shown in Figure 83. The laser beam passes through a point on the film and the film is then translated relative to a stationary laser beam. The beam direction mirrors are attached to a post separate from the translation stage. A photograph of the translation stage is shown in Figure 84.

Location of a point in the window is controlled by the stepping motors which are in turn controlled by the computer. Thus, the computer can control the translation distance with a minimum interval of 0.001 in. A discussion of the computer interface will follow in the next section.

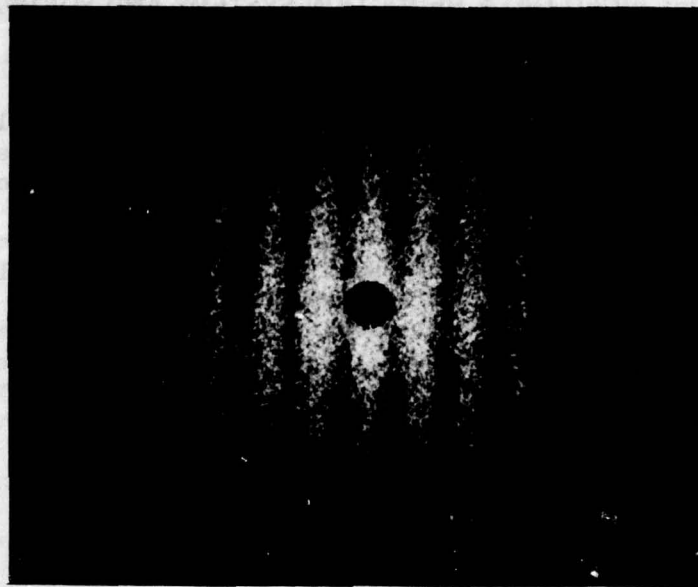


Figure 81. Typical speckle photography fringe pattern used in the optical data analysis system.

Light that is passed through the film then forms a diffraction pattern which is imaged by a vidicon camera. The image on the camera can then be viewed on a TV monitor or stored in memory in the computer.

C. Rotating Mirror Data Recording System

To increase the speed, a rotating mirror system is utilized in the data analysis of interference fringe patterns as shown in Figure 81. A schematic diagram of the basic system is shown in Figure 85. This system differs from the vidicon camera system in that only a single direction can be scanned by the mirror. However, the diffraction halo projected on the screen (Figure 82) is the same as the halo projected on the rotating mirror (Figure 85). As the mirror rotates, the fringe pattern is swept across the aperture opening in the photodiode. The aperture size is sufficiently small such that only a small beam of light passes through the opening. Therefore as the mirror rotates, the fringe pattern is swept across the face of the photodiode. The optical performance of the system was evaluated to determine some experimental parameters of the rotating mirror. The film translation stage is the same as discussed in the previous section.

The basic optical configuration of the rotating mirror analyzer is shown in Figure 86. A light ray from a divergent light source impinges on a rotating mirror at an angle of incidence ψ and is reflected to a photodiode. The divergent light source is in practice the diffraction

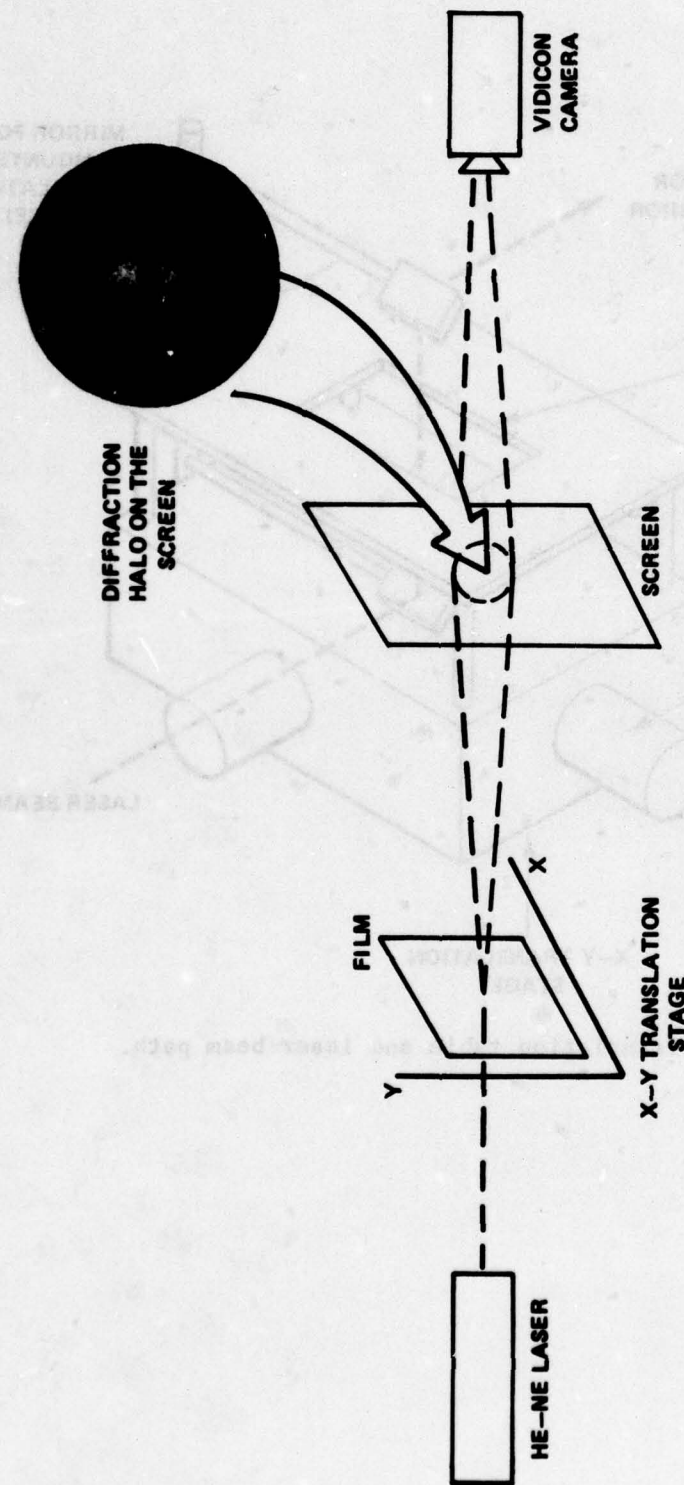


Figure 82. Optical system used for computer aided data reduction.

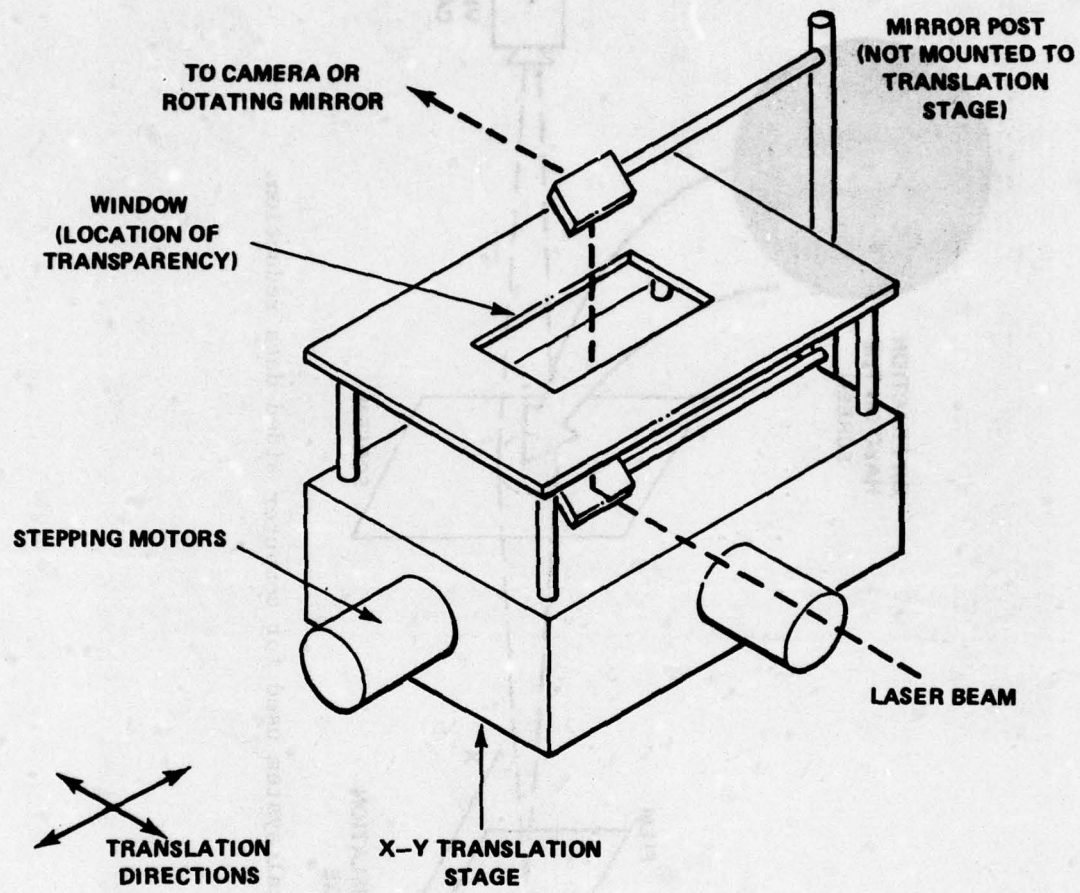


Figure 83. Translation table and laser beam path.

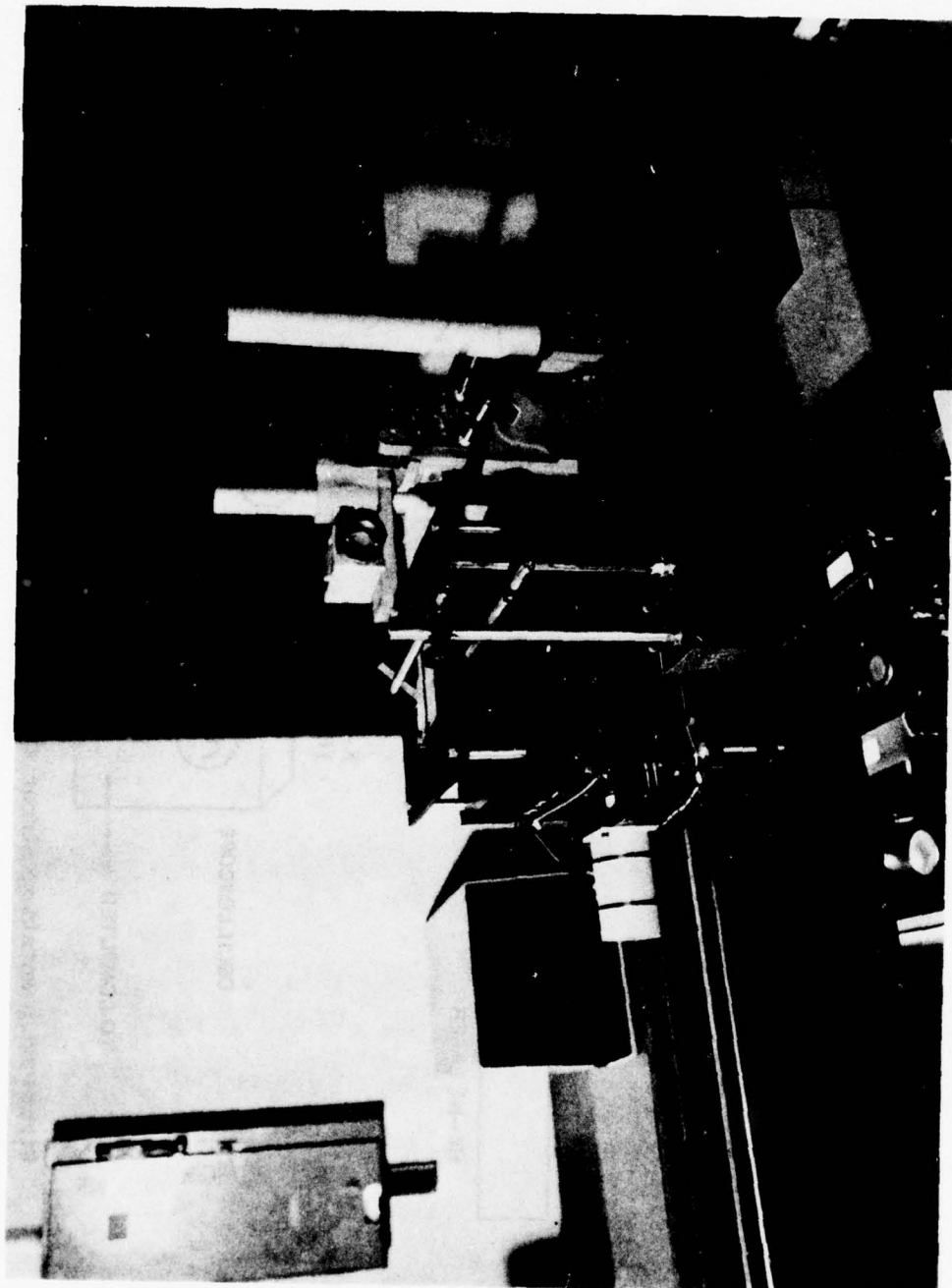


Figure 84. Photograph of the translation stage assembly.

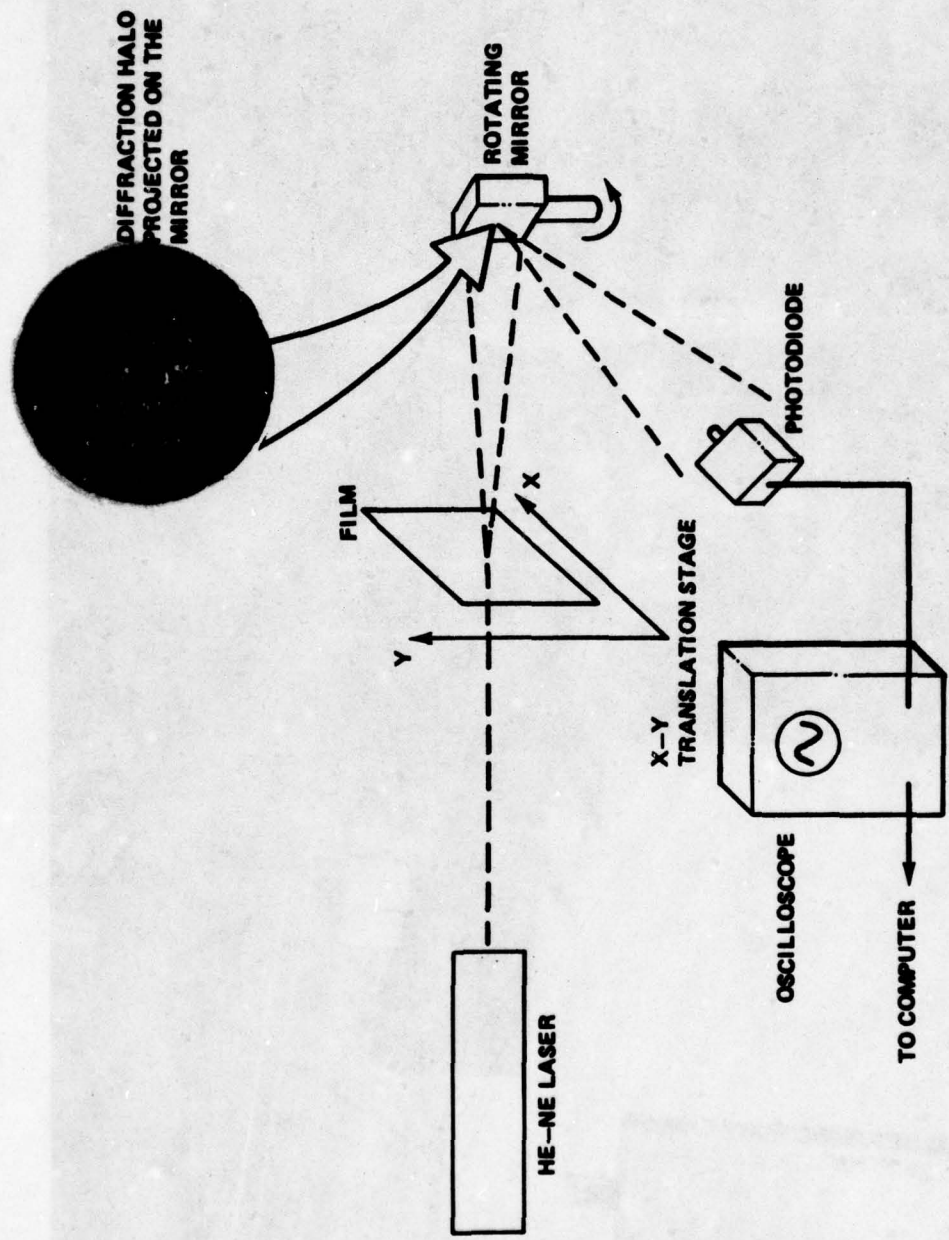


Figure 85. Rotating mirror system used for computer aided data reduction.

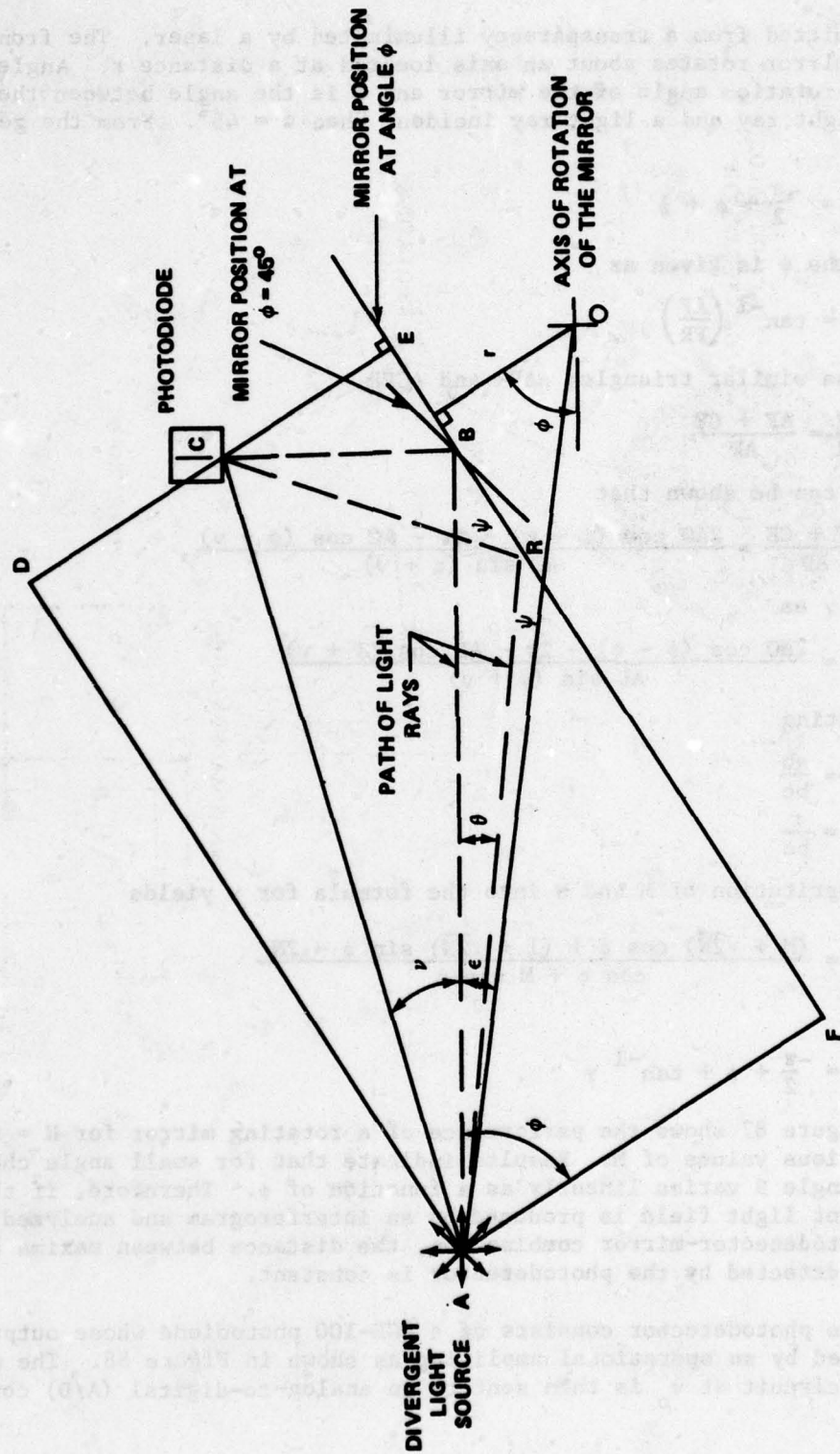


Figure 86. Optical configuration for the rotating mirror analyzer.

halo emitted from a transparency illuminated by a laser. The front surfaced mirror rotates about an axis located at a distance r . Angle ϕ is the rotation angle of the mirror and θ is the angle between the incident light ray and a light ray incident when $\phi = 45^\circ$. From the geometry shown,

$$\theta = -\frac{\pi}{2} + \phi + \psi \quad (103)$$

where the ψ is given as

$$\psi = \tan^{-1} \left(\frac{AF}{FR} \right) \quad . \quad (104)$$

From the similar triangles ΔAFR and ΔCER ,

$$\frac{AF}{FR} = \frac{AF + CE}{AD}$$

and it can be shown that

$$\frac{AF + CE}{AD} = \frac{2AO \cos(\phi - \varepsilon) - 2r - AC \cos(\phi + \nu)}{AC \sin(\phi + \nu)} \quad (105)$$

Define γ as

$$\gamma = \frac{2AO \cos(\phi - \varepsilon) - 2r - AD \cos(\phi + \nu)}{AC \sin(\phi + \nu)} \quad (106)$$

and letting

$$\begin{aligned} M &= \frac{ab}{bc} \\ N &= \frac{r}{bc} \end{aligned} \quad (107)$$

and substitution of M and N into the formula for γ yields

$$\gamma = \frac{(M + \sqrt{2N}) \cos \phi + (1 + \sqrt{2N}) \sin \phi - 2N}{\cos \phi + M \sin \phi} \quad (108)$$

and

$$\theta = -\frac{\pi}{2} + \phi + \tan^{-1} \gamma \quad . \quad (109)$$

Figure 87 shows the performance of a rotating mirror for $N = 0.25$ and various values of M . Results indicate that for small angle changes of ϕ , angle θ varies linearly as a function of ϕ . Therefore, if the divergent light field is produced by an interferogram and analyzed by the photodetector-mirror combination, the distance between maxima and minima detected by the photodetector is constant.

The photodetector consists of a SGD-100 photodiode whose output is amplified by an operational amplifier as shown in Figure 88. The output of the circuit at v_o is then sent to an analog-to-digital (A/D) converter

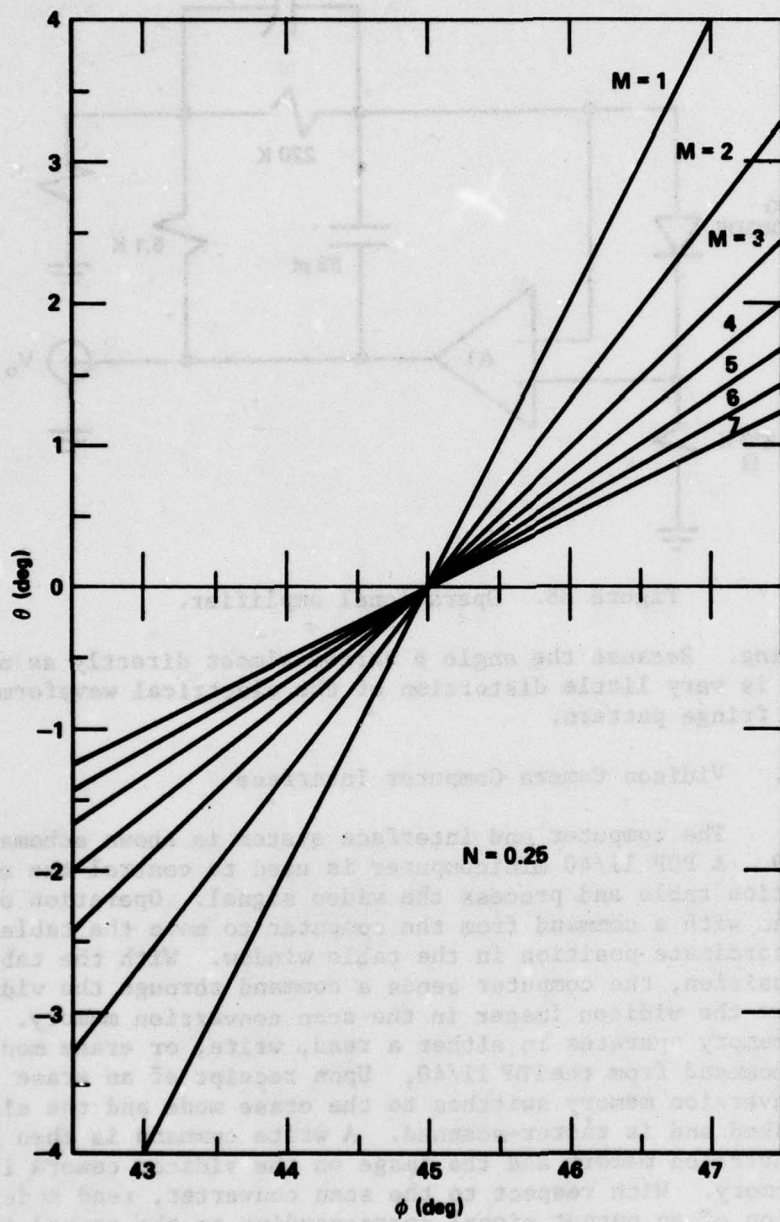


Figure 87. θ versus ϕ for $N = 0.25$.

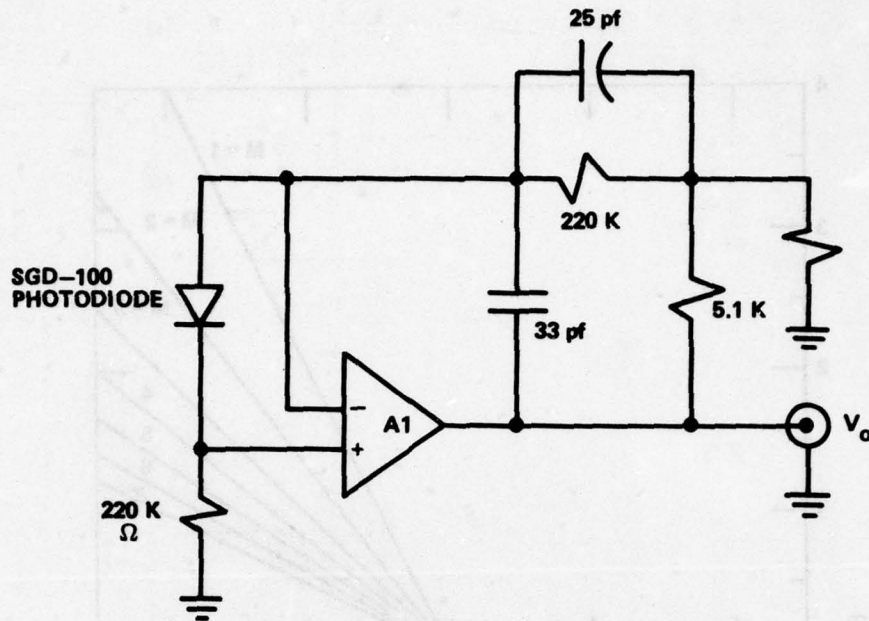


Figure 88. Operational amplifier.

for processing. Because the angle θ varies almost directly as a function of ϕ , there is very little distortion of the electrical waveform representing the fringe pattern.

D. Vidicon Camera Computer Interface

The computer and interface system is shown schematically in Figure 89. A PDP 11/40 minicomputer is used to control the motion of the translation table and process the video signal. Operation of the system begins with a command from the computer to move the table to a specified coordinate position in the table window. With the table in a specified position, the computer sends a command through the video interface to store the vidicon imager in the scan conversion memory. The scan conversion memory operates in either a read, write, or erase mode depending on the command from the PDP 11/40. Upon receipt of an erase command, the scan conversion memory switches to the erase mode and the electron beam is blanked and is raster-scanned. A write command is then given to the scan conversion memory and the image on the vidicon camera is then stored in memory. With respect to the scan converter, read mode means the generation of an output signal corresponding to the stored information. The process automatically begins at the end of the write mode and no read command is required. A command from the computer then converts the information stored in the scan conversion memory into digital form. The complete image is not processed but only selected lines of video information

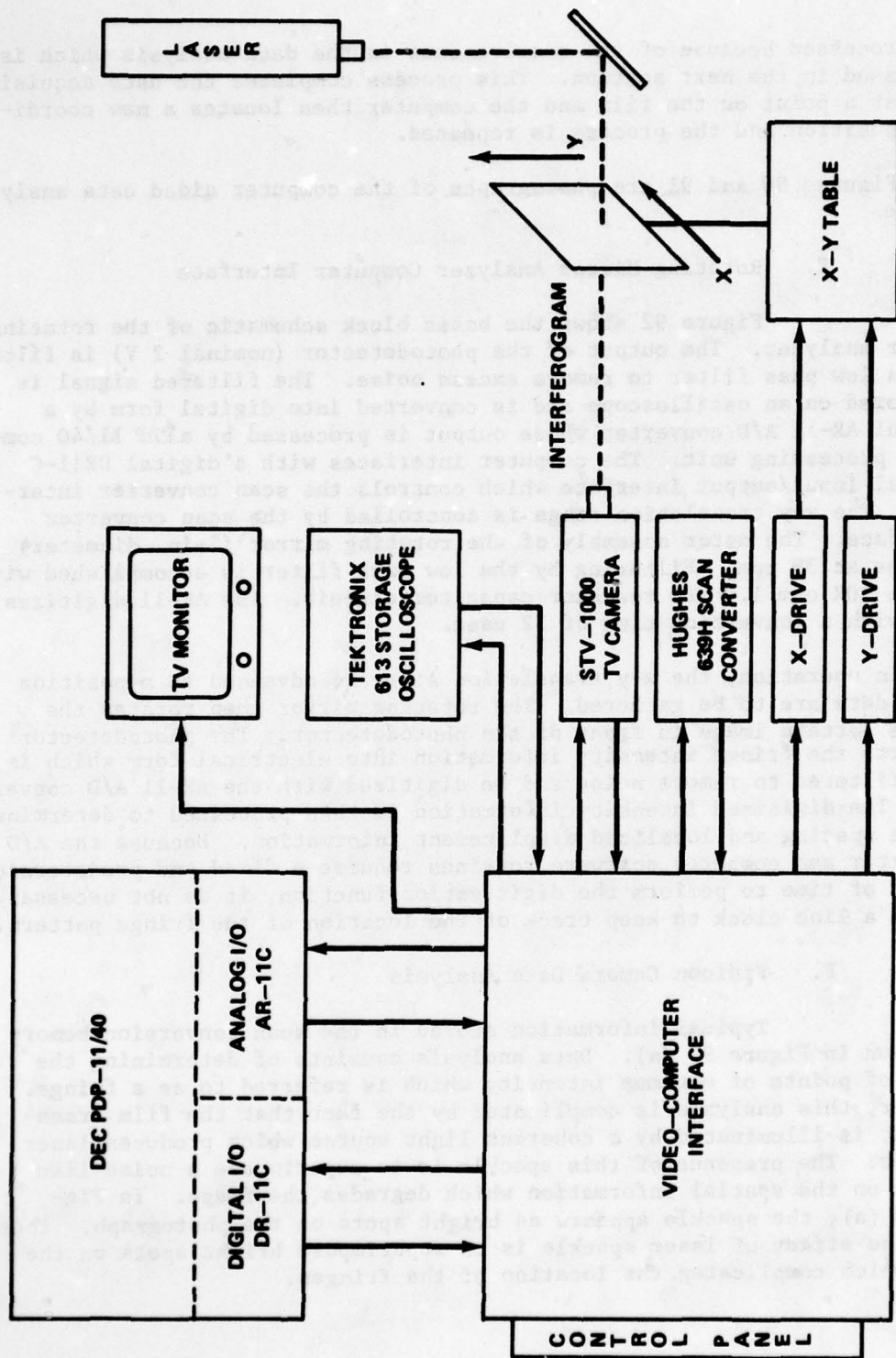


Figure 89. Computer-aided speckle analyzer.

are processed because of the requirements in the data analysis which is discussed in the next section. This process completes the data acquisition at a point on the film and the computer then locates a new coordinate position and the process is repeated.

Figures 90 and 91 are photographs of the computer aided data analysis system.

E. Rotating Mirror Analyzer Computer Interface

Figure 92 shows the basic block schematic of the rotating mirror analyzer. The output of the photodetector (nominal 2 V) is filtered with a low pass filter to remove excess noise. The filtered signal is monitored on an oscilloscope and is converted into digital form by a Digital AR-11 A/D converter whose output is processed by a PDP 11/40 computer processing unit. The computer interfaces with a digital DR11-C digital input/output interface which controls the scan converter interface. The x-y translation stage is controlled by the scan converter interface. The motor assembly of the rotating mirror (2-in. diameter) rotates at 39 rpm. Filtering by the low pass filter is accomplished with a 0 to 10K ohm 1.0 MFD resistor-capacitor circuit. The AR-11 digitizes data with a conversion time of 32 μ sec.

In operation, the x-y translation stage is advanced to a position where data are to be gathered. The rotating mirror then rotates the fringe pattern image in front of the photodetector. The photodetector converts the fringe intensity information into electrical form which is then filtered to remove noise and be digitized with the AR-11 A/D converter. The digitized intensity information is then processed to determine fringe spacing and localized displacement information. Because the A/D converter and computer software routines require a fixed and predetermined amount of time to perform the digitization function, it is not necessary to use a line clock to keep track of the location of the fringe pattern.

F. Vidicon Camera Data Analysis

Typical information stored in the scan conversion memory is shown in Figure 93 (a). Data analysis consists of determining the locus of points of minimum intensity which is referred to as a fringe. However, this analysis is complicated by the fact that the film transparency is illuminated by a coherent light source which produces laser speckle. The presence of this speckle is to superimpose a noise-like signal on the spatial information which degrades the image. In Figure 93 (a), the speckle appears as bright spots on the photograph. Therefore the effect of laser speckle is to superimpose bright spots on the film which complicates the location of the fringes.

Moire' Fringe Analyzer

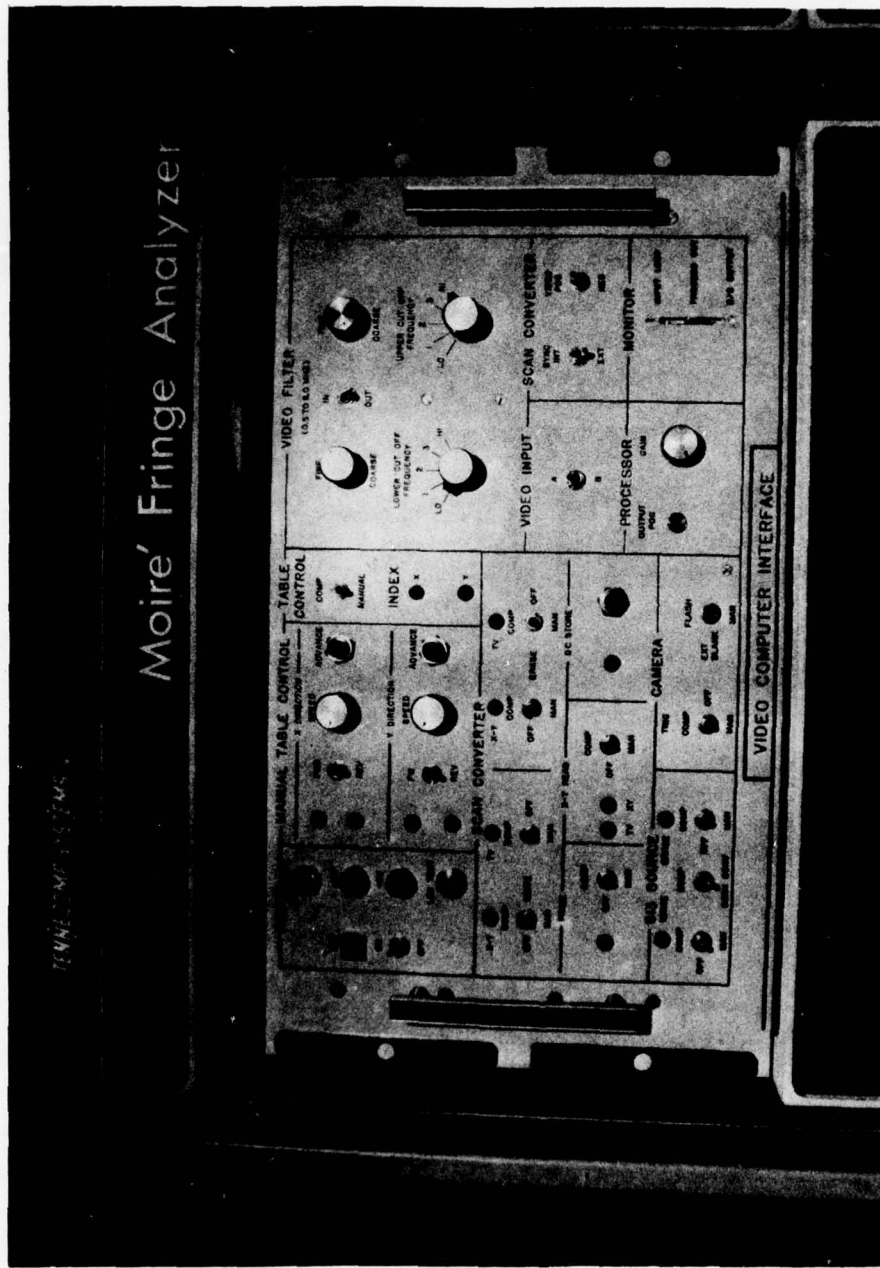


Figure 90. Video computer interface.

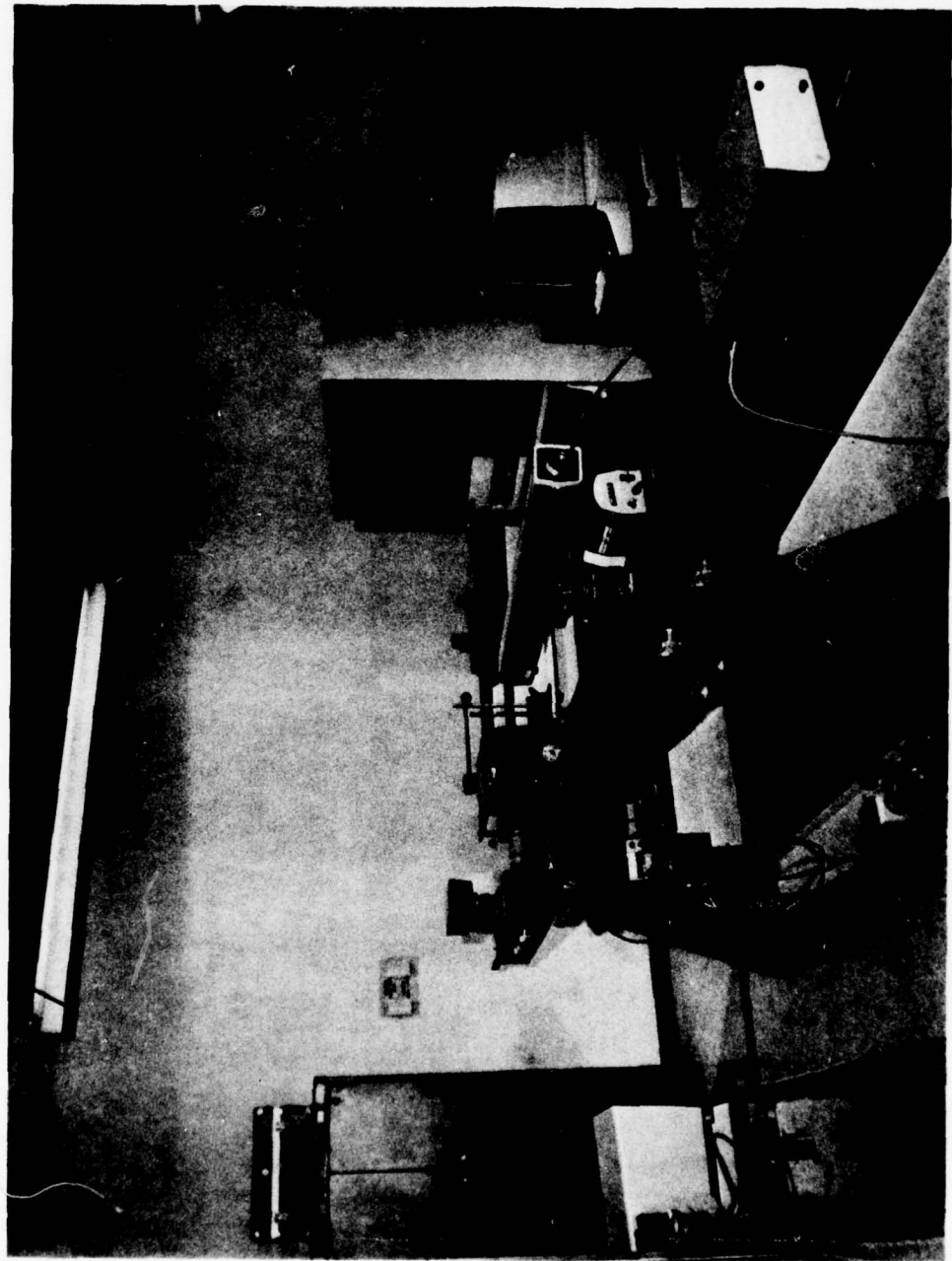


Figure 91. Complete system.

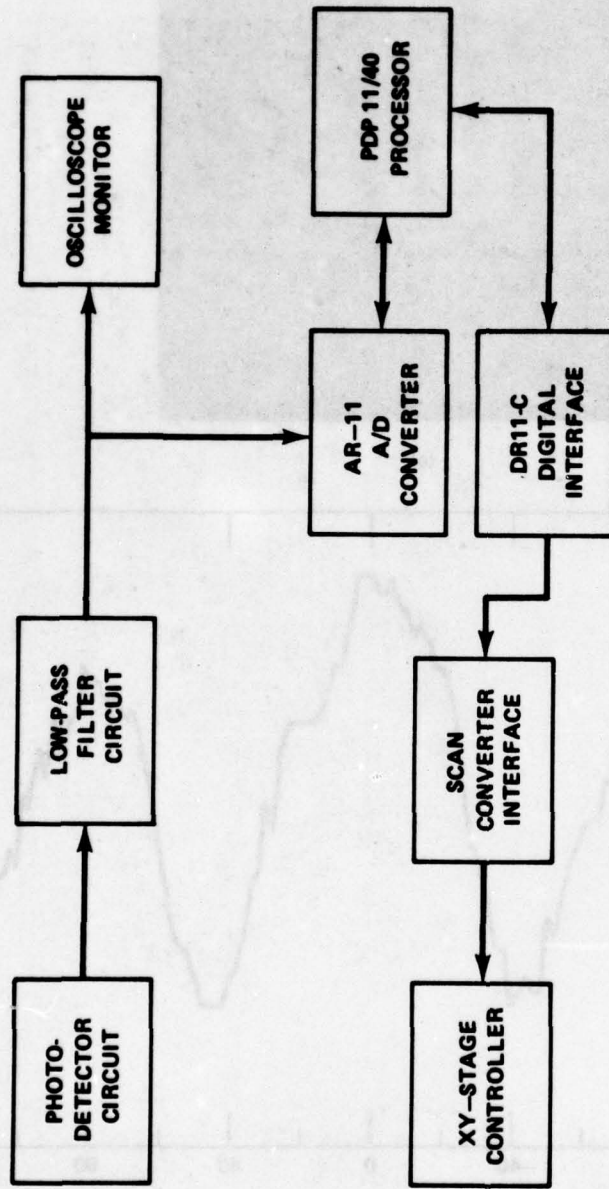
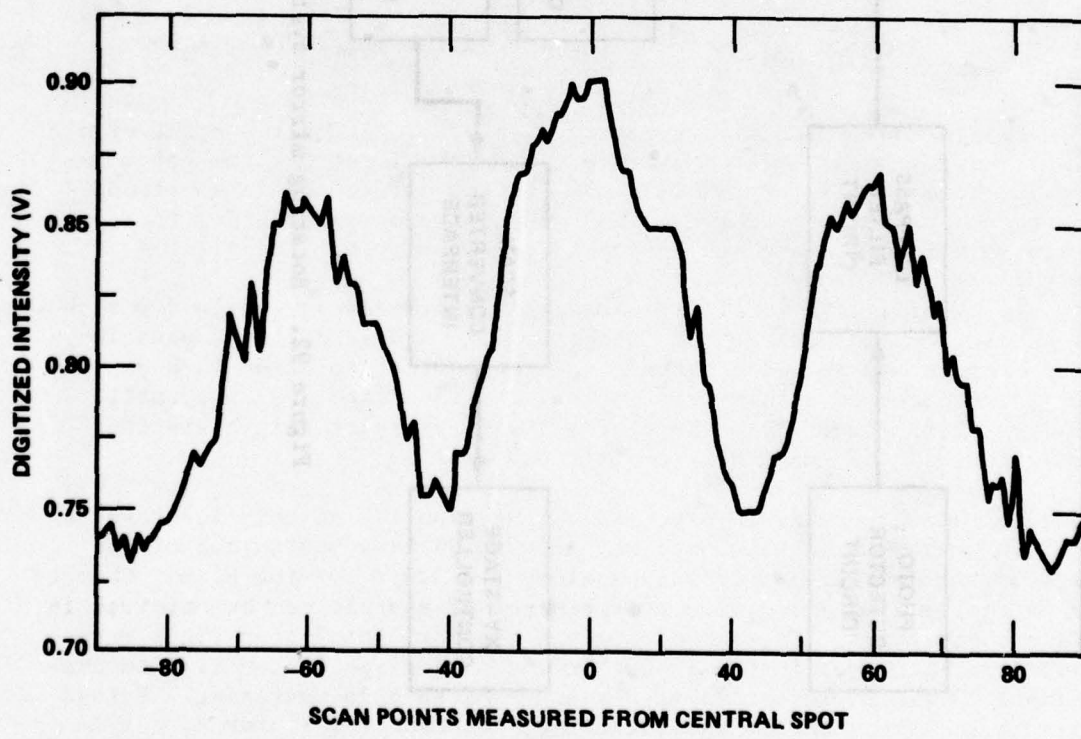


Figure 92. Rotating mirror system block diagram.



(a)



(b)

Figure 93. (a) Photograph of diffraction pattern, (b) digitized scan of a horizontal line.

In the x-y read mode, the computer receives a voltage from the scan conversion memory corresponding to an intensity at points along a scan line. This signal is stored in memory in the PDP11/40 for processing of fringe information. A digitized single scan line of the image in Figure 93 (a) is shown in 93 (b). This signal illustrates the effect of the laser speckle on the image. The image should appear as a sine wave without the presence of speckle; therefore, methods of reducing speckle noise are necessary to locate the position of a fringe.

A speckle averaging technique was developed which reduces the effect of noise in locating points of minimum intensity. Fringes which appear as parallel lines on the camera simplify the speckle averaging technique. The procedure is to digitize a single scan line and store into memory the location and value of intensity along this line. Another scan line is also digitized and stored into memory. These two scan lines, which are separated by a small distance, are then added and the result is the average of the two signals. The best scan line separation appears to be approximately 10 lines apart. The average of these two lines has the effect of reducing the speckle noise superimposed on the image. Figure 94 is the speckle average of two scan lines of the image shown in Figure 88 (a). Scan line separation of this image was 20 lines. If the scan lines of Figure 93 (b) and 94 are compared, speckle noise is reduced by averaging particularly around the points of minimum intensity.

Fringe separation is determined by first locating the point of maximum intensity from the scan average. Then the first minimum point is located to each side of this maximum and the difference in location determines the fringe spacing. The computer program used for the data analysis for this system is described in Appendix A.

An example of a cantilever beam with a transverse end load was chosen as a test for the accuracy of fringe spacing and scan line separation. This example was selected because the theoretical solution is known and fringe spacing varies from infinite at the fixed end to a small spacing at the free end. Therefore, a wide range of fringe spacing conditions can be examined from this one example.

The beam geometry is discussed in Section IV and only the results will be presented in this section. Figure 95 is a photograph of the various fringe spacing conditions along the length of the beam. Changes in fringe spacing along with the presence of speckle can be observed in these photographs. In each photograph the horizontal scan lines were above the dark spot in the center of the photograph. Scan line separation of 10 and 20 were used as a measure of speckle averaging. Fringe spacing is determined by the following [Equation (102)] for $M_1 = 1$

$$x = \frac{\lambda f}{u} \quad (110)$$

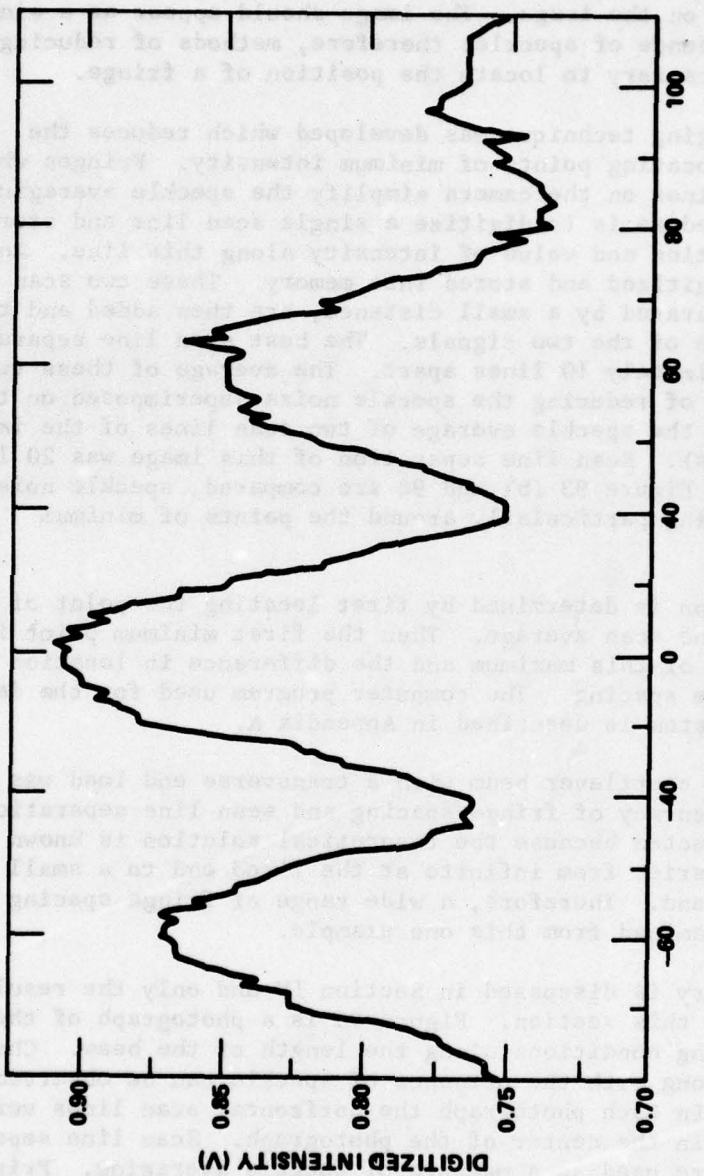
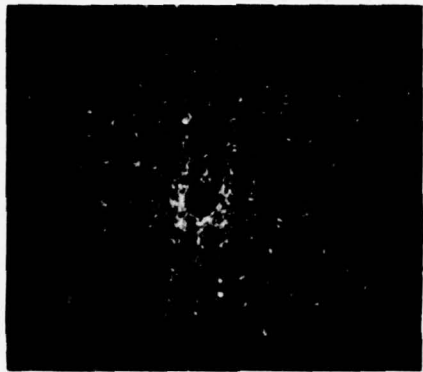


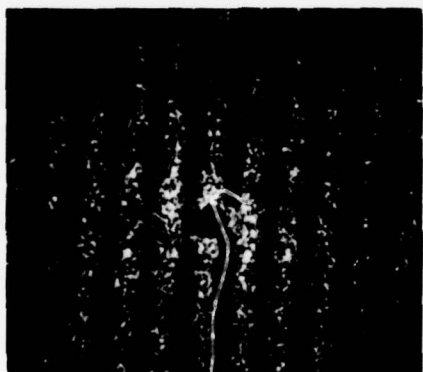
Figure 94. Average intensity of two scan lines from a diffraction pattern.



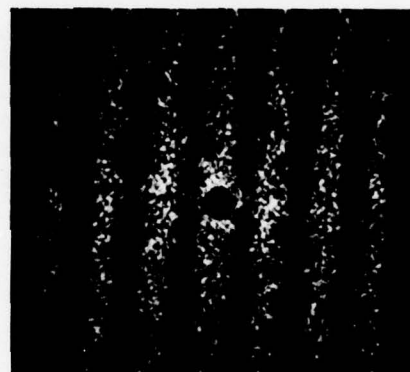
3.75 in.



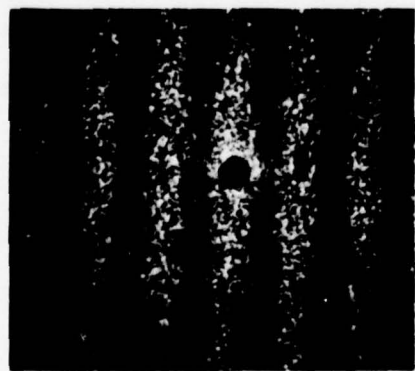
3.25 in.



2.75 in.



2.25 in.



1.75 in.



1.25 in.

Figure 95. Photographs of the diffraction pattern of the cantilever beam at various distances measured from the fixed end.

where

λ = wavelength of light

f = distance between film and transform plane

u = displacement.

If the free end deflection is denoted as δ , then the fringe spacing can be written as

$$x_D = \frac{\lambda f}{\delta} . \quad (111)$$

The ratio of displacement u to the free end displacement is related to the fringe spacing by Equation (111),

$$\frac{u}{\delta} = \frac{x_D}{x} . \quad (112)$$

This ratio was used to determine the experimental results and compared to the analytical solution. Figure 96 is a graphical display of measured values made by an observer and a computer scan with 10-line separation. Both sets of measured values are compared to the analytical solution to assess the accuracy of the measurements. Compared to the theoretical solution, both sets of measured values are within 2% of the analytical solution.

Results of a 10 and a 20 scan line separation are shown in Figure 97, which shows that the 10-line scan yields the best results. A listing of the numerical values is given in Table 2.

G. Rotating Mirror Data Analysis

A typical oscilloscope trace of an unfiltered fringe pattern from the rotating mirror system is presented in Figure 98, which shows that the presence of laser speckle produces a high frequency noise on the signal. This signal is filtered by a low pass filter to reduce the speckle effect on the signal. Figures 99(a) and (b) illustrate the comparison between a filtered and an unfiltered signal from the fringe pattern. The filtered signal then served as an analog input to the PDP 11/40 computer. Fringe spacing is then determined in this case by locating the maxima of the waveform. The maximum points are located by sampling the data and determining when the slope between three successive data point samples changes from positive to negative. Appendix B is a description of the computational procedure used in the data analysis of the rotating mirror.

To test the accuracy of the rotating mirror system, the cantilever beam example was utilized. Beam geometry is discussed in Section IV and only the results will be presented in this section. Fringe spacing

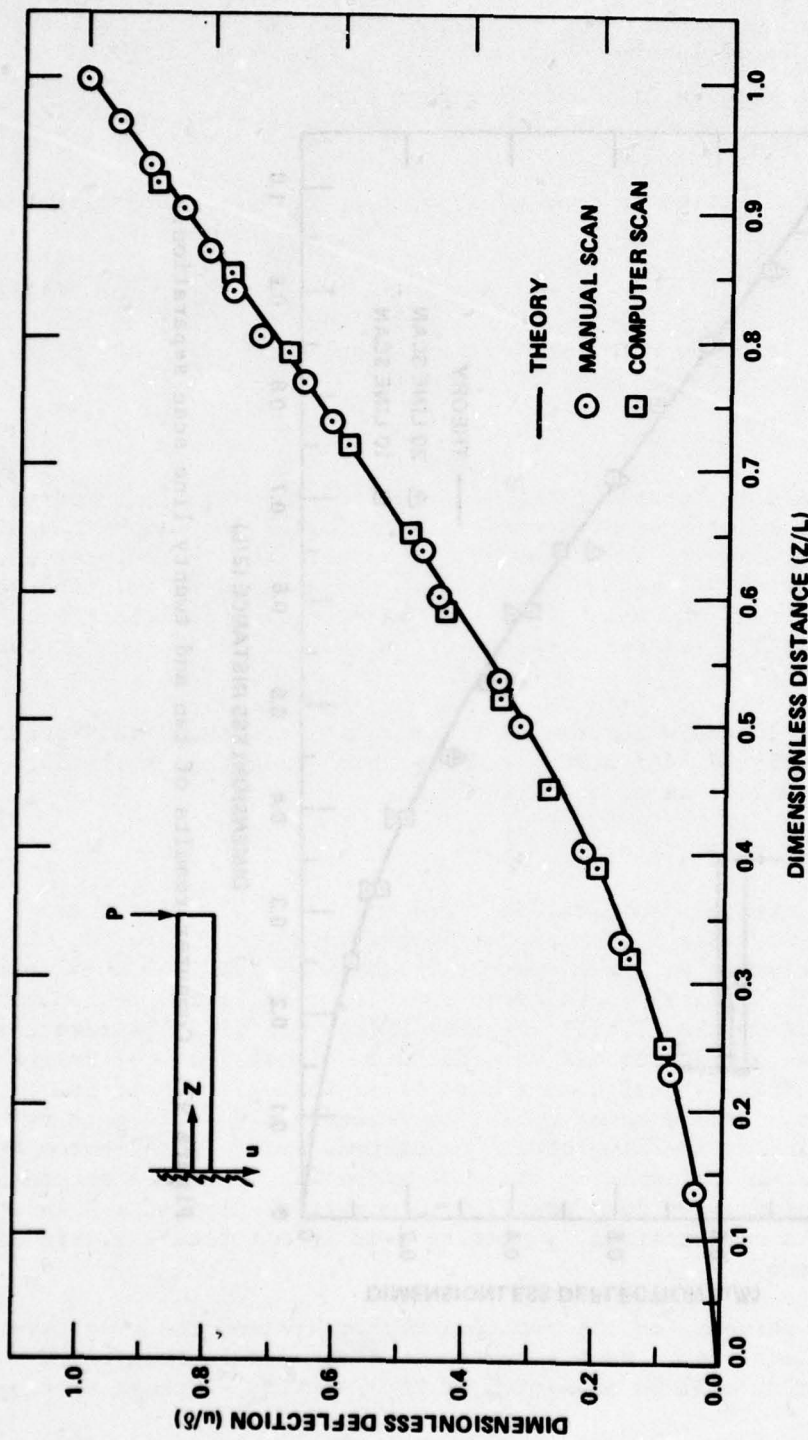


Figure 96. Comparison of fringe spacing values measured by an observer and computer scan measurement.

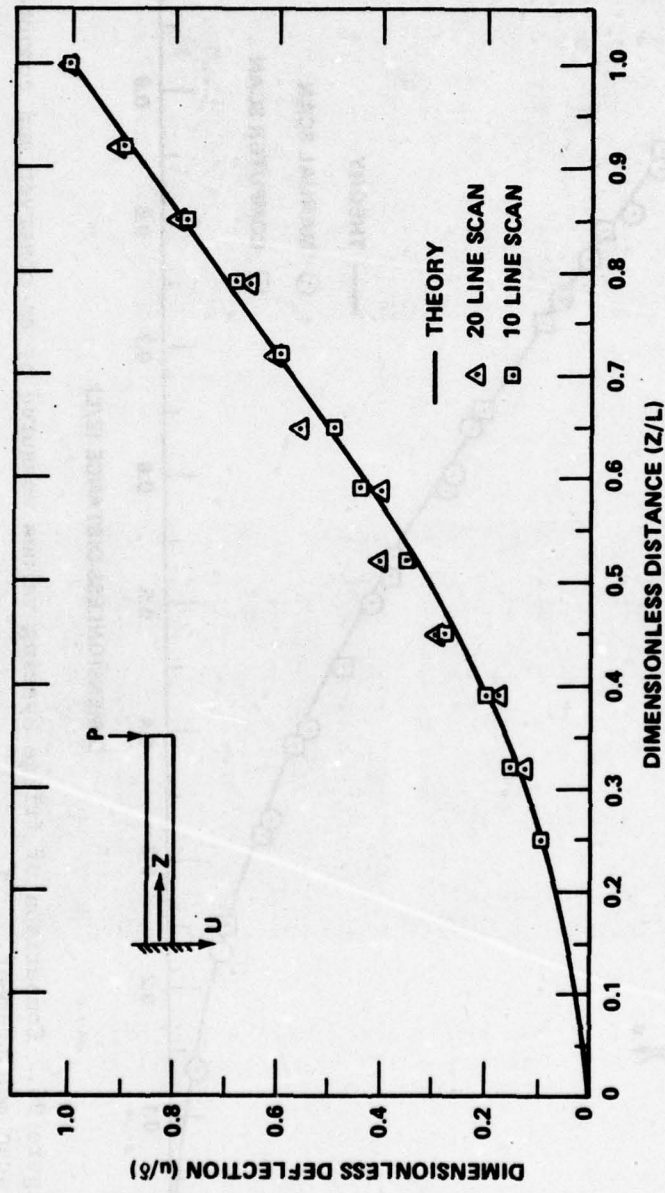


Figure 97. Computer results of ten and twenty line scan separation.

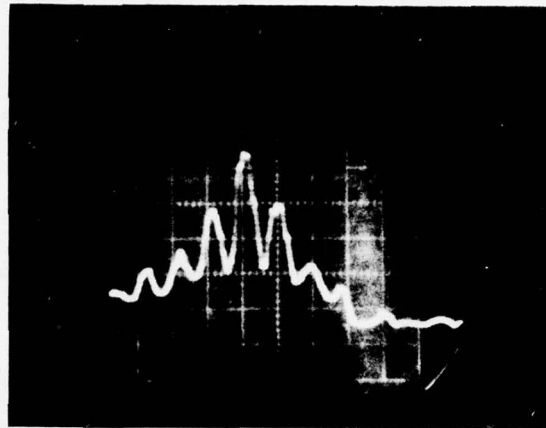
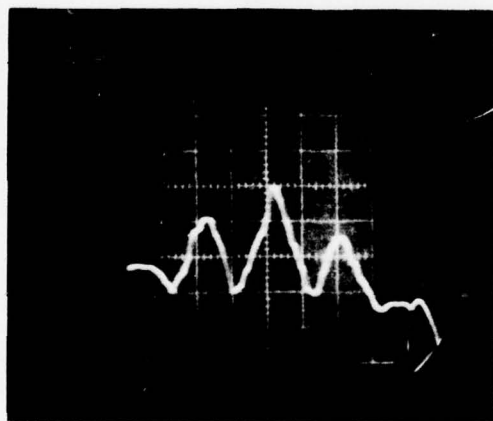
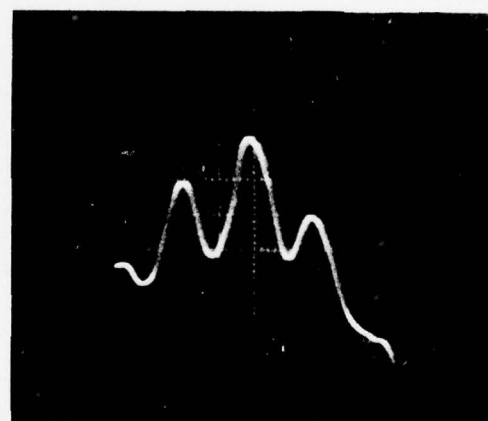


Figure 98. Oscilloscope trace of the output from the photodiode of a typical fringe pattern (horizontal sweep 5 msec/cm, vertical 0.5 V/cm).



(a)



(b)

Figure 99. (a) Unfiltered scope trace of the photodiode output, (b) Filtered trace of the same signal (horizontal sweep 5 msec/cm, vertical 0.5 V/cm).

ratio for this example was determined by Equation (112). A graphical display of the results is given in Figure 100. Compared to the theoretical solution the measured values are within 2% of the theoretical solution.

TABLE 2. RESULTS OF SCAN LINE SEPARATION FOR THE BEAM EXAMPLE

Distance from Fixed End Z (in.)	Z/L	Computer Spacing		X_D/X	
		20 lines	10 lines	20 lines	10 lines
3.75	1	18	17	1.0	1.0
3.45	0.92	20	19	0.90	0.89
3.20	0.85	23	22	0.783	0.77
2.95	0.79	24	25	0.750	0.68
2.70	0.72	30	29	0.60	0.59
2.45	0.65	32	35	0.56	0.49
2.20	0.59	45	39	0.40	0.44
1.95	0.52	45	48	0.40	0.35
1.70	0.45	64	61	0.28	0.28
1.45	0.39	93	83	0.19	0.20
1.20	0.32	136	117	0.13	0.15
0.95	0.25	-	190	-	0.09

H. Main Computer Code Description

Two computer codes have been developed to analyze interferograms using the Young's Fringe method of analysis. One of the codes utilizes the vidicon-scan converter while the other controls the rotating mirror reader assembly. These programs have been written to use the SYSLIB library routines provided under PDP's RT-11 software.

Information for controlling the system is passed from the computer to the scan converter interface via a DR11-C digital input-output interface. This device resides at the register address 767772. Any information deposited in this location is sent to the scan converter interface. Table 3 indicates the available control functions provided. The scan converter interface converts the OPCODES shown into commands which it then executes independently of the computer.

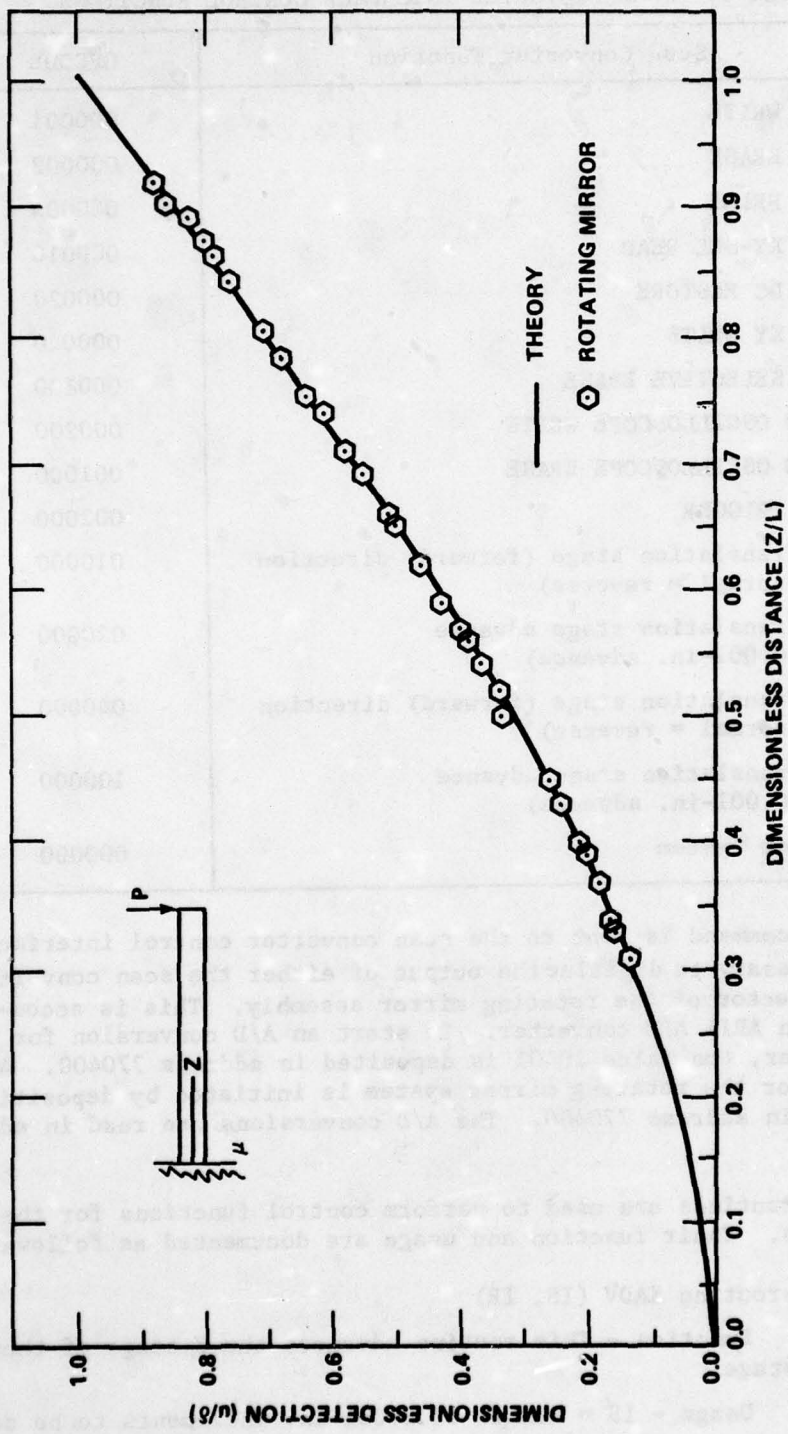


Figure 100. Comparison of fringe spacing values measured by rotating mirror system.

TABLE 3. SCAN CONVERTER INTERFACE CONTROL FUNCTIONS

Scan Converter Function	OPCODE
TV WRITE	000001
TV ERASE	000002
TV PRIME	000004
TV XY-SEL READ	000010
TV DC RESTORE	000020
TV XY WRITE	000040
TV SELECTIVE ERASE	000100
613 OSCILLOSCOPE WRITE	000200
613 OSCILLOSCOPE ERASE	001000
TV TRIGGER	002000
X-Translation stage (forward) direction (normal = reverse)	010000
X-Translation stage advance (0.001-in. advance)	020000
Y-Translation stage (forward) direction (normal = reverse)	040000
Y-Translation stage advance (0.001-in. advance)	100000
Reset System	000000

Once a command is sent to the scan converter control interface, it becomes necessary to digitize the output of either the scan converter or the photodetector of the rotating mirror assembly. This is accomplished by an AR11 A/D converter. To start an A/D conversion for the scan converter, the value 20401 is deposited in address 770400. An A/D conversion for the rotating mirror system is initiated by depositing the value 21001 in address 770400. The A/D conversions are read in address 770402.

Six subroutines are used to perform control functions for the two main programs. Their function and usage are documented as follows:

1) Subroutine XADV (IS, IR)

- a) Function - This routine advances the X-stage of the XY translation stage.
- b) Usage - IS = number of 0.001-in. increments to be advanced.

(IS > 0) advance forward
(IS < 0) advance in reverse

IR = rate at which the stage is to advance.
 $10 \leq IS \leq 32000$. The smaller values of IR increase the advance rate.

2) Subroutine YADV (IS, IR)

a) Function - This routine advances the Y-stage of the XY translation stage.

b) Usage - Same as for Subroutine XADV

3) Subroutine Store (ISD, IPD, IPC)

a) Function - This routine primes the Hughes scan converter and stores one video frame from the vidicon camera.

b) Usage - ISD = duration of store cycle (4000 = optimum value)

IPD = duration of prime cycle (4000 = optimum value)

IPC = total number of prime cycles to be performed
(IPC ≥ 1)

4) Subroutine Scan (IX, IY, ID)

a) Function - This routine digitizes the scan converter stored video and stores the data for further processing. The digitized values have a range of 0 to 1024 on a 0 to 5 V scale.

b) Usage - IY \equiv locates the position of a horizontal scan line ($0 \leq IY \leq 1024$)

IX \equiv locates the position of a vertical scan line
($0 \leq IX \leq 1024$)

ID (1, n) \equiv horizontal line digitized data ($1 \leq n \leq 1024$)

ID (2, n) \equiv vertical line digitized data ($1 \leq n \leq 1024$)

5) Subroutine PROCES (ID, IDD, IT, NNX, NNY)

a) Function - This routine searches the data produced by subroutine scan and locates the maxima and minima of it. For example, if a sinusoidal signal is provided for the filter, it will locate all the maxima and minima.

b) Usage - ID \equiv Data array from subroutine scan

IDD (1, m) \equiv locations of the maxima and minima for the horizontal scan ($1 \leq m \leq 1024$)

IDD (2, m) \equiv locations of the maxima and minima for the vertical scan ($1 \leq m \leq 1024$)

IT \equiv maximum amplitude of the input signal's noise

NNX \equiv total number of maxima and minima for the horizontal scan

NNY \equiv total number of maxima and minima for the vertical scan

6) Subroutine RLOAD (D, IS)

a) Function - This routine converts the analog signal from the rotating mirror scanner into digital form and then calculates the fringe spacing from the digitized data for the current interferogram coordinates

b) Usage - D \equiv fringe spacing

IS \equiv trigger voltage level on a scale of 0 to 1024 of +5 V

The AR11 A/D converter has an input range of 0 to 5 V with 0 V represented in digital form as 0 and 5 V as 1024.

I. Vidicon Camera Code

The vidicon Young's Fringe analyzer code is used to control the raster scanning of interferograms using the vidicon camera and scan converter. The basic operations performed by the program are as follows:

- 1) Request scan parameters for the XY translation stage.
- 2) Request scan parameters for the scan converter.
- 3) Request parameters for storing video images and filtering them.
- 4) Positioning the XY table for scanning.
- 5) Store video images.
- 6) Digitize video images.
- 7) Process the digitized video for fringe spacing and output the data.

Once the program called VTEST is started, it requests the following information:

- 1) X-axis boundaries, Y-axis boundaries - 415. This is a request for scan boundary information. An interferogram is usually made on a 4- \times 5-in. glass plate giving a total of 4000 \times 5000 possible data point

locations. Once the computer code is started, the position of the x-y stage at that time is assumed to be the (0, 0) origin location. The coordinate system for the interferogram is determined as follows. Viewing the interferogram along the laser beam where it strikes the emulsion, the beam is the z-axis, the 4-in. wide portion of the aperture is the X axis, and the 5-in. wide portion of the 4- x 5-in. aperture is the Y axis. The coordinates for a raster scan are input in 4I5 format. For example, to perform a full raster scan of a 4- x 5-in. interferogram, with the origin at the center of the interferogram, the following data are input: -2000 2000 -2500 2500.

2) X and Y increments, X and Y axis stage rates - 4I5. The X and Y axis increments are the number of steps in the X and Y directions between successive points where data are collected. The X and Y axis stage rates control the rate at which the X-Y stage advances. If in Step 1, a data scan was desired at every other point and the stages were to move at a rate of 10, the following data would be input to the computer: 00002 00002 0001000010.

3) XY-1 and XY-2 scan intersects - 4I5. These parameters control the position of the scan lines for the scan converter. Two scans in both the horizontal and vertical directions are made to calculate fringe spacing and orientation. To scan at the intersection points (500, 600) and (510, 610), the following data are input: 00500 00600 00510 00610. Two horizontal scans at coordinates 600 and 610 and two vertical scans at coordinates 500 and 510 will be made.

4) Store Delay, Prime Delay, No. Primes, Filter level - 4I5. Store delay and prime delay, control the erasure, and storage of a video frame of data. Their input values are recommended to be 4000. The No. Primes request is the number of desired primes to be performed between successive video image stores. The recommended number is 3. Filter level is a request for how large the amplitude of the noise is in the signal. If a noise level of 0.1 V is expected, then the computation of the filter level is as follows:

$$\text{FILTER LEVEL} = (0.1) \frac{1024}{5} \approx 20$$

Utilizing the recommended input data, the data input to the code would be 04000 04000 00003 00020.

5) System scale factor - F10.4. This is the scale factor for converting the television scale for measuring fringe spacing into actual physical units of measurement. To determine this factor the computer code may be run initially with a scale factor of 1. A test bar pattern of known width is then placed on the diffuser screen and the computer then determines its width in television units. By knowing the fact that:

$$\text{Localized displacement} = \frac{\text{Scale Factor}}{\text{Television Spacing of Fringes}}$$

the scale factor can be determined.

After the scan parameters are input to the computer, a raster scan will automatically occur. The switch console of the PDP 11/40 computer should be at the zero state at all times. If Switch 0 is depressed, the code will request a new filter level; if Switch 1 is depressed, the computer will rescan the same data point. These switches are to be used if the operator suspects a problem in the system. After each desired point is scanned, the computer prints out the results. Depression of the control switches should be made before the results of the current scan point are completely printed out. A typical line of output appears as follows:

X = ***** Y = ***** DX = ***** DY = ***** XS = ***** YS = *****

where

X = integer count of current horizontal scan point

Y = integer count of current vertical scan point

DX = localized displacement in the X direction

DY = localized displacement in the Y direction

XS = current X location of the scan

YS = current Y location of the scan

J. Rotating Mirror Code

The second main computer code is for raster scanning interferograms using a rotating mirror assembly. The program called RTEST requests the following information:

1) X-axis boundaries, Y-axis boundaries - 4I5: (same parameters as in VTEST)

2) X and Y axis increments, X and Y axis stage rates - 4I5: (same parameters as in VTEST)

3) Scan level, system scale factor - I5, F10. The scan level is computed from the signal voltage as follows: Measure the voltage from the photodetector which clearly denotes the start of fringe information, then compute the scan level from the formula:

$$\text{Scan level} = \text{Signal voltage} * \frac{1024}{5}$$

The system scale factor is determined as in program VTEST. Once the previously mentioned three lines of data are provided to the computer, a raster scan will automatically occur. As in program VTEST, the console

switches should all be at their zero state. In program RTEST, depression of Switch 0 causes a scan to be repeated while the depression of Switch 1 causes the computer to request a new scan level.

A typical line of output data from RTEST appears as:

X = **** Y = **** XS = **** YX = **** D = ****

where,

X = integer count of the current horizontal scan point

Y = integer count of the current vertical scan point

XS = current X location of the scan

YS = current Y location of the scan

D = localized displacement as determined by the orientation of the rotating mirror analyzer system.

The following procedure is used for running VTEST:

- 1) Power up the computer, scan converter, laser, scan converter interface, TV monitor, vidicon camera and XY-Table power supplies.
- 2) Load the RT11 monitor into the computer.
- 3) Run program VTEST.
- 4) Focus the camera and position the XY-Table to its origin point for scanning.
- 5) Place the prime, erase, TV write, XY-Table, and TV XY-SEL READ switches in the comp position. Place all console switches in their 0 position.
- 6) Input the required data to the computer.

The following procedure is used for running RTEST:

- 1) Power up the computer, scan converter, interface, photodiode power supply, laser monitor oscilloscope, and X-Y Table power supplies.
- 2) Load the RT-11 monitor into the computer.
- 3) Run Program RTEST.
- 4) Position the X-Y Table to its origin point for scanning. Adjust the signal filter.
- 5) Place the X-Y Table switch to computer and start the mirror motor. Place all console switches in their 0 state.
- 6) Input the required data to the computer.

K. Applications to Nondestructive Testing of Composite Cylinders

A computer scan was made of the speckle photograph of composite cylinders with simulated flaws shown in Figures 2 and 3. Speckle photographs of the cylinders were the same photographs used in the data analysis presented in Section VI. Computer scans were made along several sections of each cylinder to determine if the data analysis was sensitive to the simulated flaws.

Figures 101 and 102 are graphical representations of scan lines from the rotating mirror system. Scan line directions for this application was along the X direction as shown in Figure 62. Figure 101 presents the results of the fringe spacing for the simulated spot flaw. Figure 74 presents the results of fringe spacing for the longitudinal flaw. These two figures show that the computer scan is capable of detecting the flaws to the same accuracy as an observer recording the data.

VIII. COMPUTER AIDED DATA REDUCTION SYSTEMS HARDWARE AND OPERATION

A. General

The purpose of this section is to provide technical information about the video-computer interface, Model 4000, and to aid technical personnel in the operation and understanding of its electronic circuits.

This section contains a general description of the Model 4000 and the speckle analyzer system. A detailed description of the operation of each major circuit within the Model 4000 interface is also provided.

All details needed to fabricate or purchase the components of this system have been completely documented but only the block diagrams and control panel layouts are included in this report. System schematics, test points, cable systems, interfacings, pin connections, and catalog data on other components are included in Reference 15. Complete fabrication drawings were prepared and can be made available if components of this system are needed.

B. System Description

The video-computer interface panel, Model 4000, was built for the Ground Equipment and Missile Structures (GE&MS), Directorate of MIRADCOM by Sperry Support Services (SSS). The system consists of the following items:

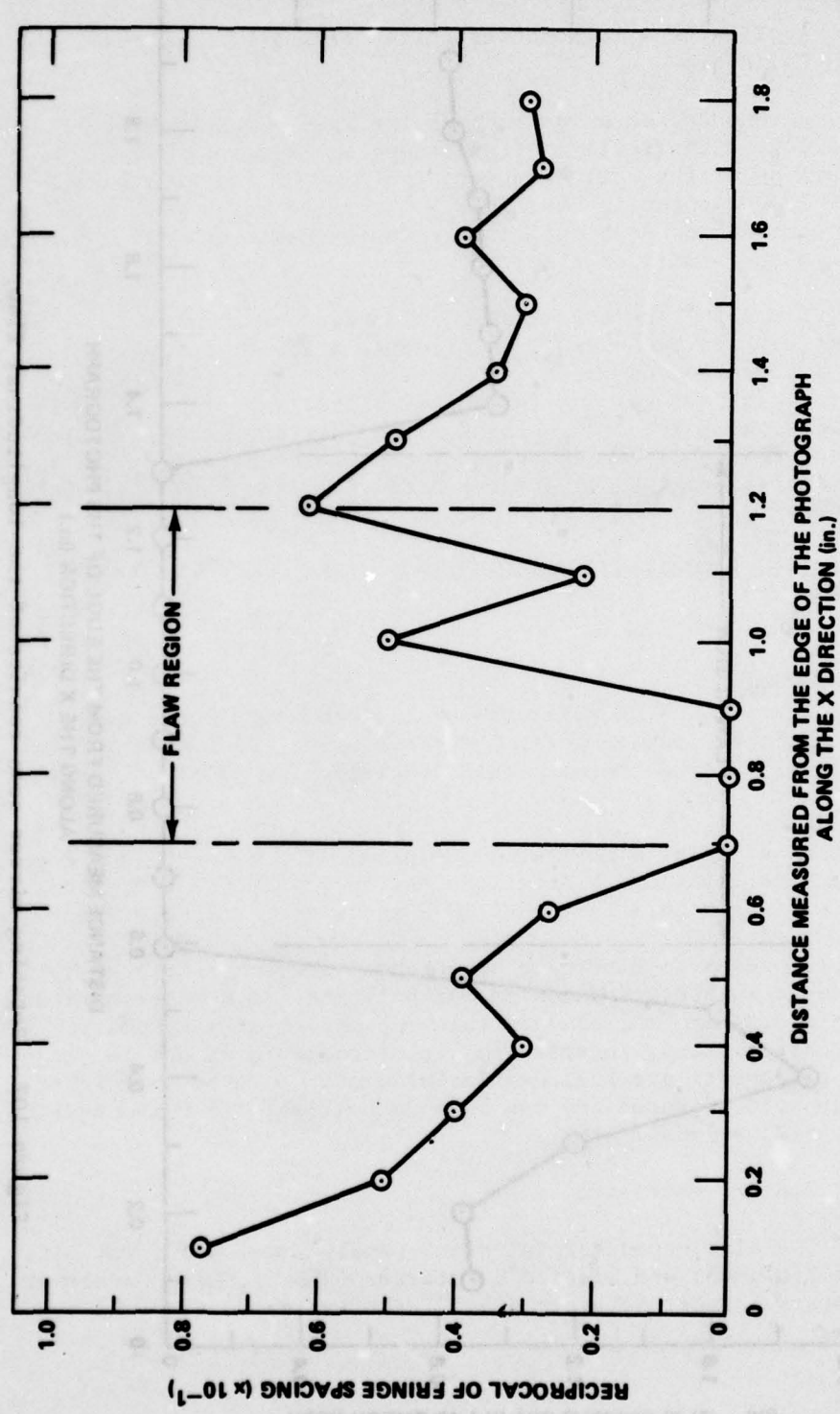


Figure 101. Rotating mirror scan results of the spot flaw.

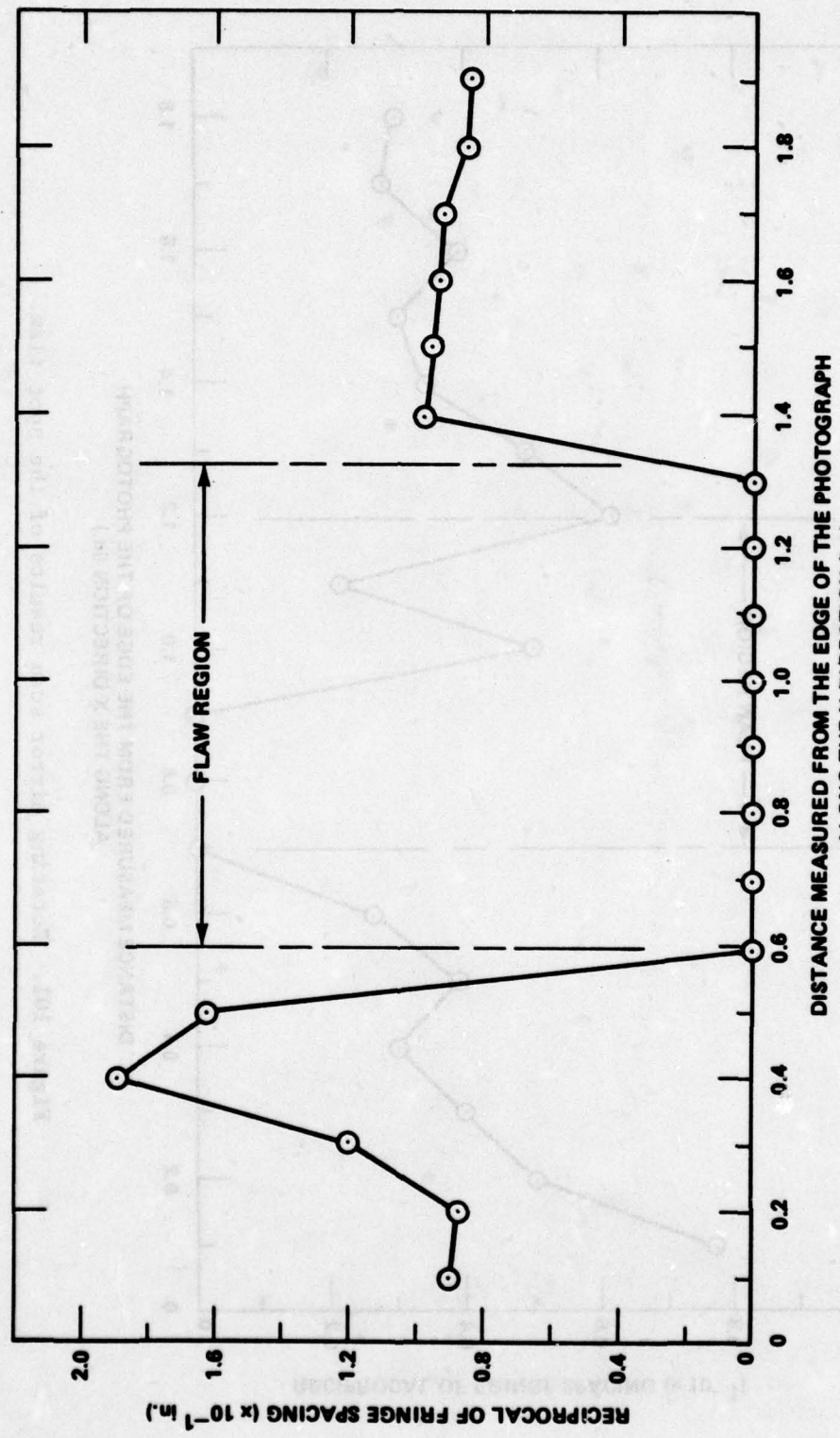


Figure 102. Rotating mirror scan results of the longitudinal flaw.

Supplier*

1) Video-computer interface panel, Model 4000.	A
2) X-Y translation table.	A
3) Television camera, optical accessories, STV 1000.	A,B
4) Minicomputer, PDP 11/40.	B
5) Laser, Model 124A.	C
6) Scan converter, Model 639.	D
7) Video storage unit, Model 613.	E

Supplier's Code: (A) SSS
(B) MIRADCOM, GE&MS Directorate
(C) Spectra Physics, Inc.
(D) Hughes
(E) Tektronix, Inc.

The video-computer interface is shown, as it fits into the Electro-mechanical Single-Beam Speckle Interferometric Analyzer System, in Figure 103. All the separate pieces of equipment, purchased by different companies, are tied together to the PDP 11/40 minicomputer with the Model 4000 interface.

The laser passes a beam of light through a hologram specimen and is reflected onto the diffusion screen. The vidicon television camera makes a picture of the image on the screen. The scan converter then stores the picture. A horizontal and vertical line is scanned and digitized by the minicomputer. The results are processed and read out on the terminal. The stored video can be seen on the monitor.

C. Electronic Subsystem Functions

The purpose of the video computer interface is to provide the required interfacing between a PDP 11/40 minicomputer and other equipment of the system shown in Figure 103. The interface also provides for the manual operation of all the additional equipment from a single source.

Included within the video computer interface panel is a video amplifier, a video filter, a video comparator, a board of electronics for manual and computer commands, and a board for motor drive commands. The block diagram of the subsystems is shown in Figure 104.

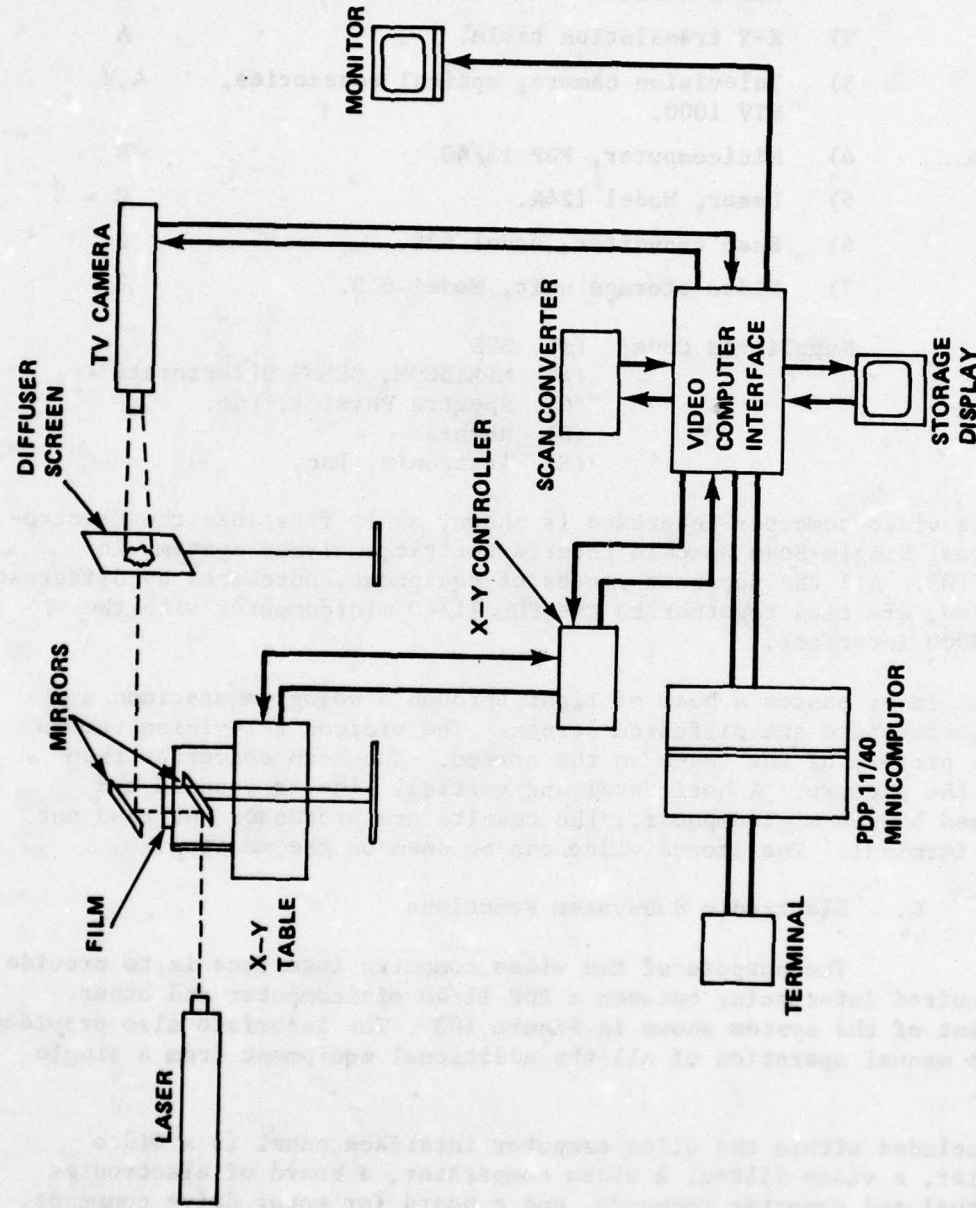


Figure 103. Electromechanical single-beam speckle interferometric analyzer system.

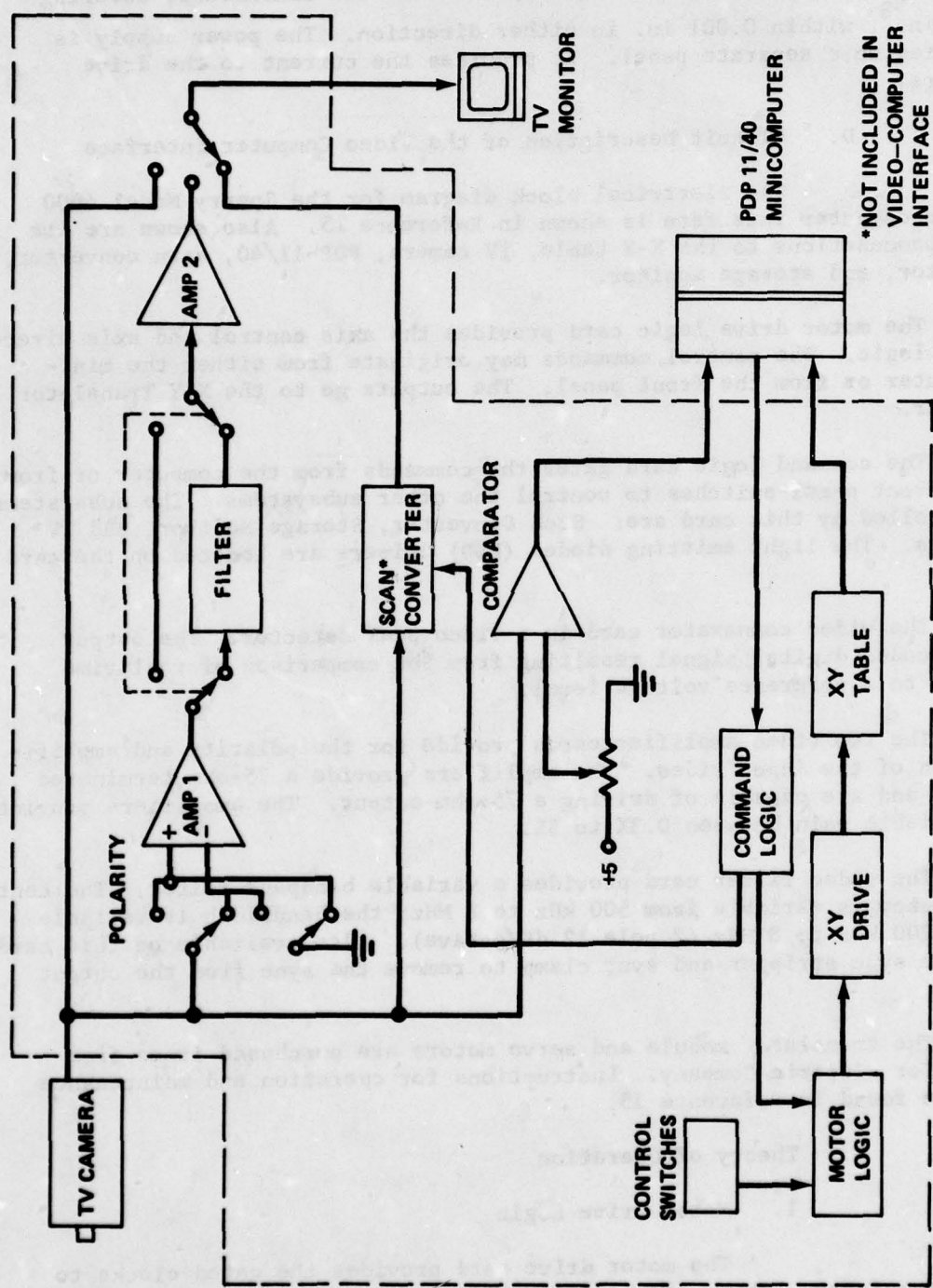


Figure 104. Video computer interface block diagram.

Also provided is an X-Y translation table and power supply. The X-Y table is capable of moving a specimen in two dimensions, covering 100 in.², within 0.001 in. in either direction. The power supply is located on a separate panel. It provides the current to the drive motors.

D. Circuit Description of the Video Computer Interface

The electrical block diagram for the Sperry Model 4000 video computer interface is shown in Reference 15. Also shown are its interconnections to the X-Y table, TV camera, PDP-11/40, scan converter, monitor, and storage monitor.

The motor drive logic card provides the axis control and axis direction logic. The control commands may originate from either the mini-computer or from the front panel. The outputs go to the X-Y Translator Driver.

The command logic card gates the commands from the computer or from the front panel switches to control the other subsystems. The subsystems controlled by this card are: Scan Converter, Storage Monitor, and TV camera. The light emitting diodes (LED) drivers are located on the card also.

The video comparator card is a video peak detector. The output is a coded digital signal resulting from the comparison of real time video to a reference voltage level.

The two video amplifier cards provide for the polarity and amplification of the input video. The amplifiers provide a 75-ohm terminated input and are capable of driving a 75-ohm output. The amplifiers provide a variable gain between 0.3X to 5X.

The video filter card provides a variable bandpass filter. The center frequency is variable from 500 kHz to 8 MHz; the bandwidth is variable from 200 kHz to 8 MHz (2 pole 12 dB/octave). Also available on this card is the sync stripper and sync clamp to remove the sync from the output video.

The translator module and servo motors are purchased items from Superior Electric Company. Instructions for operation and maintenance may be found in Reference 15.

E. Theory of Operation

1. Motor Drive Logic

The motor drive card provides the gated clocks to the translator. These clocks are called X-Motor Drive (XMD00, Forward;

XMD01, Reverse) and Y-Motor Drive (YMD00, Forward; YMD01, Reverse). They are generated from XML00 and YML00, X-Motor Logic and Y-Motor Logic. The direction of the motors is determined by the controls on the front panel. These commands are X-Direction (XDS00) and Y-Direction (YDS00). The X manual drive commands XAS00 and XAROON, set the S-R flip-flop A1. The Y manual drive commands, YAS00 and YAROON, set a similar flip-flop A1. The outputs of the flip-flops are further gated with the Computer/Manual signal CMS00 to prevent the manual operation during the computer control period. The computer commands are similar to the manual commands, but are useable only when the COMPUTER/MANUAL MODE switch is in the COMPUTER position. These commands and their functions are as follows: XSA00 and YSA00 are the X-Y stage advance; XSD00 and YSD00 are the stage direction.

2. Command Logic

The command logic card ties the Hughes Scan Converter and the Sperry STV-1000 camera to the minicomputer. The manual operation of the equipment is possible through this card. The prime, erase, write outputs to the scan converter are generated from the computer and from the front panel switches. The computer commands are, respectively, CTP00, CTE00, and CTW00. The manual commands are TPC00, TEC00, TWC00. These inputs are "OR'ED" together by the diodes C1 through CR6. The resulting outputs then are HTP00, HTE00, and HTW00, respectively. The dc restore may also be generated by the computer or manual switches. These commands trigger the one shot A3 to provide a 40-nsec pulse. The output to the scan converter is HRC00. There is a provision for manually erasing and writing. The controls are located on the front panel. The inputs to this card from these switches are called ERS00 and WRS00. Extreme care should be taken with the MANUAL WRITE switch. Should this switch be activated for more than an instant, permanent damage may occur to the scan converter. The LEDs are driven by A2, A4, and A5. The LAMP TEST switch on the front panel lights all the LEDs on the video computer interface panel.

3. Video Comparator

Video peak detection is accomplished with the use of this card. The live video is brought into Comparator A1. This signal is compared with the threshold voltage set by Potentiometer R3. The analog ground is kept isolated from the digital ground on this card by the use of Optoisolator A2. The output signal of A2 has a slow rise-time and a slow fall-time due to its inherent characteristics. The signal is fed into a Schmit-trigger inverter to provide a better digital representation of the video signal.

4. Video Amplifier

The video amplifier card provides a voltage gain of 2. This gain is provided by Video Amplifier A1. The output polarity

may be changed by the POLARITY switch on the front panel. This switch applies the video signal to the inverting or noninverting inputs. A2 is a high speed buffer amplifier. It allows the video amplifier to drive 75-ohm cables.

5. Video Amplifier 2

This card is identical to the Video Amplifier 1 with a few exceptions. The first of these is that the differential inputs are not available to A1. Secondly, the overall gain of five required by the system is achieved by this card.

6. Video Filter

The video filter is made up of a high pass filter and a low pass filter in series. The low pass filter is composed of Video Amplifier A1 and the resistor-capacitor (RC) feedback network as selected by the UPPER CUT OFF FREQUENCY controls. The high pass filter is composed of Video Amplifier A2 and the RC feedback network as selected by the LOWER CUT OFF FREQUENCY controls. The sync is removed by Comparator A3 and then it is used to gate out the sync in the video before sending it to the video filter.

F. Electronic Subsystem Controls

Before activating the video computer interface, the following initial conditions must exist:

- 1) All electronic cards are inserted in their proper positions.
- 2) All cables are run correctly with their connectors securely mated.

The video computer interface panels are shown in Figures 105 and 106.

1. Operating Control Functions

The POWER switch on the Model 4000 provides the primary power to the ± 15 V and +5 V power supplies. When this switch is in the ON position, the 115 V light as well as the +15 V, -15 V, and +5 V LEDs should turn on.

The MANUAL TABLE CONTROL portion contains the manual controls to operate the X-Y Table. These controls are useable only when the TABLE CONTROL switch is in the MANUAL position. The available controls are X and Y directions (FWD and REV), SPEED, and ADVANCE. The INDEX LEDs turn on when the X-Y Table has returned to its home position.

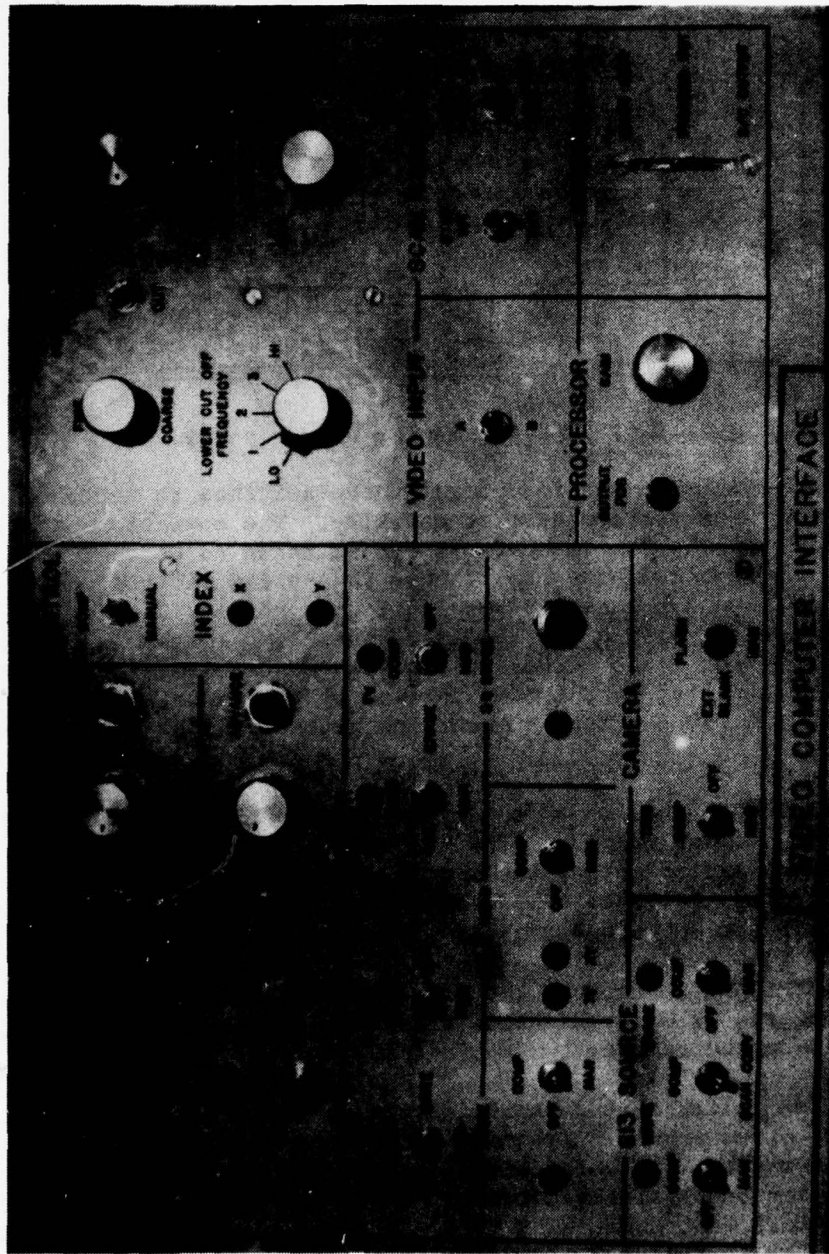


Figure 105. Video computer interface panel.

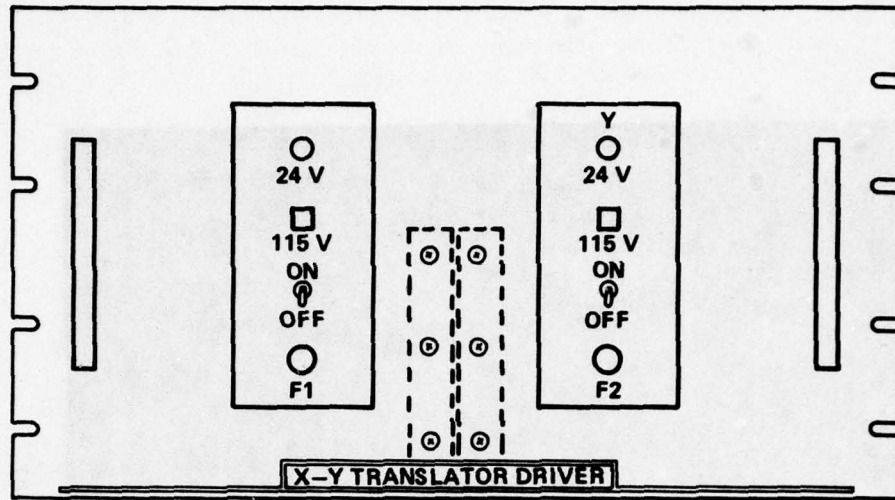


Figure 106. X-Y translator driver panel.

The SCAN CONVERTER section contains the switches to activate the scan converter from the computer or manually. The operations available are WRITE and ERASE. Extreme care should be taken to prevent the manual writing of the scan converter for longer than a few milliseconds in one location. Permanent damage may result if this switch is left in the MANUAL position for only a few seconds. The PRIME command provides a prime signal and an erase signal to the scan converter. The X-Y READ may also be controlled by the computer and by the manual switch. The direct current RESTORE pulse is generated by the push button on the panel.

The 613 SOURCE portion of the video computer interface controls the Tektronix 613 storage monitor. The 613 can be controlled in three ways. These are: the minicomputer, the manual switches, or by the video representation of the video comparator. The two functions controlled by these controls are WRITE and ERASE.

The CAMERA portion allows the STV-1000 TV camera to be operated by the computer. TRIGGER, EXTERNAL BLANKING, and FLASH may be done externally from the camera.

The video filter section contains the controls to adjust the bandwidth of the video signal. The two switches to select the cut off frequencies and the two variable controls allow for a bandwidth from 0.5 to 8 MHz or any bandwidth in between. These controls are labeled UPPER and LOWER CUTOFF FREQUENCY. The VIDEO INPUT switch provides for the selection of two different video signals A and B. The PROCESSOR GAIN determines the system gain (0.5 to 5X). The MONITOR switch selects the type of output. The INPUT LOOP mode bypasses all the electronics and sends the live video straight to the monitor. The PROCESS OUT mode allows

the video filter (and also the video gain) to be switched in. Positive and negative outputs from the scan converter can be selected by the SCAN CONVERTER VIDEO POSITIVE/NEGATIVE switch.

2. Alignment Procedures

All electronic subsystem circuits are designed to operate without the need for any special adjustments beyond those provided by the front panel controls. However, the threshold to the video comparator card (A4) may be adjusted to provide a more sensitive digital representation of the video.

To adjust the threshold, a small screwdriver should be used to turn the potentiometer on Card A4. Turning the screwdriver counterclockwise causes less sensitivity to light. At the upper limit, the output will correspond to all black; the lower limit will correspond to all white. Proper adjustment will cause a pulse at Test Point 1 that corresponds to a peak in the video. The voltage should be approximately 0.5 V at Pin 2 of A1.

IX. SUMMARY AND CONCLUSIONS

Approximately thirty fiber reinforced composite cylinders were fabricated in the in-house composite structures facility. Three types of programmed flaws were fabricated into the composite structure. The flaws consisted of delaminations between the fibers and were produced by inserting some Teflon tape in a 0.04-in.-thick cylinder wall. This type of flaw corresponds to those resulting from dirt, grease, voids, or flaws being fabricated into the structure. Spot, circumferential, and longitudinal flaws were used.

The basic theory for the analysis of the optical holographic fringe patterns was adapted to the missile launch tube or motor case geometries and boundary conditions for the specimen involved. Equations to reduce the fringe patterns to surface displacements were derived. Test fixtures and apparatus were designed and fabricated. Optical holographic fringe data were taken from specimens of each type with pressure loadings using both the double exposure and real-time methods. Fringe patterns were so sensitive that at certain loadings even the wrap angles of the fibers and the crossover regions were easily detected. Because locations of these points are well known, interference with the detection of flaws is not considered a major problem. The real-time approach is a rapid way of optimizing the loading parameters to best resolve the flaws. Each type of flaw was detectable using double-exposure holography and real-time; however, both methods require careful digitization and analysis to quantify the flaws and determine if they are critical.

Shearing speckle and single beam speckle interferometry have both been demonstrated to be able to detect the presence of flaws in fiber wound composite cylinders. Although each can detect flaws the two experimental techniques are best adapted to separate functions because they complement each other. Therefore, in an overall nondestructive testing program each technique can be utilized to perform specific functions.

The basic theory and applications of speckle shearing interferometry are presented in detail. This technique has the ability to detect flaws from a whole field approach with good fringe visibility. Furthermore, with a combination of mirrors the complete cylinder can be observed and photographed on a single photographic record. Thus, a rapid visual observation can be made for initial inspection of internal voids. The analysis of fringe formation to the deformation of circular cylinders was also presented. The resulting fringe pattern is a relatively complex function of the cylinder geometry and assigning fringe orders is not as convenient for computer aided data reduction. However qualitative analysis is very feasible using this technique.

A complete discussion of the single beam speckle photography is included. Double-exposure speckle photography is a whole field observation and the Young's Fringe technique is the point by point data interpretation. Results of the speckle photographic technique illustrate that internal voids can be detected and quantified in terms of the surface strains of the cylinder. Data analysis is the easiest to apply computer aided data reduction. Equations are easy to interpret and only fringe spacing is required. Fringe orders do not have to be assigned thus allowing for straightforward data interpretation. This technique represents a method to quantify the flaw and assess the structural integrity of the cylinders with the presence of internal voids. Data were presented to validate each technique.

A complete nondestructive testing system to detect, locate, size, and quantify flaws in fiber reinforced composite missile launch tubes and motor cases was designed including both the hardware and software. The system was assembled, interfaced, and checked out. Most of the major components were available from the laboratory but the interfacing and peripheral components required to complete the system were either designed and fabricated, or purchased. Software for a PDP 11/40 digital computer interfaced with a fringe reader and analyzer was developed and utilized to digitize the film and fringe patterns, plot the fringe density, locate the flaws on the plot, determine the flaw size, and compute the surface strains.

In summary, fringe data were taken using both double-exposure and real-time optical holography, Young's Fringe, and shearing-speckle interferometry. The data were reduced by computer and the flaws were detected, located and the approximate flaw size determined. Strains,

displacements, or stresses were determined. Optical holography yielded the best fringe resolution and the speckle techniques simplified the data reduction to strain.

For application at the end of the production line, the speckle methods are the most adaptable because they can be more easily digitized using a rotating mirror system or a vidicon system with a scan converter interfaced with a computer. As the system now exists, the shearing speckle techniques are used to inspect the whole surface for flaws. It is expected that 90% to 95% of the items will not contain flaws and can be accepted with no further testing for flaws. The remaining 5% to 10% of the items are then analyzed only in the regions where flaws are detected using Young's Fringe methods to compute the surface strains and accept or reject based on a criterion established by testing some of the first flawed cylinders from the production line. Data from these tests are more reliable because of the variations in composite materials resulting during fabrication on different production lines. A data bank from these tests is then established in the computer memory and a comparison of the surface strains versus acceptable strains is made by the computer on all future items and the item will be shown as accepted or rejected on a printout.

A system to be used at the end of a production line would be better optimized, less expensive, and simpler than some of the laboratory components used here. Complete documentation and drawings required to purchase and fabricate any components are on file in this laboratory and can be made available to personnel in Government or Government contractors in industry for the fabrication of systems to be used in production line applications. Procedures for operation of the system are presented in this report.

X. FUTURE SYSTEM IMPROVEMENTS

Further refinements of the system should be directed toward the film recording to speed up the process. It is possible to eliminate the Young's Fringe analysis and use the shearing speckle interference fringes to do both inspection and analysis.

It may be possible to eliminate the film completely and speed up the process considerably by forming the interference fringes electronically. This was explored by forming the fringes in the scan converter without success but it is still considered feasible if the patterns can be mixed on the target of the vidicon-silicon tube of the camera.

The capabilities of this system can be directed toward a production line inspection technique to assure that the design material properties of composite structures are obtained in all the items. With further development and refinement of the techniques, it is considered feasible to combine the flaw detection and materials into one test.

REFERENCES

1. Stetson, K. and Powell, R., "Hologram Interferometry," Journal of the Optical Society of America, Vol. 54, 1964, p. 1295.
2. Leith, E. N. and Upatnieks, J., "Wavefront Reconstruction with Continuous Tone Objects," Journal of the Optical Society of America, Vol. 53, 1963, pp. 1377-1381.
3. Develis, J. B. and Reynolds G. O., Theory and Applications of Holography, Addison-Wesley, 1967.
4. Caufield, H. J. and Lu, Sun, The Applications of Holography, Wiley Interscience, 1970.
5. Collier, R. J., Burchardt, C. B. and Lin, L. H., Optical Holography, Academic Press, 1971.
6. Holloway, D. C. "Holography and Its Application to Photoelasticity," M. S. Thesis (TAM REPORT 329), Department of Theoretical and Applied Mechanics, University of Illinois, Urbana, Illinois, (June 1969).
7. Mullinix, B. R., Ranson, W. F., Swinson, W. F., and Cost, T. L., Quantification of Flaws in Fibered Composite Structures Using Interferometric Fringe Patterns, US Army Missile Command, Redstone Arsenal, Alabama, 20 April 1976, Technical Report No. RL-76-18.
8. Burch, J. M. and Tokarski, J. M. J., "Production of Multiple Beam Fringes from Photographic Scatterers" 1968 Optica Acta, Vol. 15, pp. 101-111.
9. Archbold, E., Burch, J., Ennos, A., Taylor, D., "Visual Observation of Surface Vibration Nodal Patterns," Nature, Vol. 222, April 1969, p. 263.
10. Leendertz, J., "Interferometric Displacement Measurement on Scattering Surfaces Utilizing Speckle Effect," Journal on Physics E, Vol. 3, 1970, p. 214.
11. Butters, J., "Laser Holography and Speckle Patterns in Engineering Metrology," Symposium on Advanced Experimental Technology in the Mechanics of Materials, September 1970.
12. Butters, J. and Leendertz, J., "A Double Exposure Technique for Speckle Pattern Interferometry," Journal of Physics E, Vol. 4, 1971, p. 277.

13. Hung, Y., Der Hovanesian, J., "Full-field Surface-strain and Displacement Analysis of Three-dimensional Objects by Speckle Interferometry," Experimental Mechanics, Vol. 12, No. 10, October 1972, p. 454.
14. Cloud, G. L., "Quantitative Speckle-Moire Interferometry," paper presented at the 1973 Fall Meeting of the Society for Experimental Stress Analysis.
15. Himes, David, Video Computer Interface Nondestructive Test System Technical Manual, 20 September 1977, Technical Report No. SP-220-1028.

Appendix A. COMPUTER CODE FOR VIDICON CAMERA

The vidicon computer code for Young's Fringe analysis of interferograms is used to control a vidicon camera and scan converter for digitizing and processing video images. The program controls the positioning of an X-Y translation table and initiates the storage of video images. The images which are stored in a scan converter are digitized and then maxima-minima data are extracted to generate fringe spacing information and localized displacement data. The flow chart for the program is shown in Figure A-1. Operation of the computer code is as follows. After the necessary parameters concerning the scan boundary, axis step increments, and X-Y stage translation rates are given, the computer requests the locations of two vertical and two horizontal scan lines for the extraction of video data from the scan converter. Next the machine requests data concerning the erasure, storage, and filtering of video data. The final piece of information to be provided is the system scale factor. Once this information is given, the computer computes the initial coordinates for starting the raster scan of the interferogram. It then advances the X-Y stage to the calculated coordinates. The interferogram aperture is 4×5 in. and the total number of available points for scanning in the X and Y directions is 4000 and 5000, respectively. This gives 20 million possible data points for scanning.

After positioning the X-Y Table for each scan, the computer goes through a sequence of operations for extracting data. First, the scan conversion memory is erased and then one frame of video from the vidicon camera is stored. Next, the computer scans along two horizontal and two vertical lines in the scan converter extracting the video levels stored there. The data for each of the two sets of scan lines is reduced to a zero base level, averaged and squared. The data signals for the horizontal and vertical directions are then filtered and the locations of the fringe maxima and minima are determined. From this information, the fringe spacing and orientation are computed and deflection data are generated. The results are printed out and the X-Y stage advances to a new location for scanning. All scanning of the interferograms is performed in raster fashion as shown in Figure A-2. After a raster scan is completed, the computer returns to its original position. An important point to note is that the location of the X-Y stage before the raster scanning begins is considered to be the origin. This increases the flexibility in using the scanner.

Another major point in the operation of extracting fringe data is the filtering technique which is used. The input signal from the scan converter to the AR11 A/D converter is noisy due to speckle noise and some electrical noise. Therefore, the digitized scan data must be filtered. The filtering is accomplished by specifying the amplitude of the noise which is superimposed upon the desired signal. This parameter is referred to as the filter level and may be determined from the relation:

$$\text{Filter level} = \text{noise level (V)} * \frac{1024}{5}$$

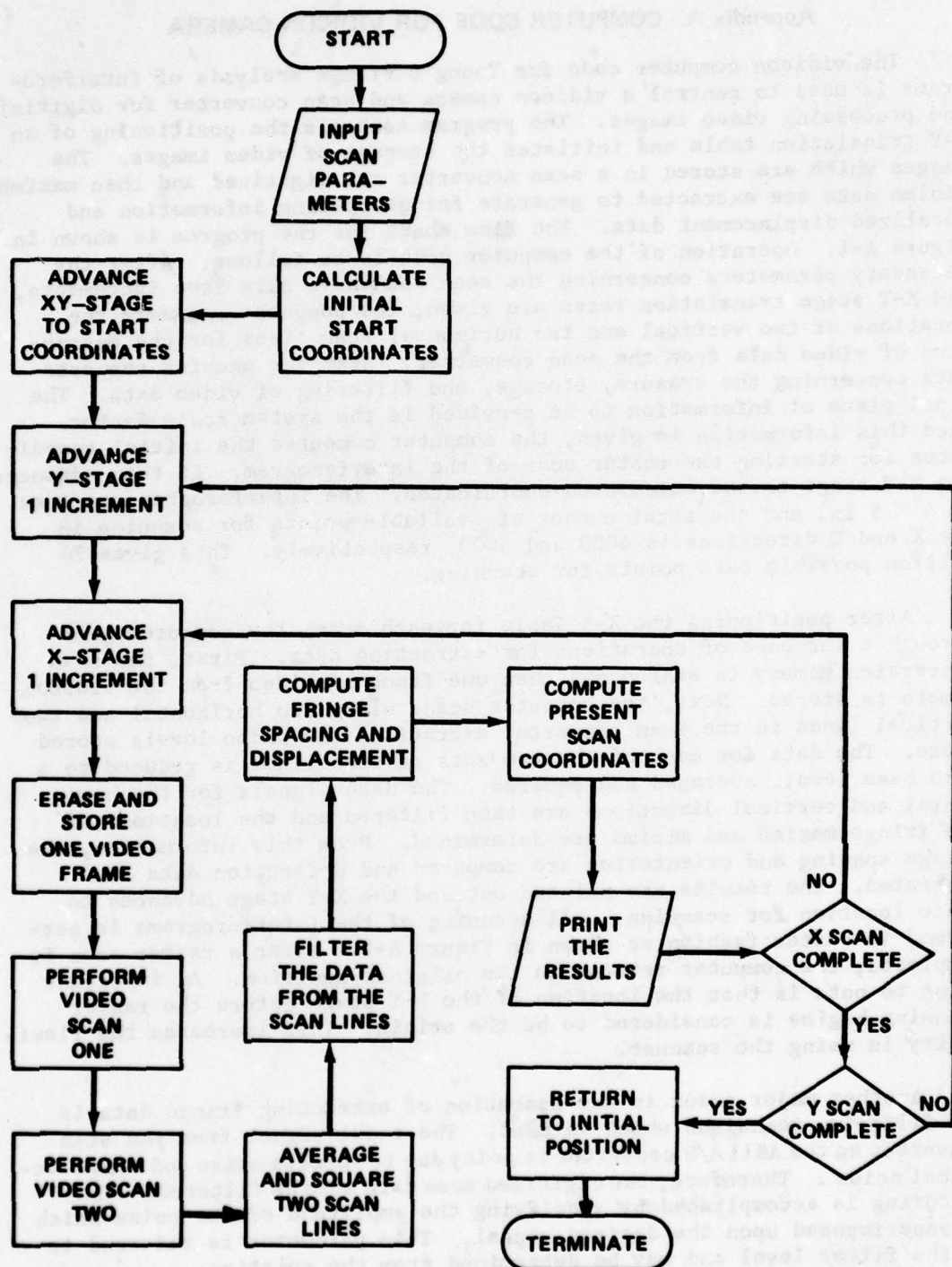


Figure A-1. Vidicon computer code flow chart for Young's Fringe analysis of interferograms.

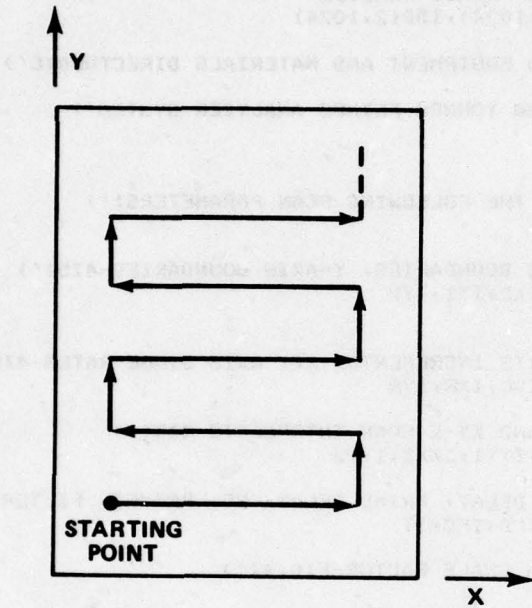


Figure A-2. Raster scanning of interferograms.

It is important to note that the filter will not function properly if the noise level approaches that of the signal level. Because speckle effects are considered to be noise then care must be taken to reduce them.

TT:=DX1:VTEST.FOR

```
C----VIDICON YOUNG'S FRINGE ANALYZER
      DIMENSION ID(2,1024),IDD(2,1024)
      WRITE(5,1)
1      FORMAT(' GROUND EQUIPMENT AND MATERIALS DIRECTORATE')
      WRITE(5,2)
2      FORMAT(' VIDICON YOUNG'S FRINGE ANALYZER SYSTEM')
      WRITE(5,3)
3      FORMAT(' ')
      WRITE(5,4)
4      FORMAT(' INPUT THE FOLLOWING SCAN PARAMETERS:')
      WRITE(5,3)
      WRITE(5,5)
5      FORMAT(' X-AXIS BOUNDARIES, Y-AXIS BOUNDARIES-4I5:')
      READ(5,6) IX1,IX2,IY1,IY2
6      FORMAT(4I5)
      WRITE(5,7)
7      FORMAT(' X&Y AXIS INCREMENTS, X&Y AXIS STAGE RATES-4I5:')
      READ(5,6) IXC,IYC,IXR,IYR
      WRITE(5,8)
8      FORMAT(' XY-1 AND XY-2 SCAN INTERSECTS-4I5:')
      READ(5,6) IXX1,IYY1,IXX2,IYY2
      WRITE(5,9)
9      FORMAT(' STORE DELAY, PRIME DELAY, NO. PRIMES, FILTER LEVEL-4I5:')
      READ(5,6) ISD,IPD,IPC,IT
      WRITE(5,18)
18     FORMAT(' SYSTEM SCALE FACTOR-F10.4:')
      READ(5,19) SF
19     FORMAT(F10.4)
C----MOVE TO THE INITIAL START POSITION
      M1=IX1-IXC
      M2=IY1-IYC
      CALL XADV(M1,IXR)
      CALL YADV(M2,IYR)
C----PERFORM THE INTERFEROGRAM SCAN
      M3=((IY2-IY1)/IYC)+1
      M4=1
      M5=((IX2-IX1)/IXC)+1
      M6=1
      DO 22 J=1,M3,1
      CALL YADV(IYC,IYR)
      DO 21 I=M4,M5,M6
      CALL XADV(IXC,IXR)
21     CONTINUE
      CALL STORE(ISD,IPD,IPC)
      CALL SCAN(IXX1,IYY1,ID)
      CALL SCAN(IXX2,IYY2,IDD)
      IXMIN=1024
      IYMIN=1024
      IXXMIN=1024
      IYYMIN=1024
      DO 10 KK=1,1024,1
      IF(IXMIN.GT.ID(1,KK)) IXMIN=ID(1,KK)
      IF(IYMIN.GT.ID(2,KK)) IYMIN=ID(2,KK)
      IF(IXXMIN.GT.IDD(1,KK)) IXXMIN=IDD(1,KK)
10     IF(IYYMIN.GT.IDD(2,KK)) IYYMIN=IDD(2,KK)
      DO 11 KKK=1,1024,1
      ID(1,KKK)=ID(1,KKK)-IXMIN
      ID(2,KKK)=ID(2,KKK)-IYMIN
      IDD(1,KKK)=IDD(1,KKK)-IXXMIN
      11    ID(2,KKK)=IDD(2,KKK)-IYYMIN
```

```

DO 12 K=1,1024,1
ID(1,K)=(ID(1,K)+IDD(1,K))/2
ID(2,K)=(ID(2,K)+IDD(2,K))/2
ID(1,K)=ID(1,K)*ID(1,K)
12 ID(2,K)=ID(2,K)*ID(2,K)
IXMAX=0
IYMAX=0
ICX=1
ICY=1
DO 13 KKKK=1,1024,1
IF(IXMAX.LT.ID(1,KKKK)) ICX=KKKK
IF(IXMAX.LT.ID(1,KKKK)) IXMAX=ID(1,KKKK)
IF(IYMAX.LT.ID(2,KKKK)) ICY=KKKK
13 IF(IYMAX.LT.ID(2,KKKK)) IYMAX=ID(2,KKKK)
CALL PROCES(ID,IDD,IT,NNX,NNY)
NDX=1024
IF(NNX.LT.3) GOTO 15
NNXM=NNX-1
DO 14 II=2,NNXM,1
14 IF(IDD(1,II).EQ.ICX) NDX=IABS(IDD(1,II+1)-IDD(1,II-1))
NDY=1024
IF(NNY.LT.3) GOTO 17
NNYM=NNY-1
DO 16 JJ=2,NNYM,1
16 IF(IDD(2,JJ).EQ.ICY) NDY=IABS(IDD(2,II+1)-IDD(1,II-1))
CONTINUE
DX=S/FLOAT(NDX)
DY=S/FLOAT(NDY)
NX=IX1+(I-1)*IXC
NY=IY1+(J-1)*IYC
WRITE(5,20) I,J,DX,DY,NX,NY
20 FORMAT(3H X=,I5,3H Y=,I5,4H DX=,E12.5,
14H DY=,E12.5,4H XS=,I5,4H YS=,I5)
ITEST=IPEEK("177570")
IF(ITEST.NE.1) GOTO 25
WRITE(5,23)
23 FORMAT(' NEW FILTER LEVEL:')
READ(5,24) IT
24 FORMAT(I5)
GOTO 26
25 IF(ITEST.EQ.2) GOTO 26
21 CONTINUE
CALL XADV(IXC,IXR)
M7=M4
M4=M5
M5=M7
M6=(-1)*M6
22 IXC=(-1)*IXC
M2=-NY
M1=-NX+IXC
CALL XADV(M1,IXR)
CALL YADV(M2,IYR)
STOP
END
*
```

TT:=DX1:XADV.FOR

```
SUBROUTINE XADV(IS,IR)
C----IS=NO. STEPS (+=FWD,-=REV)
C----IR=ADVANCE RATE OF STAGE
X=0.
IF (IS.GT.0) GOTO 3
IP=IABS(IS)
DO 2 I=1,IP,1
CALL IPOKE("167772,"000000)
CALL IPOKE("167772,"020000)
DO 1 J=1,IR,1
1 Y=SIN(X)
2 CONTINUE
GOTO 6
3 CONTINUE
DO 5 II=1,IS,1
CALL IPOKE("167772,"010000)
CALL IPOKE("167772,"030000)
DO 4 JJ=1,IR,1
4 Y=SIN(X)
5 CONTINUE
6 CONTINUE
RETURN
END
*
```

TT:=DX1:YADV.FOR

```
SUBROUTINE YADV(IS,IR)
C----IS=NO. STEPS (+=FWD,-=REV)
C----IR=ADVANCE RATE OF STAGE
  X=0.
  IF(IS.GT.0) GOTO 3
  IP=IABS(IS)
  DO 2 I=1,IP,1
  CALL IPOKE("167772,"000000)
  CALL IPOKE("167772,"100000)
  DO 1 J=1,IR,1
1   Y=SIN(X)
2   CONTINUE
  GOTO 6
3   CONTINUE
  DO 5 II=1,IS,1
  CALL IPOKE("167772,"040000)
  CALL IPOKE("167772,"140000)
  DO 4 JJ=1,IR,1
4   Y=SIN(X)
5   CONTINUE
6   CONTINUE
  RETURN
  END
*
```

TT:=DX1:STORE.FOR

```
SUBROUTINE STORE(ISD,IPD,IPC)
DO 1 I=1,IPC,1
CALL IPOKE("167772,"00)
CALL IPOKE("167772,"04)
DO 1 J=1,IPD,1
Y=0.
1 X=SIN(Y)
CALL IPOKE("167772,"00)
CALL IPOKE("167772,"01)
DO 2 K=1,ISD,1
Y=0.
2 X=SIN(Y)
CALL IPOKE("167772,"00)
RETURN
END
*
```

TT:=DX1:SCAN.FOR

```
SUBROUTINE SCAN(IX,IY,ID)
DIMENSION ID(2,1024)
C-----X SCAN THE SCAN CONVERTER
CALL IPOKE("170414,IY)
DO 1 I=1,1024,1
CALL IPOKE("170412,I)
CALL IPOKE("167772,"10)
CALL IPOKE("167772,"30)
CALL IPOKE("170400,"20401)
ID(1,I)=IPEEK("170402)
1 CALL IPOKE("167772,"00)
C-----Y SCAN THE SCAN CONVERTER
CALL IPOKE("170412,IX)
DO 2 J=1,1024,1
CALL IPOKE("170414,J)
CALL IPOKE("167772,"10)
CALL IPOKE("167772,"30)
CALL IPOKE("170400,"20401)
ID(2,J)=IPEEK("170402)
2 CALL IPOKE("167772,"00)
RETURN
END
*
```

TT:=DX1:PROCES.FOR

```
SUBROUTINE PROCES(ID,IDD,IT,NNX,NNY)
DIMENSION ID(2,1024),IDD(2,1024)
K=1
1 III=0
LC=1
LC1=1
ID1=0
J=1
2 J=J+1
ID2=IABS(ID(K,J)-ID(K,LC))
IF(ID2.GT.ID1) LC1=J
IF(ID2.GT.ID1) ID1=ID2
ITP=IABS(ID(K,J)-ID(K,LC1))
IF(ITP.LT.IT) GOTO 3
III=III+1
IF(ID(K,LC1).LT.ID(K,LC)) IDD(K,III)=-LC1
IF(ID(K,LC1).GT.ID(K,LC)) IDD(K,III)=LC1
LC=LC1
ID1=0
J=LC
3 IF(J.LT.1024) GOTO 2
IF(K.EQ.1) NNX=III
NNY=III
K=K+1
IF(K.LE.2) GOTO 1
RETURN
END
```

*

Appendix B. COMPUTER CODE FOR ROTATING MIRROR

The computer code for analyzing data from the rotating mirror assembly converts speckle fringe data into displacement information. The operation of the code is described as follows. Before an interferogram scan can begin, the operator of the system is requested to input data parameters. The computer code scans in a raster type of operation in which up to 20 million data points may be examined. Initially, the operator of the computer program sets up the boundaries for the scan by giving the computer the left most, right most, lower, and upper coordinates. Next, the increments between scan points in the X and Y directions are given along with the rates for translating the X and Y stages. This information instructs the machine for the spacing between points for which data are desired and how fast the operation of translating the X-Y stages is to occur. Finally the computer requests a scan level and system scale factor. Once the necessary information has been provided, the computer calculates the initial coordinates for scanning and advances to them.

A sequence of operations is required to raster scan an interferogram. The flow chart for the program is shown in Figure B-1 and Figure B-2. The important point to note from the figures is the method in which fringe maxima are located. Once the X-Y Table has been properly positioned, the A/D converter starts to sample a waveform similar to the one shown in Figure B-3. First the program for converting the waveform remains inactive until the signal voltage swings from below the scan level I_s to above it. The A/D converter then samples the waveform for 1000 conversions. Finally the program converts the sampled data into fringe spacing by locating the maxima and computing the spacing. The criteria for determining these maxima are indicated in Figure B-4. Whenever the slope between three successive data point samples changes from positive to negative, a maxima exists. This technique for maxima determination requires that the input signal be filtered.

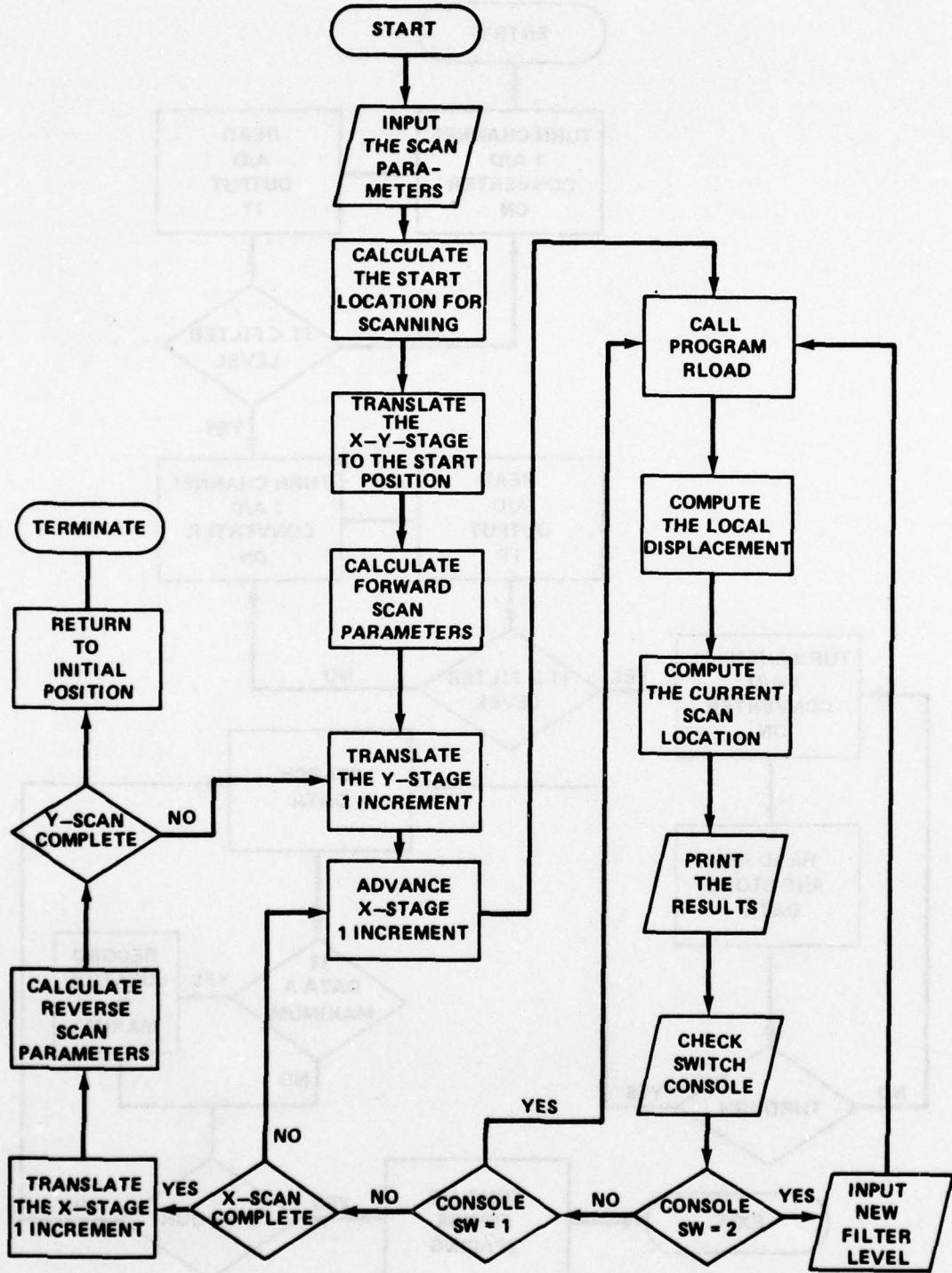


Figure B-1. Rotating mirror analyzer computer code flow chart.

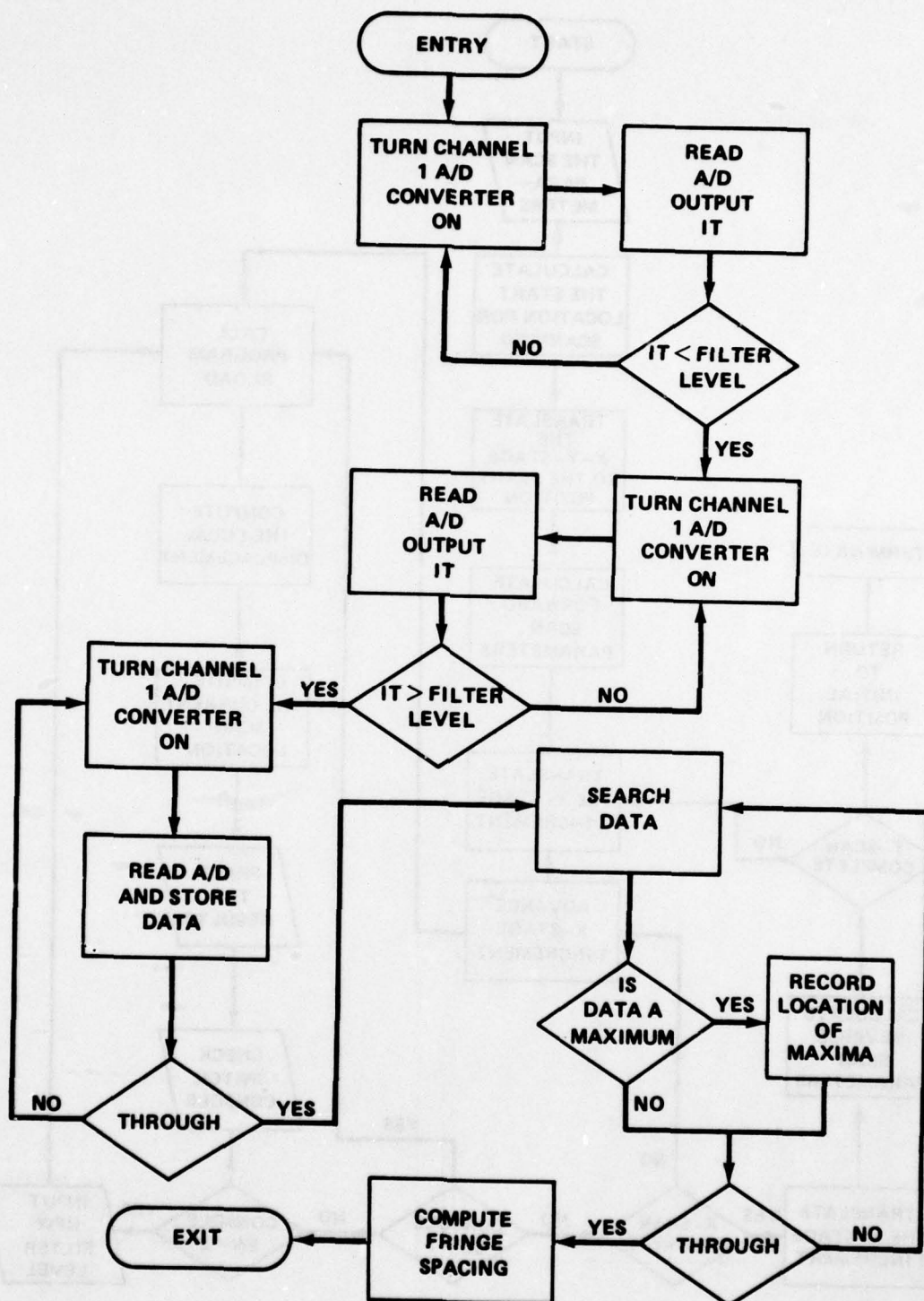


Figure B-2. RLOAD computer flow chart.

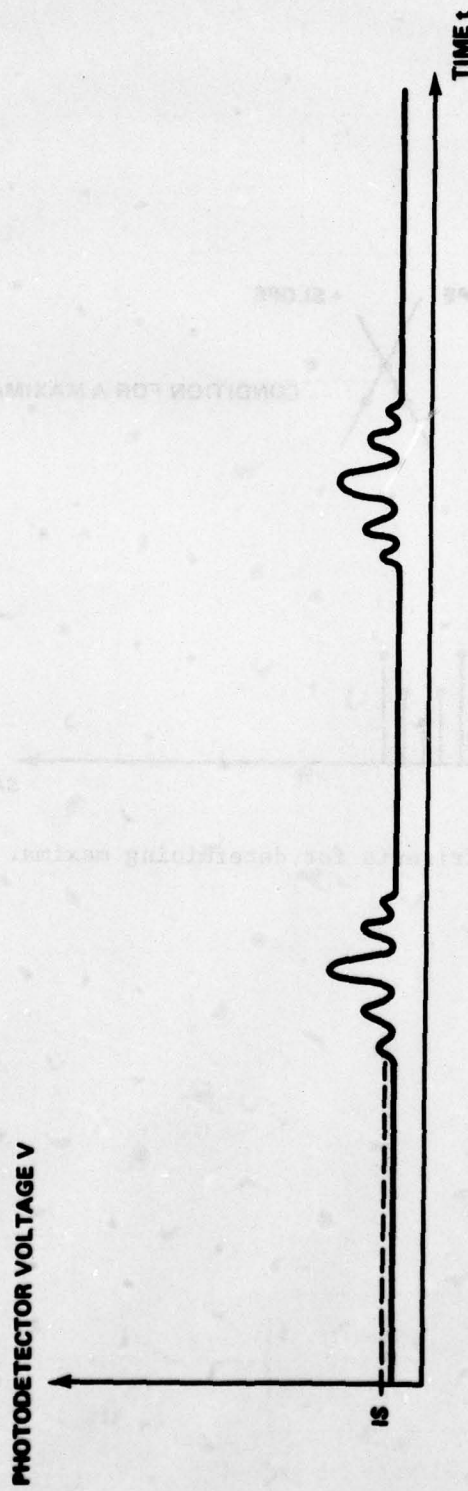


Figure B-3. Periodic photodetector output of a fringe pattern.

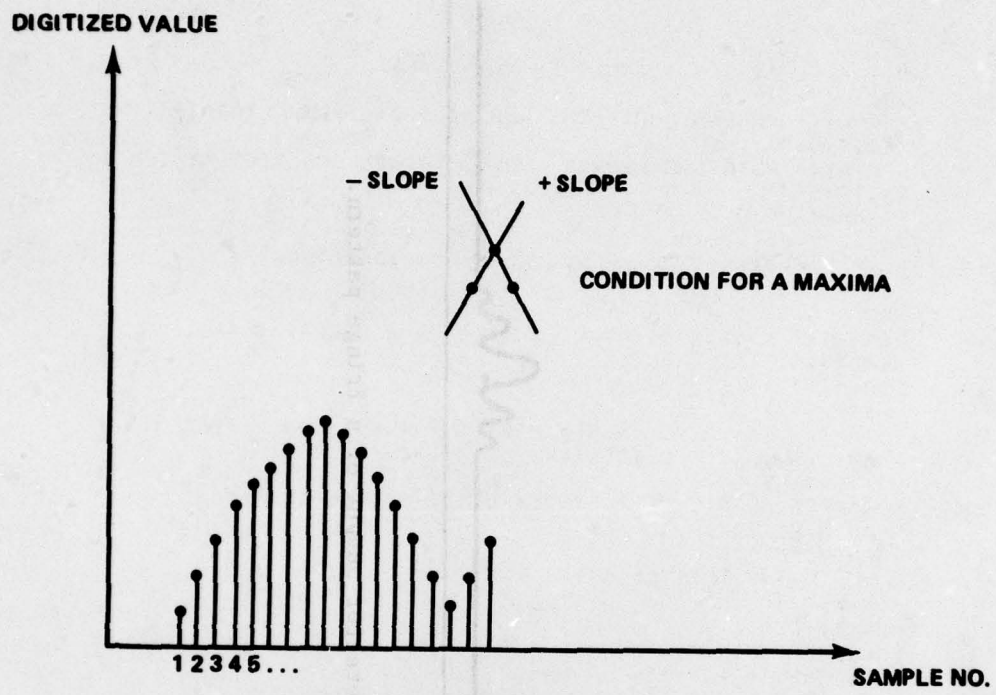


Figure B-4. Criteria for determining maxima.

TT:=DX1:RTEST.FOR

```
C-----ROTATING MIRROR YOUNG'S FRINGE ANALYZER
      WRITE(5,1)
1      FORMAT(' GROUND EQUIPMENT AND MATERIALS DIRECTORATE')
      WRITE(5,2)
2      FORMAT(' ROTATING MIRROR YOUNG'S FRINGE ANALYZER SYSTEM')
      WRITE(5,3)
3      FORMAT(' ')
      WRITE(5,4)
4      FORMAT(' INPUT THE FOLLOWING SCAN PARAMETERS:')
      WRITE(5,3)
      WRITE(5,5)
5      FORMAT(' X-AXIS BOUNDARIES, Y-AXIS BOUNDARIES-4I5:')
      READ(5,6) IX1,IX2,IY1,IY2
6      FORMAT(4I5)
      WRITE(5,7)
7      FORMAT(' X&Y AXIS INCREMENTS, X&Y AXIS STAGE RATES-4I5:')
      READ(5,8) IXC,IYC,IXR,IYR
      WRITE(5,8)
8      FORMAT(' SCAN LEVEL, SYSTEM SCALE FACTOR-I5,F10.')
      READ(5,9) IS,SF
9      FORMAT(I5,F10.4)
C-----MOVE TO THE INITIAL START POSITION
      M1=IX1-IXC
      M2=IY1-IYC
      CALL XADV(M1,IXR)
      CALL YADV(M2,IYR)
C-----PERFORM THE INTERFEROGRAM SCAN
      M3=((IY2-IY1)/IYC)+1
      M4=1
      M5=((IX2-IX1)/IXC)+1
      M6=1
      DO 22 J=1,M3,1
      CALL YADV(IYC,IYR)
      DO 21 I=M4,M5,M6
      CALL XADV(IXC,IXR)
26      CONTINUE
      CALL RLOAD(D,IS)
      D=SF/D
      NX=IX1+(I-1)*IXC
      NY=IY1+(J-1)*IYC
      WRITE(5,20) I,J,NX,NY,D
20      FORMAT(3H X=,I5,3H Y=,I5,4H XS=,I5,
14H YS=,I5,3H D=,E12.5)
      ITEST=IPEEK(*177570)
      IF(ITEST.NE.2) GOTO 25
      WRITE(5,23)
23      FORMAT(' NEW SCAN LEVEL:')
      READ(5,24) IS
24      FORMAT(I5)
      GOTO 26
25      IF(ITEST.EQ.1) GOTO 26
21      CONTINUE
      CALL XADV(IXC,IXR)
```

M7=M4
M4=M5
M5=M7
22 M6=(-1)*M6
IXC=(-1)*IXC
M2=-NY
M1=-NX+IXC
CALL XADV(M1,IXR)
CALL YADV(M2,IYR)
STOP
END
*

TT:=DX1:RLOAD.FOR

```
SUBROUTINE RLOAD(D,IS)
DIMENSION ID(1000),IL(32)
7  CALL IPOKE("170400,"21001)
    IT=IPEEK("170402)
    IF(IT.GT.IS) GOTO 7
2  CALL IPOKE("170400,"21001)
    IT=IPEEK("170402)
    IF(IT.LT.IS) GOTO 2
    DO 3 I=1,1000,1
    CALL IPOKE("170400,"21001)
3  ID(I)=IPEEK("170402)
    DO 4 J=1,1000,1
4  IF(ID(J).LT.IS) ID(J)=0
    KC=0
    NC=0
    KT=0
    DO 5 K=2,1000,1
    IF(NC.GT.32) GOTO 5
    IF(ID(K).GT.ID(K-1)) KC=1
    IF(ID(K).LT.ID(K-1).AND.KC.EQ.1) KT=1
    IF(KT.NE.1) GOTO 5
    NC=NC+1
    KC=0
    KT=0
    IL(NC)=K-1
5  CONTINUE
    IF(NC.LT.2) D=1E6
    IF(NC.LT.2) GOTO 6
    D=FLOAT(IL(NC)-IL(1))/FLOAT(NC-1)
6  RETURN
END
*
```

TT:=DX1:XADV.FOR

```
SUBROUTINE XADV(IS,IR)
C----IS=NO. STEPS (+=FWD,-=REV)
C----IR=ADVANCE RATE OF STAGE
  X=0.
  IF(IS.GT.0) GOTO 3
  IP=IABS(IS)
  DO 2 I=1,IP,1
  CALL IPOKE("167772,"000000)
  CALL IPOKE("167772,"020000)
  DO 1 J=1,IR,1
 1   Y=SIN(X)
 2   CONTINUE
  GOTO 6
 3   CONTINUE
  DO 5 II=1,IS,1
  CALL IPOKE("167772,"010000)
  CALL IPOKE("167772,"030000)
  DO 4 JJ=1,IR,1
 4   Y=SIN(X)
 5   CONTINUE
 6   CONTINUE
  RETURN
END
*
```

TT:=DX1:YADV.FOR

2915470101

```
SUBROUTINE YADV(IS,IR)
C----IS=NO. STEPS (+=FWD,-=REV)
C----IR=ADVANCE RATE OF STAGE
      X=0.
      IF(IS.GT.0) GOTO 3
      IP=IABS(IS)
      DO 2 I=1,IP,1
      CALL IPOKE("167772","000000")
      CALL IPOKE("167772","100000")
      DO 1 J=1,IR,1
      1   Y=SIN(X)
      2   CONTINUE
      GOTO 6
      3   CONTINUE
      DO 5 II=1,IS,1
      CALL IPOKE("167772","040000")
      CALL IPOKE("167772","140000")
      DO 4 JJ=1,IR,1
      4   Y=SIN(X)
      5   CONTINUE
      6   CONTINUE
      RETURN
      END
*
```

LIST OF TABLES

Table		
1	THEORETICAL CALCULATION FOR CANTILEVER BEAM	55
2	RESULTS OF SCAN LINE SEPARATION FOR THE BEAM EXAMPLE . .	132
3	SCAN CONVERTER INTERFACE CONTROL FUNCTIONS	134

LIST OF FIGURES

Figure		
1	Composite cylinder with simulated circumferential flaw. .	5
2	Composite cylinder with simulated longitudinal flaw . . .	6
3	Composite cylinder with simulated spot flow	7
4	Geometrical relationships for phase change for a deformed body	9
5	Geometry used to measure the surface deformation of cylindrical shells.	13
6	Geometrical relationships for the directions \vec{PS} and \vec{PO}	14
7	Symmetrical deformation displacement component \vec{PP}' for a circular cylinder	15
8	Geometry used to measure the radial displacement component for cylindrical shells with non-symmetrical deformation	16
9	Geometrical relationships for the \vec{PS} and \vec{PO} directions in the $X_1 - X_2$ plane.	17
10	Fringe order for symmetrical deformation of an aluminum cylinder	19
11	Typical composite cylinder.	19
12	Fringe pattern for the cylinder with a spot flaw.	20
13	Surface deformation of composite cylinder with a spot flaw, internal pressure 10 psig	22
14	Fringe pattern for the cylinder with a circumferential flaw.	23
15	Surface deformation of composite cylinder with a circumferential flaw, internal pressure 20 psig	24

Figure		Page
16	Fringe pattern for the cylinder with a longitudinal flaw.	25
17	Fringe orders of a composite cylinder with a longitudinal flaw, internal pressure 10 psig	26
18	Surface deformation of composite cylinder with a longitudinal flaw, internal pressure 10 psig.	27
19	Double-exposed hologram of the test vessel.	29
20	Flaw location under Section A at the center of the vessel.	30
21	Typical hologram of homogeneous aluminum pressure vessel	31
22	Flaw detection	33
23	Skematic of fringe pattern analyzer.	34
24	A computer graphics representation of the holographic fringe pattern from a composite cylinder	36
25	Fringe density plots by computer of the fringe patterns in Figures 23 and 24	37
26	Longitudinal disbond in a composite cylinder	39
27	Circumferential disbond in a composite cylinder.	40
28	Circumferential disbond in a composite cylinder.	41
29	Shearing speckle interferometry.	43
30	Arrangement for transform analysis	45
31	Wedge geometry	46
32	Lens geometry.	48
33	Wedge effect	48
34	Arrangement for analysis	51
35	Displacement vectors	51
36	Experimental arrangement	53
37	Theoretical fringes.	55
38	Filtered image (all lines with Argon Laser).	56
39	Photograph of cantilever beam off TV monitor	57
40	Comparison of theory and experiment.	58
41	Pressure vessel.	60
42	Pressure vessel experimental setup	61

Figure	Page
43 Circumferential flaw, filtered image	63
44 Longitudinal flaw, filtered image.	64
45 Spot flaw, filtered image.	65
46 Arrangement for single beam analysis	66
47 Arrangement for data collection.	71
48 Experimental setup	72
49 Cantilever beam.	73
50 Cantilever beam, Young's fringes	75
51 Cantilever beam, Young's fringes	75
52 Comparison of theory and experiment.	76
53 Collection of speckle interferometric data	78
54 Data analysis.	78
55 Rectangular aperture arrangement	79
56 Fraunhofer diffraction by two apertures.	82
57 Multiple apertures	84
58 Intensity distribution of multiple apertures	85
59 Cylinder with spot flaw and Young's fringes shown with the grid system.	87
60 Grid locations versus axial displacements (microinches). .	88
61 Experimental arrangement	89
62 Coordinate axis.	90
63 Fringe pictures (every 0.2 in.).	91
64 y-displacement as a function of y-coordinate for the spot flaw cylinder ($x = 0.0 - x = 0.3$).	92
65 y-displacement as a function of y-coordinate for the spot flaw cylinder ($x = 0.4 - x = 0.7$).	93
66 y-displacement as a function of y-coordinate for the spot flaw cylinder ($x = 0.8 - x = 1.1$).	94
67 y-displacement as a function of y-coordinate for the spot flaw cylinder ($x = 1.2 - x = 1.5$).	95
68 y-displacement as a function of y-coordinate for the spot flaw cylinder ($x = 1.6 - x = 1.9$).	96
69 Strain distribution for spot flaw cylinder	97

Figure	Page
70 y-displacement as a function of y-coordinate for longitudinal flaw ($x = 0 - x = 0.3$)	98
71 y-displacement as a function of y-coordinate for longitudinal flaw ($x = 0.4 - x = 0.7$)	99
72 y-displacement as a function of y-coordinate for longitudinal flaw ($x = 0.8 - x = 1.1$)	100
73 y-displacement as a function of y-coordinate for longitudinal flaw ($x = 1.2 - x = 1.5$)	101
74 y-displacement as a function of y-coordinate for longitudinal flaw ($x = 1.6 - x = 1.9$)	102
75 Strain distribution for longitudinal flaw cylinder	103
76 y-displacement as a function of y-coordinate for circumferential flaw ($x = 0 - y = 0$)	104
77 y-displacement as a function of y-coordinate for circumferential flaw ($x = 0.5 - x = 0.8$)	105
78 y-displacement as a function of y-coordinate for circumferential flaw ($x = 0.9 - x = 1.2$)	106
79 y-displacement as a function of y-coordinate for circumferential flaw ($x = 1.3 - x = 1.4$)	107
80 Strain distribution for circumferential flaw cylinder	108
81 Typical speckle photography fringe pattern used in the optical data analysis system	110
82 Optical system used for computer aided data reduction.	111
83 Translation table and laser beam path.	112
84 Photograph of the translation stage assembly	113
85 Rotating mirror system used for computer aided data reduction.	114
86 Optical configuration for the rotating mirror analyzer	115
87 θ versus ϕ for $N = 0.25$	117
88 Operational amplifier.	118
89 Computer-aided speckle analyzer.	119
90 Video computer interface	121
91 Complete system.	122
92 Rotating mirror system block diagram	123

Figure	Page
93 (a) Photograph of diffraction pattern, (b) digitized scan of a horizontal line	124
94 Average intensity of two scan lines from a diffraction pattern.	126
95 Photographs of the diffraction pattern of the cantilever beam at various distances measured from the fixed end. . . .	127
96 Comparison of fringe spacing values measured by an observer and computer scan measurement	129
97 Computer results of ten and twenty line scan separation. . . .	130
98 Oscilloscope trace of the output from the photodiode of a typical fringe pattern (horizontal sweep 5 msec/cm, vertical 0.5 V/cm)	131
99 (a) Unfiltered scope trace of the photodiode output, (b) Filtered trace of the same signal (horizontal sweep 5 msec/cm, vertical 0.5 V/cm).	131
100 Comparison of fringe spacing values measured by rotating mirror system	133
101 Rotating mirror scan results of the spot flaw.	141
102 Rotating mirror scan results of the longitudinal flaw. . . .	142
103 Electromechanical single-beam speckle interferometric analyzer system.	144
104 Video computer interface block diagram	145
105 Video computer interface panel	149
106 X-Y translator driver panel.	150

DISTRIBUTION

No. of Copies	No. of Copies	
Defense Metals Information Center Battelle Memorial Institute 505 King Avenue Columbus, Ohio 43201	1 Commander US Army Aeronautical Depot Maintenance Center (Mail Stop) Corpus Christi, Texas 78403	1
Defense Documentation Center Cameron Station Alexandria, Virginia 22314	2 Commander US Army Test and Evaluation Command Attn: DRSTE-RA Aberdeen Proving Ground, Maryland 21005	1
Commander US Army Foreign Science and Technology Center Attn: DRKST-SD3 220 Seventh Street, NE Charlottesville, Virginia 22901	1 Commander Attn: STEAP-MT Aberdeen Proving Ground, Maryland 21005	1
Office of Chief of Research and Development Department of the Army Attn: DARD-ARS-P Washington, D. C. 20301	1 Chief Bureau of Naval Weapons Department of the Navy Washington, D. C. 20390	1
Commander US Army Electronics Command Attn: DRSEL-PA-P -CT-DT -PP, Mr. Sulkolove Fort Monmouth, New Jersey 07703	1 Chief Bureau of Ships Department of the Navy Washington, D. C. 20315	1
Commander US Army Natick Laboratories Kansas Street Attn: STSNLT-EQR Natick, Massachusetts 01760	1 Naval Research Laboratory Attn: Dr. M. M. Krafft Code 8430 Washington, D. C. 20375	1
Commander US Army Mobility Equipment Research and Development Center Fort Belvoir, Virginia 22060	1 Commander Wright Air Development Division Attn: ASRC Wright-Patterson AFB, Ohio 45433	1
Director USA Mobility Equipment Research and Development Center Coating and Chemical Laboratory Attn: STSFB-CL Aberdeen Proving Ground, Maryland 21005	1 Director Air Force Materiel Laboratory Attn: AFML-DO-Library Wright-Patterson AFB, Ohio 45433	1
Commander Edgewood Arsenal Attn: SAREA-TS-A Aberdeen Proving Ground, Maryland 21010	1 Director, Army Materials and Mechanics Research Center Attn: DRXMR-PL -MT, Mr. Farrow Watertown, Massachusetts 02172	1
Commander Picatinny Arsenal Attn: SAPFA-TS-S, Mr. M. Costello Dover, New Jersey 07801	1 Commander White Sands Missile Range Attn: STEWS-AD-L White Sands Missile Range, New Mexico 88002	1
Commander Rock Island Arsenal Research and Development Attn: 9320 Rock Island, Illinois 61201	1 Deputy Commander US Army Nuclear Agency Attn: MONA-ZB Fort Bliss, Texas 79916	1
Commander Watervliet Arsenal Watervliet, New York 12189	1 Jet Propulsion Laboratory California Institute of Technology Attn: Library/Acquisitions 111-113 4800 Oak Grove Drive Pasadena, California 91103	1
Commander US Army Aviation Systems Command Attn: DRSAV-EE -MT, Mr. Vollmer St. Louis, Missouri 63166	1 Sandia Laboratories Attn: Library P. O. Box 969 Livermore, California 94550	1
	1 Commander US Army Air Defense School Attn: ATSA-CD-MM Fort Bliss, Texas 79916	1

	No. of Copies
Technical Library Naval Ordnance Station Indian Head, Maryland 20640	1
Commander US Army Materiel Development and Readiness Command Attn: DRCMT Washington, D. C. 20315	1
Headquarters SAC/NRI (Stinfo Library) Offutt Air Force Base, Nebraska 68113	1
Commander Rock Island Arsenal Attn: SARRI-RLPL-Technical Library Rock Island, Illinois 61201	1
Commander (Code 233) Naval Weapons Center Attn: Library Division China Lake, California 93555	1
Department of the Army US Army Research Office Attn: Information Processing Office P. O. Box 12211 Research Triangle Park, North Carolina 27709	1
ADTC (DLDSL) Eglin Air Force Base, Florida 32542	1
University of California Los Alamos Scientific Laboratory Attn: Reports Library P. O. Box 1663 Los Alamos, New Mexico 87545	1
Commander US Army Materiel Development and Readiness Command Attn: DRCRD DRCDL 5001 Eisenhower Avenue Alexandria, Virginia 22333	1
Superior Technical Services, Inc. 4308 Governors Drive Attn: T. Ward Huntsville, Alabama 35805	1
DRSMI-LP, Mr. Voigt	1
DRDMI-X	1
-T, Dr. Kobler	1
-TL, Mr. Lewis	1
-TLA, Mr. Pettey	1
-TLA, Dr. Mullinix	175
Mr. Schaeffel	12
-EA	2
-EAA	2
-EAS	1
-EAM	1
-EAP	1
-EAR	1
-EAT	3
-ICBB	1
-TBD	3
-TI (Record Set) (Reference Copy)	1